

CHEMIA

**STUDIA
UNIVERSITATIS BABEȘ-BOLYAI
CHEMIA**

3/2013

EDITORIAL BOARD
STUDIA UNIVERSITATIS BABEȘ-BOLYAI
CHEMIA

ONORARY EDITOR:

IONEL HAIDUC - Member of the Romanian Academy

EDITOR-IN-CHIEF:

LUMINIȚA SILAGHI-DUMITRESCU

EXECUTIVE EDITOR:

CASTELIA CRISTEA

EDITORIAL BOARD:

PAUL ȘERBAN AGACHI, Babeș-Bolyai University, Cluj-Napoca, Romania

LIVAIN BREAU, UQAM University of Quebec, Montreal, Canada

HANS JOACHIM BREUNIG, Institute of Inorganic and Physical Chemistry,
University of Bremen, Bremen, Germany

MIRCEA DIUDEA, Babes-Bolyai University, Cluj-Napoca, Romania

JEAN ESCUDIE, HFA, Paul Sabatier University, Toulouse, France

ION GROSU, Babeș-Bolyai University, Cluj-Napoca, Romania

EVAMARIE HEY-HAWKINS, University of Leipzig, Leipzig, Germany

FLORIN DAN IRIMIE, Babeș-Bolyai University, Cluj-Napoca, Romania

FERENC KILAR, University of Pecs, Pecs, Hungary

BRUCE KING, University of Georgia, Athens, Georgia, USA

ANTONIO LAGUNA, Department of Inorganic Chemistry, ICMA, University of
Zaragoza, Zaragoza, Spain

JURGEN LIEBSCHER, Humboldt University, Berlin, Germany

KIERAN MOLLOY, University of Bath, Bath, UK

IONEL CĂȚĂLIN POPESCU, Babeș-Bolyai University, Cluj-Napoca, Romania

CRISTIAN SILVESTRU, Babeș-Bolyai University, Cluj-Napoca, Romania

<http://chem.ubbcluj.ro/~studiachemia/>; studiachemia@chem.ubbcluj.ro
http://www.studia.ubbcluj.ro/serii/chemia/index_en.html

YEAR
MONTH
ISSUE

Volume 58 (LVIII) 2013
SEPTEMBER
3

S T U D I A
UNIVERSITATIS BABEȘ-BOLYAI
CHEMIA

3

Desktop Editing Office: 51ST B.P. Hasdeu, Cluj-Napoca, Romania, Phone + 40 264-40.53.52

CUPRINS – CONTENT – SOMMAIRE – INHALT

ANA-MARIA CORMOS, ABEL SIMON, Dynamic Modeling of Carbonator from Calcium-Looping Process used for Carbon Capture	7
DANIELA CIOLOBOC, MARIANN-KINGA ARKOSI, RADU SILAGHI-DUMITRESCU, A New Protocol for Purifying Human Serum Albumin	19
PÉTER SIMON, KLÁRA PÁSZTOR-HUSZÁR, ISTVÁN DALMADI, GABRIELLA KISKÓ, LIVIA SIMON-SARKADI, Biogenic Amine Content in Cheese Produced with Different Selected Lactic Acid Bacterial Strains	25
FLAVIA POP, LIVIU GIURGIULESCU, ANCA DUMUȚA, ZORICA VOȘGAN, The Influence of Frozen Storage on Fatty Acids Composition for Alimentary Animal Fats	31
ALEXANDRU OKOS, AUREL POP, CÉLINE DARIE, PIERRE BORDET, High Pressure - High Temperature Synthesis and Phase Characterization of PbVO ₃ Perovskite Compound	39
GYULA TOLNAI, ISTVAN SAJO, EMIL HOLCZER, FIAMMETTA KORMOS, IRINA TARSICHE, DORIN MANCIULA, Sb/SnO ₂ Nanostructured Anticorrosive Coatings on Metals	45
ROXANA BOSTAN, SIMONA VARVARA, MARIA POPA, LIANA MARIA MURESAN, Evaluation of Phenothiazine as Environmentally Friendly Corrosion Inhibitor for Bronze in Synthetic Acid Rain	53

MIHAELA-DANIELA GAVRIL (DONOSE), UDO SCHMIDT, CONSTANTIN GHEORGHIES, ALINA-MIHAELA CANTARAGIU, ADRIANA ISPAS, ANDREAS BUND, Electrochemical Preparation of Co-Cu Alloy Nanowires and their Characterisation	63
FLORIN ALIN HANC-SCHERER, PETRU ILEA, Electrochemical Reduction of CO ₂ on lead Electrode. I. Cyclic Voltammetry and Long Time Electrosynthesis Studies	75
NABEEL E. ARIF, ROSLAN HASNI, The Connectivity Index of Pamam Dendrimers	85
SAEID ALIKHANI, CHANGIZ ESLAHCHI, MOHAMMAD ALI IRANMANESH, Harary Index of an Infinite Family of Dendrimer Nanostars	93
VIRGINIA BUCILA, MONICA STEFU, BEATA SZEFLER, Octahedral CNT Junctions as P-Type Networks	101
LUBANG WANG, MINGJUN HU, Omega and Sadhana Polynomials of Two Classes of Molecular Graphs	117
DOINA A. TODEA, SZENDE TONK, ANCUȚA E. TIUC, ANAMARIA TÖRÖK, CARMEN MÂNZATU, GABRIEL KATONA, CORNELIA MAJDIK, Efficient Degradation of Phenol with <i>Pseudomonas Putida</i> Cells for the Production of Pure Water	125
DOINA A. TODEA, SZENDE TONK, ANCUȚA E. TIUC, ANAMARIA TÖRÖK, CARMEN MÂNZATU, GABRIEL KATONA, CORNELIA MAJDIK, Continuous Flow Waste Water Purification with Immobilized <i>Cells</i>	135
GORAN V. JANJIĆ, MILOŠ K. MILČIĆ, VESNA B. MEDAKOVIĆ, Influence of Supramolecular Structure in the Crystals on Water / Aromatic Parallel Alignment Interactions	143
SZILÁGYI BOTOND, BARABÁS RÉKA, Continuous Precipitation: a Model Based Stability Analysis	155
ELENA PREDĂ, MANUELA MARIA MINCEA, COSMIN IONAȘCU, ALEXANDRU VALENTIN BOTEZ, VASILE OSTAFE, An Ultrahigh Performance Liquid Chromatography - Mass Spectrometry Method for the Analyses of Phenol Derivatives from Waters	167

Studia Universitatis Babes-Bolyai Chemia has been selected for coverage in Thomson Reuters products and custom information services. Beginning with V. 53 (1) 2008, this publication is indexed and abstracted in the following:

- Science Citation Index Expanded (also known as SciSearch®)
- Chemistry Citation Index®
- Journal Citation Reports/Science Edition

DYNAMIC MODELING OF CARBONATOR FROM CALCIUM-LOOPING PROCESS USED FOR CARBON CAPTURE

ANA-MARIA CORMOS^a, ABEL SIMON^a

ABSTRACT. Carbon capture and storage (CCS) technologies are mitigation measures aimed to reduce CO₂ emissions from energy and other energy-intensive sectors. Among various CCS technologies, chemical looping systems (e.g. the calcium-looping process) are considered as potential solutions to reduce CO₂ capture energy penalty. The paper presents a dynamic mathematical model of carbonation reactor of calcium-looping process to be used for carbon capture in fossil fuel-based power plants. The mathematical model described the particle distribution in carbonator according a 1D model for fast fluidization presented by Kunii and Levenspiel. The CO₂ adsorption efficiency in the carbonator is divided in two terms, taking into account the dense and lean regions of the bed.

Keywords: carbon capture, Ca-looping process, dynamic mathematical modeling

INTRODUCTION

Power generation sector which use fossil fuels (coal, lignite, natural gas etc.) is a major contributor to the increase of carbon dioxide concentration in the atmosphere and it consequently leads to global warming [1]. In order to limit the climate change modifications, it is now widely recognized that large-scale reductions in carbon dioxide (CO₂) emissions are required. However, the first generation CCS technology, i.e. scrubbing with amines, is energy intensive [2] and, thus, results in a substantial decrease in the overall plant efficiency (in the range of 10 net electrical percentage points [1]). To reduce the costs associated with the capture of CO₂, 2nd and 3rd generation CCS technologies, such as carbonate looping or chemical looping combustion (CLC) have been proposed [3]. The basic idea of the calcium looping process is to use calcium oxide as sorbent of CO₂, through the theoretically reversible, reaction: $\text{CaO} + \text{CO}_2 \leftrightarrow \text{CaCO}_3$.

^a Babeş-Bolyai University, Faculty of Chemistry and Chemical Engineering, Arany Janos 11, RO-400028 Cluj-Napoca, Romania, cani@chem.ubbcluj.ro

The use of a Ca-based sorbent as a CO₂ acceptor was first patented in 1933 and assessed by other scientists for sorption-enhanced hydrogen production [4], the application of a Ca-based sorbent in a post-combustion configuration was first proposed by Shimizu et al. (1999) [5]. The experimental validation of the Ca-looping concept has progressed rapidly. The experimental investigating of the cyclic CO₂ capture process occurring limestone have been performed in different reactor set-ups, e.g. thermogravimetric analysers [6,7], packed bed reactors [8, 9] or fluidized bed reactors [10-13] a rapid decrease in CO₂ uptake with number of repeated cycles of carbonation and calcination was reported.

In fluidized bed reactors configuration, carbon dioxide in the flue gas of a coal-fired power plant is captured by its reaction with calcium oxide in a fluidized bed reactor (carbonator) and removed at high temperature from the gaseous phase by producing CaCO₃. After new recovery, decarbonized flue gas is vented in to the atmosphere while calcium carbonate converted back into CaO and gaseous CO₂ in a calciner. The regenerated sorbent produced in the calciner is then returned to the carbonator for a new sorption cycle, while the CO₂-rich gas is cooled and compressed for permanent storage after final purification (figure 1).

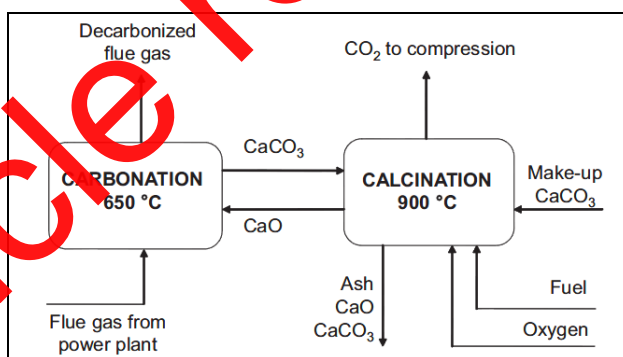


Figure 1. Scheme of the carbonate looping process [14]

Some studies on plant modeling and simulation have also been published to estimate the performance of complete power plants, which confirm the inherent thermodynamic advantages of the Ca-looping concept [5, 14, 15]. Abanades et al. [11] adapted the model proposed by Kunii and Levenspiel [16] for two-region reactor: bubble and emulsion to the conditions of the experiments carried out in a fluidised bed carbonator and included a full kinetic model for the carbonation reaction in two stages proposed by Bhatia and Perlmutter [17]. According to this kinetic model, carbonation reaction takes places in two stages at different reaction rate: a first regime of chemical reaction control where

reaction occurs at the highest velocity and a second period of product layer diffusion control due to the fact that the CaCO_3 layer thickness increases. The models proposed by Hawthorne et al. [18]; Lasheras et al. [14] and Romano [19] have been based on the core-annulus model of Kunii and Levenspiel [20] and considered the reactor as a circulating fluidized bed where two zones were distinguished: a bottom dense zone and a lean one located above. The most detailed reactor model has been considered which was developed by Romano (2012) [19] that evaluated the CO_2 concentration profiles in the core and wall zone of the dense part, and the CO_2 profile in the lean zone. But a detailed dynamic model to describe the dynamic behaviour have not presented. Using modelling and simulation methods, the potential applications of calcium based chemical looping system to generate simultaneously hydrogen and power with almost total decarbonisation of the coal was investigated too [21]. The goal of this paper is to develop and validate against experimental data published in literature a dynamic model of the carbonator of a Ca-looping process and to investigate the effects of different operating conditions on its performance.

MATHEMATICAL MODELING

The mathematical model of carbonator is expressed by referring to an ideal plug-flow reactor and includes partial differential equations (PDE) to describe the time and space dependent parameters [19].

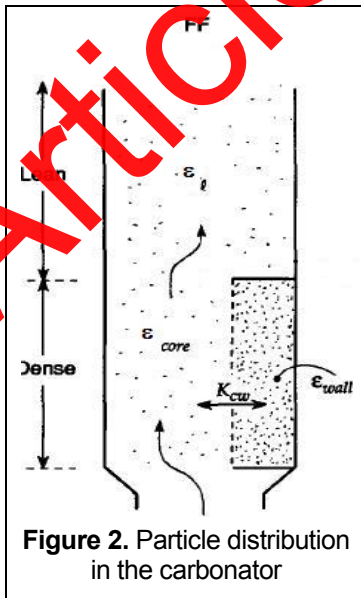


Figure 2. Particle distribution in the carbonator

The particles distribution in the carbonator is determined by a 1D model for fast fluidization as presented by Kunii and Levenspiel [16]. In this model, the reactor is divided into two regions: the dense region, in the lower part of the riser, where the volume fraction of the solids, ϵ_{sd} is constant, and the lean region where the volume fraction of solids decreases exponentially with height. In the dense zone, ϵ_{sd} value depends on the superficial velocity u_0 and the mean particle diameter d_p . In case of fast fluidization for ϵ_{sd} value a ranges 0.06–0.2 has been suggested by Kunii and Levenspiel [20]. The radial distribution consists of dense bottom zone is divided in two: a leaner core zone and a denser wall zone with solid volumetric fractions of ϵ_{sc} and ϵ_{sw} , respectively, figure 2 [16,20].

The hydrodynamics of circulating fluidized beds

Given the total reactor height H_t , the lean and dense zone height H_l , H_d and mass of solids in each zone W_l , W_d could be determinate using the following equations [20].

$$H_l = \frac{1}{a} \ln \frac{(\varepsilon_{sd} - \varepsilon_s^*)}{(\varepsilon_{se} - \varepsilon_s^*)} \quad (1)$$

$$H_d = H_t - H_l \quad (2)$$

$$W_d = A_t \rho_s H_d \varepsilon_{sd} \quad W_l = A_t \rho_s H_l f_l \quad (3)$$

where

$$f_l = \varepsilon_s^* + \frac{\varepsilon_{sd} - \varepsilon_{se}}{H_l a} \quad (4)$$

The decay constant (a) used in equation 4 is determined from the values ranging from 2 to 7 s^{-1} proposed for the constant au_0 [20].

The volume fraction of solids at the reactor exit ε_s^* could be determinate by following equation:

$$\varepsilon_s^* = \frac{G_s^*}{(u_0 - u_T) \cdot \rho_s} \quad (5)$$

$$\varepsilon_s^* = \frac{G_s^*}{u_0 \cdot \rho_s} \quad (6)$$

The mass velocity of solids at the exit of the riser G_s^* can be calculated as a function of terminal velocity u_T and superficial gas velocity u_0 assuming spherical particles [22].

$$G_s^* = 23.7 \rho_g u_0 \exp\left(-5.5 \frac{u_T}{u_0}\right) \quad (7)$$

The terminal free-fall velocity u_T , depends on the particle diameter d_p , solid and gas density ρ_s , ρ_g and the viscosity μ of the gas under the given conditions [20].

$$d_p^* = d_p \left[\frac{\rho_g (\rho_s - \rho_g) g}{\mu^2} \right]^{1/3} \quad (8)$$

$$u_T^* = \left[\frac{18}{(d_p^*)^2} + \frac{0,591}{(d_p^*)^{1/2}} \right]^{-1} \quad (9)$$

$$u_T = u_T^* \left[\frac{\mu(\rho_s - \rho_g)g}{\rho_g^2} \right]^{1/3} \quad (10)$$

Mass balance

The particle conversion model proposed by Grasa et al. [23] similar to that proposed by Bhatia and Perlmutter [17] is used in this work. According to this model, the correlation which defines the carbonation degree X can be expressed according to a first order kinetic law where the kinetic constant k_r is a function of the carbonation degree itself [17]:

$$\frac{dX}{dt} = k_r (C_{CO_2} - C_{CO_2,eq}) = k_r S_N (1-X)^{2/3} (C_{CO_2} - C_{CO_2,eq}) \quad (11)$$

On base of particle conversion model the material balance for the lean region is:

$$\frac{d(C_{CO_2} - C_{CO_2,eq})}{dt} = u_0 \frac{d(C_{CO_2} - C_{CO_2,eq})}{dz} - \xi \varepsilon_{sl} \eta_i k_{ri} (C_{CO_2} - C_{CO_2,eq}) \quad (12)$$

The dense region is divided into a wall and core region, where the material balances are described bellow.

For core zone:

$$\begin{aligned} \frac{d(C_{CO_2,c} - C_{CO_2,eq})}{dt} = & - \\ & - u_c \frac{d(C_{CO_2,c} - C_{CO_2,eq})}{dz} - \frac{\xi V_{s,c}}{V_{g,c}} k_{ri} (C_{CO_2,c} - C_{CO_2,eq}) - \\ & - k_{cw} (C_{CO_2,c} - C_{CO_2,w}) \end{aligned} \quad (13)$$

For wall zone:

$$\begin{aligned} A_{g,w} \frac{d(C_{CO_2,w} - C_{CO_2,eq})}{dt} = & - \\ & - A_{g,w} u_w \frac{d(C_{CO_2,w} - C_{CO_2,eq})}{dz} - A_{g,w} \frac{\xi V_{s,w}}{V_{g,w}} k_{ri} (C_{CO_2,w} - C_{CO_2,eq}) + \\ & + A_{g,c} k_{cw} (C_{CO_2,c} - C_{CO_2,w}) \end{aligned} \quad (14)$$

where,

$$k_{ri} = \frac{k_r \rho_s}{M_s} \quad (15)$$

and $\xi_{k_{ri}}$ - is the kinetic and volume ratio between the potentially active solids (CaO and CaCO₃) and the total solids [19]. By combining the developed model of process with an optimization algorithm and the experimental data published by Charitos et al. in 2011 [24], the $\xi_{k_{ri}}$ values was been estimated.

The equilibrium CO₂ concentration ($C_{CO_2,eq}$) is express by equilibrium pressure the equation proposed by Garcia-Labiano [25] (equation 16).

$$p_{CO_2,eq} = 4.137 \cdot 10^{12} \exp\left(-\frac{20474}{T}\right) \quad (16)$$

RESULTS AND DISCUSSION

The mathematical model developed has been implemented in the equation oriented numerical computing environment Matlab/Simulink 2008. The dynamic model of carbon dioxide capture by Ca-looping has been validated with data collected from pilot plant, published by Charitos et al. [24] and Rodriguez et al. [12].

A summary of the fluidization column characteristics and operating data, used in this work is presented in Table 1 [19, 20, 24].

Table 1. Model parameters

Parameter	Carbonator
Mean particle size, d_p [μm]	170/350
Height, H_t [m]	12.4
Diameter, D [m]	0.07
Gas velocity, u_0 [m/s]	4 - 6
Inlet CO ₂ concentration, C_{CO_2in} [mol/m ³]	1.48
Temperature, T [°C]	650
Pressure, p [bar]	1
Fluidization regime	Fast

In Table 2, decay of the CO₂ carrying capacity, X_N , vs. the carbonation/ calcination cycle number N , for the German limestone used by IFK pilot plant [12] and value calculated by process simulator is presented.

Table 2. Pilot plant data and simulated results

	N = 1		N = 5		N = 10		N = 20	
	exp	sim	exp	Sim	exp	Sim	exp	sim
$C_{CO_2,in}$ [mol/m ³]	1.4856	1.4856	1.4856	1.4856	1.4856	1.4856	1.4856	1.4856
$C_{CO_2,out}$ [mol/m ³]	0.624	0.6934	1.07	1.1036	1.203	1.221	1.307	1.3058
X [-]	0.58	0.53	0.28	0.26	0.19	0.18	0.12	0.12

The superficial velocity of the gas has a major effect on the particle distribution in the fast fluidized bed [20]. The height of the dense region decreases with the increasing of the superficial velocity of the gas. The most of the carbonation reaction takes place in the dense region, therefore at smaller superficial gas velocities much higher carbonation degree can be achieved (Figure 3).

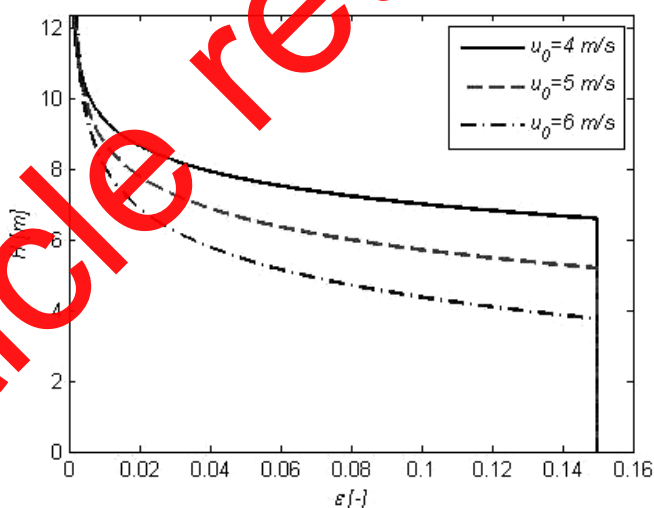


Figure 3. Vertical distribution of solid with variable superficial gas velocity

The particle diameters of the solid have effect on the particle distribution in the fast fluidized bed [21]. The height of the dense region decreases with changing of the superficial velocity of the gas and solid particle diameter (figure 4).

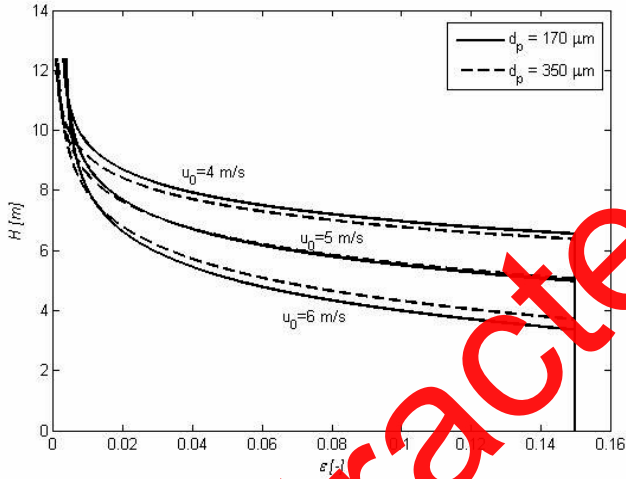


Figure 4. Solid distribution in fast fluidization with variable superficial gas velocity (u_0) and particle diameter (d_p),

The most part of the carbonation reaction takes place in the dense region and more precisely within the wall zone as can be seen from figure 5. Increasing the superficial velocity of the gas the difference between the concentration of the carbon dioxide in the wall and core zone becomes more significant. In the wall zone the volume fraction of solids is higher than in the core zone, the concentration drop there is more noticeable.

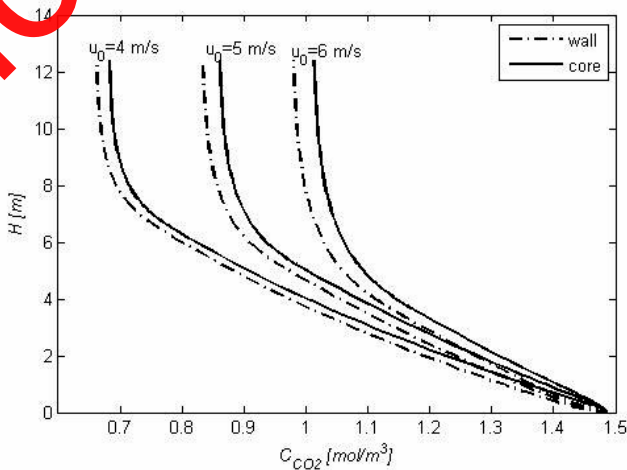


Figure 5. CO_2 concentration profile for carbonator for variable superficial gas velocity

In accord with experimental data, the model predicts that in every carbonation-calcination cycle the sorbent capacity decreases significant with the number of cycles. Figure 6 presents the variation of carbon dioxide concentration with carbonation/calcination number.

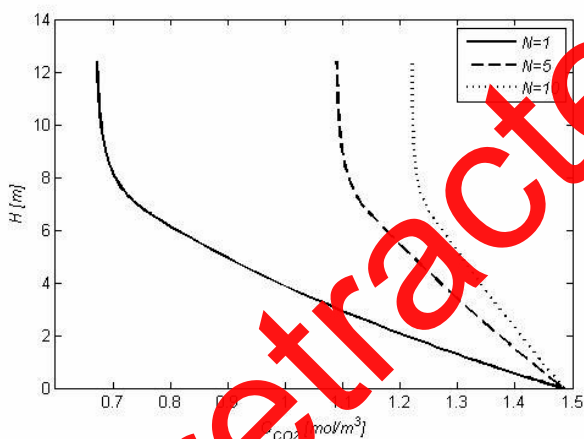


Figure 6. Mean CO₂ concentration profile for carbonator for variable carbonation/calcination cycle number

CONCLUSIONS

The dynamic carbon capture evaluation has a highly important role in establishing optimal operation procedure for power plants equipped with CCS. It is widely known that fossil power plants are required to be operated in dynamic scenario due to the timely variation of the grid demand.

In this paper, a dynamic mathematical model of carbonation reactor from calcium-looping process for carbon capture in fossil fuel-based power plants, was developed.

In the developed model has been taken into consideration the particle distribution in the reactor and the deactivation of the sorbent with the number of cycles (N). The particle distribution in the carbonator is described according to the 1D model for fast fluidization presented by Kunii and Levenspiel. The CO₂ adsorption efficiency in the carbonator is divided in two terms taking into account the dense and lean regions of the fluidized bed.

All mathematical equations used in this model have been implemented in Matlab /Simulink 2008. The dynamic model of CO₂ capture process has been validated with data collected from pilot plant, published in literature.

The simulation results showed more than 90 % of the total CO₂ capture has occurred in the dense region of the carbonator. The height of the dense region decreases significantly from 6.5 m to 4 m with the increasing of the

superficial gas velocity from 4 m/s to 6 m/s, for carbonator. Moreover, within the dense zone a small difference can be noticed in capture efficiency in the wall and core zone which becomes significant at higher gas velocities.

Nomenclature

u_0	superficial gas velocity in the reactor (m/s)
d_p	particle diameter (m)
H_t	total height of the reactor (m)
H_l	height of the lean region (m)
H_d	height of the dense region (m)
W_l	mass of solids in the lean region (kg)
W_d	mass of solids in the dense region (kg)
W_t	mass of solids in the reactor (kg)
a	decay constant for solid fraction in the lean region (m^{-1})
A_t	cross-sectional area of the reactor (m^2)
f_l	average value of the volume of solids in the lean region (-)
G_s^*	saturated mass flux of solids (kg/m^2s)
u_T	terminal velocity of particle falling through the gas (m/s)
g	acceleration of gravity (m/s^2)
k_r	first order kinetic constant of the carbonation reaction ($m^4/mol/s$)
k_s	intrinsic kinetic constant of the carbonation reaction ($m^4/mol/s$)
S_N	the specific surface area available for reaction in particle having experienced N calcination-carbonation cycles (m^{-1})
A_w	cross-sectional area in the wall zone (m^2)
A_c	cross sectional area in the core zone (m^2)
C_{CO_2}	average concentration of carbon dioxide in a generic CFB riser cross-section (mol/m^3)
$C_{CO_2,c}$	concentration of carbon dioxide in the core zone (mol/m^3)
$C_{CO_2,w}$	concentration of carbon dioxide in the wall zone (mol/m^3)
k_{cw}	core-wall mass transfer coefficient (s^{-1})
k_{ri}	first order kinetic constant of the carbonation reaction (s^{-1})
$p_{CO_2,eq}$	equilibrium carbon dioxide partial pressure
t	time (s)
V_M	molar volume (m^3/mol)
M_i	molecular weight of specie i (kg/kmol)

Greek letters

ϵ_{sd}	volume fraction of solids in the dense region (-)
ϵ_{sc}	volume fraction of solids in the core zone (-)
ϵ_{sw}	volume fraction of solids in the wall zone (-)
ϵ_s	saturated carrying capacity of a gas (-)
ϵ_{se}	volume fraction of solids at the reactor exit (-)

ε_{sl}	volume fraction of solids in the lean region (-)
ρ	density (kg/m^3)
μ	viscosity (Pa·s)
η	contacting efficiency in the CFB riser with respect to an ideal plug flow

ACKNOWLEDGMENTS

This work was supported by a grant of the Romanian National Authority for Scientific Research, CNCS - UEFISCDI, project PNII-CT-FRS 2011-1/2ERC: "Innovative systems for carbon dioxide capture applied to energy conversion processes".

REFERENCES

- [1] Intergovernmental Panel on Climate Change (IPCC), CO₂ capture and storage **2007**, <www.ipcc.ch> accessed 06/05/2011.
- [2] J.D. Figueroa, T. Fout, S. Plasynski, H. McIlvired, R. Srivastava, Advances in CO₂ capture technology - The U.S. Department of Energy's Carbon Sequestration Program, *International Journal of Greenhouse Gas Control*, **2008**, 2, 9.
- [3] International Energy Agency (IEA) GHG R&D Programme, High temperature solid looping cycles network, **2012**.
- [4] D.P. Harrison, *Industrial & Engineering Chemistry Research*, **2008**, 47, 6486.
- [5] T. Shinzui, T. Hirama, H. Hosoda, K. Kitano, M. Inagak, K. Tejima, *Industrial & Engineering Chemistry Research*, **1999**, 77, 62.
- [6] C.S. Gresta, J.C. Abanades, *Industrial & Engineering Chemistry Research*, **2006**, 45, 846.
- [7] V. Manovic, E.J. Anthony, *Environmental Science Technology*, **2009**, 43, 7117.
- [8] D. Alvarez, M. Pena, A.G. Borrego, *Energy & Fuels*, **2007**, 21, 1534.
- [9] P. Sun, J.R. Grace, C.J., Lim, E.J. Anthony, *Industrial & Engineering Chemistry Research*, **2008**, 47, 2024.
- [10] P.S. Fennell, R. Pacciani, J.S. Dennis, J.F. Davidson, A.N. Hayhurst, *Energy & Fuels*, **2007**, 21, 2072.
- [11] C.J. Abanades, E.J., Anthony, D.Y. Lu, C. Salvador, D. Alvarez, *Environmental and Energy Engineering*, **2004**, 50, 1614.
- [12] N. Rodriguez, M. Alonso, J.C. Abanades, *Energy Procedia*, **2011**, 4, 393.
- [13] C. Salvador, D.Y. Lu, E.J. Anthony, C.J. Abanades, *Chemical Engineering Journal*, **2003**, 96, 187.
- [14] A. Lasheras, J. Ströhle, A. Galloy, B. Eppele, *International Journal of Greenhouse Gas Control*, **2011**, 5, 686.

- [15] L.M. Romeo, Y. Lara, P. Lisbona, J.M. Escosa, *Chemical Engineering Journal*, **2009**, 147, 252.
- [16] D. Kunii, O. Levenspiel, *Powder Technology*, **1990**, 61, 193.
- [17] S.K. Bhatia, D.D. Perlmutter, *AIChE*, **1983**, 29, 79.
- [18] C. Hawthorne, M. Trossmann, P. Galindo Cifre, A. Schuster, G. Scheffknecht, *Energy Procedia*, **2009**, 1, 1387.
- [19] M.C. Romano, *Chemical Engineering Science*, **2012**, 69, 2571.
- [20] D. Kunii, O. Levenspiel, *Chemical Engineering Science*, **1997**, 52, 2471.
- [21] C.C. Cormos, A.M. Cormos, *International Journal of Hydrogen Energy*, **2013**, 38, 2306.
- [22] A. Johansson, F. Johnsson, B. Leckner, *Chemical Engineering Science*, **2007**, 62, 561.
- [23] G.S. Grasa, J.C. Abanades, M. Alonso, F. González, *Chemical Engineering Journal*, **2008**, 137, 561.
- [24] A. Charitos, N. Rodríguez, C. Hawthorne, M. Alonso, M. Zieba, B. Arias, G. Kopanakis, G. Scheffknecht, J.C. Abanades, *Industrial & Engineering Chemistry Research*, **2011**, 50, 9685.
- [25] F. Garcia-Labiano F., A. Abad, I. F. deDiego, P. Gayan, J. Adanez, *Chemical Engineering Science*, **2002**, 57, 2381.

A NEW PROTOCOL FOR PURIFYING HUMAN SERUM ALBUMIN

DANIELA CIOLOBOC^a, MARIANN-KINGA ARKOSI^a,
RADU SILAGHI-DUMITRESCU^a

ABSTRACT. The possible applications of human serum albumin into the design of blood substitutes with diminished capacity of getting involved in reactions that generate nitrogen reactive species lead us to reevaluate the purification procedures and to propose a modified precipitation procedure that over the economic advantages allows the isolation of other useful fractions.

Keywords: *human serum albumin, hemoglobin, blood substitutes, autooxidation*

INTRODUCTION

Albumin has a large number of biotechnological applications. Among these, we have recently proposed alleviation of prooxidant reactivity in artificial oxygen carriers ("blood substitutes"). Hemoglobin-albumin copolymers indeed displayed a decreased prooxidant activity compared not only to free hemoglobin but also to glutaraldehyde-polymerized hemoglobin [1] Furthermore, tests on animal models and on cell cultures reveal a better performance of hemoglobin-albumin copolymers, compared to simple hemoglobin polymers [1,2].

Many methods of recovering albumin from serum or plasma are described in the literature, one of the most used at large scale being Cohn's cold precipitation with ethanol [3]. Other methods include decreasing the ionic strength of plasma [4] or addition of fatty acids in order to precipitate globulins, addition of zinc ions or trichloroacetic acid to cold ethanol, or ammonium sulfate precipitation [5] combine the low temperature ethanol precipitation with ammonium sulfate fractionation [6] or with chromatography [7,8,9,10,11], or utilization of polyethylene glycol as precipitation reagent [6]. A protocol is described here for purification of human serum albumin, and proof of concept is given as to its potential use as antioxidant in hemoglobin-based blood substitutes.

^a "Babes-Bolyai" University, Str. Kogălniceanu, Nr. 1, RO-400084 Cluj-Napoca, Romania,
arkosi.mariann@gmail.com

RESULTS AND DISCUSSION

Human serum albumin was prepared using combined fractionation methods with ammonium sulfate and ethanol as presented Figure 1. This method has the advantage of obtaining highly purified albumin with the possibility of recovering other plasma proteins without the risk of irreversible denaturation. Compared to the Cohn cold ethanol precipitation method [3] this method is more cost-effective due to the fact that less ethanol and cooling agent are required for albumin isolation.

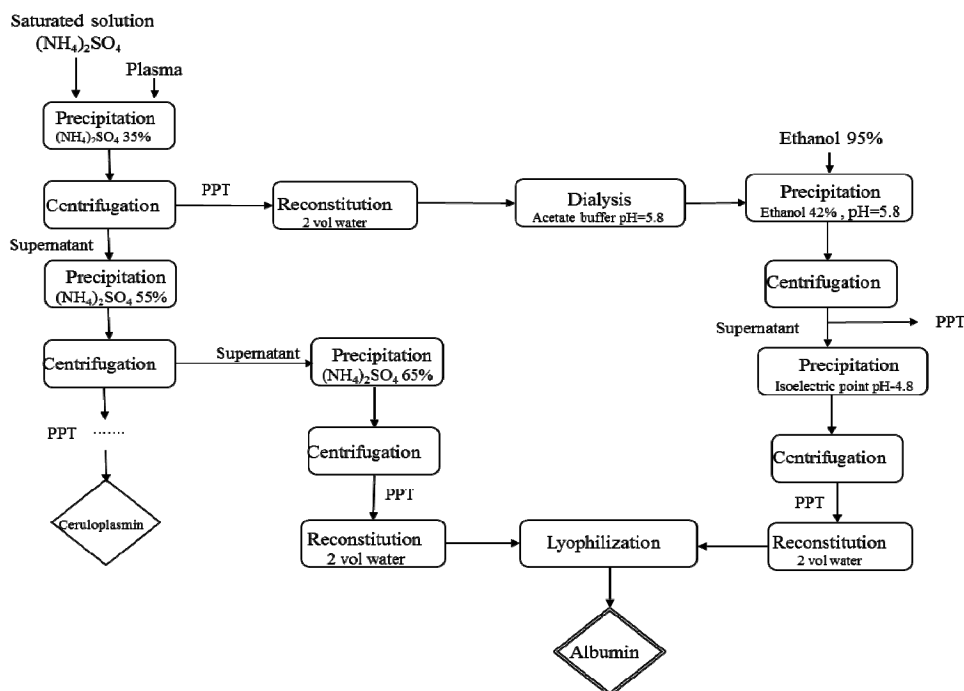


Figure 1. Human serum albumin preparation - operation flow chart.

Another advantage of the proposed method is its potential to be applied at large scale due to the relatively simple operations which do not require any considerable investment in equipments. Purification methods that include steps like electrodenatation [12], gel-filtration, ion exchange and affinity chromatography [7,10,11,13] or heating plasma in the presence of ethanol and stabilizers [14] are rarely applied in industry.

In the chosen purification protocol the first fractionation step was precipitation with ammonium sulfate at 35%, at 5^o Celsius, under stirring for 15 minutes, followed by a 15-minute centrifugation at 9000 rpm. Precipitate

was collected, re-suspended in two volumes of acetate buffer pH=5.8 and 150mM sodium chloride, and dialyzed. The supernatant was further precipitated with ammonium sulfate at 55% and centrifuged at 12000 rpm for 15 minutes; the second precipitate was kept for further purification procedures required for ceruloplasmin isolation while the supernatant was collected, precipitated with ammonium sulfate at 65% and centrifuged at 12000 rpm for 25 minutes; the precipitate was reconstituted with two volumes of ultrapure water and lyophilized.

In order to increase the recovery percentage after dialysis the fraction was precipitated with ethanol at 42% concentration, pH=5.8 at -5^o Celsius and centrifuged for 30 minutes at 12000 rpm; the supernatant, containing mainly albumin was further precipitated at isoelectric point pH=4.8. After stirring for 1 hour the mixture was allowed to age overnight before centrifugation; the obtained paste was reconstituted with two volumes of ultrapure water and lyophilized.

Figure 2 shows the results obtained by polyacrylamide gel electrophoresis analysis applied to various samples saved during fractionation: the supernatant saved from the precipitation with 55 % concentration ammonium sulfate (1) contains a large amount of different proteins while the precipitate collected after precipitation with 65% ammonium sulfate (2) contains as major fraction HSA which is accompanied by two other proteins with similar molecular weight. The fraction isolated after precipitation with ethanol at pH=5.8(3,4) contains three other proteins along with the HSA. The fraction obtained by precipitation at the isoelectric point contains as major component the albumin (5,6). If compared with commercially available HSA (AppliChem, purity grade min. 96%) on an SDS-PAGE gel, the fraction obtained with the above procedure shows a reasonable purity (Figure 3).

Figure 4 illustrates a proof-of-principle case where HSA can be useful as antioxidant in a blood substitute preparation. Thus, glutaraldehyde-polymerized hemoglobin¹⁶ was subjected to an autooxidation experiment over the course of eight hours. UV-vis spectra were recorded during the incubation at 37 °C in PBS buffer of poly-hemoglobin, in the absence or presence of HSA and BSA, respectively. These spectra illustrate the degree of autooxidation (transition from the physiologically-useful oxy form to the oxidized met, ferric form) in terms of decreases in absorbance at 540 and 580 nm (characteristic of oxy hemoglobin), alongside increases in absorbance at 630 nm (characteristic of met hemoglobin). The autooxidation degree for each time point was defined as

$$\text{defined as } \frac{A_{630,t} - A_{574,t}}{A_{630,oxi} - A_{574,oxi}}.$$

After four hours incubation, this ratio was 0.76 for the polymerized hemoglobin; larger values (hence suggestive of less autooxidation over the course of the experiment) were computed for the samples containing HSA

(0.82) and BSA (0.85). The BSA data are in line with our previous observations on its ability to slow down autooxidation in blood substitutes [1,15]; it is, however, the first time that HSA was tested in the same context. It appears that HSA behaves similarly to BSA (as expected), although a slight difference does appear to exist in favor of the BSA.

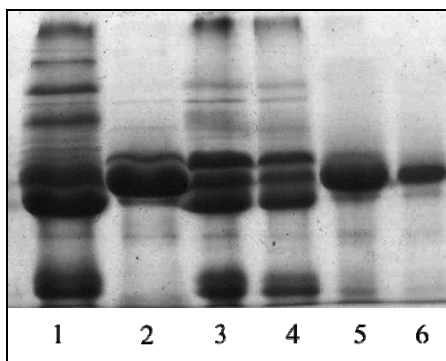


Figure 2. Monitoring the human serum albumin purity by 14% SDS-PAGE.
1 – supernatant from precipitation with 35% ammonium sulfate,
2 – precipitate from precipitation with 65% ammonium sulfate,
3,4 – supernatant from precipitation with ethanol;
5,6 – precipitate from precipitation at isoelectric point.

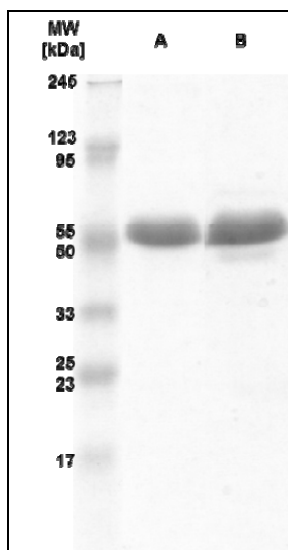


Figure 3. Comparison of commercially available HSA (lane A, 6 ng) with purified human serum albumin (lane B, identical to the fraction in lane 6, Figure 2) on a 14% SDS-PAGE gel.

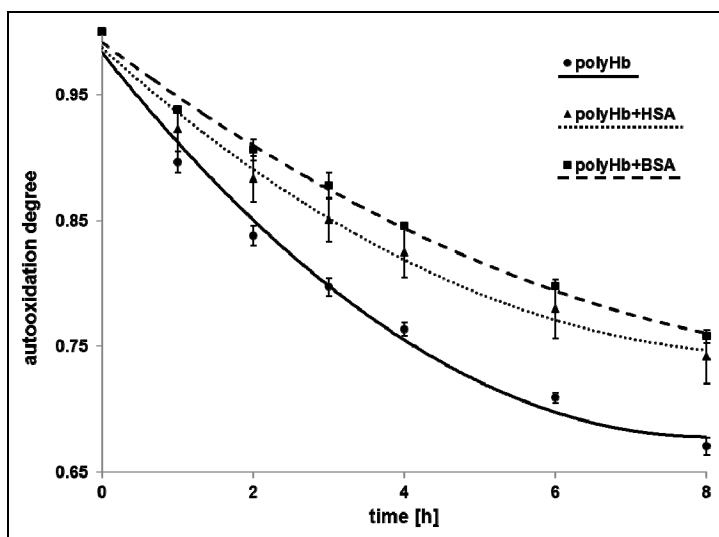


Figure 4. Second order decay of the physiologically-useful oxy form of glutaraldehyde-polymerized hemoglobin upon incubation at 37 °C in PBS buffer, in the presence or absence of HSA and BSA, respectively.

CONCLUSIONS

To conclude, we have reported here a new protocol for purifying human serum albumin from plasma, for use in biotechnological applications such as those involving antioxidant protection in artificial oxygen carriers (“blood substitutes”) or chemotherapy.

EXPERIMENTAL SECTION

Proteins were and manipulated in phosphate buffer saline (PBS) unless otherwise mentioned. Human serum albumin (HSA) was purified from plasma following a protocol that combines two fractionation methods namely precipitation with ammonium sulfate and cold ethanol precipitation [3,5]. Human serum albumin was isolated from the fractions remained from ceruloplasmin precipitation with ammonium sulfate. Frozen plasma was obtained from four healthy donors that gave their consent to the sample collection.

The purification of the HSA was monitored by electrophoresis using 14% SDS-PAGE or native PAGE gels, controlled by an electrophoresis power supply Consort EV233. The denaturing SDS gels were stained with Bradford acidic solution for total protein staining. UV-vis spectra were recorded on Agilent 8453 (Agilent, Inc.) instrument.

Polymerized hemoglobin was prepared as previously described [1,13], bovine serum albumin was a commercial preparation identical to that used in our previous experiments on hemoglobin [1].

ACKNOWLEDGMENTS

Financial support from the Romanian Ministry for Education and Research grant PCCE 140/2008 and from a research fellowship to MKA from the Babes-Bolyai University is gratefully acknowledged.

REFERENCES

- [1] Iacob, B.; Deac, F.; Cioloboc, D.; Damian, G.; Silaghi-Dumitrescu, R. *Artif Cells Blood Substit Immobil Biotechnol* **2011**, *39*, 293-7.
- [2] Fedorov, A.N.; Iarochkin, V.S.; Koziner, V.B.; Hachaturian, A.A.; Rozenberg, G.I., *Dokl Akad Nauk SSSR* **1978**, *243*, 1324-6.
- [3] Cohn, E.J.; Strong, L.E.; Hughes, J.W.L.; Mulford, D.J.; Ashworth, J.N.J. *Am. Chem. Soc.* **1946**, *68*, 459-475.
- [4] Nitschmann, H.; Kistler, P.; Renefer, H.R.; Hassig, A.; Joss, A. *Vox. Sang* **1956**, *1*, 183-200.
- [5] Mahn, A; Ismail, M; *J Cromatogr.B*, **2012**, *879*, 3645-8.
- [6] Amagasaki, Y.M; Hirakata, E.T., *US Patent 4197238*, **1980**.
- [7] Tanaka, K.; Shigueoka, E.M.; Sawatani, E.; Dias, G.A.; Arashiro, F.; Campos, T.C.X.B.; Nakao Braz, H.C. *J Med Biol Res* **1998**, 3111.
- [8] Curling, J.M.; Berglof, J.; Lindquist, L.O.; Erkiesson, S. *Vox Sang.* **1977**, *33*, 97-107.
- [9] Jiang, L.; Hea, L., Fountoulakis, M.; *J. Cromatogr. A*, **2004**, *1023*, 317.
- [10] Burnouf, T.; *Bioseparation*, **1991**, *1*, 383.
- [11] Burnouf, T.; Radosevich M.; *J Biochem Biophys Methods*, **2001**, *49*, 575.
- [12] Deac, F.; Todea, A.; Silaghi-Dumitrescu, R. In *Metal Elements in Environment, Medicine and Biology Tome IX*; Silaghi-Dumitrescu, R., Garban, G., Eds.; Cluj University Press: Cluj-Napoca, Romania, **2009**.
- [13] Hao, Y. *Vox. Sang.***1979**, *365*, 313-20.
- [14] Ouchterlony, O. *Progr. Allergy* **1958**, *5*, 1-78.
- [15] Fischer-Fodor, E.; Mot, A.; Deac, F.; Arkosi, M.; Silaghi-Dumitrescu, R. *J Biosci* **2011**, *36*, 215-21.

BIOGENIC AMINE CONTENT IN CHEESE PRODUCED WITH DIFFERENT SELECTED LACTIC ACID BACTERIAL STRAINS

PÉTER SIMON^a, KLÁRA PÁSZTOR-HUSZÁR^b, ISTVÁN DALMADI^b,
GABRIELLA KISKÓ^c, LIVIA SIMON-SARKADI^{a*}

ABSTRACT. The aim of the work was to study the effect of selected *Lactobacillus* strains having different decarboxylase activities on the formation of biogenic amines during manufacturing and storage of semi-hard cheeses produced under laboratory conditions. Results were compared with cheese made with a starter culture generally used in the dairy industry. The present experiment proved that cheeses fermented with selected *Lactobacillus* strains contained lower amounts of biogenic amines, especially tyramine and histamine, than the sample fermented by mixed lactic acid bacterial culture.

Keywords: *biogenic amines, cheese, starter cultures*

INTRODUCTION

Biogenic amines (BAs) are aliphatic, alicyclic or heterocyclic low molecular weight bases. They can be found in all kind of food products at low level.

In fermented foods BAs are mainly formed due to the microbial decarboxylation of free amino acids [1]. Among BA producers are starter and non-starter bacteria [2]. The microorganisms involved in fermentation process can cause high concentrations of BAs.

The consumption of high amounts of BAs can cause several problems to the consumer. The determination of the toxicity threshold is difficult, since it is dependent on the individual response and on the presence of co-factors [3]. In the European Union a limit is established for histamine

^a *Budapest University of Technology and Economics, Department of Applied Biotechnology and Food Science, Budapest, Hungary, * sarkadi@mail.bme.hu*

^b *Corvinus University of Budapest, Department of Refrigeration and Livestock Products Technology, Budapest, Hungary*

^c *Corvinus University of Budapest, Department of Microbiology and Biotechnology, Budapest, Hungary*

in fish (200 mg/kg) [4]. Some countries have regulated the maximum amounts of histamine in different foods at a national level. There are recommendations for histamine (100 mg/kg), tyramine (100-800 mg/kg) and phenylethylamine (30 mg/kg) [5].

Cheeses represent an ideal condition for amine production, i.e. the presence of free amino acids and the presence of bacteria which is able to decarboxylase amino acids [6]. Several efforts have been made in food science and in the food industry to reduce or to prevent formation of biogenic amines in food. Using selected starter culture is one of the most encouraging methods for the reduction of biogenic amine content in food [7,8,9].

The aim of this work was to study the influence of three selected *Lactobacillus* strains (*Lactobacillus paracasei* subsp. *paracasei* 2750, *Lactobacillus fermentum* DT41, *Lactobacillus curvatus* 2770) on the formation of BAs during manufacturing and storage in cheese.

RESULTS AND DISCUSSION

Microbiological analysis

Figure 1 illustrates the development of the total microflora over a period of 6 weeks. The total viable counts varied between 8-9 log CFU/g depending on the used starter culture. At the end of the first week in the cheese made with the industrial starter culture the total aerobic plate count was slightly lower than in cheeses made with *Lactobacillus* strains. During the 6 weeks of storage this difference reduced, and at the end of the 6 weeks, the plate counts were around 8 log CFU/g in all types of cheeses.

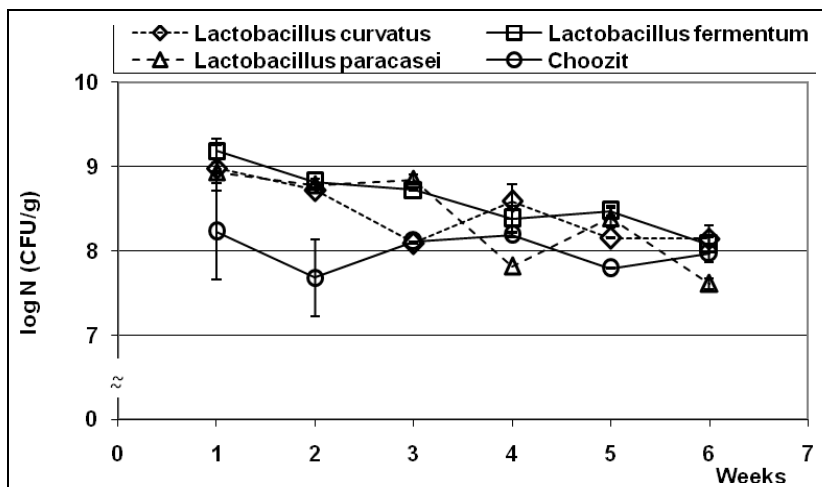


Figure 1. Aerobic plate counts of cheese samples during 6 weeks of storage at 13 °C

Biogenic amine analysis

The changes of total BA content of cheeses are summarized in Figure 2. The amount of total BAs was significantly lower in cheeses made with *Lactobacillus* strains than in cheese made with industrial starter culture (Choozit). The total BA content ranged between 25-42 $\mu\text{g/g}$, 25-85 $\mu\text{g/g}$, 14-112 $\mu\text{g/g}$ and 3-207 $\mu\text{g/g}$ in samples inoculated with *Lactobacillus curvatus*, *Lactobacillus fermentum*, *Lactobacillus paracasei* and Choozit Cheese Culture, respectively.

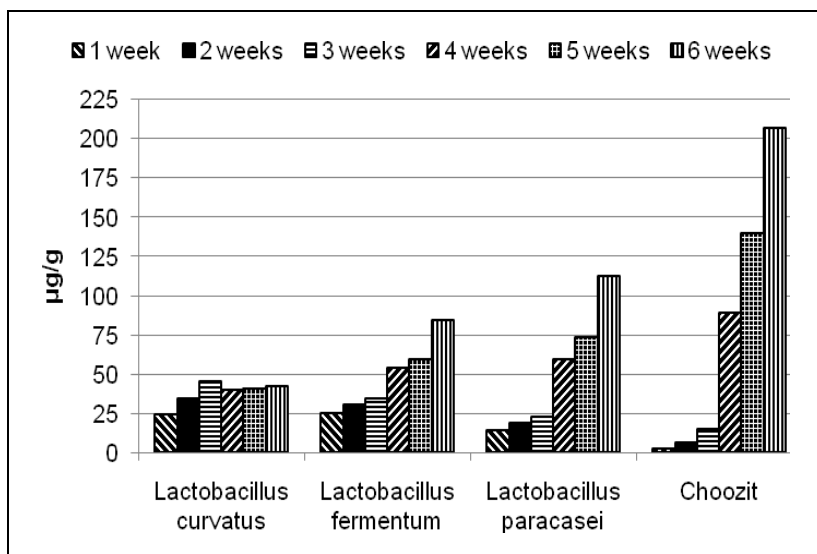


Figure 2. Changes of biogenic amines in cheese samples inoculated with different starter cultures during 6 weeks of storage

The biogenic amines determined were cadaverine (Cad), putrescine (Put), histamine (Him) and tyramine (Tym). Cad and Put were the major amines in cheeses with selected *Lactobacillus* strains (Fig. 3,4,5), while Tym and Him were the predominant BAs in cheese manufactured with Choozit Cheese Culture (Fig. 6).

The biogenic amine content was significantly lower in samples inoculated with selected *Lactobacillus* strains than in samples manufactured with the cheese culture used in the dairy industry. The BA composition was much better (no Tym and lower Him content) in cheeses made with selected starter cultures, than in cheeses made with the industrial starter culture “Choozit Cheese Culture”.

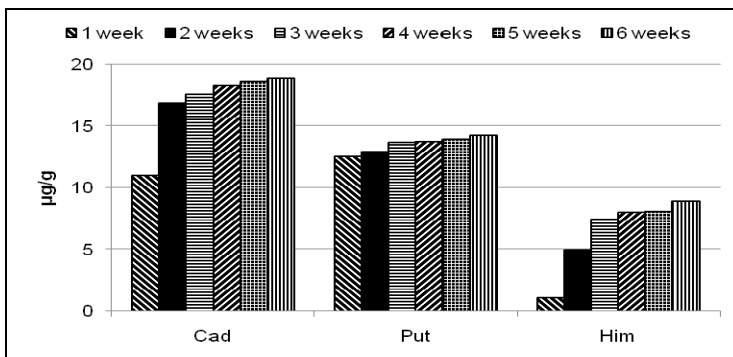


Figure 3. Changes of biogenic amines in cheese samples inoculated with *Lactobacillus curvatus* 2770 during 6 weeks of storage

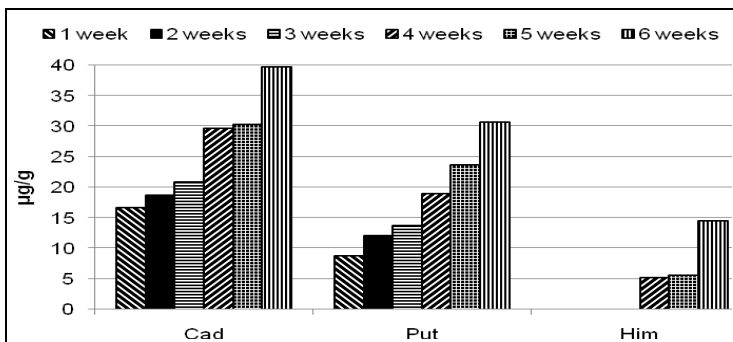


Figure 4. Changes of biogenic amines in cheese samples inoculated with *Lactobacillus fermentum* DT 41 during 6 weeks of storage

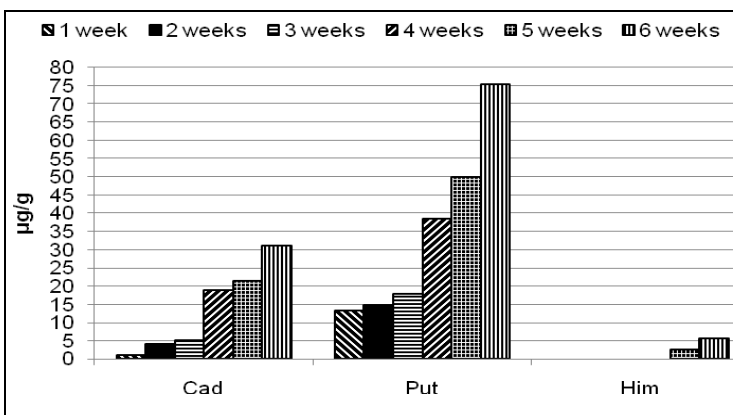


Figure 5. Changes of biogenic amines in cheese samples inoculated with *Lactobacillus paracasei* subsp. *paracasei* 2750 during 6 weeks of storage

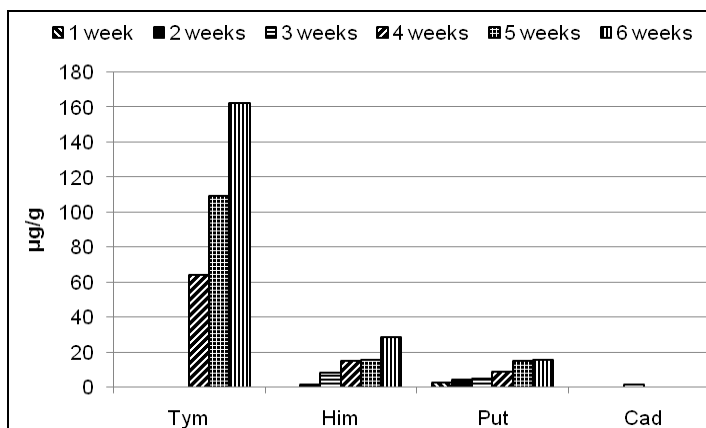


Figure 6. Changes of biogenic amines in cheese samples inoculated with Choozit during 6 weeks of storage

CONCLUSIONS

Our results indicates that it is recommended to use selected starter cultures to obtain a healthier product regarding the biogenic amine content and composition of cheeses.

EXPERIMENTAL SECTION

Cheese manufacture

10 litres of pasteurized, non-homogenized bovine milk with 2,8 % fat content (Dabastej Ltd., Dabas, Hungary) was heated to 30°C during continuous agitation (15 traverses per minute) in a laboratory-scale stainless steel jacketed cheese vat (FT20 Cheese Vat, Armfield Ltd., UK). Then 2,5 g of CaCl₂ were added. Four various starter cultures with different decarboxylase activity were used in the experiments: *Lactobacillus fermentum* DT41, *Lb. curvatus* 2770, *Lb. paracasei* subsp. *paracasei* 2750 and Choozit Cheese Culture used in the dairy industry (Danisco A/S, Denmark). Milk was inoculated by the starter culture and 5 cm³ of rennet were added (Chy-Max Special, Ch. Hansen, Denmark). Milk was allowed to coagulate. After coagulation the curd was cut. The curd-whey mixture was gradually heated to 39°C (2°C/12 min) under continuous agitation. When 39°C was reached the curd-whey mixture was stirred for 1 more hour. Then whey was drawn and curds were put into a hoop and put into a cheese press. Pressure was increased continuously up to 5 kg/cheese kg. Cheese was pressed overnight at room temperature then removed from the press and put into brine (20% salt concentration) for 24 hours. Then cheese was dried for 1 day at room temperature and vacuum packaged in Cryovac BB4L foil bags (Sealed Air Corporation, USA) (oxygen permeability 30 cm³/m²/24 h at 23°C, 0% RH and 1 bar). The four various

cheeses were stored at $13\pm 2^{\circ}\text{C}$ in a cooling cabinet (J 600-2, Thermotechnika Ker. Ltd., Hungary). Samples were taken every week until the cheese samples were used up (6 weeks). After sampling cheeses were vacuum packaged again and put back to storage.

Microbiological analysis

Aerobic plate counts were determined as follows: 10 g of sample was placed in a stomacher bag (with nylon mesh bag, pore size 1.0 mm) with 40 cm^3 of diluents (1 g peptone; 8.5 g NaCl in 1000 cm^3 distilled water). Five-time dilution cheese homogenates were stomached for 2 minutes, and 10-fold dilution series were prepared. These were routinely cultivated on Plate Count Agar (PCA, MERCK). PCA plates were incubated at 30°C for 2-3 days. Samples were taken regularly for aerobic plate count determination during 6 weeks of storage.

Biogenic amine analysis

Samples (2 g) were extracted with 10 cm^3 10% trichloroacetic acid for 1h at room temperature, at 100 rpm using a Laboshake (Gerhardt, Germany). Samples were filtered through a $0.25\text{ }\mu\text{m}$ membrane filter (Nalgene, USA). Biogenic amine analysis was performed with an AA 400 Amino Acid Analyser (Ingos, Czech Republic) [10].

ACKNOWLEDGMENTS

This work was supported by the Hungarian Scientific Research fund and the National Office for Research and Technology (NKTH-OTKA CK-78013).

REFERENCES

- [1] M.H. Silla Santos, *Int. J. Food Microbiol* **1996**, 29, 213-231.
- [2] A.X. Roig-Sagues, A.P. Molina, M.M. Hernandez-Herrero, *European Food Research and Technology* **2002**, 215, 96-100.
- [3] A. Halász, Á. Baráth, L. Simon-Sarkadi, W. Holzapfel, *Trends Food Sci. Technol* **1994**, 51, 42-49.
- [4] *European Council Directive* **1991**, 91/493/EEC.
- [5] B. ten Brink, C. Damink, H.M. Joosten, J.H. Huis in 't Veld, *International Journal of Food Microbiology* **1990**, 11, 73-84.
- [6] J.E. Stratton, R.V. Hutkins, S.L. Taylor, *Journal of Food Protection* **1991**, 54, 460-470.
- [7] S. Bover-Cid, M. Hugas, M. Izquierdo-Pulido, M. C. Vidal-Carou, *Journal of Food Protection* **2000**, 63, 237-243.
- [8] A.M. Baka, E.J. Papavergou, T. Pragalaki, J.G. Bloukas, P. Kotzekidou, *LWT-Food Science and Technology* **2011**, 44, 54-61.
- [9] W. Sriphochanart, W. Skolpap, *Journal of Food Processing and preservation* **2011**, 35, 291-298.
- [10] E. Csomós, L. Simon Sarkadi, *Chrom. Suppl.* **2002**, 56, 185-188.

THE INFLUENCE OF FROZEN STORAGE ON FATTY ACIDS COMPOSITION FOR ALIMENTARY ANIMAL FATS

FLAVIA POP^{a*}, LIVIU GIURGIULESCU^a, ANCA DUMUȚA^a,
ZORICA VOȘGAN^a

ABSTRACT. The purpose of this research was to monitor the storage stability of 2 types of alimentary animal fats (poultry fat and fish oil) during frozen storage (-15...-18°C) by fatty acids profile determination in order to follow the variation in saturated and unsaturated fatty acids proportion. Determination of chemical composition of animal fats is important in establishing physicochemical and organoleptic parameters, nature and proportion of fatty acids conferring specific characteristics to them. In the case of fresh poultry fat, in the largest proportion were determined oleic, linoleic and palmitic acids.

Fatty acids variation was correlated with hydrolysis process when fatty acids were released from triglycerides structure and with oxidation process when the degree of unsaturation decreased, due to unsaturated fatty acids oxidation.

Keywords: *fatty acids, alimentary animal fats, frozen storage, oxidation*

INTRODUCTION

Lipids entered in the composition of living matter from the very beginnings of the life on Earth. Lipids, a heterogeneous class of natural compounds, esters of alcohols with fatty acids are strictly indispensable components in human nutrition, performing many functions in the body [1]. Storage of animal fats even in frozen conditions affects in time the physicochemical, sensory and nutritional properties determining lipolytic or oxidative rancidity and may result in reduction of their validity.

Fatty acids represent the variable structure of lipids, the characteristics of the fats being conferred by the nature and proportion of fatty acids that enters into their composition [2]. From unsaturated fatty acids, linoleic, linolenic and arachidonic acids have a particularly importance, they are also called essential fatty acids because they can not be synthesized by the body and they must be brought by food intake [3].

^a *Technical University of Cluj-Napoca, North University Center of Baia Mare, Chemistry and Biology Department, 76A Victoriei Str., 430122, Baia Mare, Romania, flavia_marie@yahoo.com*

Lipolytic alteration occurs due to hydrolytic degradation of lipids from fat composition. Hydrolysis process is catalyzed by lipases that release fatty acids from triglycerides structure [3, 4].

Oxidative rancidity involves the oxidation of unsaturated fatty acids, especially polyunsaturated fatty acids (PUFA) and generates compounds that affect food quality by altering of color, flavour, texture, nutritional value and food safety [4, 5].

The photosensitised route is an alternative oxidative pathway that involves the direct reaction of excited singlet oxygen (1O_2) to unsaturated lipids in the presence of sensitizers [7]. In the peroxidation of unsaturated fatty acids, lipid hydroperoxides form during the propagation phase. These compounds are unstable and decompose rapidly, giving rise to a range of new free radicals and other non-radical compounds, including alkoxy and alkyl radicals, aldehydes, ketones, as well as a variety of carboxyl compounds that form a complex mixture of secondary lipid oxidation products. Volatiles such as hexanal and pentanal have been associated with the development of undesirable flavours and have been proposed as potential markers of fresh product quality [8, 9].

The purpose of the research was to study if there are significant changes in fatty acids composition for alimentary animal fats during frozen storage, when advanced hydrolysis and oxidation processes were installed, which represents the original part of the work, Samet-Bali et al., Sağdıç et al. reported variations in fatty acids composition for cow milk fat and butter produced from goat's milk during storage [10, 11].

RESULTS AND DISCUSSION

The study of changes in chemical composition for poultry fat and fish oil after 6 months of storage during freezing when hydrolysis and oxidative processes were installed represents one of the original aspect of the work, fatty acids variation in time is an indicator of their stability regarding alterative processes.

Chemical composition of fresh poultry fat was the following: 30.56% SFA, 42.38% MUFA and 27.49% PUFA and presented a soft consistency. In the largest proportion were determined oleic (37.33%), linoleic (25.63%) and palmitic (23.36%) acids. For fresh poultry fat was determined a SFA : MUFA : PUFA = 1.11 : 1.54 : 1 ratio, and essential fatty acids : non-essential fatty acids = 1 : 1.54.

Figure 1 illustrates sample chromatogram for fresh poultry fat in which fatty acids are recorded in the form of peaks separated from each other by increasing the chain length.

THE INFLUENCE OF FROZEN STORAGE ON FATTY ACIDS COMPOSITION ...

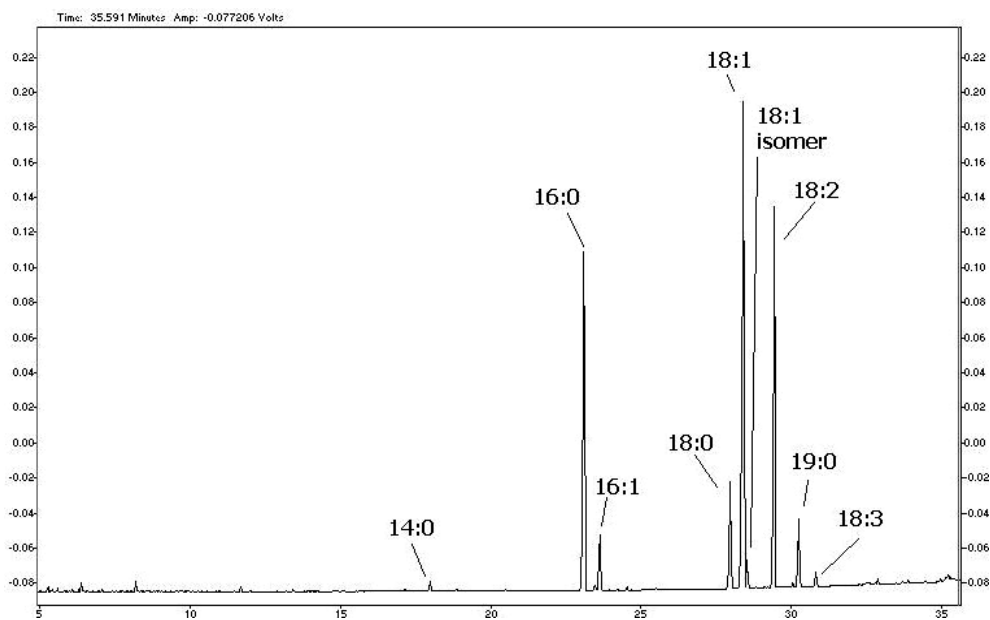


Figure 1. Gas chromatogram of fresh poultry fat

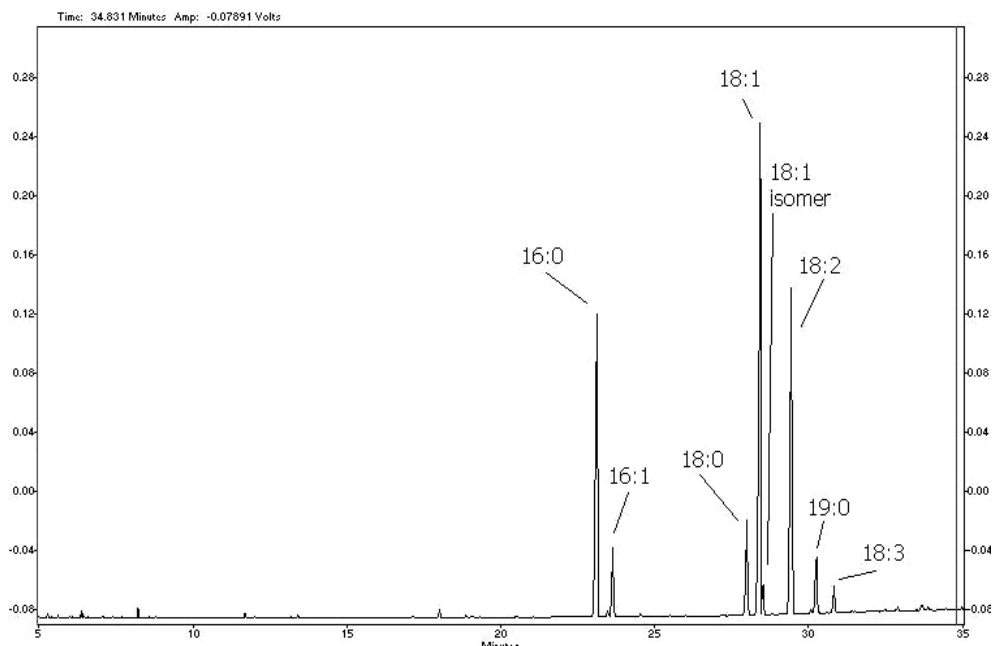


Figure 2. Gas chromatogram of poultry fat to 6 months under frozen storage

Poultry fat after 6 months under frozen storage presented an increase in SFA from 30.56% to 30.98% and a decrease in MUFA from 42.38% to 41.79%, and for PUFA a decrease from 27.49% to 26.22%, PUFA showed the significant variations. In the case of oxidized poultry fat, palmitic and stearic acids showed an increase, miristic acid was not detected, and palmitoleic, oleic, vaccenic, linoleic and alfa-linolenic acids showed a decrease compared to fresh fat, but linoleic acid showed the greatest variability (fig. 2). For oxidized poultry fat was found a SFA : MUFA : PUFA = 1.27 : 1.60 : 1 ratio, and essential fatty acids : nonessential fatty acids = 1 : 1.60.

It was concluded that the increase of saturated fatty acids content is due to the installation of hydrolysis leading to the release of acids from triglycerides structure, which translates also through the increase of titrable acidity, and the decrease of MUFA and PUFA is due to unsaturated fatty acids oxidation at the same time with the decrease of iodine value.

Fresh fish oil presented the following chemical composition: 20.39% SFA, 44.56% MUFA and 35.05% PUFA. The main determined fatty acids were: oleic (17.14%), *cis*-5,8,11,14,17 eicosapentaenoic (17.05%), *cis*-11-eicosenoic (10.81%), palmitoleic (10.12%), palmitic (17.90%) and arachidonic (9.81%) acids. Docosahexaenoic acid (DHA) has not been detected probably due to its oxidation during the extraction process. The most valuable fatty acid from fish lipids composition is considered to be ω -3 eicosapentaenoic acid (C20:5-EPA) due to its positive influence on the health. Figure 3 illustrates sample chromatogram for fresh fish oil.

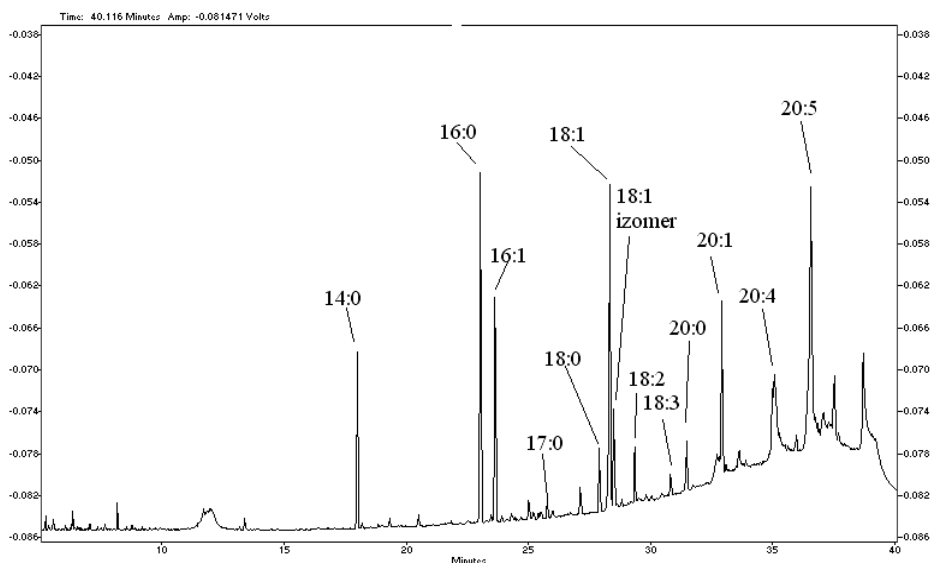


Figure 3. Gas chromatogram of fresh fish oil

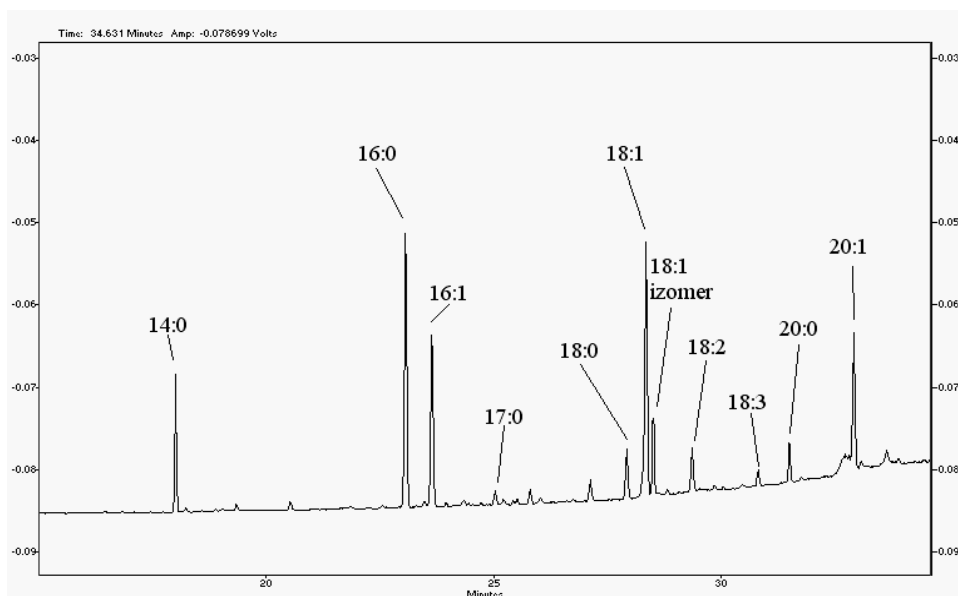


Figure 4. Gas chromatogram of fish oil to 6 months under frozen storage

In fish oil sample after 6 months freezing, SFA content increased from 20.39% to 21.58%, MUFA content decreased from 44.56% to 43.80%, and PUFA content decreased from 35.05% to 33.37%, PUFA showed the significant variations (fig. 4).

Arachidonic and *cis*-5,8,11,14,17 eicosapentaenoic acids were not detected, which also highlights the early installation of oxidation in the case of fish oil. For oxidized fish oil was found a SFA : MUFA : PUFA = 1 : 2.09 : 1.60 ratio, and essential fatty acids : nonessential fatty acids = 1 : 1.30.

It should be noted that in the case of poultry fat after 6 months congelation, mono and polyunsaturated fatty acids content was not so pronounced as in the case of fish oil, but the increase of saturated fatty acids content was more pronounced.

Variations in fatty acids content with a more significant decrease for unsaturated fatty acids were found in the case of milk powder storage at ambient temperature and at 15°C [12].

Manat et al., observed changes in fatty acid profile during frozen storage of sardines. Fresh sardines had a content of 45.9% SFA, 16.7% MUFA and 35.7% PUFA, from PUFA, DHA was the most abundant followed by EPA. The authors found a reduction in PUFA content during storage, especially of EPA which decreased from 6.14% to 5.33% in the 6th day and to 4.96% in the 15th day, and a decrease in DHA from 19.7% to 18.6% in

the 6th day and to 18.5% in the 15th day. The study showed a decrease in PUFA in the 15th day storage by 8.1%, in MUFA by 9.7% and an increase in SFA by 2.3% [13].

Fátima Aparecida Ferreira de Castro et al., reported that oleic acid was found in the highest proportion in carp fillet, followed by linoleic and palmitic acid. The authors also determined an increase in arachidonic acid after 45 days of frozen storage, and a increase in DHA after 15 days under skin removal, suggesting that these acids were found in the subcutaneous layer [14].

It was concluded that the most pronounced changes in fatty acids composition took place in fish oil, which suggests that it is more susceptible to alterative processes due to its higher content of unsaturated fatty acid. Hydrolysis and oxidation processes were installed earlier in fish oil than in poultry fat.

CONCLUSIONS

During frozen storage there was a decrease in fatty acids content in order: PUFA>MUFA>SFA, but these variations are quite small, and storage time did not significantly affect fatty acids profile.

It was concluded that the increase of saturated fatty acids content was due to hydrolysis leading to the release of acids from triglycerides structure, and the decrease of MUFA and PUFA was due to unsaturated fatty acids oxidation. During frozen storage there are changes in fatty acids composition, that is an indicator of their stability to alterative processes.

In the case of poultry fat the changes in fatty acids composition were not so pronounced, which suggests that it can be preserved for a long period of time under freezing.

EXPERIMENTAL SECTION

Samples

Poultry fat was obtained by raw material fat melting, collected from broilers, male and female, packed in unvacuumated plastic bags, and stored under freezing. Fish oil was obtained by Soxhlet extraction from farmed carp fillets, packaged in brown glass tubes, airtight, was stored under freezing (-15...-18°C) and for each fat was determined the chemical composition in fresh state and after 6 months of storage under freezing, when alterative processes were installed.

Physicochemical examination

Fatty acid composition was determined using gas chromatography (GC) Shimadzu GC-17 A coupled with flame ionisation detector FID. Gas chromatography column is Alltech AT-Wax, 0.25 mm I.D., 0.25 μm thick stationary phase (polyethylene), used helium as carrier gas at a pressure of 147 kPa, temperature of the injector and detector was set to 260°C, the oven programme was the following: 70°C for 2 min., then the temperature was raised up to 150°C with a gradient of 10°C/min., a level of 3 min. and the temperature was raised up to 235°C with a gradient of 4°C/min.

Samples preparation for GC analysis: were weight 50 mg sample, was add 1 mL benzene, from dilution were taking 100 μL and mixed with 200 μL internal standard (nonadecanoic acid 19:0), 1 mL benzene, 2 mL methanol, 4 drops H_2SO_4 conc. and was heated at 80°C for 2 hours. Then we passed to esters extraction: esterified sample was passed into a separating funnel, were added 10 mL hexane and 2 mL distilled water, the upper was retained, filtered on cellulose filter, dried with a rotary evaporator, then was dissolved in 1 mL hexane and 1 μL sample was injected into gas chromatograph.

The method consists in transformation of fatty acids in methyl esters in the sample under analysis, followed by separation of components on a chromatography column, their identification by comparison with standard chromatograms and quantitative determination of fatty acids. By chromatography separation the sample chromatogram is obtained in which fatty acids are recorded in the form of peaks separated from each other by increasing the chain length. Results were expressed as w/w (%) of total fatty acids [15, 16].

REFERENCES

- [1] C. Banu, N. Preda, S. Vasu, „Produsele alimentare si inocuitatea lor”, Technical Press, Bucharest, **1982**, chapter 3.
- [2] D. Ciobanu, R. Ciobanu, „Chimia produselor alimentare”, Technical-INFO Press, Chişinău, **2001**, chapter 1.
- [3] D.A. Huhges, *Nutr. Food Sci.*, **1995**, 95(2), 12.
- [4] J.G. Akamittath, C.J. Brekke, E.G. Schanus, *J. Food Sci.*, **1990**, 55, 1513.
- [5] E. Carrasco, R. Tárrega, M.R. Ramírez, F.J. Mingoarranz, R. Cava, *Meat Sci.*, **2007**, 69, 609.
- [6] M. Tofană, „Aditivi alimentari. Interacţiunea cu alimentul”, Academicpress, Cluj-Napoca, **2006**, chapter 6.

- [7] N. Berset, M.E. Cuvelier, *Sci. des Alim.*, **1996**, 16, 219.
- [8] J.P. Cosgrove, D.F. Church, W.A. Pryor, *Lipids*, **1997**, 22, 299.
- [9] K.L.A. Davies, A.L. Golberg, *J. Biol. Chem.*, **1998**, 262, 8220.
- [10] O. Samet-Bali, M.A. Ayadi, H. Attia, *Food Sci. Tech.*, **2009**, 30, 74.
- [11] O. Sağdıç, M. Dönmez, M. Demirci, *Food Contr.*, **2004**, 15, 485.
- [12] J.L. Chávez-Servín, A. Castellote, M. Martín, C. López-Sabater, *Food Chem.*, **2010**, 107, 558.
- [13] N. Manat, B. Sootawat, W. Visessanguan, C. Faustman, *Food Chem.*, **2006**, 99, 83.
- [14] F.A. Ferreira de Castro, H.M. Pinheiro Sant'Ana, F. Milagres Campos, M. Brunoro Costa, M. Silva, A.L. Salaro, S. Carmo Castro Franceschini, *Food Chem.*, **2011**, 103, 1080.
- [15] ***Romanian standard SR ISO 661, Bucharest, **1998**.
- [16] ***Romanian standard SR ISO 14082, Bucharest, **2003**.

HIGH PRESSURE - HIGH TEMPERATURE SYNTHESIS AND PHASE CHARACTERIZATION OF PbVO_3 PEROVSKITE COMPOUND

ALEXANDRU OKOS^{a,b}, AUREL POP^{a*}, CÉLINE DARIE^b,
PIERRE BORDET^b

ABSTRACT. Perovskite compound PbVO_3 was synthesized under high-temperature and high-pressure conditions. In this paper we report a new set of milder reaction conditions in which PbVO_3 can still be prepared. The effect of the synthesis parameters on phase purity is analysed. The crystalline structure of samples was characterised by X-ray diffraction (XRD) measurements. Rietveld analysis of X-ray powder diffraction pattern revealed that the material stabilized in a tetragonal perovskite phase.

Keywords: PbVO_3 , high pressure – high temperature synthesis, XRD

INTRODUCTION

PbVO_3 is a perovskite compound of AVO_3 type (A is a divalent or trivalent cation) that is a strong candidate as a multiferroic compound. It attracts a lot of interest due to its simple structure (tetragonal, space group P4mm [1-8]) which allows a deeper understanding of the connection between the structure and the properties of this material. PbVO_3 was first synthesised by Shpanchenko et al in 2004 [1] from stoichiometric mixtures of PbO and VO_2 or PbO , V_2O_3 and V_2O_5 . He observed that PbVO_3 can only be prepared by solid state reaction under high-pressure high-temperature conditions (HP-HT) [1]. This result has been confirmed in the following years by all authors who prepared bulk PbVO_3 samples [1-5]. Shpanchenko's best samples were obtained at HP in the range of 4-6 GPa and HT in the range of 700-750°C [1]. The best samples however contained $\text{Pb}_3\text{V}_2\text{O}_8$ and $\text{PbV}_6\text{O}_{11}$ as impurities [1]. Nevertheless he was able to describe the structure of PbVO_3 . Belik prepared better samples one year later from a mixture of PbO , V_2O_3 and V_2O_5 at HP = 6 GPa and HT = 1000°C [2]. He succeeded in reducing the amount of impurities by regrinding the samples and applying a

^a Babes-Bolyai University, Faculty of Physics, Str. Kogălniceanu 1, RO-400084 Cluj-Napoca, Romania, * Corresponding author: aurel.pop@phys.ubbcluj.ro

^b Néel Institute, CNRS/UJF, UPR2940, 25 rue des Martyrs, BP 166, 38042, Grenoble cedex 9.

second HP-HT treatment in the same conditions as the first one. Unfortunately, his samples still contained enough impurities to hinder measurements of magnetic susceptibility and electric polarization [2]. Tsirlin also prepared PbVO_3 samples using as starting products PbO and VO_2 under HP-HT conditions [4] with the best samples obtained at 5 GPa and 950°C maintained for 2 hours [4]. However magnetic impurities were still present [4]. The conditions in which PbVO_3 is obtained are too rough for the HP-HT equipments [9]. We present the results of samples synthesis at a relatively low pressure of only 4 GPa and temperatures ranging from 650 to 1000°C , and the investigation of structure and phase purity of PbVO_3 .

RESULTS AND DISCUSSION

Figure 1 shows XRD patterns recorded for samples S1, S2 and S3, which were obtained by using the following synthesis HT: 650°C , 900°C and 1000°C respectively. For single phase PbVO_3 , the Miller indices (hkl) were attributed for peaks diffraction as in reference [1].

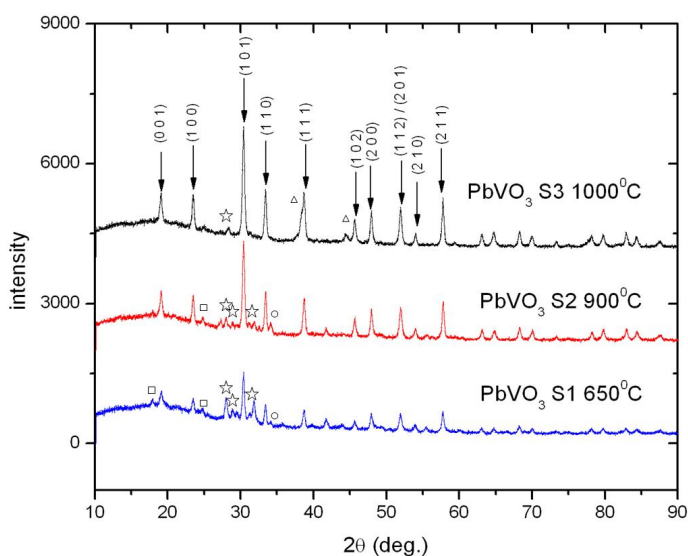


Figure 1. The XRD spectra of samples PbVO_3 obtained at the same high pressure (4 GPa) and different temperatures 650°C , 900°C and 1000°C respectively. The impurity phase $\text{Pb}_3\text{V}_2\text{O}_8$ is marked with star, $\text{PbV}_6\text{O}_{11}$ is marked with circle, $\text{Pb}_3(\text{CO}_3)_2(\text{OH})_2$ is marked with square and Au is marked with triangle.

The additional peaks, were identified from the impurity phases: $\text{Pb}_3\text{V}_2\text{O}_8$ (marked with star), $\text{PbV}_6\text{O}_{11}$ (marked with circle), and $\text{Pb}_3(\text{CO}_3)_2(\text{OH})_2$ (marked with square). Sometimes gold dust from the capsule mixed with the sample. Gold diffraction peaks are marked with triangles.

The diffraction peaks for the impurity phases were indexed based on structural data available in literature. Structural information for Pb₃V₂O₈ was taken from references [10, 11, 12], for PbV₆O₁₁ from [13, 14] and for Pb₃(C O₃)₂(O H)₂ from references [15,16], respectively. We found that the quality of the samples, defined by the phase purity, varies with the reaction conditions.

An almost single phase sample was obtained at 4 GPa and 1000° C (the “best” sample, S3) and the “worst” sample was obtained at 4 GPa and 650°C (sample S1). It can be easily observed that the intensities of the diffraction peaks corresponding to the impurity phases are comparable to those of the main phase for the “worst” sample. The same impurity peaks vanish almost completely in the “best” sample. Pb₃V₂O₈ is reported to be formed alongside PbVO₃ which might suggest that its presence is unavoidable [1, 2]. The presence of PbV₆O₁₁ phase causes problems in the acquisition of magnetic measurements since it is antiferromagnetic (with the transition at about 90 K) and the signal produced by PbV₆O₁₁ covers the signal of PbVO₃. The third identified impurity was the hydrocerussite, Pb₃(C O₃)₂(O H)₂, which gives no magnetic signal. Also, it is the least frequently encountered impurity. The mass percentages of the phases present in the sample S3 (the “best” sample) were calculated from FullProf, by assuming the presence of minority phases Pb₂V₃O₈ and PbV₆O₁₁, respectively. The results are as follows:

PbVO ₃	91.6 %
Pb ₂ V ₃ O ₈	5.9 %
PbV ₆ O ₁₁	2.4 %

The amount of PbV₆O₁₁ is beyond the detection limit of 5% of typical diffractometers so the presence of this impurity is hard to be confirmed by XRD. In the XRD pattern of S3 an additional impurity can be observed. This is gold that got mixed with the sample during the opening of the capsule. Since gold did not participate in the PbVO₃ forming reaction, its percentage was not calculated. The χ^2 value for the Rietveld refinement is 2.45. The X-ray powder peaks of our PbVO₃ phase were indexed by assuming a tetragonal structure in the space group P4mm (no. 99) [1]. The following lattice parameters were obtained: a = b = 3.8 Å and c = 4.67 Å, (Table 1). Figure 2 shows the Rietveld refinement for the S3 (the best sample). Table 1 shows that the structural data for PbVO₃ is in agreement with the previous results [1,2,3,6]. In figure 2, the experimental peaks of XRD diffraction data is marked with circles. The calculated XRD pattern is shown in a continuous line. The ticks under the diagrams mark the position of the Bragg peaks of each phase taken into the refinement as following. The first row of ticks shows the reflections for the main phase, PbVO₃. The second row shows the reflections for Pb₃V₂O₈. The third row of ticks shows the peaks of PbV₆O₁₁. Finally, the fourth row shows the Bragg reflections of gold. The difference between the experimental and calculated diagrams is shown by the continuous line located under the rows of ticks.

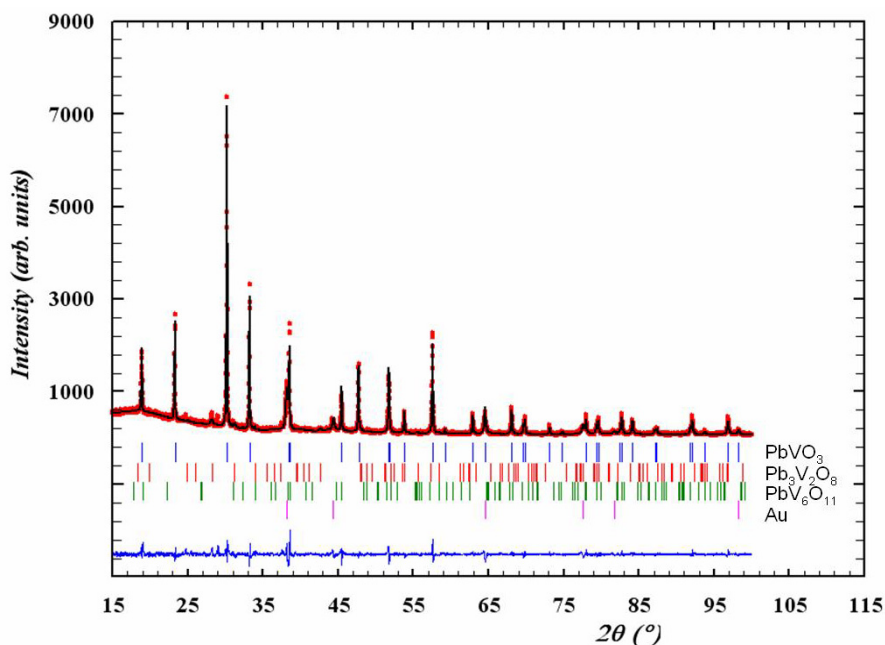


Figure 2. Rietveld refinement for PbVO_3 . Experimental, calculated, and difference X-ray patterns for PbVO_3 .

Table 1. Structural data for PbVO_3 .

Space group/ Lattice parameters	Atom types / positions / occupancy					
	Type	Wyckoff	x	y	z	occ.
P 4 m m	Pb	1b	0.5	0.5	0.56	1
a = 3.80	V	1a	0	0	0	1
b = 3.80	O1	1a	0	0	0.3	1
c = 4.67	O2	2c	0.5	0	-0.14	2

CONCLUSIONS

Samples with majority of phase PbVO_3 were obtained by solid state reaction method, using a new set of milder reaction conditions at HP = 4 GPa and HT in the range of 650°C to 1000°C. XRD shows that along with the majority PbVO_3 phase some minority phases are present. By increasing HT from 650°C to 1000°C, the intensity of the Bragg peaks for the minority phases decreases, and the impurity phases were diminished. PbVO_3 samples prepared by using HP = 4 GPa only, show a tetragonal structure with unit cell parameters in good agreement with previously reported results [1, 2, 3, 4].

EXPERIMENTAL SECTION

Bulk samples of PbVO₃ were synthesised by solid-state reaction method under high pressure (HP) and high temperature (HT). It is known that bulk PbVO₃ can only be synthesised under HP-HT conditions [1-6] at pressures as high as 8 GPa and temperatures over 1000° C. The typical reaction conditions are at the very limits of endurance for the machines and considering the high cost of the parts (pistons and cambers) and the fact that their lifespan is inversely proportional to the applied pressure we decided to search for other, milder, conditions at which we would still obtain the same product.

Samples were prepared at the Néel Institute, Grenoble, France (Laboratory of Structure and Properties of Materials - Extreme Conditions, SPMCE). We used a route for the synthesis of PbVO₃ at a relatively low pressure of only 4 GPa and temperatures ranging from 650 to 1000° C.

The chemical equation for the PbVO₃ synthesis is the following:



PbO₂ is used to provide the “additional” oxygen required for the oxidation of vanadium from 3+ to 4+.

Stoichiometric ratios of high purity PbO, PbO₂, V₂O₃ were mixed in an agate mortar for 30 minutes. The powder mixture obtained was sealed in a gold capsule which was mounted in the pressure cell of a BELT type apparatus. The applied HP-HT treatment consisted in submission for 30 min to a pressure of 4 GPa and a temperature between 650 and 1000° C.

The diagram of the HP-HT treatment is shown in figure 3.

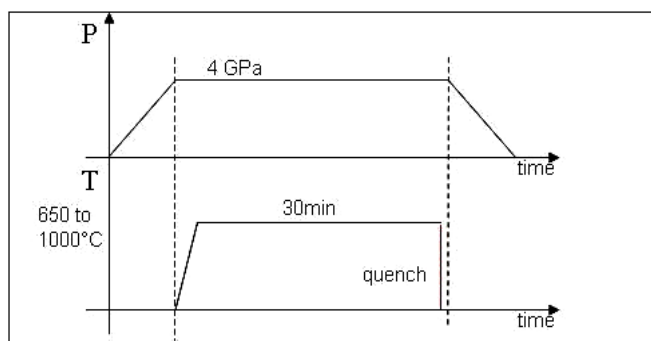


Figure 3. The diagram of HT-HP treatment program.

The following samples were obtained: S1 (T=650°C), S2 (T=900°C), S3 (T=1000°C). X-Ray diffraction was used for phases analysis and to characterise samples crystalline structure. XRD patterns were recorded with a Siemens D5000 diffractometer equipped with a Cu anode and a monochromator filtering the Cu K α 1 radiation.

Samples were measured in transmission (Stoe) geometry, with a step size of 0.016 degrees and 0.4 seconds counting time / step. In order to reduce the noise and for a better resolution, the representative samples were analysed by using a Bruker D8 diffractometer, also working in transmission geometry.

The phases were identified using the EVA software, by comparison to the database. The crystallographic data were refined using the Rietveld code with the FullProf software.

ACKNOWLEDGEMENTS

This work was possible with the financial support of the Sectoral Operational Programme for Human Resources Development 2007-2013, co-financed by the European Social Fund, under the project number POSDRU/107/1.5/S/76841 with the title „Modern Doctoral Studies: Internationalization and Interdisciplinarity”.

REFERENCES

- [1] R.V. Shpanchenko, V.V. Chernaya, A.A. Tsirlin, P.S. Chizhov, D.E. Sklovsky, and E. V. Antipov, *Chemistry of materials*, **2004**, *16*, 3267.
- [2] Alexei A. Belik, M. Azuma, Takashi Saito, Yuichi Shimakawa, Mikio Takano, *Chemistry of materials*, **2005**, *17*, 269.
- [3] Kengo Oka, Ikuya Yamada, Masaki Azuma, Soshi Takeshita, Kohki H. Satoh, Akihiro Koda, Ryosuke Kadono, Mikio Takano, and Yuichi Shimakawa, *Inorganic Chemistry*, **2008**, *47*, 7355.
- [4] A. Tsirlin, A. Belik, R. Shpanchenko, *Physical Review B*, **2008**, *77*, 092402.
- [5] Angel Arevalo-Lopez, M. Alario-Franco, *High Pressure Research*, **2008**, *28*, 509.
- [6] Lane W. Martin, M. Chi, Teruyasu Mizoguchi, Jens Kreisel, *Applied Physics Letters* **2007**, *90*, 062903.
- [7] Nicola A. Hill, *Journal of Physical Chemistry*, **2000**, *104*, 6694.
- [8] Jens Kreisel, W. Kleemann, R. Haumont, *Reflets de la Physique*, **2008**, *8*, 10.
- [9] H. Tracy Hall, *The Review of Scientific Instruments*, **1960**, *31*, 2.
- [10] J.M. Kiat, P. Garnier, M. Pinot, *Journal of Solid State Chemistry*, **1991**, *91*, 339.
- [11] J.M. Kiat, P. Garnier, G. Calvarin, M. Pinot, *Journal of Solid State Chemistry*, **1993**, *103*, 490.
- [12] Prangya Parimita Sahoo, Etienne Gaudin, Jacques Darriet T.N. Guru Row, *Inorganic Chemistry*, **2010**, *49*, 5603.
- [13] O. Mentre, F. Abraham, *Journal of Solid State Chemistry*, **1996**, *125*, 91.
- [14] Olivier Mentre, Anne-Claire Dhaussy, Francis Abraham, *Journal of Solid State Chemistry*, **1997**, *130*, 223.
- [15] J.M. Cowley, *Acta Crystallographica*, **1956**, *9*, 391.
- [16] P. Martinetto, M. Anne, E. Dooryhée, P. Walter, G. Tsoucaris, *Acta Crystallographica*, **2002**, *58*, 82.

Sb/SnO₂ NANOSTRUCTURED ANTICORROSIVE COATINGS ON METALS

GYULA TOLNAI^a, ISTVAN SAJO^a, EMIL HOLCZER^b,
FIAMMETTA KORMOS^b, IRINA TARSICHE^c, DORIN MANCIULA^d

ABSTRACT. The paper reports on the structural and mechanical properties of ATO (Antimony doped tin dioxide) thin coatings obtained by the by sol-gel one step multiple-dip coating technique on Ti, Cu and stainless steel substrates. Surface morphology, microstructure, composition, roughness and hardness of the obtained coatings were determined by using SEM (Scanning Electron Microscopy), AFM (Atomic Force Microscopy), EDX (Energy Dispersive X-ray Microanalysis) and XRD (X-ray Diffraction) measurements. Corrosion resistance was evaluated from corrosion potential measurements in 0.5 M H₂SO₄, 0.5 M NaOH and 0.5 M NaCl solutions. Adherent, nanostructured ATO coatings with long term corrosion resistance were obtained on all types of metal substrates.

Keywords: ATO, nanostructured thin coating, microstructure, roughness, hardness, corrosion resistance.

INTRODUCTION

Coating is a covering that is applied to the surface of a substrate in order to improve properties such as appearance, adhesion, corrosion resistance, wear resistance, optical transparency and gas sensitivity.

The choice of coating materials is strongly related to their chemical composition, purity, crystallinity, thermal stability, adhesion while the coating technologies must fulfill requirements related to complexity, overall cost and environment safety.

The conventional coating methods intended for metals corrosion protection such as plating with Cr, Ni, Zn, show several drawbacks such as: high energy consumption, discharge of process effluents containing hazardous chemical species, expensive technologies for effluents purification [1].

^a Chemical Research Center of the Hungarian Academy of Sciences, str. Pusztaszeri 59-67, Budapesta, Ungaria

^b Dekra Certifications SRL, str. C. Brâncuși, nr. 131, RO-400458 Cluj-Napoca, Romania

^c Universitatea "Babeș-Bolyai", Facultatea de Chimie și Inginerie Chimică, str. Kogălniceanu, Nr. 1, Cluj-Napoca, RO-40084, Romania itarsiche@chem.ubbcluj.ro

^d Universitatea "Babeș-Bolyai", Facultatea de Știința Mediului, str. Kogălniceanu, Nr. 1, RO-40084, Cluj-Napoca, Romania

A modern approach of coating is by using the nanostructured thin film technologies. Nanostructured inorganic or mixed inorganic-organic materials became of interest for many areas in the last decades [2].

Among the techniques used for preparing thin films, sol-gel seems to be preferred due to the large variety of precursors composition, many processing options, generation of many complex micro- and nanostructures, low thermal stress of the substrate, simple coating procedures. This technique was used with a wide variety of substrates: glass, ceramics, metals, polymers [3-5].

The use of nanostructured ATO thin films as protective coatings for glass or metals is based on their outstanding properties such as high mechanical resistance, very good chemical stability and antistatistical properties [6-9].

The paper presents the obtaining procedure of ATO nanostructured thin coatings deposited on metal substrates, namely Ti, Cu and stainless steel by sol-gel one step multiple-dip coating technique. The results regarding the structural and mechanical characteristics of the obtained coatings (surface morphology, microstructure, roughness, hardness) and corrosion behavior are shown.

RESULTS AND DISCUSSIONS

It is a well known fact that the mechanical, electrochemical and long term stability of a coating is strongly influenced by the coating quality expressed in terms of uniformity, microstructure, crystallinity, constituent particles size, roughness, hardness and adherence.

The ATO thin films intended for protective coatings must fulfill the same quality requirements. When ATO coatings are prepared by sol-gel dip coating technique, these characteristics depend on preparation conditions such as: composition of the precursor (doping degree), number of dippings, annealing temperature [10].

The surface morphology of the ATO coatings prepared according the experimental conditions described, was investigated by SEM. The images were taken for the ATO coatings obtained after air drying at 60°C only and annealing, as well (figures 1-3).

The SEM images show that, in all cases, annealing led to more uniform, compact and free of crack coatings and good conformal coverage of the substrate surface. Also, one may observe that the ATO coating on Cu substrate is formed of larger particles while the coatings on Ti and stainless steel substrates appear to be formed of smaller particles having comparable dimensions.

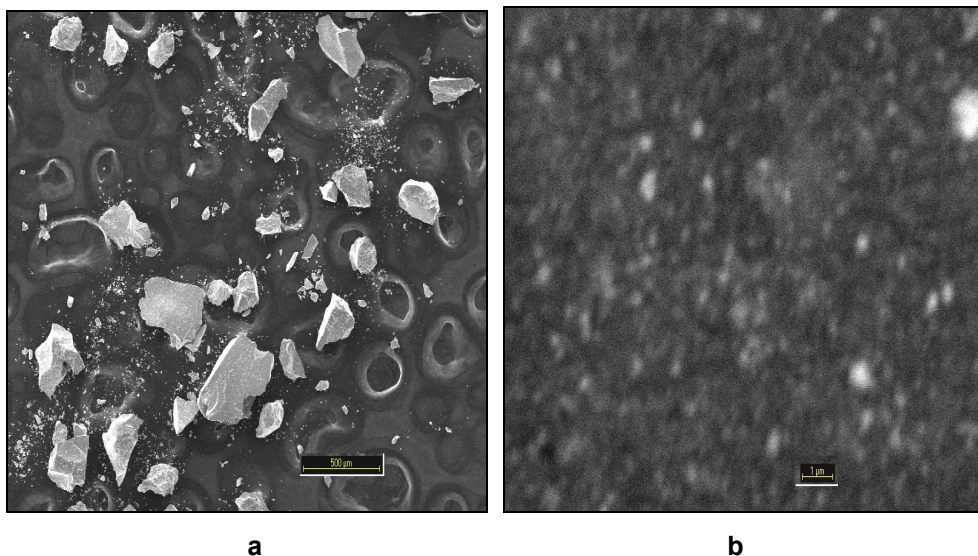


Figure 1. SEM images of ATO coating on Ti: a) after air drying at 60⁰C; b) after annealing

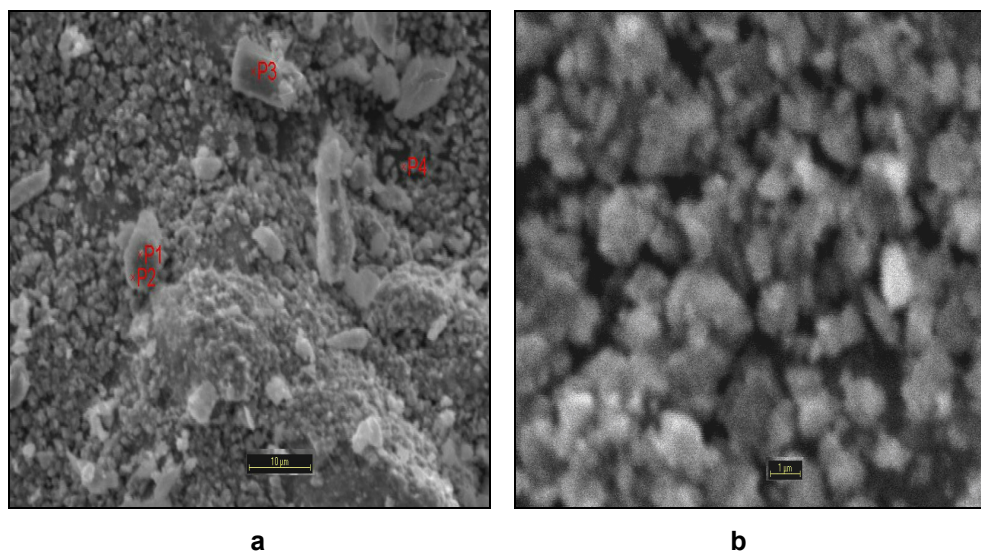


Figure 2. SEM images of ATO coating on Cu: a) after air drying at 60⁰C; b) after annealing

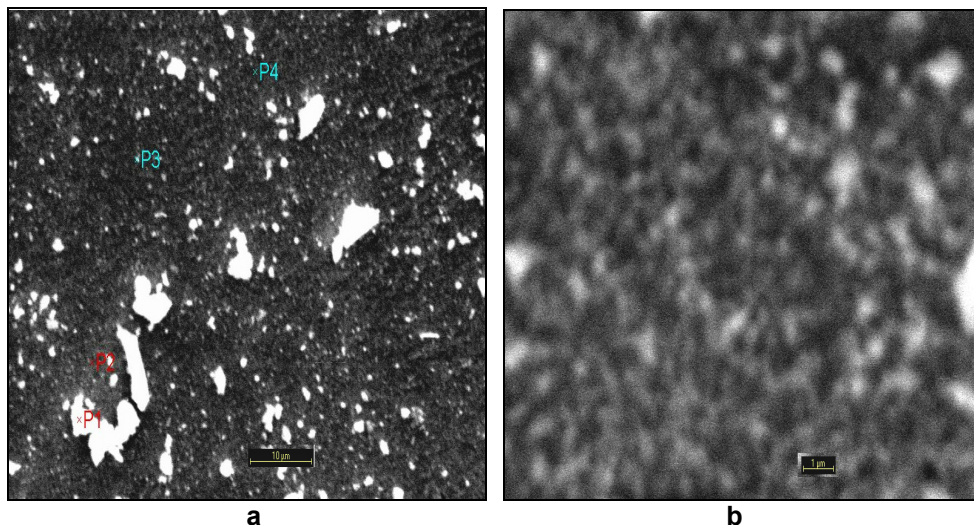


Figure 3. SEM images of ATO coating on stainless steel: a) after air drying at 60°C; b) after annealing

The XRD patterns taken for the coatings obtained after annealing confirmed their polycrystalline structure and showed diffraction peaks belonging to the tetragonal rutile structure of SnO₂ with a preferred orientation along the plane (101) while the ATO coatings obtained after air drying only show an almost single crystalline structure (figure 4).

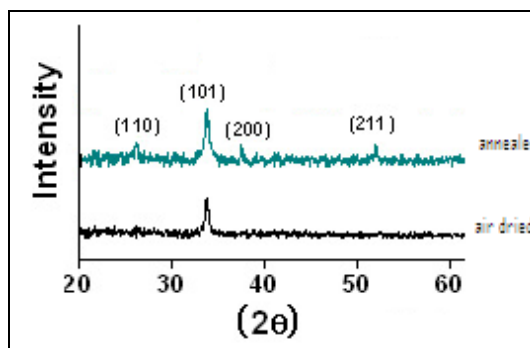


Figure 4. XRD spectra for the air dried only and annealed ATO coatings on stainless steel substrate

Also, the XRD patterns didn't show any difference in the crystalline structure of the ATO coatings related to the nature of the substrate. The grain sizes were calculated by using the Scherrer's equation and are presented in table 1.

The composition of the annealed ATO coatings was determined by EDX analysis. A typical spectrum is shown in figure 5.

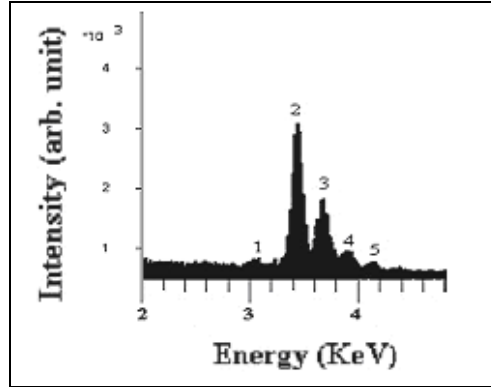


Figure 5. EDX spectrum of annealed ATO coating deposited on Ti

The appearance of the peaks at 3.045 keV (Sn L₁-peak 1), 3.444 keV (Sn L_{α1}-peak 2), 3.905 keV (Sn L_{β2} – peak 3), 4.101 keV (Sb L_{β2}-peak 4) and 4.248 keV (Sb Ly₁-peak 5) which are characteristic lines of Sn and Sb confirmed the presence of both elements in the ATO coating.

Surface roughness and hardness have a major impact on the corrosion resistance of the coating. For the annealed ATO coatings these parameters were determined from AFM measurements on the basis of height images obtained in tapping mode (figure 6) and nanoindentation, respectively. The obtained results are summarized in table 1.

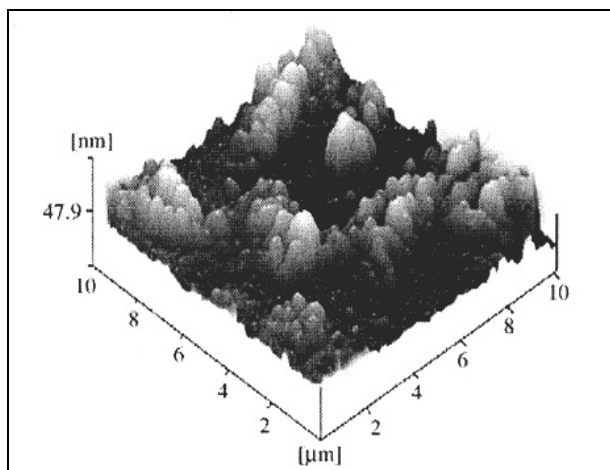


Figure 6. AFM image of ATO coating on Ti substrate

Table 1. ATO coatings physical characteristics

Substrate	Physical characteristics		
	Particle size [nm]	Roughness [min-max]	Hardness [MPa]
Stainless steel	95	12-150	5,3 ± 0,05
Copper	120	45-330	3,4 ± 1,2
Titanium	72	12-130	5,9 ± 1,1

The data in table 1 show that the ATO coatings obtained on Ti and stainless steel show comparable mechanical characteristics while the coating on Cu differ with respect to particle size, roughness and hardness. The determined data are in good agreement with the information provided by SEM images and with literature data which shows that with grain size decreasing, the hardness of the coating increases [11].

The corrosion resistance of the ATO coatings was evaluated by recording the corrosion potential in 0.5 M H₂SO₄, 0.5 M NaOH and 0.5 M NaCl solutions for 120 days. A typical overall variation of the corrosion potential is shown in figure 7.

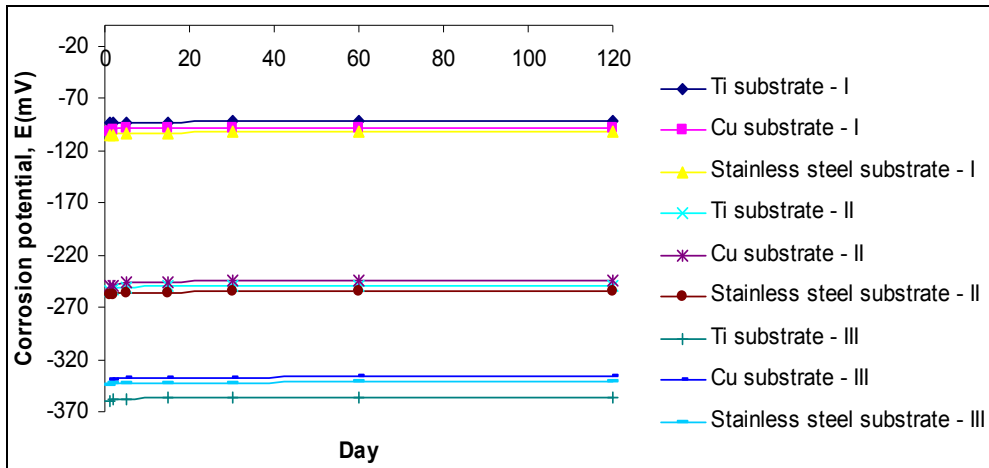


Figure 7. Variation of the corrosion potential (work electrode: annealed ATO coating deposited on Ti, Cu or stainless steel substrate): I - 0.5 M H₂SO₄; II - 0.5 M NaOH; III - 0.5 M NaCl.

The data in figure 7 show a very small long term variation of the corrosion potential (2-4 mV) which indicates a passive behaviour of the ATO coating in the chemical media under investigation. No significant behaviour differences were observed as a function of substrate nature and ATO coating roughness and hardness.

CONCLUSIONS

ATO thin coatings on metal substrates (Cu, Ti, stainless steel) were prepared by sol-gel multiple-dip coating technique and their physical, mechanical and corrosion resistance was examined by SEM, XRD, EDX, AFM and corrosion potential measurements.

The SEM measurements revealed that the coatings are more uniform and also free of cracks after annealing. Also, the ATO coatings on Cu substrate are formed of larger particles than the coatings on Ti or stainless steel.

XRD patterns showed the polycrystalline structure of the annealed ATO coatings with diffraction peaks belonging to the rutil structure of SnO₂. No difference in the crystalline structure related to the nature of the substrate was observed. The grain sizes belong to the nanoscale (70-120 nm), the coatings on Ti and stainless steel containing smaller particles, their size being 72 nm and 95 nm, respectively. By using EDX measurements, on the basis of the characteristic lines, it was established that Sn and Sb are present in the ATO coatings chemical composition.

Roughness and hardness measurements showed comparable values for the ATO coatings on Ti and stainless steel substrates while those on Cu substrate showed higher roughness and lower hardness, which is in good agreement with the information provided by SEM images and the calculated grain sizes.

The corrosion potential measurements for a period of 120 days showed the passive behaviour of the ATO coatings with no significant difference in the corrosion potential evolution related to the nature of the substrate or roughness and hardness of the ATO coating.

By using sol-gel multiple-dip coating technique, nanostructured ATO thin coatings were prepared on Cu, Ti and stainless steel substrates with long term corrosion resistance.

EXPERIMENTAL SECTION

Reagents and materials

SnCl₄·5H₂O, (Sigma), SbCl₃ (Fluka), ethanol (Fluka), tartaric acid (Fluka), H₂SO₄ (Fluka), NaOH (Fluka), NaCl (Fluka), reagent grade.

The metal substrates made of Ti, Cu, stainless steel plates 20x20x0.8 mm³, were treated with H₃PO₄ 2 M at 60C° for 15 min, followed by washing with distilled water and acetone and drying in air for 15 min. This cleaning procedure slightly increases surface roughness and subsequently, improves the coating adhesion to the substrate.

Obtaining of ATO coatings

The sol was obtained from a precursor with the following composition: 100 ml 0.2 M SnCl₄ and 15 ml 0.5 M SbCl₃ both in ethanol. The precursor was stirred for 1.5 hours with tartaric acid.

The coatings were obtained by one step multiple-dip coating using a Nima Tensiometer. The substrates were immersed into the sol with 10 mm/min constant speed and withdrawn in the same conditions. The operation was repeated 10 times. The coated substrates were dried 30 min at 60°C. A second series of coatings was prepared following the same procedure but instead of air drying only they were annealed for 15 minutes at 350°C too.

Characterisation of ATO coatings

The surface morphology of both air dried only and annealed coatings was investigated by SEM on a HITACHI electron microscope.

Crystalline structure and composition were established by XRD and EDX measurements by using a Philips PW 3710 diffractometer with Cu-K α source. The scanning range was 20-60°.

Roughness and hardness were determined by AFM and nanoindentation measurements with a Veeco Dimension 3100 Atomic Force Microscope with a Nanoidenter III controller.

Evaluation of ATO coatings corrosion behaviour

Half-cell potential measurements were performed in a classic two electrode cell by using as work electrode the coated substrates and as reference electrode a Ag/AgCl, KCl sat. (Radiometer, France). The corrosion potential was recorded by using an Infinitron, model 800, high impedance voltmeter.

The measurements were done in 0.5 M H₂SO₄, 0.5 M NaOH and 0.5 M NaCl solutions during 120 days, with everyday reading of the potential.

REFERENCES

- [1] P. Donghee, S.Y. Yeoung, J.H. Ji, P.M. Jong, *Industrial and Engineering. Chemistry Research*, **2006**, *45*, 5059.
- [2] U.K. Mudali, S. Ningshen, A.R. Shankar, *Pure and Applied Chemistry*, **2011**, *83*, 2079.
- [3] B. Benrabah, A. Bouaza, A. Kadari, M.A. Maaref, *Superlattices and Microstructures*, **2011**, *50*, 591.
- [4] B. Benrabah, A. Bouaza, S. Hamzaoui, A. Dehbi, *The European Physical Journal Applied Physics*, **2009**, *48*, 30301.
- [5] M.M. Koebel, D.Y. Nadargi, G. Jimenez- Cadena, Y.E. Romanyuk, *ACS Applied Materials & Interfaces*, **2012**, *4*, 2464.
- [6] A. Assia, O. Ratiba, M. El Mahdi, K. Mohamed, *International Journal of Chemical and Biological Engineering*, **2009**, *2*, 1.
- [7] S. Wu, Q.N. Zhao, D.K. Miao, Y.H. Dong, *Journal of Rare Earths*, **2010**, *28*, 189.
- [8] S. Sharma, A.M. Volosin, D. Schmitt, D.K. Seo, *Journal of Materials Chemistry A*, **2013**, *3*, 699.
- [9] S. Sladkevich, A.A. Mikhaylov, P.V., Prikhodchenko, T.A. Tripolskava, O. Lev, *Inorganic Chemistry*, **2010**, *49*, 9110.
- [10] T.M. Hammad, N.K. Hejazy, *International Nano Letters*, **2012**, *2*, 7.
- [11] D.C. Woo, C.Y. Koo, H.C. Ma, L.H. Young, *Transactions on Electrical and Electronic Materials*, **2012**, *13*, 241.

EVALUATION OF PHENOTHIAZINE AS ENVIRONMENTALLY FRIENDLY CORROSION INHIBITOR FOR BRONZE IN SYNTHETIC ACID RAIN

ROXANA BOSTAN^{a,b*}, SIMONA VARVARA^b, MARIA POPA^b,
LIANA MARIA MURESAN^a

ABSTRACT. Inhibition performance of phenothiazine as safe corrosion inhibitor for bronze in a solution containing Na₂SO₄ and NaHCO₃ (pH=5) that simulates an acid rain in an urban environment was investigated by potentiodynamic polarization and electrochemical impedance measurements. The results showed that phenothiazine is a fairly efficient inhibitor towards bronze corrosion, even when added in μM concentration range. The inhibition efficiency of phenothiazine increases with its concentration and attains a value higher than 91% at 150 μM concentration level. The adsorption of phenothiazine on bronze surface obeys the Langmuir's isotherm. Phenothiazine was proved to be a promising environmentally-safe alternative to the harmful corrosion inhibitors used for the protection of bronze against corrosion in aggressive media.

Key words: *bronze, corrosion, phenothiazine, electrochemical impedance spectroscopy, polarisation curve*

INTRODUCTION

The corrosion of copper and bronze in acidic media is a major problem affecting numerous sculptures, ornamental work materials and archaeological artefacts, but also industrial applications (battery connectors, distribution systems etc.) [1].

One of the most efficient alternatives to prevent bronze dissolution in aggressive media is the use of corrosion inhibitors. Nevertheless, many common corrosion inhibitors widely used to protect copper [2-4] and its alloys from corrosion [5-8], such as chromates [9], organic compounds containing heteroatoms with high electronic density (*i.e.* nitrogen, sulphur and oxygen) or those containing multiple aromatic bonds [10] are harmful substances and most of them cannot be biodegraded [11].

^a Department of Chemical Engineering, "Babes-Bolyai" University, 11 Arany Janos St., 400028 Cluj-Napoca, Romania

^b Department of Exact Sciences and Engineering, "1 Decembrie 1918" University, 11-13 Nicolae Iorga St., 510009 Alba-Iulia, Romania, a_roxananadina@yahoo.com

Nowadays, the increasing consciousnesses of the health and ecological policies for the use of chemicals have changed the traditional approach of corrosion inhibition science [12]. Consequently, the utilization of these compounds has been limited by their degree of toxicity [13] and the current research focuses on the development of new “green” inhibitors, compounds having good inhibition efficiency, but low or zero risk of environmental pollution [8].

In this context, the present research aims to investigate the inhibition properties of phenothiazine on bronze corrosion in a solution containing Na_2SO_4 and NaHCO_3 (pH=5) that simulates an acid rain in urban environments. In small concentrations, phenothiazine is not toxic, neither noxious towards human beings or the environment, is relatively cheap, easy to produce in high purity and is used in the antihistaminic drugs production [14]. Moreover, some derivatives of phenothiazine have been already reported as efficient corrosion inhibitors for copper-based alloys [15].

Electrochemical techniques, such as potentiodynamic polarization and electrochemical impedance spectroscopy measurements (EIS) were used to gain more information on the inhibition mechanism of phenothiazine on bronze corrosion.

RESULTS AND DISCUSSION

Potentiodynamic polarization measurements

Fig. 1 shows cathodic and anodic polarization scans recorded for bronze in $0.2 \text{ g L}^{-1} \text{ Na}_2\text{SO}_4 + 0.2 \text{ g L}^{-1} \text{ NaHCO}_3$ (pH=5) solution at 25°C , in the absence and presence of various concentrations of phenothiazine over the range $1 - 150 \mu\text{M}$.

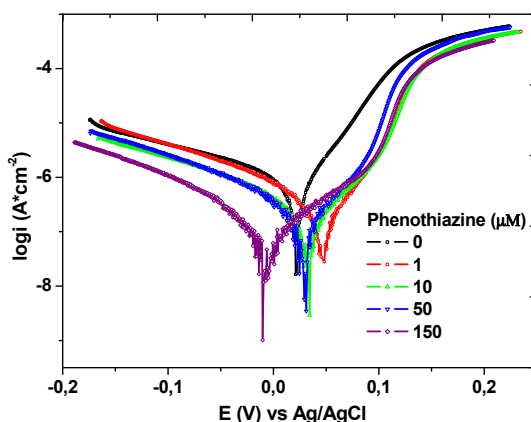


Figure. 1. Tafel polarization curves for bronze corrosion in $\text{Na}_2\text{SO}_4/\text{NaHCO}_3$ solution (pH 5) with various concentrations of phenothiazine.
Scan rate: 10 mV/min.

From Fig. 1, it can be observed that both the anodic metal dissolution and oxygen reduction reactions are hindered when different concentrations of phenothiazine are added to the corrosive solution. A shift of the corrosion potential towards more positive values as compared to the E_{corr} value calculated for blank solution could be also observed in the presence of phenothiazine at concentrations below 100 μM . In the presence of higher concentration of phenothiazine (150 μM), the corrosion potential is negatively shifted.

The corrosion parameters derived from these curves, such as corrosion potential (E_{corr}), cathodic and anodic Tafel slopes (β_c and β_a) and corrosion current density (i_{corr}) are summarized in Table 1. The values of inhibition efficiency (IE) of the phenothiazine as a function of its concentration are also presented in Table 1.

The IE values were calculated according to the following equation:

$$IE = \frac{i_{\text{corr}}^0 - i_{\text{corr}}}{i_{\text{corr}}^0} \times 100 \quad [\%] \quad (1)$$

where i_{corr}^0 and i_{corr} are the values of the corrosion current densities in absence and in presence of phenothiazine, respectively.

Table 1. Corrosion parameters obtained from the polarization curves

Inhibitor	conc. (μM)	E_{corr} (mV/ Ag/AgCl)	i_{corr} ($\mu\text{A}/\text{cm}^2$)	$-\beta_c$ (mV/dec)	β_a (mV/dec)	IE (%)
Blank	0	22	0.66	172	46	-
Phenothiazine	1	47	0.22	81	55	66.6
	10	34	0.17	89	60	74.2
	50	31	0.11	65	43	83.3
	150	-10	0.06	54	71	90.9

The values of the corrosion current density decrease with increasing phenothiazine concentration and the inhibition efficiency attains the highest value of 90.9% in the presence of 150 μM phenothiazine.

The presence of the different concentrations of phenothiazine in the corrosive media change significantly the cathodic (β_c) Tafel slopes. In the case of anodic (β_a) Tafel slope, the values obtained in the presence of different concentrations of phenothiazine are not significantly different from the value obtained in the absence of phenothiazine, which means that phenothiazine has a stronger effect on the cathodic oxygen reduction process, probably by blocking the O_2 access to the bronze surface.

Electrochemical impedance spectroscopy measurements

Fig. 2 shows the impedance spectra of bronze electrode immersed in $0.2 \text{ g L}^{-1} \text{ Na}_2\text{SO}_4 + 0.2 \text{ g L}^{-1} \text{ NaHCO}_3$ (pH 5) solution, in the absence and in the presence of various concentrations of phenothiazine (1 to $150 \mu\text{M}$), represented as Nyquist and Bode plots.

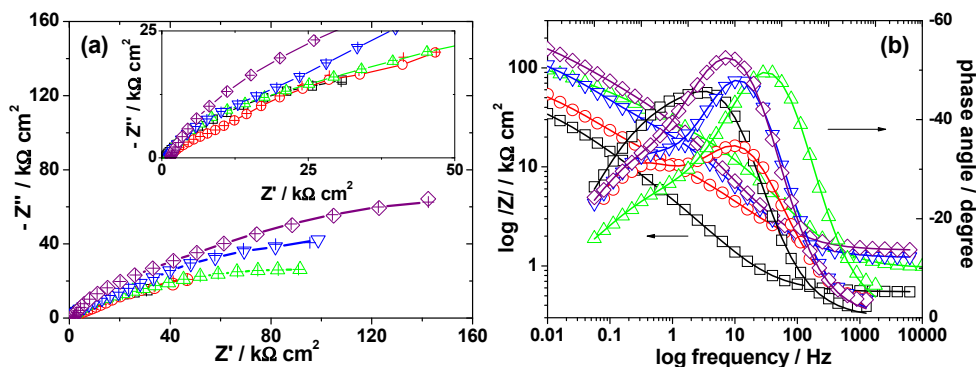


Figure 2. Nyquist (a) and Bode (b) plots of bronze electrode in $\text{Na}_2\text{SO}_4/\text{NaHCO}_3$ (pH 5) solution, in the absence and in the presence of different concentrations of phenothiazine (μM): (\square) 0; (\circ) 1; (\triangle); 10; (∇) 50; (\diamond) 150. The symbol (---+---) corresponds to the fitted data.

It can be noticed that all experimental plots have a depressed semicircular shape in the complex impedance plane, with the centre under the real axis (Fig. 2). This behaviour is typical for solid metal electrodes that show frequency dispersion of the impedance data and could be attributed to roughness and other inhomogeneities of the solid surface [16]. Consequently, constant phase elements (CPEs) represented by the terms, Q and n are often used nowadays instead of pure capacitances to represent the depressed features of the capacitive loops.

The impedance of the CPE is given by [17]:

$$Q = Z_{\text{CPE}(\omega)} = [C(j\omega)^n]^{-1} \quad (2)$$

where j is an imaginary unit and ω is the angular frequency in rad s^{-1} .

The equivalent circuit used for fitting the experimental data is presented in Fig. 3, where R_e corresponds to the electrolyte resistance, the parameter R_{ct} coupled with Q_d describe the charge transfer process at the electrolyte/bronze interface, while the low frequency elements, R_F and Q_F correspond to an oxidation-reduction process taking place at the electrode surface, probable involving the corrosion products layers accumulated at the interface. A similar circuit was formerly used by K. Marusic *et al.* [18] to explain bronze corrosion in the presence of 4-methyl-1-p-tolylimidazole.

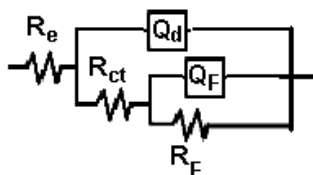


Figure 3. Equivalent electrical circuit used to reproduce the experimental data

The good agreement between the experimental and the calculated values of the impedance from Fig. 2 indicates that (2RQ) equivalent electrical circuit properly reproduce the experimental data corresponding to the bronze corrosion in weak acidic solution, in the absence and in the presence of the phenothiazine, respectively.

The values of the pseudo-capacitances associated with the CPEs were recalculated using the equation [17]:

$$C = (R^{1-n}Q)^{1/n} \quad (3)$$

The variations of the calculated R-C parameters as a function of the organic inhibitor concentration are illustrated in Fig. 4.

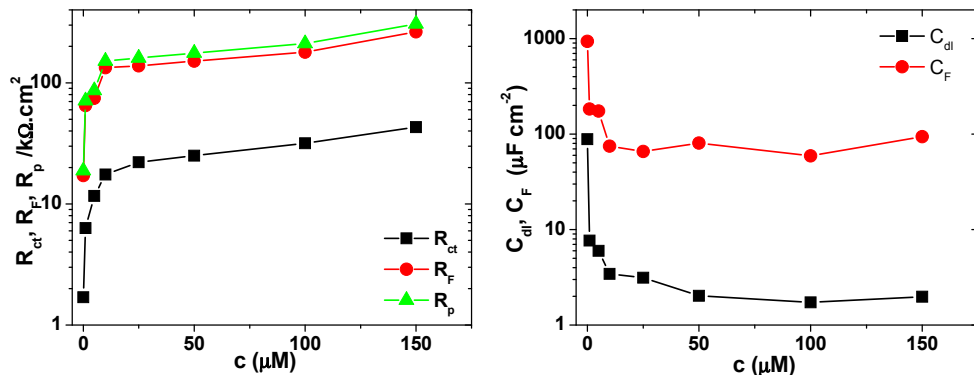


Figure 4. Calculated EIS data for bronze corrosion in $\text{Na}_2\text{SO}_4/\text{NaHCO}_3$ (pH 5) solution, without and with the addition of different concentrations of phenothiazine

In the blank solution, the calculated value of capacitance C_{dl} is $88.3 \mu\text{F} \cdot \text{cm}^{-2}$, plausible for a double layer capacitance, thus validating the model used for experimental data simulation. In the presence of phenothiazine, the C_{dl} values decrease as a consequence of inhibitor adsorption on the bronze surface leading to a smaller area of the electrode directly in contact with the electrolyte under the corrosion product layer or to a less conductive nature of this film.

The values of the charge transfer resistance, R_{ct} , significantly increase with the organic compound concentration, being related to the corrosion protection effect of the phenothiazine molecule. This effect is enhanced upon increasing phenothiazine concentration.

With increasing the phenothiazine concentration, the faradaic resistance R_F values increase, while simultaneously the C_F decreases. Consequently, it was assumed that the adsorption of the organic compounds on the bronze surface hinders the formation of the corrosion products and stabilizes the species covering the electrode, which became less susceptible to redox processes and confer better protection to the electrodic surface [15].

It is common knowledge that, in the presence of a redox process taking place at the bronze surface, the parameter which is closer related to the corrosion rate is the polarisation resistance, R_p .

Consequently, the R_p values, calculated as the sum of the two resistances (R_{ct} and R_F) were used to determine the inhibition efficiency of phenothiazine, as a function of their concentration, according to following equation:

$$IE = \frac{R_p - R_p^0}{R_p} \quad (4)$$

where R_p^0 and R_p are the polarisation resistances in electrolytes without and with inhibitor, respectively.

As it can be seen in Table 2, the inhibition efficiency values, calculated from ac impedance results show the same trend as those estimated from the polarization measurements. In the investigated experimental conditions, the maximum IE value (93.8 %) was obtained in the presence of 150 μM phenothiazine.

Table 2. Corrosion parameters obtained from the impedance measurements

Inhibitor	c (μM)	IE (%)	θ
Blank	0	-	-
Phenothiazine	1	73.5	0.731
	5	78.2	0.854
	10	87.5	0.903
	25	88.3	0.923
	50	89.3	0.932
	100	91.1	0.946
	150	93.8	0.961

Adsorption isotherm

Basic information on the interaction between the inhibitor and the metal surface can be provided by the adsorption isotherm.

The experimental data obtained from EIS measurements were used to determine the adsorption characteristics of phenothiazine on bronze in $\text{Na}_2\text{SO}_4/\text{NaHCO}_3$ (pH 5) solution.

The values of the surface coverage degree, θ for different inhibitor concentrations, calculated according to the equation (5) are presented in Table 2.

$$\theta = \frac{R_{ct} - R_{ct}^0}{R_{ct}} \quad (5)$$

where R_{ct}^0 and R_{ct} are the charge transfer resistances in electrolytes without and with inhibitor, respectively.

In the investigated conditions, the plots of the experimental θ values to various adsorption isotherms (Langmuir, Frumkin and Temkin) showed that the adsorption of phenothiazine on bronze surface follows the Langmuir isotherm (Fig. 5), according to the following equation:

$$\frac{c}{\theta} = \frac{1}{K} + c \quad (6)$$

where K is the adsorption equilibrium constant, c represents the phenothiazine concentration expressed in molar units.

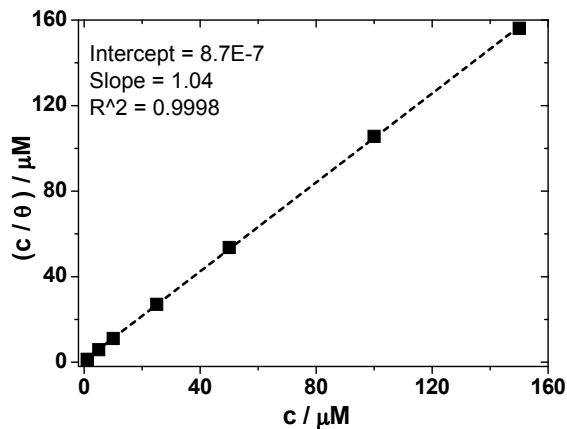


Figure 5. Langmuir adsorption isotherm of phenothiazine on the bronze surface in $\text{Na}_2\text{SO}_4/\text{NaHCO}_3$ (pH 5) solution, at 25^o C

The plot of c/θ versus c yields to a straight line with slope close to unit (Fig. 5) confirming that the adsorption of phenothiazine on bronze surface obeys the Langmuir isotherm.

The standard free enthalpy of adsorption ΔG_{ads}^0 was determined from the adsorption equilibrium constant, K according to the following equation [19]:

$$\Delta G_{ads}^0 = -RT \ln(55.5K) \quad (7)$$

where 55.55 represents the molar concentration of water in solution (mol dm^{-3}), R is the gas constant and T is the absolute temperature.

The calculated ΔG_{ads}^0 value of -44.5 kJ/mol suggests that the adsorption of phenothiazine on bronze is spontaneous and occurs mainly by chemisorption.

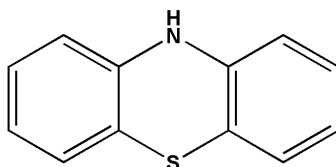
CONCLUSIONS

The ability of phenothiazine to hinder bronze corrosion in a simulated acid rain was examined in order to understand the processes leading to the inhibition of metal dissolution. Both potentiodynamic polarization and impedance spectroscopy studies demonstrate the inhibiting properties of this molecule, even when added at μM concentration range. The protective effectiveness of phenothiazine on bronze corrosion increases with increasing the inhibitor concentration and reaches a value higher than 91% at a concentration level as low as $150 \mu\text{M}$. Similarly to other molecules containing N and S in their structure, the inhibitive action of phenothiazine is a consequence of its adsorption on the bronze surface forming a blocking barrier against corrosion. The adsorption process of phenothiazine follows the Langmuir isotherm.

The environmentally friendly properties of phenothiazine make it favourable to be used in practice, replacing some toxic corrosion inhibitors, in accordance with the ecological policies for the use of chemicals.

EXPERIMENTAL

The molecular structure of the phenothiazine is presented in Scheme 1.



Scheme 1. Molecular structure of phenothiazine

The corrosive medium employed was an aqueous aerated solution of $0.2 \text{ g L}^{-1} \text{ Na}_2\text{SO}_4 + 0.2 \text{ g L}^{-1} \text{ NaHCO}_3$, acidified to $\text{pH}=5$ by addition of dilute H_2SO_4 , that was prepared from analytical grade reagents and distilled water. This solution simulates an acidic rain in urban environment [15]. The presence of sulphate simulates the pollution by sulphur dioxide frequently induced by petroleum nowadays and coal at ancient time [18]. The presence of carbonate ions is due to the natural composition of air, *i.e.* 0.033% [18]. The working electrode used in this study was prepared from a cylindrical bar of bronze (Cu-94.03, Sn-3.31, Pb-0.24, Zn-1.44, Ni-0.25, Fe-0.22, Si-0.51, at. %). The electrode was sealed with epoxy resin and only its cross section (0.28 cm^2) was allowed to contact the aggressive solutions. Prior to each experiment, the electrode was mechanically ground using successive grades of silicon carbide paper up to grade 2400, and then rinsed with distilled water and finally degreased with ethanol.

A three-electrode cell consisting of a bronze working electrode, a platinum counter electrode and a silver–silver chloride ($\text{Ag}|\text{AgCl}, \text{KCl}_{\text{sat}}$) electrode as reference electrode was used for the measurements. All electrochemical experiments were performed at room temperature without stirring, using a PAR model 2273 potentiostat controlled by a PC computer.

Before each experiment, the bronze electrode was left at the open circuit potential for 1 hour in the corrosive solution to establish the steady state condition. After measuring the open circuit potential, polarization curves were recorded at constant sweep rate of 10 mV/min , in the potential range from -200 to $+200 \text{ mV}$ with respect to the open circuit potential.

Electrochemical impedance spectroscopy measurements (EIS) were carried out at the open circuit potential after 1 hour immersion of the bronze electrode in the corrosive medium. The impedance spectra were acquired in the frequency range 10 kHz to 10 mHz at 10 points per hertz decade with an AC voltage amplitude of $\pm 10 \text{ mV}$. The impedance data were interpreted on the basis of equivalent electrical circuits, using the ZSimpWin V3.21 software for fitting the experimental data.

REFERENCES

- [1] M. Wadsak, T. Aastrup, I.O. Wallinder, C. Leygraf, M. Schreiner, *Corrosion Science*, **2002**, 44, 791.
- [2] E.S.M. Sheriff, R.M. Erasmus, J.D. Comins, *International Journal of Electrochemical Science*, **2007**, 306, 96.
- [3] M.M. El-Naggar, *Journal of Materials Science*, **2000**, 35(24), 6189.

- [4] W. Qafsaoui, Ch. Blanc, N. Pébère, A. Srhiri, G. Mankowski, *Journal of Applied Electrochemistry*, **2000**, 30, 959.
- [5] S. Varvara, L.M. Muresan, K. Rahmouni, H. Takenouti, *Corrosion Science*, **2008**, 50, 2596.
- [6] I. Ignat, S. Varvara, L. Muresan, *Studia UBB Chemia*, **2006**, L1, 127.
- [7] M. Behpour, S.M. Ghoreishi, M. Salavati-Niasari, B. Ebrahimi, *Materials Chemistry and Physics*, **2008**, 107, 153.
- [8] K.F. Khaled, *Materials Chemistry and Physics*, **2008**, 112, 104.
- [9] M.M. Antonijevic, M.B. Petrovic, *International Journal of Electrochemical Science*, **2008**, 3, 1.
- [10] M. Behpour, S.M. Ghoreishi, N. Soltani, M. Salavati-Niasari, *Corrosion Science*, **2009**, 51, 1073.
- [11] D. Zhang, L. Gao, G. Zhou, K.Y. Lee, *Journal of Applied Electrochemistry*, **2008**, 38, 71.
- [12] O. Olivares-Xometl, N.V. Likhanova, M.A. Dominguez-Aguilar, E. Arce, H. Dorantes, P. Arellanes-Lozada, *Materials Chemistry and Physics*, **2008**, 110, 344.
- [13] K. Barouni; L. Bazzi; R. Salghi; M. Mihit; B. Hammouti; A. Albourine, S. Issami E., *Materials Letters*, **2008**, 62, 3325.
- [14] R.R. Gupta, *Bioactive molecules, Elsevier Science.*, **1988**, vol 4.
- [15] R. Bostan, S. Varvara, L. Găină, L.M. Muresan, *Corrosion Science*, **2012**, 6, 275
- [16] F. Bentiss, M. Lebrini, M. Lagrenée, M. Traisnel, A. Elfarouk, H. Vezin, *Electrochimica Acta*, **2007**, 52, 6865.
- [17] I.D. Raistrick, J.R. MacDonald, D.R. Franceschetti, "Impedance Spectroscopy Emphasizing Solid Materials and Systems", Wiley, New York **1987**, pp. 27–84.
- [18] K. Marusic, H.O. Curkovic, H. Takenouti, *Electrochimica Acta*, **2011**, 56, 7491.
- [19] H. Ashassi-Sorkhabi, D. Seifzadeh, M.G. Hosseini, *Corrosion Science*, **2008**, 50, 3363.

ELECTROCHEMICAL PREPARATION OF Co-Cu ALLOY NANOWIRES AND THEIR CHARACTERISATION

MIHAELA-DANIELA GAVRIL (DONOSE)^a, UDO SCHMIDT^b,
CONSTANTIN GHEORGHIES^a, ALINA-MIHAELA CANTARAGIU^a,
ADRIANA ISPAS^b, ANDREAS BUND^b

ABSTRACT. In this study, Co-Cu alloy nanowires were grown in anodic aluminium oxide (AAO) template obtained through one-step anodisation method of aluminium-magnesium alloy (Al 95%) in oxalic acid solution at constant voltage of 40 V. The electrodeposition of Co-Cu alloy nanowires into the 10 µm thickness of AAO template with pore average diameter of 40 nm was studied using a single bath containing both cobalt and copper ions. The galvanostatic reverse pulse plating was chosen as preparation method of Co-Cu alloy nanowires at room temperature. The optimal operation parameters required during the preparation method were established by cyclic voltammetry (CV) experiments. The electrochemical deposition was performed at current densities ranging between 20-50 mA/cm² during 60 min. The physical and chemical properties of Co-Cu alloy nanowires have been investigated through scanning electron microscopy (SEM), transmission electron microscopy (TEM), energy dispersive X-ray spectroscopy (EDS), X-ray fluorescence spectroscopy (XRF) and focused-ion-beam-microscopy (FIB) techniques.

Keywords: Al, anodisation, AAO template, Co-Cu alloy nanowires, electrodeposition, reverse pulse plating, FIB, TEM.

INTRODUCTION

Nowadays we witnessed a development of high density information on magnetic storage. It has been demonstrated that ferromagnetic wires having a high aspect ratio can be prepared using porous alumina (Al₂O₃) as template [1].

Various magnetic wires have been synthesized using different methods and types of templates. In our days the electrodeposition of Co alloys nanowires with Ni, Fe or Cu is intensively studied due to the special properties of these

^a "Dunarea de Jos" University of Galati, Faculty of Sciences, Chemistry, Physics and Environment Department, 800008 Galati, Romania

^b Technische Universität Ilmenau, FG Elektrochemie und Galvanotechnik, 98693 Ilmenau, Germany, donosemihaela@yahoo.com

alloys [2-4]. In particular, the magnetoresistance and giant magnetoresistance (GMR) of these alloys is of great interest [5,6]. The controlled production of Co-Cu alloy nanowire arrays has attracted a great interest recently owing to their application in technologies related with magnetic information storage [7]. Piraux was the first who observed a GMR around 15% at room temperature in Co/Cu alloy nanowires [8]; after that, Blondel et al. obtained a GMR of 14% for Co/Cu and 10% for FeNi/Cu multilayered nanowires [9]. Evans et al. showed that the Co-Ni-Cu/Cu multilayer nanowires grown in AAO templates present a 55% GMR at room temperature and 115% GMR at low temperature [10].

The purpose of this research was to synthesis Co-Cu alloy nanowires in AAO template, without separation of the aluminium and by thinning the barrier oxide layer [11], by pulse reverse plating method. This deposition technique was chosen because its advantages: adjustment of pulse current density to obtain alloys with specific composition and uniform deposits over the entire area of the sample [12].

For this, the AAO template was obtained through one-step anodisation of AlMg₃ substrate in an acidic solution. The structure and the morphology of the nanowires obtained were also studied.

RESULTS AND DISCUSSION

In Fig. 1a and b it can be seen the effect of the aluminium substrate (97% purity) pretreatment on the pore arrangement due to the anodisation process. The figure shows typical SEM micrographs of AAO template surface formed through aluminium anodisation and after reducing the thickness of the barrier layer.

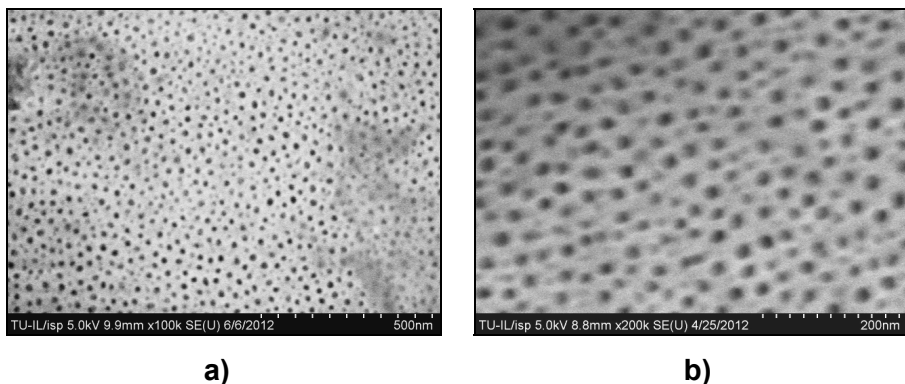


Figure 1. SEM micrographs of AAO template surfaces of self-ordered pore arrays obtained from oxalic acid at 40 V for 20 min (100000× and 200000× magnifications)

The average pore diameters for AAO template obtained in one-step anodisation method from oxalic acid solution were ca. 40 nm, and the pores were generally distributed in a honeycomb shape, in a hexagonal lattice. The results are in agreement with the literature [19]

The second step in the preparation process of metallic nanowires was to study the main characteristics of deposited Co, Cu and Co-Cu alloy by means of the CV technique [20].

Fig. 2 shows typical cyclic voltammograms of AAO template electrode obtained in oxalic acid recorded in Cu^{2+} (Fig.2a), Co^{2+} and Co-Cu ions solutions (Fig.2b) during one cycles. For all CV measurements, the potential scanning was started at 1.0 V towards the negative potential direction until -2.0 V was reached, and then reversed to the starting potential, at 10 mV/s scan rate.

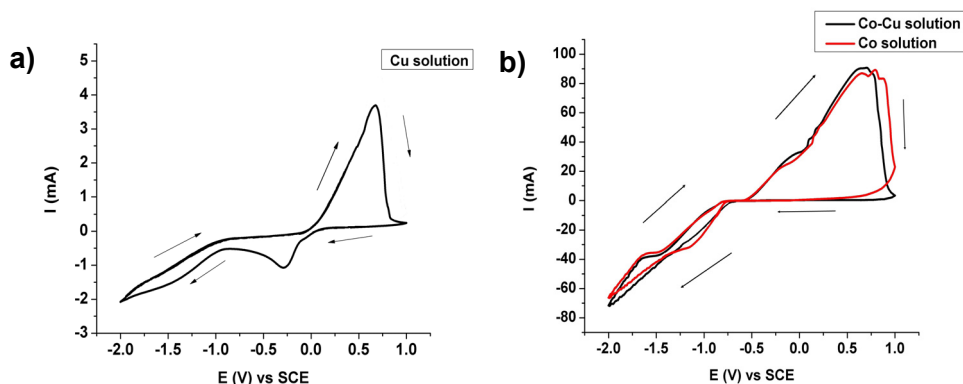


Figure 2. Cyclic voltammograms obtained in: (a) 0.99 g/L CuSO_4 , (b) 119 g/L CoSO_4 and 0.99 g/L CuSO_4 + 119 g/L CoSO_4

Fig. 2a shows cyclic voltammogram of 0.99 g/L CuSO_4 solution with a cathodic scan limit of -2 V. Specific cathodic and anodic peaks corresponding to copper are formed in Cu^{2+} solution. Therefore, the apparent reduction and dissolution peaks are observed at -0.281 and 0.6 V respectively. Over -1.1 V vs. SCE the current increase can be associated with water decomposition and hydrogen formation processes.

Cyclic voltammograms of AAO template electrode obtained in Co and Co-Cu solutions are shown in Fig. 2b.

Cobalt electrodeposition process occurred under -1 V potential. In the direct scan from -1.1 to -2 V vs. SCE a current increasing could be observed due to the strong hydrogen evolution. The hydrogen production occurs because cobalt is less noble than the hydrogen, as can be seen in standard reduction potential of cobalt. In the reverse potential scan we can observe first a very small shoulder due to the hydrogen oxidation around 0 V potential (25 mA) followed by an intense peak centred at a potential around 0.65 V (80 mA) corresponding to the dissolution of the previously deposited Co.

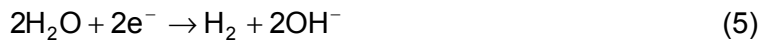
From the direct scan of AAO template in Co-Cu solution it can be seen that the current increases from ca. -0.65 V. A first cathodic reduction peak and an anodic dissolution peak at -1.2 and 0.7 V respectively were observed.

The information acquired from cyclic voltammetry was used to establish the PRP conditions, namely, the values of the currents to be used in the cathodic and anodic pulse sequences.

During the electrochemical deposition process, the metallic phase is produced by the Co^{2+} and Cu^{2+} reduction reaction in sulphate solution. The main electrochemical reactions during the Co^{2+} and Cu^{2+} depositions [21] from aqueous solution are the following:



There are also several possible side reactions that can occur simultaneously:



Other literature sources describe the electrodeposition of metallic nanowires by using direct current [22], or pulse plating [23]. In this study, our goal was to prepare Co-Cu nanowires by galvanostatic PRP due to its advantages over the other methods mentioned above in the literature, as it will be described in the following.

The potential response and current used in the PRP depositions as function of time are shown in Fig. 3.

In our case, after 60 ms (pulse plating period), the plating current (-0.05 A) is interrupted by a shorter reverse-plating period (10 ms; 0.05 A current) when a lightly dissolution of the deposited layer during pulse-plating period occurs.

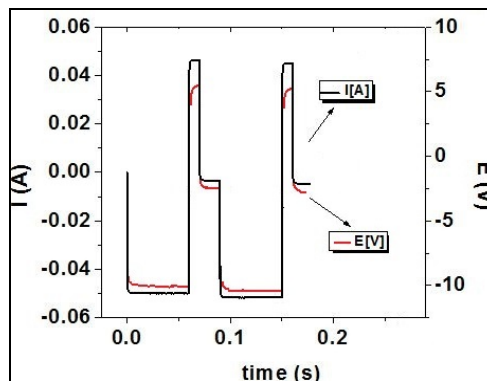


Figure 3. The form of the current used and of the potential response of the system in a sequence of PRP deposition

During off-time period when zero current is applied the ions migrate in the bath preparing for an uniform distribution in deposition time [24].

The ions of the active species diffuse in the channels and then the formation of the nanowires starts.

The HRTEM (high resolution TEM) images of Co-Cu alloy nanowires electrodeposited by PRP at a 50 mA/cm^2 current density were separated from AAO template and the results obtained are shown in Fig. 4. TEM preparation procedure of Co-Cu alloy nanowire specimens includes the following steps: dissolving of the AAO template in 1 M NaOH solution [25], rinsing by distilled water, centrifuged of the obtained suspensions with nanowires. At the end of this procedure, a drop of suspension containing Co-Cu alloy nanowires was put on a gold grid for the TEM investigations.

The nanowires diameter (about 40 nm) and their length (about $1.60 \mu\text{m}$) correspond to the alumina nanopores shape and size precisely.

Fig. 4c confirmed the typical internal structure of Co-Cu alloy nanowires, obtained when the TEM microscopy. The bright zone here corresponds to the Co-rich phase and the darker regions indicate the Cu. One can also observe in Fig. 4 c that the deposits seem to be crystalline.

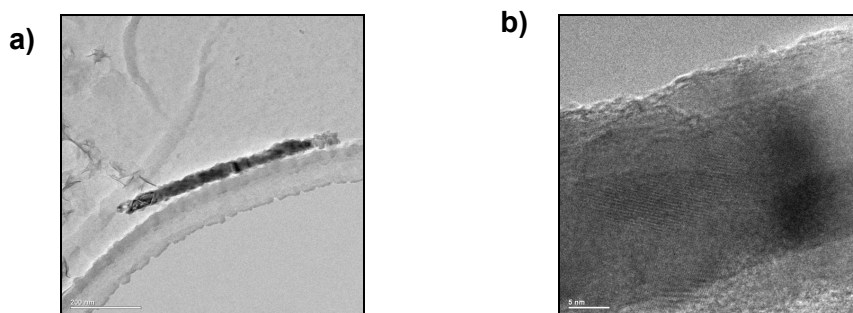


Figure 4. TEM images of Co-Cu alloy nanowires prepared by PRP method at 50 mA/cm^2 cathodic pulse in AAO template. Scale bar: (a) 200 nm, (b) 5 nm

The elemental composition of Co-Cu alloy samples electrodeposited by PRP method was analyzed by means of XRF (Fig. 5) and EDS (Figs. 6 and 7). The alloy composition was determined in cross-section and locally on nanowire surface.

Fig. 5 indicates the variation in Co and Cu concentration in the alloy nanowires as a function of the current density used in the cathodic step, as given by XRF analysis.

The increasing current density implied the incorporation of more Co in the nanowires. Cu concentration decreases with increasing of the current density. One explanation for this behavior is that the Cu deposition is mass transport controlled, while the Co deposition is under mixed control.

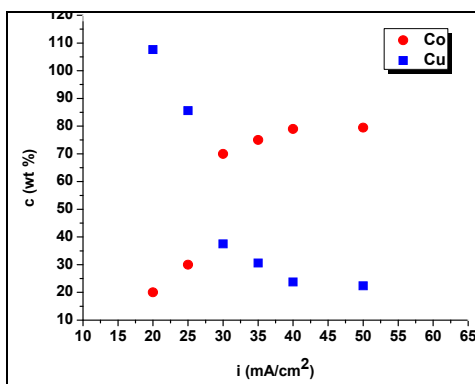


Figure 5. Evolution of Co and Cu concentrations from alloy nanowires as function of current density determined by XRF

The metals concentration of Co-Cu alloy nanowires obtained at 50 mA/cm² current density from a sulphate solution with 3.8 pH has been measured also by EDS analysis (Fig. 6).

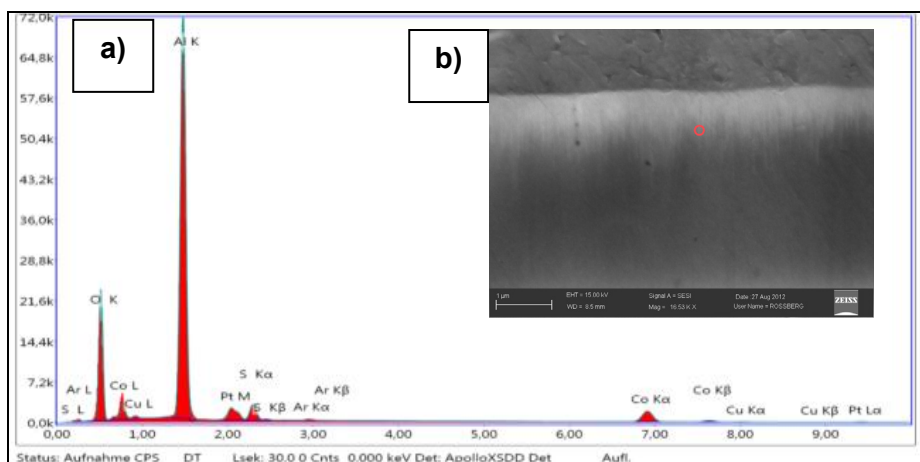


Figure 6. Cluster Co-Cu alloy nanowires embedded in AAO template: a) EDS analysis and b) FIB image in cross section (at upper right side)

The EDS spectrum of Co-Cu alloy nanowires within AAO template in one spot is given in Fig. 6a and consists of significant elementary peaks (Table 1).

EDS qualitative analysis marks out the presence of Co and Cu peaks arisen from the deposition, oxygen and aluminium peaks appeared from the AAO template while platinum peak appear due to the sputtering process (the samples were sputtered with Pt before the FIB and EDS analysis, in order to increase their conductivity). Five minutes sputtering time was sufficient to obtain a continuous and uniform platinum thin film.

Table 1. Co-Cu alloy nanowires EDS quantitative analysis

Element	Wt. (%)	At. (%)
Co	16.1	6.9
Cu	1.4	0.6
Al	44.0	41.3
O	30.1	47.8
Pt	4.8	0.6

The formation of Co-Cu alloy nanowires in the pore structure in cross section was studied by means of FIB technique. Fig. 6b illustrates FIB micrograph of cluster metallic nanowires still integrated into the porous AAO template, maintaining the above described working conditions.

EDS peaks (Fig. 6a) are in according to XRF results (Fig. 5) marking out a large amount of Co and a small concentration of Cu by a locally detection (Fig. 6b, spot 2).

The nanowires electrodeposited in AAO template at 50 mA/cm² current density were ca. 1.60 μm lengths and 40 nm diameter, as described also above. EDS on single Co-Cu alloy wire was also performed, in parallel to TEM, after the AAO template was dissolved in NaOH (1M) to expose the wires (Fig. 7a). Fig. 7b indicates high resolution TEM of individual alloy nanostructure.

The single Co-Cu alloy nanowires contained 80 wt.%-Co and 20 wt.%-Cu, as indicated by the EDS (Fig. 7a).

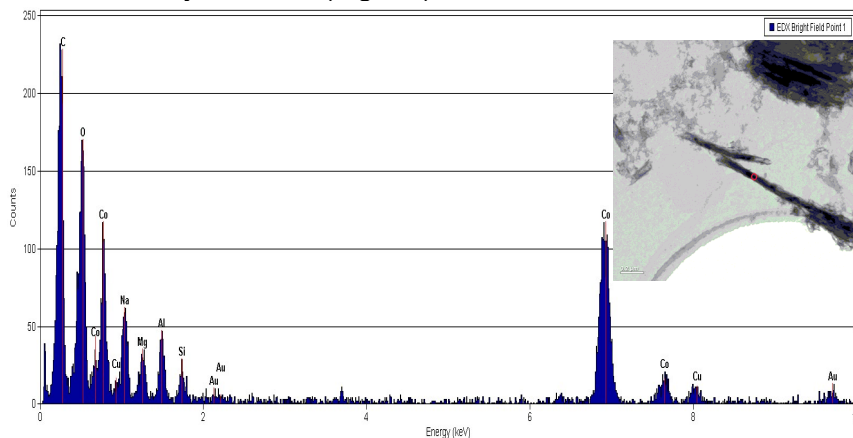


Figure 7. Individual Co-Cu alloy nanowire: a) EDS spectrum and b) TEM image (at upper right side)

Therefore, XRF results (Fig. 5) were in good agreement with EDS analysis of individual metallic alloy nanowires, which means that the material is chemically homogeneous.

However, the qualitative EDS examination on bigger area in a cross-section of the sample had indicated the presence of Al and O, beside the Co and Cu.

The XRD patterns (Fig. 8) of the annealed Co-Cu alloy nanowire samples have been recorded at room temperature, in order to study the relationship between the structure of the nanowires, their composition and the annealing temperatures. These deposits were prepared in the same conditions as those used for the foregoing analysis, at higher current density (50 mA/cm^2), when maximum Co concentration was observed.

The metallic nanostructures were annealed at temperatures below the melting point of aluminium (680°C), namely, at 150 , 300 and 350°C respectively. This study is useful to explain the crystallographic variation influenced by the annealing temperature and chemical composition.

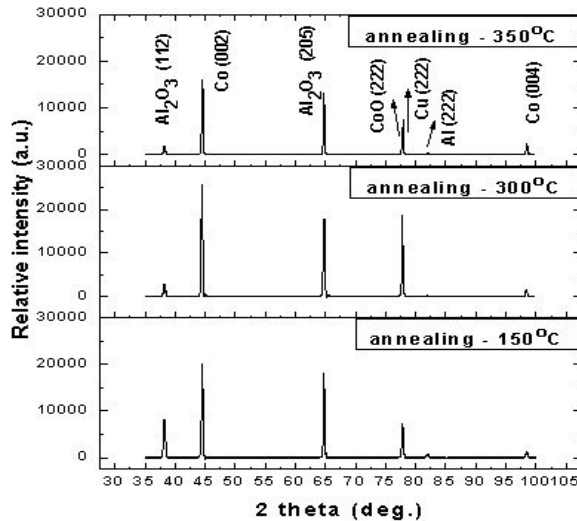


Figure 8. XRD patterns of Co-Cu alloy nanowires deposited at 50 mA/cm^2 current density and annealed at 150 , 300 and 350°C temperature

Bragg's reflections for Co-Cu alloy nanowires are observed at 2θ values of 38.06° , 44.6° , 64.0° , 77.54° , 77.8° , 81.72° , 98.71° . The crystalline planes of Al_2O_3 , Co, Cu, aluminium and CoO could be identified. Aluminium peak resulted from the substrate used for AAO template and Al_2O_3 derived from under-layer used for nanowires respectively.

The annealed electrodeposited alloys contain the ϵ -Co phase with hexagonal close-packed lattice (hcp) and Cu phase with face-centred cubic (fcc) lattice. According to the Joint Committee on Powder Diffraction Standards (JCPDS) card the more important phases in this study have been identified as 00-001-1278 for Co and 00-004-0836 corresponding to Cu phase respectively. CoO peak with fcc lattice according to JCPDS 00-001-1227. CoO characteristic line formation can be attributed to the metallic Co annealing.

Noticeable changes in phase composition and peak broadening are observed over the range of annealing temperature. The highest intensity peaks of Co and Cu respectively appeared when the deposits have been annealed at 300°C. Thereby, it's about the Co peak corresponding to the (002) reflection and the (222) plane of Cu which is lower than Co. Therefore, a correlation between the chemical composition (Co:Cu 4:1) and fine crystalline structure (Figs. 5, 6, 7) could be made. As the annealing temperature of the samples increases, the amount of ϵ -Co phase diminishes and an obvious peak corresponding to Co (004) structure increases in intensity.

Reduced intensity peaks at higher temperatures (above 350°C) could be observed indicating the weak Co-Al₂O₃ interactions. In this case, the observed increase in the peak broadening is due to decreasing CoO crystallites grain size compared to average Al₂O₃ pore size.

EXPERIMENTAL DETAILS

The AAO template was synthesized by one-step anodisation method. Al₂O₃ layer was grown on the aluminium-magnesium electrodes (circular sector shaped), in oxalic acid solution at 40 V constant voltage [13]. In these experiments the counter was a net platinum electrode, and the AlMg₃ substrates were the working electrodes.

In order to electrodeposit the wished metallic nanowires in the AAO template, the last one must be conductive. After anodisation an Al₂O₃ barrier layer is formed in the AAO templates, that is not conductive and that hinders the tries to electrodeposit any metal onto it. Therefore the Al₂O₃ barrier layer was thinned electrochemically by successive reduction of the anodisation voltage and pores diameter widening was obtained in sulphuric acid [14].

The surface morphological features of AAO template were examined by means of scanning electron microscopy (SEM) technique using Hitachi S 4800 device operating at an accelerating voltage of 5 kV.

The deposition of Cu, Co and Co-Cu nanowires in the AAO template was firstly studied by cyclic voltammetry (CV), from sulphate based electrolytes. CVs experiments were performed in a three electrode cell: AAO template was the working electrode, and calomel electrode and platinum net were used as reference and counter electrodes, respectively. All measurements have been performed at room temperature.

The electrodeposition of Co-Cu alloy nanowires was performed from one electrolyte which contains both type of ions (Co²⁺ and Cu²⁺), based on the previous reports of Yahalom and Zadok from 1986 for the Cu-Ni system [15].

The Co-Cu alloy nanowires were electrodeposited in AAO template by galvanostatic pulse reverse plating (PRP) method [16] using two electrode systems (platinum sheet as anode and AAO template as working electrode).

The bath composition was 119 g/L CoSO_4 , 1 g/L CuSO_4 , and 25 g/L H_3BO_3 . The pH of solution varied between 3.8 and 4.0 and different current densities ($20\div 50 \text{ mA/cm}^2$) were applied. The deposition experiments were performed using a HEKA PG310 (Heka Elektronik Dr. Schulze GmbH) potentiostat/galvanostat.

The internal structure of nano-sized Co-Cu alloy wires (diameter < 40 nm) was examined using transmission electron microscopy (TEM).

The morphological characteristics and chemical composition of Co-Cu alloy nanowires were investigated using the focused-ion-beam (FIB) microscopy, energy dispersive X-ray (EDS) and X-ray fluorescence (XRF, from Fisherscope, Germany) spectroscopies. For FIB and EDS techniques, a cross section in the AAO template was required. Thus, the samples were cut and embedded in epoxy resin. An accurate manually polishing of the cross-section of the nanowires was necessary and initiated with coarse polishing papers having different grains (from 800 to 4000) [17]. After each polishing step the samples were rinsed in distilled water.

Some of the Co-Cu nanowires were annealed in order to check if the structure of the wires changes with the temperature, fact that can influence their optical and magnetic properties, and thus, their industrial applications [18]. These deposits were prepared from sulphate solutions with pH of 3.8 at 50 mA/cm^2 current density. The annealing procedure was conducted, in air atmosphere, in a stove at different temperatures: 150, 300 and 350°C for a period of 3 h.

The crystallographic characteristics of these samples were analysed by means of X-ray diffractometry (XRD). X-ray diffraction patterns were obtained from Philips PW 1830 diffractometer at room temperature using monochromated CuK_α radiation ($\lambda = 1.54 \text{ \AA}$). Routine patterns for phase identification were collected with a scanning step of $0.1^\circ \text{ min}^{-1}$ in 2θ over the angular range 30 and 100° with a collection time of 5 s per step.

CONCLUSIONS

The AAO template was obtained by one-step anodisation method of AlMg_3 substrates in oxalic acid solution at 40 V potential for 20 min. The roughness degree of substrate was the most important factor which could influence the nanopores linearity and symmetry respectively.

The AAO template morphology shows homogeneity and spherical shape of pores as well as a hexagonal lattice of nanopores. The average diameter of nanopores was of 40 nm, as indicated by SEM.

The information acquired from cyclic voltammograms was used to establish the PRP electrochemical conditions. The galvanostatic PRP was used to obtain Co-Cu alloy nanowire depositions from acidic sulphate solution at 50 mA/cm^2 current density with fine structure and superior physical properties than many metals.

From XRF examination Co and Cu concentrations from alloy nanowires varied with the cathodic current density used in deposition. Cu was deposited preferentially at lower current density where as Co-rich alloy were obtained at higher current density due to the mass transport limitation of the Cu during the deposition process.

The shape, size and crystallographic orientation of clusters of Co-Cu alloy nanowires embedded in AAO template were studied by means of FIB microscopy. After the AAO template was dissolved, high resolution TEM analyses were performed. Nanowires of ca. 1.60 μm length were thus analyzed.

The chemical composition of an individual alloy nanowire was investigated using EDS and XRF spectroscopies. The quantitative assay of Co-Cu alloy nanowire indicated that they contain 80 wt.%-Co and 20 wt.%-Cu. XRF results were agreement with the EDS analysis, proving that the material is chemically homogeneous.

An annealing treatment of Co-Cu alloy nanowires was required to assure their thermal stability under 350°C. This study is useful to explain the crystallographic variation induced by the annealing temperature.

The internal structure of the annealed Co-Cu alloy nanowire samples was studied at room temperature by means of XRD method. The crystallization process varied with the annealing temperature and Co and Cu concentration showing ϵ -Co phase with hexagonal close-packed lattice and face-centred cubic lattice of electrodeposited Cu.

ACKNOWLEDGMENTS

This work was financially supported by the Project SOP HRD - TOP ACADEMIC 76822. The authors would also thank Prof. PhD. Viorica MUSAT („Dunarea de Jos” University of Galati, Faculty of Metallurgy Materials Science and Environment) for the annealing treatment, Diana Roßberg (TU Ilmenau, FG Werkstoffe der Elektrotechnik) and Dr. rer. nat. Thomas Kups (TU Ilmenau, Zentrum für Mikro- und Nanotechnologien) for their kind assistance with TEM and FIB measurement.

REFERENCES

- [1] R.C. Furneaux, W.R. Rigby, A.P. Davidson, *Nature*, **1989**, 337, 147.
- [2] A. Ghahremaninezhad, A. Dolati, M. Kazemeini, *Int. J. of Mod. Phys. B*, **2008**, 22, 3013.
- [3] M. Almasi Kashi, A. Ramazani, A.S. Esmaeily, *IEEE Transactions on Magnetics*, **2013**, 49, 116.
- [4] Y. Ueda and M. Ito, *Jpn. J. Appl. Phys.*, **1994**, 33, 403.

- [5] S.Y. Zhang, Q.Q. Cao, *Jpn. J. Appl. Phys.*, **1996**, 79, 6261.
- [6] I. Bakonyi and L. Peter, *Progr. Mater. Sci.*, **2010**, 55, 107.
- [7] Y. Rheem, B. Yoo, *Journal of Magnetism*, **2007**, 12, 124.
- [8] L. Piraux, J.M. George, J.F. Despres, C. Leroy, E. Ferain et al., *Appl. Phys.*, **1994**, 65, 2484.
- [9] A. Blondel, J.P. Meier, B. Doudin, J.P. Ansermet, *Appl. Phys.*, **1994**, 65, 3019.
- [10] P.R. Evans, G. Yi, and W. Schwarzacher, *Appl. Phys.* **2000**, 76, 481.
- [11] K. Nielsch, F. Müller, A.P. Li, and U. Gösele, *Adv. Mater.*, **2000**, 12, 582;
- [12] M.S. Chandrasekar, Malathy Pushpavanam, *Electrochim. Acta*, **2008**, 53, 3313.
- [13] H. Masuda and K. Fukuda, *Science*, **1995**, 268, 1466.
- [14] F.S. Fedorov, I. Mönch, C. Mickel, K. Tschulik, B. Zhao, M. Uhlemann, A. Gebert, and J. Eckert, *J. Electrochem. Soc.*, **2013**, 160, D13.
- [15] J. Yahalom, O. Zadok, *J. Mat. Sci.*, **1987**, 22, 499.
- [16] D. Gupta, A. Nayak, J. Mazher, R. Sengar, K. Joshi, R. Pandey, *J. of Materials Science*, **2004**, 39, 1615.
- [17] E. Gomez, A. Labarta, A. Llorente, E. Valle's, *Surface and Coatings Technology*, **2002**, 153, 261.
- [18] W. Li, G.A. Jones, Y. Peng, T.H. Shen, and G. Hill, *J. Appl. Phys.*, **2005**, 97, 104306.
- [19] F. Keller, M.S. Hunter, D.L. Robinson, *J. Electrochem. Soc.*, **1953**, 1009, 411;
- [20] L. Mentar, *Orient. J. Chem.*, **2011**, 27, 477.
- [21] Cynthia G. Zoski – *Handbook of Electrochemistry*, Elsevier, **2007**.
- [22] Soon Mee Choi, Jiung Cho, Young Keun Kim, Cheol Jin Kim, *Solid State Phenomena*, **2007**, 124-126, 1233.
- [23] Pullini D, Busquets-Mataix D., *ACS Appl Mater Interfaces.*, **2011**, 3, 759.
- [24] J.J. Kelly, P.E. Bradley, D. Landolt, *J. Electrochem. Soc.*, **2000**, 147, 2975.
- [25] Z.L. Xiao, C.Y. Han, U. Welp, H.H. Wang, W.K. Kwok, G.A. Willing, J.M. Hiller, R.E. Cook, D.J. Miller, and G.W. Crabtree, *Nano Lett.*, **2002**, 2, 1293.

ELECTROCHEMICAL REDUCTION OF CO₂ ON LEAD ELECTRODE. I. CYCLIC VOLTAMMETRY AND LONG TIME ELECTROSYNTHESIS STUDIES

FLORIN ALIN HANC-SCHERER^a, PETRU ILEA^a

ABSTRACT. Carbon dioxide electrochemical reduction (CDER) was investigated on Pb electrode in a conventional three electrodes cell and a filter-press electrochemical reactor at ambient temperature and pressure. The electrolysis was conducted in Na₂SO₄, Na₂SO₄+Na₂CO₃ and Na₂CO₃ solutions for 4h. The formation of formate as a product of reduction depends on the type of electrolyte and pH value. The highest current efficiency (35%) was obtained in sulphate solution at 5mA/cm² current density.

Keywords: carbon dioxide reduction, formic acid production, lead electrode

INTRODUCTION

Carbon dioxide (CO₂) is recognized as a major contributor to climate change due to human activities (human factor). The main areas of activities that emit CO₂ and have greatly increased CO₂ concentrations in the atmosphere are the combustion of fossil fuels (oil, natural gas, coal), the transportation of goods and people and deforestation (making it difficult to remove CO₂ from the atmosphere).

The reduction of CO₂ emissions was examined *via* different paths, among the most important ones are the following: chemical [1], thermochemical [2], photochemical [3, 4] and electrochemical reduction [1-5]. The last mentioned way is a promising and efficient process that allows recycling of CO₂ to valuable products (CO, HCOOH, MeOH, CH₄, C₂H₄) [6-9].

Electrochemical conversion of CO₂ depends on a number of specific parameters (electrode material, electrolyte solution, temperature, pressure) that can lead to high current yields of products [6, 7, 10].

Since hydrogen evolution is a competing reaction (HER), metals with high overpotential for hydrogen evolution, such as *sp* group (Hg, In, Pb, Cd, Sn) have higher efficiencies for CO₂ reduction. These electrodes tend to favor the formation of formic acid with high current efficiency [9, 11-13].

^a Babeş-Bolyai University, Faculty of Chemistry and Chemical Engineering, 11 Arany Janos Street, Cluj-Napoca, 400028, Romania, pilea@chem.ubbcluj.ro

Formic acid as a reduction product on Pb, Sn, Cd electrodes is important because it represents an alternative fuel for direct liquid fuel cells (DLFCs). Direct formic acid fuel cells (DFAFC) have higher open circuit potentials (1.45 V) and current densities [14-17]. Lead has the advantage that it is easy to process and is available on the market at a reasonable price. The most important thing is that the overpotential for hydrogen evolution reaction on Pb is higher than that on the other metals (In, Sn, Cd) [18].

Based on the above considerations the present work is focused on the study of electrochemical reduction of CO₂ in different aqueous electrolytes (Na₂SO₄ and Na₂CO₃) using a lead cathode. The ultimate goal of the research was to convert carbon dioxide into fuel (formic acid/formate) for use in fuel cells.

RESULTS AND DISCUSSION

Voltammetric experiments

To highlight the cathodic reduction of CO₂, cyclic voltammetry (CV) studies were carried out at lead electrode. The reactions that occurred on lead electrode in alkaline media at 25°C and their electrochemical potential vs standard hydrogen electrode (SHE) are shown below [19]:



In order to study the carbon dioxide electrochemical reduction (CDER) first experiments were performed using Na₂CO₃ 0.5M (deaerated by bubbling Ar) and saturated with CO₂ (Figure 1). In the presence of carbonate ions a wave is observed at a potential of ca. -1.45 V/ Ag/AgCl/KCl_{sat} due to reduction of the ions. When CO₂ is bubbled a well-defined reduction peak is observed at -1.6V due to CO₂ reduction.

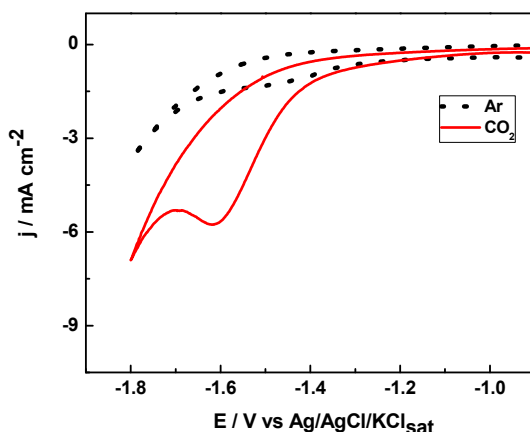


Figure 1. Cyclic voltammograms on Pb electrode at 50 mV s⁻¹ in 0.5 M Na₂CO₃ with and without CO₂.

The current density peak (-5.6 mA/cm^2) for CO₂ reduction to formate is close to the data from literature [20, 21].

Cyclic voltammograms recorded in Na₂SO₄ electrolyte are presented in (Figure 2A).

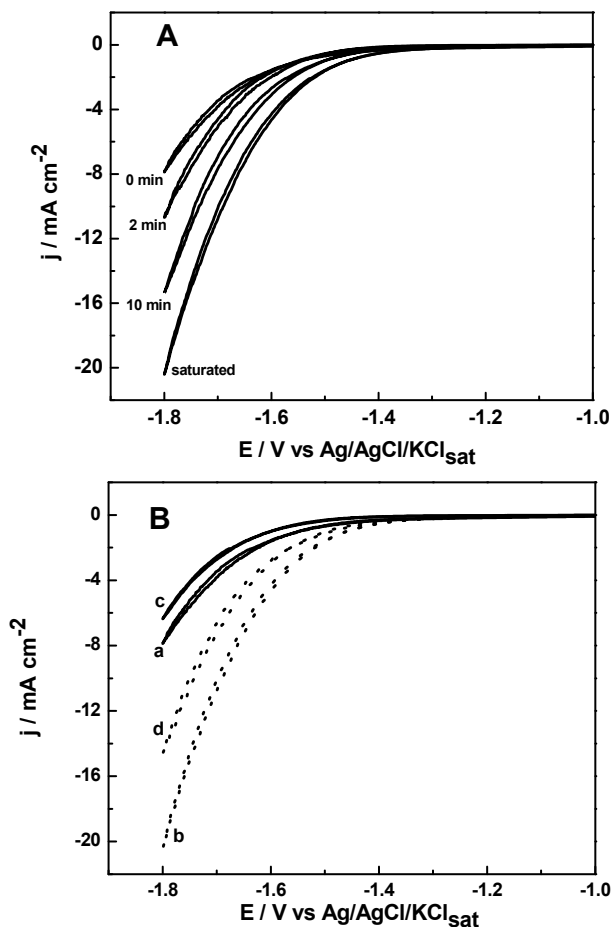


Figure 2. Cyclic voltammograms on Pb electrode at 50 mV s^{-1} in: **(A)** Na₂SO₄ 0.6 M, at different times of bubbling CO₂, in **(B)** (a) Ar atmosphere Na₂SO₄ 0.6M, (b) CO₂ saturated Na₂SO₄ 0.6M (c) Ar atmosphere Na₂SO₄ 0.6M+Na₂CO₃ 0.1M, (d) CO₂ saturated Na₂SO₄ 0.6M +Na₂CO₃ 0.1M.

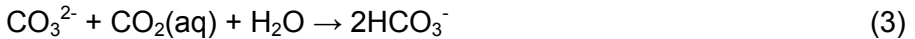
When the voltammetry was made under Ar atmosphere, only HER is active. The cathodic current, obtained in CO₂-saturated Na₂SO₄ solution, started to increase at more positive potential (ca. -1.4 V) than cathodic current obtained in Ar atmosphere (-1.49 V). In view to observe the influence of CO₂ concentration,

the gas was bubbled at different intervals of time. After each bubbling time cyclic voltammograms were recorded (Figure 2A). The onset potential of the cathodic current shifts more positively with increasing CO₂ concentration.

Current efficiency for product depends on the ratio CO₂-H₂O in the electrolyte solution. For a molecular ratio CO₂-H₂O about 0.25 current efficiency of HCOOH is equal to current efficiency of H₂. Values under 0.25 encourage hydrogen evolution reaction and CO₂ reduction significantly decreases [10].

Cyclic voltammograms obtained in Na₂SO₄ electrolyte with Na₂CO₃ are presented in (Figure 2B). In this case the cathodic current obtained is much smaller than that obtained in the absence of Na₂CO₃.

The presence of Na₂CO₃ in the electrolyte increases the pH of the solution. The predominant species in high alkaline solution are the carbonate ions, according to the E-pH diagram performed by Hori [22], which means that this compound is not reactive at the electrode surface. By lowering the pH solution due to CO₂ bubbling, CO₂ reacts with CO₃²⁻ ions which are converted into HCO₃⁻ as described in equation 3 [10]:



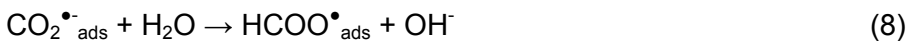
At pH = 8.5 equilibriums states between CO_{2(aq)}, HCO₃⁻ and CO₃²⁻ are achieved:



followed by:



The formation of bicarbonate ions simultaneously with the consumption of carbonate and OH⁻ ions results in decreasing of the pH value in the bulk solution [23]. This may explain the decrease of the speed for CDER in the presence of CO₃²⁻ ions. This observation is confirmed by the mechanism of electrosynthesis of formate ions, on lead electrode, which according to the literature [10] consists of the following steps:



Based on cyclic voltammetry data the current efficiency (CE) can be estimated for each type of electrolyte by dividing the amount of charge consumed for CDER (Q_{CDER}) to total amount of charge consumed (Q_{total}) as described in Table1.

Table 1. Current efficiency evaluated by CV measurements for different types of electrolytes

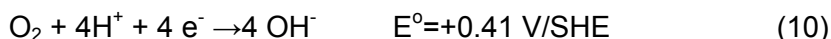
Type of electrolyte	pH	Q _{total} (mAs)	Q _{CDER} (mAs)	CE (%)
Na ₂ CO ₃ (0.5M) + CO ₂	10.6	10.4	4.0	38
Na ₂ SO ₄ (0.6M)+ CO ₂	6.3	12.8	7.9	62
Na ₂ SO ₄ (0.6M)+Na ₂ CO ₃ (0.1M) + CO ₂	7.5	8.7	5.0	58

From the values presented in Table 1 it can be seen the electrolyte solution saturated with CO₂ is beneficial to the process regardless of the type of electrolyte.

Long time electrosynthesis (LTE) of formate in filter-press electrochemical reactor with metallic lead cathode

Following the results obtained by cyclic voltammetry experiments, studies were continued by electrolysis measurements. These experimental data are necessary because they could determine the formation of formate ions during the electrolysis by quantitative chemical analysis

In the cathodic compartment of the reactor, CO₂(aq) is reduced to formate according to equation (1) in parallel with equation (2), while the reaction at anode is:



Current efficiencies calculate for formate ions during LTE are presented in Figure 3A.

Changing sulphate anion with carbonate anion or adding carbonate to sulphate solution leads to a decrease in current efficiency. The modification in CE appears to be influenced by changes in pH (what was observed in cyclic voltammetry experiments).

The Na₂CO₃ and Na₂SO₄ 0.6M + Na₂CO₃ 0.1M solutions have a pH value greater than 10 which makes the reaction (1) to be less favourable. In this case adsorbed CO₂ in solution will react with carbonate to bicarbonate according to the reaction (3).

The poor current efficiencies obtained in the carbonate presence is due to CO₃⁻ species whose reaction with CO₂ reaction (3) competing reaction (1) and leading to an inhibition of the formation of formate.

LTE measurements were also performed at different current densities (Figure 3B).

As can be observed in Figure 3B, increasing the current density typically lowers the formate current efficiency. This was observed by Udupa et al. [24] and can be attributed mainly to CO₂ concentration polarization [19].

The experiments undertaken by Koleli et al. [25] on Pb electrode showed a dependence of the formate current efficiency on current density, while results obtained on Sn [26] show an increasing of current efficiency with decreasing current. We observed a similar trend (decreasing in current efficiency with increasing current) for carbonate/sulphate solutions.

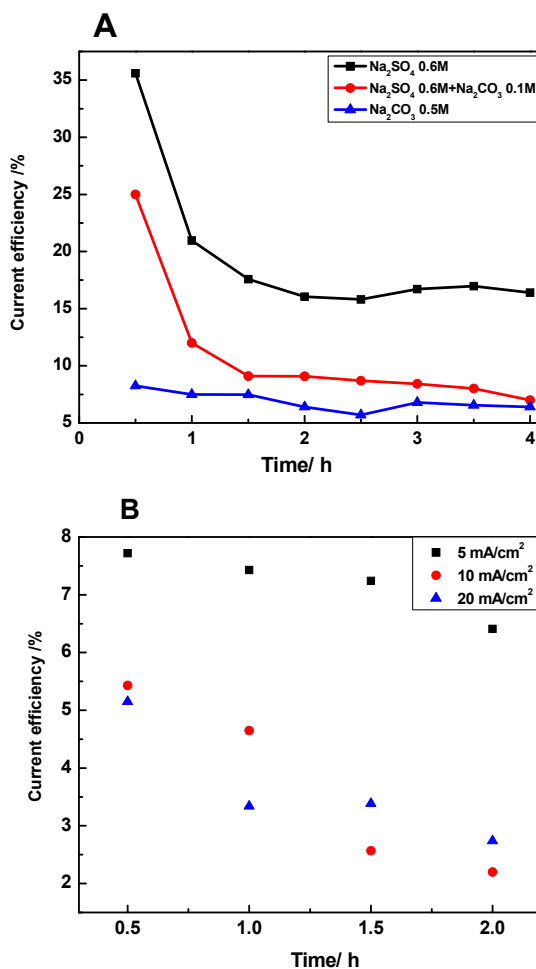


Figure 3. (A) Current efficiencies for formate evolution during LTE for different type of electrolyte saturated with CO₂ at 5 mA/cm²; (B) in 0.5 mol L⁻¹ Na₂CO₃ saturated with CO₂ at different current densities

Due to the H₂-evolution, the current efficiencies for the HCOO⁻ formation decreases with the rising of the electrolysis time.

After 30–45 minutes of electrolysis, a cathode deactivation was observed (the corresponding current efficiencies decreased with 15% in the case of Na₂SO₄ electrolyte-Figure 3A).

"Poisoning" of the cathode over time has been observed for CO₂ electroreduction on copper electrodes [27–31], and some effects of this deactivation have been indicated on *sp* group (In, Pb, Sn) electrodes. Koleli and al. [32] show that the current efficiency decreased in time during electrolysis thus the highest current efficiency for formic acid production obtained in carbonate solution on Pb after 30 min. was 39% and after 120 min. CE was 10% respectively. Kapusta and al. [33] showed that low efficiency was due to the formation of organometallic complexes on the tin electrode, this situation favouring hydrogen evolution reaction as a competitive reaction.

CONCLUSIONS

The electrochemical reduction of CO₂ on lead plate electrode in aqueous Na₂CO₃ and Na₂SO₄ electrolyte by cyclic voltammetry and LTE in a filter-press electrochemical reactor was studied.

Measurements showed that CO₂ electroreduction at formate depends on the type of electrolyte and pH value. The highest current efficiency for HCOO⁻ production (35%) (see figure 3A) was obtained in sulphate solution. Long time electrosynthesis showed that CE is favored by low current densities (5mA/cm²). Further research is needed to minimize the disadvantage of operating at low current densities.

EXPERIMENTAL SECTION

Voltammetric experiments

Experiments were carried out in an undivided conventional three electrodes cell ($V = 12 \text{ cm}^3$) at 25 °C. The working electrode consisted of a lead wire with a geometric surface area of 0.12 cm². The current densities were normalized with the geometric surface area. The reference electrode used in all measurements was Ag/AgCl/KCl_{sat} and the counter electrode used was a Pt wire. The electrolytes used were Na₂CO₃ 0.5M and Na₂SO₄ 0.6M solutions prepared from the solid salt and double distilled water (Double D Still, JENCONS, England). Measurements have been done with a computer controlled tripotentiostat DXC 240. Carbon dioxide and argon gases were purchased from Linde.

Filter-press electrochemical reactor

A filter-press type electrochemical reactor was used in this study. The cell contained two compartments one cathodic and one anodic separated by a Nafion 324 cation-exchange membrane. The working electrode (cathode) was a lead plate (99.99% Pb), while a Dimensionally Stable Anode (DSA/O₂)

plate was used as the counter- electrode (anode). The area of the working and DSA electrodes was 10 cm^2 . The reference electrode $\text{Ag}/\text{AgCl}/\text{KCl}_{\text{sat}}$ was placed close to the Pb cathode. A schematic representation of the filter-press electrochemical reactor is shown in Figure 4.

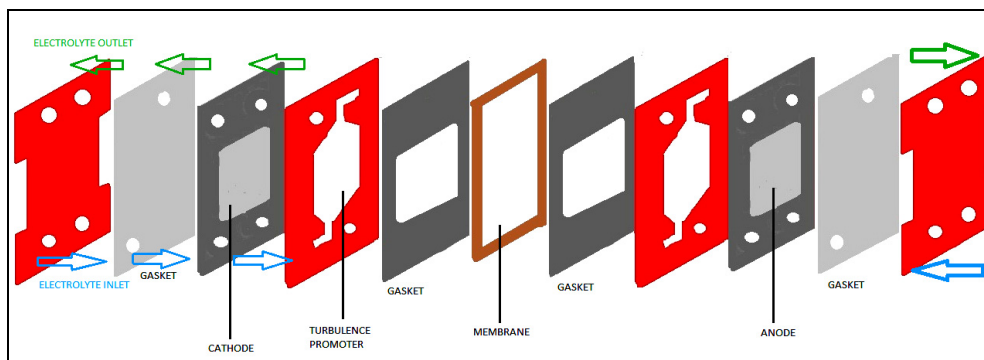


Figure 4 Scheme of the filter-press electrochemical reactor

Electrochemical experiments were carried out in continuous mode for 4h under ambient temperature and pressure conditions. Each electrolyte was circulated through its own compartment using peristaltic pumps with a flow rate of 200 mL min^{-1} . Measurements have been done galvanostatically with PC controlled PARSTAT 2273 and Datronix Electrochemical System, composed by DXC 236 potentiostat connected to a PC through National Instruments (NI) DAQ hardware. The software packages used have been developed in our laboratory in NI Labview soft.

The aqueous solution used in our experiments as catholyte and anolyte were Na_2CO_3 and Na_2SO_4 . Before the start of each experiment, catholyte was deaerated with Ar for 30 minutes then CO_2 was bubbled into the catholyte solution until saturation, and then continuous CO_2 bubbling was maintained throughout the experiment. The lead cathode was ground flat with fine emery paper, then polished with alumina powder and rinsed with double distilled water.

Samples were taken from 30 to 30 minutes and the formate content was analysed by the permanganate method. This procedure consisted of: 1) reacting the sample solutions with an excess of potassium permanganate solution, 2) adding an excess of oxalic acid solution and 3) re-titrating the solution with KMnO_4 [34].

ACKNOWLEDGMENTS

The authors wish to thank for the financial support of the Sectorial Operational Programme for Human Resources Development 2007 – 2013, co-financed by the European Social Fund, under the project number POSDRU/107/1.5/S/76841 with the title “Modern Doctoral Studies: Internationalization and Interdisciplinarity”.

REFERENCES

- [1] M. Aulice Scibioh, B. Viswanathan, *Proc. Indian Natn. Sci. Acad.*, **2004**, 70, A, 3, 407-462.
- [2] C.E. Bamberger, P. R. Robinson, *Inorg. Chim. Acta*, **1980**, 42, 133-137.
- [3] G. Centi, S. Perathoner, *Catalysis Today*, **2009**, 148, 191-205.
- [4] K. Kalyanasundaram and M. Graetzel, *Current Opinion in Biotechnology*, **2010**, 21, 298-310.
- [5] Y. Lu, Z. Jiang, S. Xu, H. Wu, *Catalysis Today*, **2006**, 115, 263-268.
- [6] M. Jitaru, D.A. Lowy, M. Toma, B.C. Toma, L. Oniciu, *J. Appl. Electrochem.*, **1997**, 27, 875-889.
- [7] C.M. Sánchez-Sánchez, V. Montiel, D.A. Tryk, A. Aldaz and A. Fujishima, *Pure and Applied Chemistry*, **2001**, 73, 12, 1917-1927.
- [8] R.P.S. Chaplin, A.A. Wragg, *J. Appl. Electrochem.*, **2003**, 33, 1107-1123.
- [9] B. Eneau-Innocent, D. Pasquier, F. Ropital, J.-M. Léger, K.B. Kokoh, *Applied Catalysis B: Environmental*, **2010**, 98, 65-71.
- [10] Y. Hori, "Electrochemical CO₂ reduction on Metal Electrodes". *Modern Aspects of Electrochemistry*, Number 42, Springer, New York, **2008**.
- [11] F. Koleli, T. Atilan, N. Palamut, A.M. Gizir, *J. Appl. Electrochem.*, **2003**, 33, 447-450.
- [12] S. Ikeda, T. Takagi, K. Ito, *Bull. Chem. Soc. Jpn.*, **1987**, 60, 2517-2522.
- [13] M. Todoroki, K. Hara, A. Kudo, T. Sakata, *J. Electroanal. Chem.*, **1995**, 394, 199-203.
- [14] S. Ha, C.A. Rice, R.I. Masel, A. Wieckowski, *J. Power Sources*, **2002**, 112, 655-659.
- [15] X Wang, J. Hu, I-M. Hsing, *J. Electroanal. Chem.*, **2004**, 562, 73-80.
- [16] J-H. Choi, K-J. Jeong, Y. Dong, J. Hanb, T-H. Limb, J-S. Lee, Y.-E. Sung, *J. Power Sources*, **2006**, 163, 71-75.
- [17] X. Yu, P.G. Pickup, *J. Power Sources*, **2008**, 182, 124-132.
- [18] Allen J. Bard, *Encyclopedia of Electrochemistry of the Elements*, Marcel Dekker, Inc. New York and Basel, **1973**, Volume IX, Part A.
- [19] H. Li, Colin Oloman, *J. Appl. Electrochem.*, **2006**, 36, 1105-1115.
- [20] Y. Hori, K. Kikuchi, S. Suzuki, *Chemistry letters*, **1985**, 1695-1698.
- [21] Y. Hori, H. Wakebe, T., Tsukamoto, O, Koga, *Electrochimica Acta* **1994**, 39, 1833.
- [22] Y. Hori, S. Suzuki, *Bull. Chem. Soc. Jpn.*, **1982**, 55, 660.
- [23] B. Innocent, D. Pasquier, F. Ropital, F. Hahn, J.-M. Leger, K.B. Kokoh, *Applied Catalysis B: Environmental*, **2010**, 94, 219-224.
- [24] K.S. Udupa, G.S. Subramanian and H.V.K. Udupa, *Electrochimica Acta*, 1971, 16, 1593-1598.
- [25] F. Koleli, D. Balun, *Applied Catalysis A: General*, **2004**, 274, 237-242.

- [26] Hui Li, Colin Oloman, *J. Appl. Electrochem.*, **2005**, 35, 955-965.
- [27] D.W. DeWulf, T. Jin, A.J. Bard, *J. Electrochem. Soc.* **1989**, 136, 1686-1691.
- [28] S. Wasmus, E. Cattaneo, *Electrochimica Acta*, **1990**, 35, 771-775.
- [29] G. Kyriacou, A. Anagnostopoulos, *J. Electroanal. Chem.*, **1992**, 322, 233-246.
- [30] B. Jermann, J. Augustynski, *Electrochimica Acta*, **1994**, 39, 1891-1896.
- [31] Jaeyoung Lee, Yongsug Tak, *Electrochimica Acta*, **2001**, 46, 3015-3022.
- [32] F. Koleli, T. Atilan and N. Palamut, *J. Appl. Electrochem.*, **2003**, 33, 447-450.
- [33] S. Kapusta and N. Hackerman, *J. Electrochem. Soc.*, **1983**, 130, 3, 607-613.
- [34] F. Albert, N. Barbulescu, C. Holszky, C. Greff, "Analiză chimică organică", Ed. Tehnică, București, **1970**.

THE CONNECTIVITY INDEX OF PAMAM DENDRIMERS

NABEEL E. ARIF^a, ROSLAN HASNI^b

ABSTRACT. The m -order connectivity index is an extension of the Randić (simple) connectivity index that counts the connectivity of all paths of length m in G . A dendrimer is a hyperbranched molecule built up from branched units called monomers. In this paper, the 2-order, 3-order and 4-order connectivity indices of an infinite family of PAMAM dendrimers are computed.

Keywords: Randić connectivity index, Graph, Dendrimer

INTRODUCTION

A simple graph $G = (V, E)$ is a finite nonempty set $V(G)$ of objects called vertices together with a (possibly empty) set $E(G)$ of unordered pairs of distinct vertices of G called edges. In chemical graphs, the vertices of the graph represent the atoms of the molecule and the edges represent the chemical bonds.

A single number that characterizes the molecular graph is called a graph theoretical invariant or topological index. Among the many topological indices considered in chemical graph theory, only a few have been found noteworthy in practical applications, connectivity index being one of them. The molecular connectivity index χ provides a quantitative assessment of branching of molecules. Randić (1975) first addressed the problem of relating the physical properties of alkanes to the degree of branching across an isomeric series [1]. Kier and Hall (1986) extended χ index to higher orders and introduced modifications to account for heteroatoms [2].

Molecular connectivity indices are the most popular class of indices (Trinajstić [3]). They have been used in a wide spectrum of correlating applications, including physicochemical properties (e.g. boiling point, solubility, partition coefficient etc.) and biological (activities such as antifungal effect, an esthetic effect, enzyme inhibition etc.) (Murray et al. [4], Kier and Hall [5]).

^a School of Mathematical Sciences, Universiti Sains Malaysia, 11800 USM, Penang, Malaysia

^b Department of Mathematics, Faculty of Science and Technology Universiti Malaysia Terengganu, 21030 Kuala Terengganu, Terengganu, Malaysia, hroslan@umt.edu.my

Let G be a simple connected graph of order n . For an integer $m \geq 1$, the m -order connectivity index of an organic molecule whose molecule graph G is defined as

$${}^m \chi(G) = \sum_{i_1 \dots i_{m+1}} \frac{1}{\sqrt{d_1 \dots d_{m+1}}},$$

where $i_1 \dots i_{m+1}$ runs over all paths of length m in G and d_i denote the degree of vertex v_i , and in particular, 2-, 3- and 4-order connectivity indices are defined as follows:

$${}^2 \chi(G) = \sum_{i_1 i_2 i_3} \frac{1}{\sqrt{d_1 d_2 d_3}} \quad {}^3 \chi(G) = \sum_{i_1 i_2 i_3 i_4} \frac{1}{\sqrt{d_1 d_2 d_3 d_4}}$$

and ${}^4 \chi(G) = \sum_{i_1 i_2 i_3 i_4 i_5} \frac{1}{\sqrt{d_1 d_2 d_3 d_4 d_5}}$.

Dendrimers are hyper-branched macromolecules with a rigorously tailored architecture. They can be synthesized, in a controlled manner, either by a divergent or a convergent procedure. Dendrimers have gained a wide range of applications in supra-molecular chemistry, particularly in host guest reactions and self-assembly processes. Their applications in chemistry, biology and nanoscience are unlimited.

Recently, some researchers investigated the m -order connectivity index and m -sum connectivity index for some families of dendrimers, where $m = 2$ and 3 (see [6-12]).

Note that one of the first studies on the topology of dendrimers was performed by Diudea and Katona [13].

In this paper, we will study the 2-order, 3-order and 4-order connectivity indices of an infinite family of PAMAM dendrimers.

RESULTS AND DISCUSSIONS

In this section, we shall compute 2-order, 3-order and 4-order connectivity indices of a class of dendrimers, namely, PAMAM dendrimers by construction of dendrimer generations G_n which has grown n stages. We denote simply this graph by $PD_1[n]$. Figure 1 shows generations G_3 has grown 3 stages.

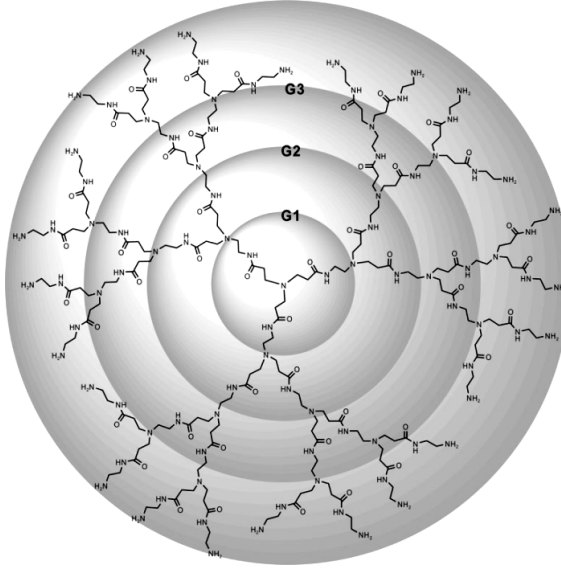


Figure 1. PAMAM dendrimer of generation G_n has grown 3 stages, denoted by $PD_1[n]$

Below we give our main results.

Theorem 1. Let $n \in \mathbb{N}_0$. The second-order connectivity index of $PD_1[n]$ is computed as follows

$${}^2\chi(PD_1[n]) = \frac{1}{4}[(3\sqrt{2} + 10\sqrt{3} + 4\sqrt{6} + 6) + (3\sqrt{2} + 12\sqrt{3} + 4\sqrt{6} + 3)(2^{n+1} - 2)]$$

Proof. For this structure, the core means that the number of stages equal to zero. Firstly, we compute ${}^2\chi(PD_1[0])$. Let $d_{i_1 i_2 i_3}$ denote the number of 2-paths whose three consecutive vertices are of degree i_1, i_2, i_3 , respectively. By the same way, we use $d_{i_1 i_2 i_3}^{(n)}$ to mean $d_{i_1 i_2 i_3}$ in n -th stages. Particularly, $d_{i_1 i_2 i_3}^{(n)} = d_{i_1 i_2 i_3}^{(n-1)}$. By Figure 2, one can verify that

$$d_{122}^{(0)} = 3, d_{222}^{(0)} = 3, d_{223}^{(0)} = 9, d_{232}^{(0)} = 6, d_{231}^{(0)} = 6.$$

It is easy to see that in the core of this structure as vertices are labeled in Figure 2, we have $d_{122}^{(0)} = 3$ which is $d_{i_9 i_8 i_7}^{(0)} = 3, d_{222}^{(0)} = 3$ which is $d_{i_6 i_7 i_8}^{(0)} = 3, d_{223}^{(0)} = 9$, which are $(d_{i_3 i_2 i_1}^{(0)} = 3 + d_{i_2 i_3 i_4}^{(0)} = 3 + d_{i_7 i_6 i_5}^{(0)} = 3), d_{232}^{(0)} = 6$ which are $(d_{i_2 i_1 i_2}^{(0)} = 3 + d_{i_3 i_4 i_6}^{(0)} = 3)$ and $d_{231}^{(0)} = 6$ which are $(d_{i_3 i_4 i_5}^{(0)} = 3 + d_{i_6 i_4 i_5}^{(0)} = 3)$.

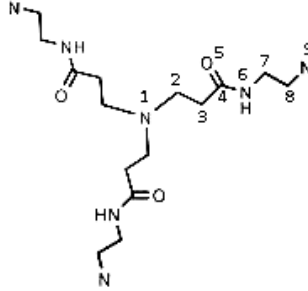


Figure 2. The core of PAMAM dendrimer $PD_1[0]$

Therefore, we have that

$$\begin{aligned} {}^2\chi(PD_1[0]) &= \frac{3}{\sqrt{1 \times 2 \times 2}} + \frac{3}{\sqrt{2 \times 2 \times 2}} + \frac{9}{\sqrt{2 \times 2 \times 3}} + \frac{6}{\sqrt{2 \times 3 \times 2}} + \frac{6}{\sqrt{2 \times 3 \times 1}} \\ &= \frac{1}{4}[(3\sqrt{2} + 10\sqrt{3} + 4\sqrt{6} + 6)] \end{aligned}$$

Secondly, we construct the relation between ${}^2\chi(PD_1[n])$ and ${}^2\chi(PD_1[n-1])$ for $n \geq 1$.

By simple reduction, we have

$$\begin{aligned} d_{122}^{(n)} &= d_{122}^{(n-1)} + 3 \times 2^{n-1}, \quad d_{222}^{(n)} = d_{222}^{(n-1)} + 6 \times 2^{n-1}, \\ d_{223}^{(n)} &= d_{223}^{(n-1)} + 21 \times 2^{n-1}, \quad d_{232}^{(n)} = d_{232}^{(n-1)} + 15 \times 2^{n-1}, \\ d_{231}^{(n)} &= d_{231}^{(n-1)} + 12 \times 2^{n-1}, \end{aligned}$$

and for any $(i_1 i_2 i_3) \neq (122), (222), (223), (232), (231)$, we have $d_{i_1 i_2 i_3}^{(n)} = 0$.

Therefore,

$$\begin{aligned} {}^2\chi(PD_1[n]) &= {}^2\chi(PD_1[n-1]) + \left(\frac{3}{\sqrt{1 \times 2 \times 2}} + \frac{6}{\sqrt{2 \times 2 \times 2}} \right. \\ &\quad \left. + \frac{21}{\sqrt{2 \times 2 \times 3}} + \frac{15}{\sqrt{2 \times 3 \times 2}} + \frac{12}{\sqrt{2 \times 3 \times 1}} \right) \times 2^{n-1} \\ &= {}^2\chi(PD_1[n-1]) + \frac{1}{4}(3\sqrt{2} + 12\sqrt{3} + 4\sqrt{6} + 3) \times 2^n. \end{aligned}$$

From above recursion formula, we have

$$\begin{aligned} {}^2\chi(PD_1[n]) &= {}^2\chi(PD_1[n-1]) + \frac{1}{4}(3\sqrt{2} + 12\sqrt{3} + 4\sqrt{6} + 3) \times 2^n \\ &= {}^2\chi(PD_1[n-2]) + \frac{1}{4}(3\sqrt{2} + 12\sqrt{3} + 4\sqrt{6} + 3)(2^n + 2^{n-1}) \end{aligned}$$

$$\begin{aligned} & \vdots \\ & = {}^2\chi(PD_1[0]) + \frac{1}{4}(3\sqrt{2} + 12\sqrt{3} + 4\sqrt{6} + 3)(2^n + 2^{n-1} + \dots + 2^2 + 2) \end{aligned}$$

Hence,

$${}^2\chi(PD_1[n]) = \frac{1}{4}[(3\sqrt{2} + 10\sqrt{3} + 4\sqrt{6} + 6) + (3\sqrt{2} + 12\sqrt{3} + 4\sqrt{6} + 3)(2^{n+1} - 2)]$$

The proof is now complete.

Theorem 2. Let $n \in \mathbb{N}_0$. The third-order connectivity index of $PD_1[n]$ is computed as follows

$${}^3\chi(PD_1[n]) = \frac{1}{4}[(3\sqrt{2} + 4\sqrt{3} + 5\sqrt{6} + 2) + (3\sqrt{2} + 8\sqrt{3} + 12\sqrt{6} + 4)(2^n - 1)]$$

Proof. We compute ${}^3\chi(PD_1[0])$ and let $d_{i_1 i_2 i_3 i_4}$ denote the number of m3-paths whose four consecutive vertices are of degree i_1, i_2, i_3, i_4 , respectively. By the same way, we use $d_{i_1 i_2 i_3 i_4}^{(n)}$ to mean $d_{i_1 i_2 i_3 i_4}$ in n -th stages. Particularly, $d_{i_1 i_2 i_3 i_4}^{(n)} = d_{i_1 i_2 i_3 i_4}^{(n)}$.

In Figure 2, one can verify that

$$d_{1222}^{(0)} = 3, d_{2223}^{(0)} = 3, d_{2231}^{(0)} = 6, d_{2232}^{(0)} = 12, d_{3223}^{(0)} = 3.$$

We can see that in the core of this structure as vertices are labeled in Figure 2, we have $d_{1222}^{(0)} = 3$ which is $d_{i_9 i_8 i_7 i_6}^{(0)} = 3$, $d_{2223}^{(0)} = 3$ which is $d_{i_8 i_7 i_6 i_4}^{(0)} = 3$, $d_{2231}^{(0)} = 6$ which are $(d_{i_7 i_6 i_4 i_5}^{(0)} = 3 + d_{i_2 i_3 i_4 i_5}^{(0)} = 3)$, $d_{2232}^{(0)} = 12$ which are $(d_{i_2 i_4 i_2 i_3}^{(0)} = 6 + d_{i_2 i_3 i_4 i_6}^{(0)} = 3 + d_{i_7 i_6 i_4 i_3}^{(0)} = 3)$ and $d_{3223}^{(0)} = 3$ which is $d_{i_1 i_2 i_3 i_4}^{(0)} = 3$.

Therefore, we have that

$$\begin{aligned} {}^3\chi(PD_1[0]) &= \frac{3}{\sqrt{1 \times 2 \times 2 \times 2}} + \frac{3}{\sqrt{2 \times 2 \times 2 \times 3}} + \\ & \frac{6}{\sqrt{2 \times 2 \times 3 \times 1}} + \frac{12}{\sqrt{2 \times 2 \times 3 \times 2}} + \frac{3}{\sqrt{3 \times 2 \times 2 \times 3}} \\ &= \frac{1}{4}(3\sqrt{2} + 4\sqrt{3} + 5\sqrt{6} + 2) \end{aligned}$$

Now, we construct the relation between ${}^3\chi(PD_1[n])$ and ${}^3\chi(PD_1[n-1])$ for $n \geq 1$

By simple reduction, we have

$$\begin{aligned} d_{1222}^{(n)} &= d_{1222}^{(n-1)} + 3 \times 2^{n-1}, & d_{2223}^{(n)} &= d_{2223}^{(n-1)} + 6 \times 2^{n-1}, \\ d_{2231}^{(n)} &= d_{2231}^{(n-1)} + 12 \times 2^{n-1}, & d_{2232}^{(n)} &= d_{2232}^{(n-1)} + 30 \times 2^{n-1}, \\ d_{3223}^{(n)} &= d_{3223}^{(n-1)} + 6 \times 2^{n-1} \end{aligned}$$

and for any $(i_1 i_2 i_3 i_4) \neq (1222), (2223), (2231), (2232), (3223)$ we have $d_{i_1 i_2 i_3 i_4}^{(n)} = 0$.

Thus,

$$\begin{aligned} {}^3\chi(PD_1[n]) &= {}^3\chi(PD_1[n-1]) + \left(\frac{3}{\sqrt{1 \times 2 \times 2 \times 2}} + \frac{6}{\sqrt{2 \times 2 \times 2 \times 3}} \right. \\ &\quad \left. + \frac{12}{\sqrt{2 \times 2 \times 3 \times 1}} + \frac{30}{\sqrt{2 \times 2 \times 3 \times 2}} + \frac{6}{\sqrt{3 \times 2 \times 2 \times 3}} \right) \times 2^{n-1} \\ &= {}^3\chi(PD_1[n-1]) + \frac{1}{8}(3\sqrt{2} + 8\sqrt{3} + 12\sqrt{6} + 4) \times 2^n \\ &= {}^3\chi(PD_1[n-2]) + \frac{1}{8}(3\sqrt{2} + 8\sqrt{3} + 12\sqrt{6} + 4)(2^n + 2^{n-1}) \\ &\quad \vdots \\ &= {}^3\chi(PD_1[0]) + \frac{1}{8}(3\sqrt{2} + 8\sqrt{3} + 12\sqrt{6} + 4)(2^n + 2^{n-1} + \dots + 2^2 + 2) \end{aligned}$$

Hence,

$${}^3\chi(PD_1[n]) = \frac{1}{4}[(3\sqrt{2} + 4\sqrt{3} + 5\sqrt{6} + 2) + (3\sqrt{2} + 8\sqrt{3} + 12\sqrt{6} + 4)(2^n - 1)]$$

The proof is now complete.

Theorem 3. Let $n \in \mathbb{N}_0$. The fourth-order connectivity index of $PD_1[n]$ is computed as follows

$${}^4\chi(PD_1[n]) = \frac{1}{4}[(3\sqrt{2} + 3\sqrt{3} + 2\sqrt{6} + 2) + (5\sqrt{2} + 9\sqrt{3} + 3\sqrt{6} + 4)(2^n - 1)]$$

Proof. Similar to that of Theorems 1 and 2, we compute ${}^4\chi(PD_1[0])$ and let $d_{i_1 i_2 i_3 i_4 i_5}^{(n)}$ denote the number of 4-paths whose five consecutive vertices are of degree i_1, i_2, i_3, i_4, i_5 , respectively. We use $d_{i_1 i_2 i_3 i_4 i_5}^{(n)}$ to mean $d_{i_1 i_2 i_3 i_4 i_5}^{(n)}$ in n -th stages. Particularly, $d_{i_1 i_2 i_3 i_4 i_5}^{(n)} = d_{i_5 i_4 i_3 i_2 i_1}^{(n)}$. By Figure 2, one can verify that

$$d_{12223}^{(0)} = 3, \quad d_{22231}^{(0)} = 3, \quad d_{22232}^{(0)} = 3, \quad d_{22322}^{(0)} = 6, \quad d_{23223}^{(0)} = 9, \quad d_{13223}^{(0)} = 3, \quad d_{32223}^{(0)} = 0.$$

Also we can see that in the core of this structure as vertices are labeled in Figure 2, we have $d_{12223}^{(0)} = 3$ which is $d_{i_9 i_8 i_7 i_6 i_4}^{(0)} = 3$, $d_{22231}^{(0)} = 3$ which is $d_{i_3 i_2 i_1 i_2 i_3}^{(0)} = 3$, $d_{22232}^{(0)} = 3$ which is $d_{i_8 i_7 i_6 i_4 i_3}^{(0)} = 3$, $d_{22322}^{(0)} = 6$ which are $(d_{i_3 i_2 i_1 i_2 i_3}^{(0)} = 3 + d_{i_2 i_3 i_4 i_6 i_7}^{(0)} = 3)$, $d_{23223}^{(0)} = 9$ which are $(d_{i_2 i_1 i_2 i_3 i_4}^{(0)} = 6 + d_{i_6 i_4 i_3 i_2 i_1}^{(0)} = 3)$ and $d_{13223}^{(0)} = 3$ which is $d_{i_5 i_4 i_3 i_2 i_1}^{(0)} = 3$.

Therefore,

$$\begin{aligned} {}^4\chi(PD_1[0]) &= \frac{3}{\sqrt{1 \times 2 \times 2 \times 2 \times 3}} + \frac{3}{\sqrt{2 \times 2 \times 2 \times 3 \times 1}} + \\ &\frac{3}{\sqrt{2 \times 2 \times 2 \times 3 \times 2}} + \frac{6}{\sqrt{2 \times 2 \times 3 \times 2 \times 2}} \\ &+ \frac{9}{\sqrt{2 \times 3 \times 2 \times 2 \times 3}} + \frac{3}{\sqrt{1 \times 3 \times 2 \times 2 \times 3}} \\ &= \frac{1}{4}[(3\sqrt{2} + 3\sqrt{3} + 2\sqrt{6} + 2)]. \end{aligned}$$

We now study the relation between ${}^4\chi(PD_1[n])$ and ${}^4\chi(PD_1[n-1])$ for $n \geq 1$, that is

$$\begin{aligned} d_{12223}^{(n)} &= d_{12223}^{(n-1)} + 3 \times 2^{n-1}, \quad d_{22231}^{(n)} = d_{22231}^{(n-1)} + 6 \times 2^{n-1}, \\ d_{22232}^{(n)} &= d_{22232}^{(n-1)} + 12 \times 2^{n-1}, \quad d_{22322}^{(n)} = d_{22322}^{(n-1)} + 15 \times 2^{n-1}, \\ d_{23223}^{(n)} &= d_{23223}^{(n-1)} + 12 \times 2^{n-1}, \quad d_{13223}^{(n)} = d_{13223}^{(n-1)} + 6 \times 2^{n-1}, \\ d_{32223}^{(n)} &= d_{32223}^{(n-1)} + 3 \times 2^{n-1} \end{aligned}$$

and for any $(i_1 i_2 i_3 i_4 i_5) \neq (12223), (22231), (22232), (22322), (23223), (13223), (32223)$, we have $d_{i_1 i_2 i_3 i_4 i_5}^{(n)} = 0$.

Thus,

$$\begin{aligned} {}^4\chi(PD_1[n]) &= {}^4\chi(PD_1[n-1]) + \\ &\left(\frac{3}{\sqrt{1 \times 2 \times 2 \times 2 \times 3}} + \frac{6}{\sqrt{2 \times 2 \times 2 \times 3 \times 1}} \right. \\ &+ \frac{12}{\sqrt{2 \times 2 \times 2 \times 3 \times 2}} + \frac{15}{\sqrt{2 \times 2 \times 3 \times 2 \times 2}} \\ &\left. + \frac{12}{\sqrt{2 \times 3 \times 2 \times 2 \times 3}} + \frac{6}{\sqrt{1 \times 3 \times 2 \times 2 \times 3}} \right) \end{aligned}$$

$$\begin{aligned}
 & + \frac{3}{\sqrt{3 \times 2 \times 2 \times 2 \times 3}}) \times 2^{n-1} \\
 & = {}^4\chi(PD_1[n-1]) + \frac{1}{8}(5\sqrt{2} + 9\sqrt{3} + 3\sqrt{6} + 4) \times 2^n \\
 & = {}^4\chi(PD_1[n-2]) + \frac{1}{8}(5\sqrt{2} + 9\sqrt{3} + 3\sqrt{6} + 4)(2^n + 2^{n-1}) \\
 & \vdots \\
 & = {}^4\chi(PD_1[0]) + \frac{1}{8}(5\sqrt{2} + 9\sqrt{3} + 3\sqrt{6} + 4)(2^n + 2^{n-1} + \dots + 2^2 + 2)
 \end{aligned}$$

Hence,

$${}^4\chi(PD_1[n]) = \frac{1}{4}[(3\sqrt{2} + 3\sqrt{3} + 2\sqrt{6} + 2) + (5\sqrt{2} + 9\sqrt{3} + 3\sqrt{6} + 4)(2^n - 1)]$$

The proof is now complete.

CONCLUSION

In this paper, we have discussed the 2-order, 3-order and 4-order connectivity indices of the PAMAM dendrimers. We believe that the results in this paper can be extended to the study of m -order connectivity index of PAMAM dendrimers where $m \geq 5$. Another direction is to investigate the m -order connectivity index of PAMAM dendrimers and other families of dendrimers, in general.

REFERENCES

- [1] M. Randic, *J. Am. Chem. Soc.*, **1975**, *97*, 6609.
- [2] L.B. Kier and L.H. Hall, *Molecular connectivity in structure activity analysis*, John Wiley, London, **1986**.
- [3] N. Trinajstic, *Chemical Graph Theory*, revised ed., CRC Press, Boca Raton, **1992**.
- [4] L.B. Kier, L.H. Hall, W.J. Murray, M. Randic, *J. Pharm. Sci.*, **1975**, *64*, 1971.
- [5] L.B. Kier and L.H. Hall, *Molecular connectivity in chemistry and drug research*, Academic Press, New York, **1976**.
- [6] A.R. Ashrafi, P. Nikzad, *Digest J. Nanomater. Biostruct.*, **2009**, *4(2)*, 269.
- [7] M.B. Ahmadi, M. Sadeghimehr, *Digest J. Nanomater. Biostruct.*, **2009**, *4(4)*, 639.
- [8] N.E. Arif, R. Hasni, *Studia UBB Chemia*, **2012**, *LVII (4)*, 7.
- [9] S. Chen, J. Yang, *Int. Math. Forum*, **2011**, *6(5)*, 223.
- [10] A. Madanshekaf, M. Ghaneei, *Digest J. Nanomater. Biostruct.*, **2011**, *6(2)*, 433.
- [11] J. Yang, F. Xia, S. Chen, *Int. J. Contemp. Math. Sciences*, **2011**, *6(5)*, 215.
- [12] H. Wang, H. Hua, *Digest J. Nanomater. Biostruct.*, **2010**, *5(2)*, 497.
- [13] M.V. Diudea and G. Katona, in: Newkome, G.A. Ed., *Advan. Dendritic Macromol.* **1999**, *4*, 135.

HARARY INDEX OF AN INFINITE FAMILY OF DENDRIMER NANOSTARS

SAEID ALIKHANI^a, CHANGIZ ESLAHCHI^b,
MOHAMMAD ALI IRANMANESH^{a*}

ABSTRACT. Let G be a simple graph. The Harary index of G is defined as the sum of reciprocal distances. Dendrimer nanostars form a new group of macromolecules that show photon funnels just like artificial antennas and also are resistant to photo-bleaching. In this paper we compute the Harary index for an infinite family of dendrimer nanostars.

Keywords: *Harary index; Wiener index; Dendrimer nanostar.*

INTRODUCTION

A simple graph $G = (V, E)$ is a finite nonempty set $V(G)$ of objects called vertices, together with a (possibly empty) set $E(G)$ of unordered pairs of distinct vertices of G called edges. In chemical graphs, the vertices of the graph correspond to the atoms of the molecule, and the edges represent the chemical bonds.

In theoretical chemistry, molecular structure descriptors (also called topological indices) are used for modeling physico-chemical, pharmacologic, toxicologic, biological and other properties of chemical compounds [1,2]. There exist several types of such indices, especially those based on graph theoretical distances. In 1993 Plavsic et al. [3] and Ivanciuc et al. [4] independently introduced a new topological index, named Harary index, in honor of Frank Harary on the occasion of his 70th birthday. This topological index is derived from the reciprocal distance matrix and is related to a number of interesting physico-chemical properties [5-9].

The Harary index is defined as the half-sum of the elements in the reciprocal distance matrix (also called the Harary matrix [10]):

^a *Department of Mathematics, Yazd University, 89195-741, Yazd, I.R.Iran*

^b *Department of Mathematics, Shahid Beheshti University, G.C. Tehran, I.R. Iran,
iranmanesh@yazduni.ac.ir*

$$H(G) = \sum_{\{u,v\} \subseteq V(G)} \frac{1}{d(u,v)},$$

where $d(u,v)$ denotes the distance between vertices u and v and the sum goes over all the pairs of vertices.

The Wiener index of a connected graph G is denoted by $W(G)$ and is defined as the sum of distances between all pairs of vertices in G [11]:

$$W(G) = \sum_{\{u,v\} \subseteq V(G)} d(u,v).$$

Dendrimers are a new class of polymeric materials. They are highly branched, mono-disperse macromolecules. The structure of these materials has a great impact on their physical and chemical properties. As a result of their unique behavior, dendrimers are suitable for a wide range of biomedical and industrial applications. Recently some people investigated the mathematical properties of these nanostructures [12-22].

In the next section, we present a method to compute the Harary index for an infinite family of dendrimer nanostars.

MAIN RESULTS

In this section we shall compute the Harary index for a family of dendrimer nanostars. We consider the dendrimer grown n steps denoted $D_1[n]$. Figure 1 shows $D_1[4]$. Note that there are three edges between each two hexagons in this dendrimer.

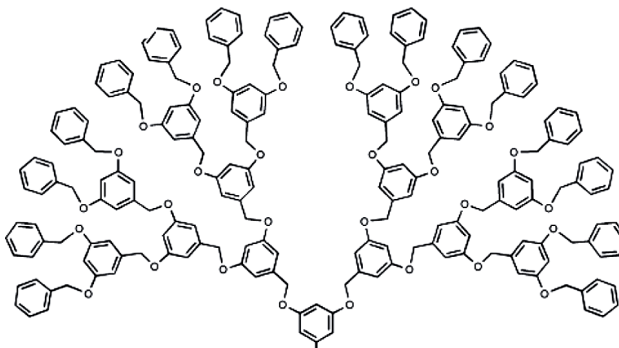


Figure 1. Dendrimer $D_1[4]$ of generation 1-4.

Recall that in computer science, a binary tree is a tree data structure in which each node has at most two child nodes, usually distinguished as “left” and “right”. Nodes with children are parent nodes, and child nodes may contain references to their parents. Outside the tree, there is often a reference to the “root” node (the ancestor of all nodes), if it exists. Any node in the data structure can be reached by starting at root node and repeatedly following references to either the left or right child.

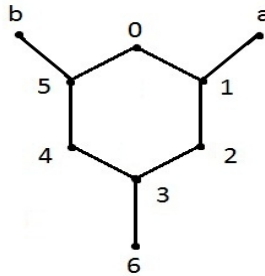


Figure 2. Labeled hexagon.

We label each vertices of hexagon with three pendant edges as shown in Figure 2. Let us denote the first hexagon (root) of $D_1[n]$ by symbol O We also denote the right child and the left child of O by $O(1)$ and $O(2)$, respectively. Let $O(x_1 \dots x_{k-1})$ be a dendrimer which has grown until $(k-1)$ -th stage. As was shown above, we shall denote its left and right child by $O(x_1 \dots x_{k-1}1)$ and $O(x_1 \dots x_{k-1}2)$, respectively. Now suppose that $x, y \in \{0, 1, \dots, 6, a, b\}$. By $x(O(x_1 \dots x_i))$, we mean the vertex x in hexagon $O(x_1 \dots x_i)$. We shall compute the distance of two arbitrary vertices $x(O(x_1 \dots x_i))$ and $y(O(y_1 \dots y_j))$.

Theorem 1. *The distance of two arbitrary vertices $x(O(x_1 \dots x_i))$ and $y(O(y_1 \dots y_j))$ is obtained as follows:*

1. $d(x(O), y(O(y_1 \dots y_j))) = \begin{cases} d(x, a) + d(y, 6) + 5j - 4; & y_1 = 1, \\ d(x, b) + d(y, 6) + 5j - 4; & y_1 = 2; \end{cases}$
2. $d(x(O(x_1 \dots x_k)), y(O(x_1 \dots x_k x_{k+1} \dots x_j))) = d(x(O), y(O(x_{k+1} \dots x_j)))$.
3. $d(x(O(x_1 \dots x_k)), y(O(y_1 \dots y_j))) = d(x, 6) + d(y, 6) + 5(j + i - 2r) + 6,$

where r is defined as $r = \min\{i : x_i \neq y_i\}$.

Proof. It is straightforward and follows from the construction of $D_1[n]$.

Now we try to compute the Harary index of $D_1[n]$. Consider the following polynomial as Harary polynomial of which value at $x=1$ gives the Harary index of a graph.

$$H(G, x) = \sum_{\{u,v\} \subseteq V(G)} \frac{1}{d(u,v)} x^{d(u,v)}.$$

The following theorem gives the coefficient of x^i of $H(D_1[n], x)$ for $1 \leq i \leq 5$. Our method led us to develop an approach for computing the coefficient x^i in $H(D_1[n], x)$ for $i \geq 6$ (see Theorem 4).

Theorem 2.

1. The coefficient of x in $H(D_1[n], x)$ is $2^{n+4} - 9$.
2. The coefficient of x^2 in $H(D_1[n], x)$ is $12 \times 2^n - 8$.
3. The coefficient of x^3 in $H(D_1[n], x)$ is $\frac{27 \times 2^n - 22}{3}$.
4. The coefficient of x^4 in $H(D_1[n], x)$ is $\frac{23 \times 2^n - 22}{4}$.
5. The coefficient of x^5 in $H(D_1[n], x)$ is $\frac{28(2^n - 1)}{5}$.

Proof.

1. The coefficient of x in $H(D_1[n], x)$ is the number of edges of $D_1[n]$. It is easy to see that the number of its edges is $2^{n+4} - 9$.

2. To evaluate the coefficient of x^2 , we compute the number of pair vertices which have distance 2 and are in different hexagons. So we have to consider two cases of Part (i) of Theorem 1, that is $d(x, a) + d(y, 6) + 5j - 4 = 2$ or $d(x, b) + d(y, 6) + 5j - 4 = 2$. In the both cases $j = 1$. In the first case $\{d(x, a), d(y, 6)\} = \{0, 1\}$ or for the second case $\{d(x, b), d(y, 6)\} = \{0, 1\}$. Obviously $y = 6$ is one of the answers. For this case there are two cases (1,6) and (5,6). Also if $d(y, 6) = 1$, then $y = 3$ and $x = a$ or $x = b$. Therefore we have four solutions: $(a(O), 3(O(1)), (b(O), 3(O(2))), (1(O), 6(O(1))))$ and $(5(O), 6(O(2)))$. Now by considering the Part (ii) of the Theorem 1 all of the pair vertices of distance 2 are:

$$(a(O(x_1 \dots x_k)), 3(O(x_1 \dots x_k 1))), (1(O(x_1 \dots x_k)), 6(O(x_1 \dots x_k 1))), (1 \leq k \leq n-1). \\ (b(O(x_1 \dots x_k)), 3(O(x_1 \dots x_k 2))), (5(O(x_1 \dots x_k)), 6(O(x_1 \dots x_k 2)))$$

Therefore the number of solutions are $4(2^n - 1)$. By the other hand, there are 12 pair vertices of distance 2 in any hexagon, and so the coefficient of x^2 is $\frac{1}{2}(4(2^n - 1) + 12(1 + 2 + \dots + 2^{n-1}) + 8(2^n)) = \frac{4(2^n - 1) + 12(2^n - 1) + 8(2^n)}{2} = 12 \times 2^n - 8$

3. The proof of part (iii), (iv), and (v) are similar to proof of part(ii).

Theorem 3.

1. The diameter of $D_1[n]$ is $10n + 4$. 2. The radius of $D_1[n]$ is $5n + 4$.

Proof.

1. It is obvious that the most distances between two vertices of this graph are between $x \in O(x_1 \dots x_n)$ and $y \in O(y_1 \dots y_n)$, where $x_1 \neq y_1$ and $x = y = 0$. By Theorem 1(iii) we have

$$d(0O(x_1, \dots, x_n), 0O(y_1, \dots, y_n)) = 2d(0, 6) + 5((2n - 2) + 6) = 10n + 4.$$

2. Note that the radius of a graph G is $r(G) = \min_x \max_y \{d(x, y) \mid y \in V(G)\}$.

This minimum occurs when $x = 6 \in O$ and the maximum of $\{d(6, y) \mid y \in V(D_1[n])\} = 5n + 4$ and this occurs when $y = 0O(x_1 \dots x_n)$ by Theorem 1(i).

Now we shall compute the coefficient of x^l in $H(D_1[n], x) = \frac{1}{l} \sum x^l$, where $l \geq 6$. We need the following lemma, of which proof can be obtained directly by considering all the possibilities.

Lemma 1. *Let x, y, a and 6 be vertices of hexagons of $D_1[n]$ with the positions shown in Figure 2. Then we have the following table:*

Case	Equation	No. of solutions
1	$d(x, a) + d(y, 6) = 4$	13
2	$d(x, 6) + d(y, 6) = 4$	14
3	$d(x, a) + d(y, 6) = 0$	1
4	$d(x, a) + d(y, 6) = 5$	13
5	$d(x, 6) + d(y, 6) = 5$	14
6	$d(x, a) + d(y, 6) = 6$	18
7	$d(x, 6) + d(y, 6) = 1$	2
8	$d(x, 6) + d(y, 6) = 6$	16

Case	Equation	No. of solutions
9	$d(x, a) + d(y, 6) = 2$	5
10	$d(x, 6) + d(y, 6) = 7$	12
11	$d(x, 6) + d(y, 6) = 2$	5
12	$d(x, 6) + d(y, 6) = 7$	12
13	$d(x, a) + d(y, 6) = 3$	8
14	$d(x, a) + d(y, 6) = 8$	9
15	$d(x, 6) + d(y, 6) = 3$	8
16	$d(x, 6) + d(y, 6) = 8$	9

Proof. It is straightforward and is obtained directly by considering all the possibilities.

Here we state the main theorem of this paper which gives the coefficients of x^l in $H(D_1[n], x)$ for $l \geq 6$. First we use the following notations:

$$A = 2^{n+1} - 2^q, \quad B = 2^{n+1} - 2^{q+1}, \quad C = 2^{n+1} - 2^{q+2},$$

$$D = \sum_{r=0}^{\lfloor \frac{2n-q+3}{2} \rfloor} (2n - q - 2r + 1), \quad E = \sum_{r=0}^{\lfloor \frac{2n-q+2}{2} \rfloor} (2n - q - 2r - 2).$$

Theorem 4. Suppose that the Harary polynomial of $D_1[n]$ is

$$H(D_1[n], x) = \sum_{u, v \in V} \frac{1}{d(u, v)} x^{d(u, v)} = \frac{1}{d(u, v)} \sum_{l=1}^{10n+4} a_l x^l.$$

Then for every $l \geq 6$, we have

$$a_l = \begin{cases} 13A + 14D; & \text{if } l \equiv 0 \pmod{5}, \\ B + 13C + 14D; & \text{if } l \equiv 1 \pmod{5} \\ 18A + 16D + 2E; & \text{if } l \equiv 2 \pmod{5} \\ 12A + 5B + 12D + 5E; & \text{if } l \equiv 3 \pmod{5} \\ 8B + 9D + 8E; & \text{if } l \equiv 4 \pmod{5}. \end{cases}$$

Proof. We prove the theorem for case $l \equiv 0 \pmod{5}$. Let $l = 5q$, for some $q \in \mathbb{N}$. Therefore we have $d(x, a) + d(y, 6) + 5j - 4 = 5q$ and so $d(x, a) + d(y, 6) = 4$. By Lemma 1 there are 13 cases. By solving the equation of Theorem 1 (i) we will have $q = j$, and by Part (ii) of this theorem the number of all possibilities are

$$13 \times 2^q (1 + 2 + \dots + 2^{n-q}) = 13(2^{n+1} - 2^q) = 13A.$$

Now by considering the part (iii) of Theorem 1, we have to find the number of solutions of $d(x,6)+d(y,6)+5(i+j-2r)+6=5q$. When $d(x,6)+d(y,6)=4$ this equation has solution, and this occurs for 14 different cases by Lemma 1. With substituting in this equation we have $i+j=q+2r-2$, where $r \leq i, j \leq n$. This equation is equivalent to $i' + j' = q - 2$, ($0 \leq i', j' \leq n - r$) or equivalent to $i'' + j'' = 2n - 2r - q + 2$, where i'' and j'' are non-negative. By inclusion-exclusion principle the number of solutions of this equation is

$$D = \sum_{r=0}^{\lfloor \frac{2n-q+3}{2} \rfloor} (2n - q - 2r + 1).$$

Since there are 14 cases for this part, we have $a_i = 13A + 14D$ and the proof is complete.

We have the following result:

Corollary 1. *The Harary index of $D_1[n]$ is*

$$H(D_1[n]) = (2^{n+4} - 9) + \frac{1}{2}(24 \times 2^n - 16) + \frac{1}{3}(27 \times 2^n - 22) + \frac{1}{4}(23 \times 2^n - 22) + \frac{1}{5}(28(2^n - 1)) + \frac{1}{l} \sum_{l=6}^{10n+4} a_l x^l,$$

where a_l is obtained in Theorem 4.

REFERENCES

- [1] R. Todeschini, V. Consonni, "Handbook of molecular descriptors", Wiley-VCH, Weinheim, **2000**, 209-212.
- [2] R. Todeschini, V. Consonni, "Molecular Descriptors for Chemoinformatics", Wiley-VCH, Weinheim, **2009**, 371-375.
- [3] D. Plavisić, S. Nikolić, N. Trinajstić, Z. Mihalić, *J. Math. Chem.* **1993**, *12*, 235.
- [4] O. Ivanciuc, T.S. Balaban, A.T. Balaban, *J. Math. Chem.* **1993**, *12*, 309.
- [5] O. Ivanciuc, T. Ivanciuc, A.T. Balaban, *J. Chem. Inf. Comput. Sci.* **1998**, *38*, 395.
- [6] J. Devillers, A.T. Balaban (eds), "Topological indices and related descriptors in QSAR and QSPR", Gordon and Breach, **1999**, Amsterdam.
- [7] M.V. Diudea, *J. Chem. Inf. Comput. Sci.* **1997**, *37*, 292.
- [8] M.V. Diudea, T. Ivanciuc, S. Nikolić, N. Trinajstić, *MATCH Commun. Math. Comput. Chem.* **1997**, *35*, 41.
- [9] I. Gutman, *Indian J. Chem.* **1997**, *36A*, 128.
- [10] H. Yousefi-Azari, A.R. Ashrafi, A. Bahrami and J. Yazdani, *Asian J. Chem.*, **2008**, *20*, 15.

- [11] H. Hosoya, *Bull. Chem. Soc. Japan*, **1971**, *44*, 2332.
- [12] B. Klajnert, M. Bryszewska, *Acta Biochim. Polon.*, **2001**, *48*, 199.
- [13] S. Alikhani, M.A. Iranmanesh, *J. Comput. Theoret. Nanosci.*, **2010**, *7*, 2314.
- [14] A.R. Ashrafi and M. Mirzargar, *Indian J. Chem.*, **2008**, *47A*, 535.
- [15] N. Dorosti, A. Iranmanesh and M.V. Diudea, *MATCH Commun. Math. Comput. Chem.*, **2009**, *62*, 389.
- [16] M. Ghorbani and M. Songhori, *Iranian J. Math. Chem.*, **2010**, *1*, 57.
- [17] A. Iranmanesh and N.A. Gholami, *MATCH Commun. Math. Comput. Chem.*, **2009**, *62*, 371.
- [18] M. Mirzargar, *MATCH Commun. Math. Comput. Chem.*, **2009**, *62*, 363.
- [19] K. Nagy, Cs.L. Nagy and M.V. Diudea, *Studia UBB Chemia*, **2010**, *55(1)*, 77.
- [20] A.R. Ashrafi, H. Shabani, M.V. Diudea, *Studia UBB Chemia*, **2010**, *55(4)*, 137.
- [21] K. Nagy, Cs.L. Nagy, M.V. Diudea, *MATCH Commun. Math. Comput. Chem.* **2010**, *65*, 163.
- [22] M.V. Diudea, A.E. Vizitiu, M. Mirzargar, A.R. Ashrafi, *Carpath. J. Math.*, **2010**, *26*, 59.

OCTAHEDRAL CNT JUNCTIONS AS P-TYPE NETWORKS

VIRGINIA BUCILA^a, MONICA STEFU^a AND BEATA SZEFLER^{b*}

ABSTRACT. Octahedral carbon nanotube CNT junctions designed by map operations are extended to 3D periodic structures in the Euclidean space, thus P-type surface being decorated with a variety of polyhedral motifs. They can be seen as nets of spongy sp^2 covalently bonded carbon atoms or nets of aluminosilicates, called zeolites. Topological, energetic and crystallographic aspects are discussed.

Keywords: 3-periodic structures, octahedral junctions, cubic network,

INTRODUCTION

A covalent lattice, consisting of sp^2 carbon atoms, can be embedded in a triple periodic minimal surface, particularly in a P-type surface. Carbon allotropes, having the structure of a simple cubic network, were named *periodic schwarzites*, in the honor of H. A. Schwarz [1,2], who first investigated, in the early nineteenth century, their differential geometry. The nodes of the cubic network can be assimilated to nanotube junctions and can be decorated by using some map operations. A map M is a combinatorial representation of a closed surface (i.e., covering, tessellation). Map operations are some topological operations enabling generation and/or transformation of a given map into new maps.

Recall Euler's basic relations in polyhedra [3,4]: $\sum d v_d = 2e$ and $\sum s f_s = 2e$, where e are the number of edges, v_d are the number of vertices of degree d and f_s the number of s -gonal faces /faces of size s . The two relations are joined into a third formula: $v - e + f = \chi(M) = 2(1 - g)$ with χ being the Euler *characteristic* and g is the genus [5] (i.e., the number of simple tori to which a given structure can be reduced, or the number of structure's holes; $g=0$ for the sphere or the plane and $g=1$ for a simple torus).

^a Faculty of Chemistry and Chemical Engineering, Babes-Bolyai University, 400028 Cluj, Romania

^b Department of Physical Chemistry, Collegium Medicum, Nicolaus Copernicus University, Kurpińskiego 5, 85-950, Bydgoszcz, Poland, beata.szefler@cm.umk.pl

Positive/negative χ values indicate positive/negative curvature of a lattice. An embedding is a representation of a graph on a closed surface such that no crossing lines appear [5].

In view of generating the desired nanotube junctions, we present here only four composite map operations, the reader being invited to consult some related references [6,7].

Leapfrog Le [8,9], can be obtained by two successive operations:

$$Le(M) = Du(P_3(M)) = Tr(Du(M))$$

where Du is the Poincaré dual, P_3 is the triangulation while Tr is the truncation. The transformed map parameters are: $Le(M)$; $v = s_0 f_0 = d_0 v_0$; $e = 3e_0$; $f = v_0 + f_0$ with the subscript zero denoting the parameters in the parent map. The number of vertices in $Le(M)$ is d_0 times larger than in the parent map, irrespective of its tessellation. Since in trivalent maps Le multiplies 3-times the number of original vertices, it is also called the *tripling* operation. Le rotates the parent s -gonal faces by π/s . The most common example is the leapfrogging of dodecahedron Do : $Le(Do) = C_{60}$.

Quadrupling Q or *chamfering* [8,10-12] is achieved by the following sequence:

$$Q(M) = E_-(Tr_{P_3}(P_3(M)))$$

where E_- means the (old) edge deletion of the truncation Tr_{P_3} of each vertex introduced by P_3 capping. The vertex multiplication ratio in a Q -transformed map is $d_0 + 1$ irrespective of the original map tessellation: $Q(M)$; $v = (d_0 + 1)v_0$; $e = 4e_0$; $f = f_0 + e_0$.

Vertex multiplication factor m induced by a map operation, on a trivalent map, is calculated by the Goldberg's polynomial [13]: $m = (a^2 + ab + b^2)$; $a \geq b$; $a + b > 0$, with a, b being integers. The m factor is also related to the formula giving the volume of truncated pyramid, of height h : $V = mh/3$, coming from the ancient Egypt. For $Le(1,1)$; $m=3$ while for $Q(2,0)$; $m=4$.

Septupling S_1 is a third composite operation [14], with $S_1(2,1)=7$. It was also called *Capra* Ca (the goat, in Romanian [15]), corresponding to the *leapfrog* English children game. S_1 is achieved by truncation Tr_{P_5} of the face centered vertices introduced by P_5 pentangulation (see above the definition for $Q(M)$). Note that P_5 involves an E_2 (i.e., edge trisection). This operation preserves the original vertices while the parent s -gonal faces are twisted by $\pi/2s$. It can be written as:

$$S_1(M) = Ca(M) = Tr_{P_5}(P_5(M))$$

The vertex multiplication ratio in $S_1(M)$ is $2d_0 + 1$ irrespective of the original map tiling: $S_1(M)$; $v_1 = v_0 + 2e_0 + s_0f_0 = (2d_0 + 1)v_0$; $e_1 = 7e_0$; $f_1 = s_0f_0 + f_0$.

S_1 insulates any parent face by its own hexagons, while Le or Q introduce hexagons that are shared between two parent faces. Figure 1 illustrates some nanostructures designed by map operations.

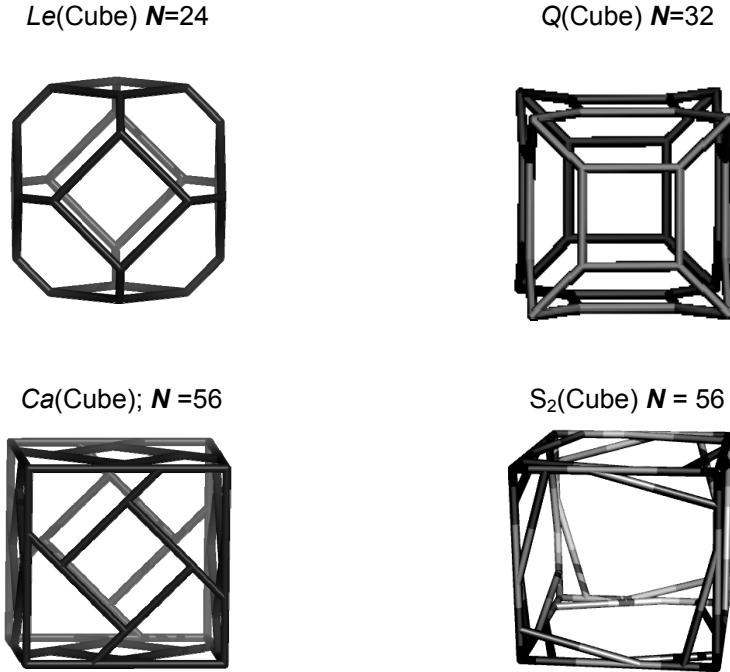


Figure 1. Four composite operations applied to the Cube

S_1 can continue with an E_n homeomorphic operation on the edges bounding the parent-like faces (*i.e.*, those resulted by Tr_5), thus resulting open maps with all polygons of the same $(6+n)$ size. This last operation is called the *Opening* Op_n operation [16,17]. The transformed map parameters are as follows: $Op(S_1(M))$; $v(Op(S_1)) = v + s_0f_0 = (3d_0 + 1)v_0$; $e(Op(S_1)) = 9e_0$ and $f(Op(S_1)) = f - f_0 = s_0f_0$.

Septupling S_2 [14] is the twin operation of S_1 , because the two $S_k(M)$ transformed maps form complementary lattices (see below). It can be achieved by putting four vertices on each edge of the parent map M (*i.e.*, the E_4 operation) and next join these new vertices in the order $(-1, +3)$:

$$S_2 = J_{(-1,+3)}(E_4(M))$$

The transformed map parameters are identical to the S_1 operation: $S_2(M) = S_1(M)$; $v = (2d_0 + 1)v_0$; $e = 7e_0$; $f = s_0f_0 + f_0$. It insulates the parent faces by pentagon triples and the transformed maps are non-chiral ones. However, chirality can be introduced by the opening operation Op_{2a} , realized by two points put on alternative edges of a boundary, thus getting twice folding of the parent faces. The transformed map parameters are:

$$Op_{2a}(S_2(M)); v_{Op(S_{2a})} = (4d_0 + 1)v_0; e_{Op(S_{2a})} = 11e_0; f_{Op(S_{2a})} = s_0f_0.$$

An opening operation $Op_1(S_2(M))$ is also known [6, 14].

Sequences of such operations enable the decoration of various surfaces, with both positive and negative curvature. Graphite as reference, has zero curvature. The negative curvature can be induced by 7-size or larger rings, while rings of size 5 or less generate positive curvature. Negatively curved structures can form infinite periodic networks. A tessellation made by a single type of polygons is called Platonic; when two types of polygonal faces exist, the covering is called Archimedean [7].

Multi-tori [18] are complex structures consisting of more than one single torus (i.e., hyper ring). They can result by self-assembly of some repeating units/monomers, formed by spanning of cages/fullerenes and can appear in spongy carbon [19] and in natural zeolites [20], as well. Multi-tori can grow either spherically (3D /three-dimensional) or linearly, in forming arrays of various complexity [7]. The above operations have been performed by the original software CVNET [21]

NET CONSTRUCTION

The hypothetical carbon cubic networks herein discussed were designed by joining (with the Nano Studio original software [22]) opened octahedral carbon nanotube CNT junctions. Open objects can be designed by the *Opening Op* operation, applied consecutively to the regular map operations. The most used map operations are: *Leapfrog* – $Le_{1,1}$, *Quadrupling* – $Q_{2,0}$, *Capra* – $Ca_{2,1}$, which are applied to the Cube or Cube-derived maps for obtaining octahedral junctions necessary to build a P-type network.

Figures 2–5 present 10 new 3-periodic structures, designed at TOPO GROUP Cluj. Crystallographic investigation was performed by an original software, called “Atom”, developed at our group in collaboration with Prof. Davide Proserpio, University of Milan, Italy [23].

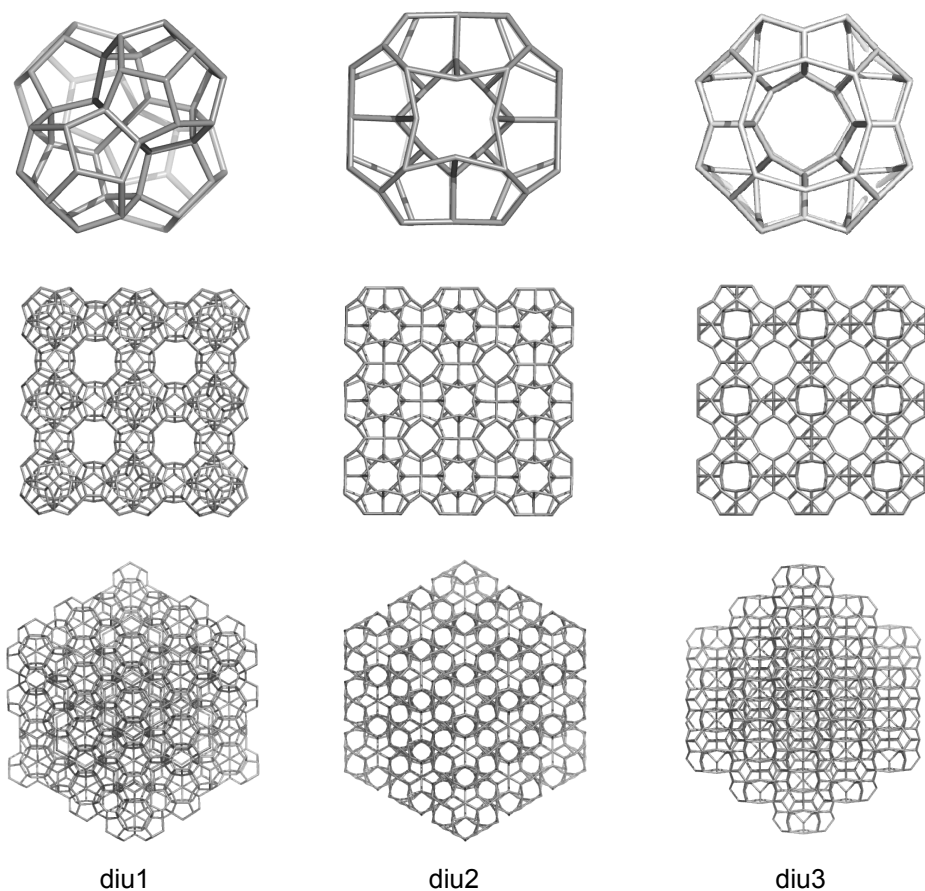


Figure 2. The cubic networks diu1, diu2, diu3, denoted by Diudea’s name

The structures were noted by the shortened Diudea’s name, *diu*. The crystallographic description of these hypothetical crystal networks is given in Appendix.

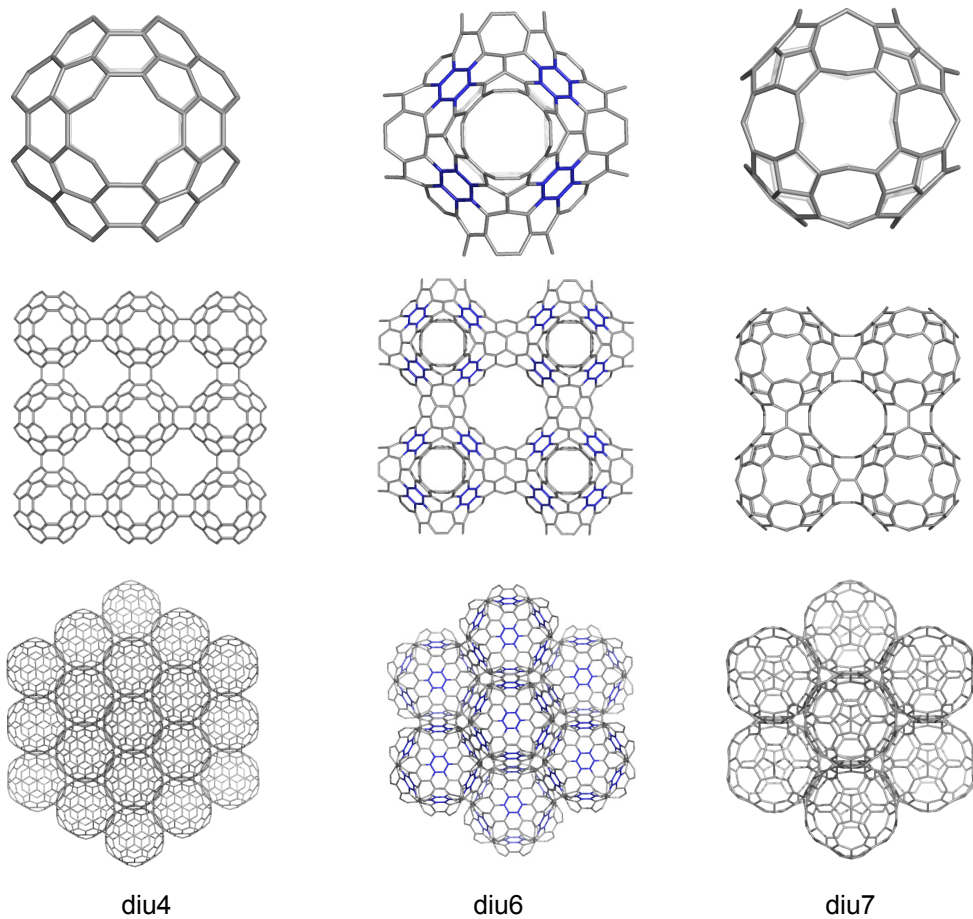


Figure 3. The cubic networks diu4, diu6, diu7

OCTAHEDRAL CNT JUNCTIONS AS P-TYPE NETWORKS

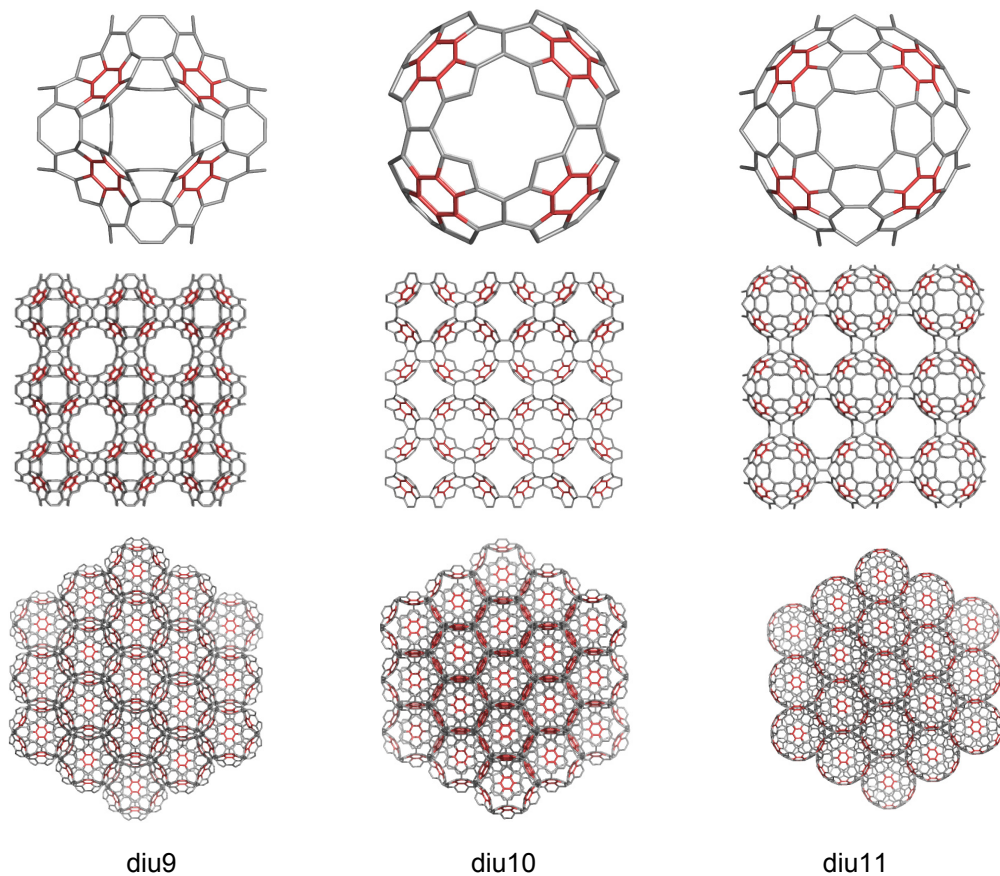


Figure 4. The cubic networks diu9, diu10 and diu11

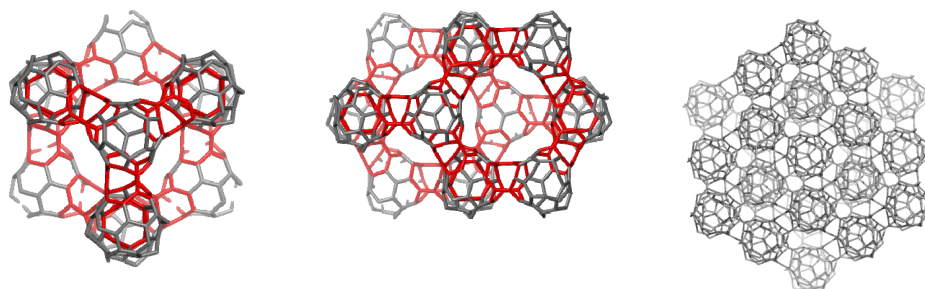


Figure 5. The diamondoid network diu5

STABILITY OF STRUCTURES

Evaluating the cohesive energy of the hypothetical crystal networks is over the aim of this paper. However, for some small constructive units we computed single point energies on optimized geometries at Hartree-Fock HF (HF/6-31G**) level of theory. The calculations were performed in gas phase by Gaussian 09 [24]. It was necessary to use relatively large computational effort for this examination, due to the size of the structures. Data are listed in Table 1.

Table 1. Total energy E_{tot} per atom (kcal/mol) and HOMO-LUMO HL Gap, at Hartree-Fock HF (HF/6-31G**) level of theory for some units of some Sumanene-based structures.

Structure	Structural unit	No. C atoms	HF/6-31G(d,p) (au)	E_{tot} /atom (au/mol)	HF_Gap (eV)
1	C ₆₀	60	-2271.830	-37.864	7.418
2	diu9	216	-8206.401	-37.993	6.442
3	diu10	168	-6389.018	-38.030	6.637
4	diu11	192	-7298.367	-38.012	6.044

As a reference structure, we considered C₆₀, the most referred structure in Nanoscience. This test of stability was done to support the idea that sumanene, a real molecule [25,26], can be used to synthesize structural units for more elaborated nanostructures (e.g. diu9 to diu11), eventually called “ordered Schwarzites”, embedded in the P-surface. From Table 1 it is clear that such units show a stability comparable to the well-known C₆₀ reference structure, thus being possible candidates for laboratory synthesis.

CONCLUSIONS

Operations on maps are useful tools in the design of polyhedral nanostructures. Octahedral carbon nanotube junctions can be extended to 3D periodic nanostructures in the Euclidean space, thus decorating the P-type surface by a variety of polyhedral motifs. Topological, energetic and crystallographic aspects were discussed. For some finite small units, data suggest a good stability, thus being promising for future laboratory synthesis.

ACKNOWLEDGMENTS

Virginia R. Bucila acknowledges that this work was possible with the financial support of the Sectorial Operational Programme for Human Resources Development 2007-2013, co-financed by the European Social Fund, under the project number POSDRU/107/1.5/S/76841 with the title „Modern Doctoral Studies: Internationalization and Interdisciplinarity”.

REFERENCES

- [1] H.A. Schwarz, „Über Minimalflächen“, Monatsber. Berlin Akad., **1865**.
- [2] H.A. Schwarz, „Gesammelte Matematische Abhandlungen“, Springer, Berlin, **1890**.
- [3] L. Euler, *Comment. Acad. Sci. I. Petropolitanae*, **1736**, 8, 128.
- [4] L. Euler, *Novi Comment. Acad. Sci. I. Petropolitanae* **1758**, 4, 109.
- [5] F. Harary, “Graph Theory”, Addison - Wesley, Reading, M.A., **1969**.
- [6] M.V. Diudea, “Nanomolecules and Nanostructures - Polynomials and Indices”, MCM series, no. 10, Univ. Kragujevac, Serbia, **2010**.
- [7] M.V. Diudea, Cs.L. Nagy, “Periodic Nanostructures”, Springer, **2007**.
- [8] V. Eberhard, „Zur Morphologie der Polyeder“, Leipzig, Teubner, **1891**.
- [9] P.W. Fowler, *Chem. Phys. Lett.*, **1986**, 131, 444.
- [10] M.V. Diudea, P.E. John, *MATCH Commun. Math. Comput. Chem.*, **2001**, 44, 103.
- [11] M.V. Diudea, P.E. John, A. Graovac, M. Primorac, T. Pisanski, *Croat. Chem. Acta*, **2003**, 76, 153.
- [12] M.V. Diudea, *Forma* (Tokyo), **2004**, 19, 131.
- [13] M. Goldberg, *Tôhoku Math. J.*, **1937**, 43, 104.
- [14] M.V. Diudea, *J. Chem. Inf. Model.*, **2005**, 45, 1002.
- [15] M.V. Diudea, *Studia UBB Chemia*, **2003**, 48 (2), 3.
- [16] M.V. Diudea, M. Stefu, P.E. John, A. Graovac, *Croat. Chem. Acta*, **2006**, 79, 355.
- [17] M.V. Diudea, Ed., *Nanostructures, Novel Architecture*, Nova, N.Y., 2005.
- [18] M.V. Diudea, M. Petitjean, *Symm. Culture, Sci.*, **2008**, 19, 285.
- [19] G. Benedek, H. Vahedi-Tafreshi, E. Barborini, P. Piseri, P. Milani, C. Ducati, and J. Robertson, *Diamond Relat. Mater.*, **2003**, 12, 768.
- [20] M. Laniecki, W. Zmierzczak, *Zeolites*, **1991**, 11, 18.
- [21] M. Stefu, M.V. Diudea, CVNET software, Babes-Bolyai University, 2005.
- [22] Cs.L. Nagy, M.V. Diudea, Nano Studio software, Babes-Bolyai University, 2009.
- [23] V. Bucila, C.I. Bucila, D.M. Proserpio, ATOM software, Babes-Bolyai University and Università degli Studi di Milano, Italia 2012.
- [24] Gaussian 09, M.J. Frisch, G.W. Trucks, H.B. Schlegel, G.E. Scuseria, M.A. Robb, J.R. Cheeseman, G. Scalmani, V. Barone, B. Mennucci, G.A. Petersson, H. Nakatsuji, M. Caricato, X. Li, H.P. Hratchian, A.F. Izmaylov, J. Bloino, G. Zheng, J.L. Sonnenberg, M. Hada, M. Ehara, K. Toyota, R. Fukuda, J. Hasegawa,

M. Ishida, T. Nakajima, Y. Honda, O. Kitao, H. Nakai, T. Vreven, J.A. Montgomery, J.E. Peralta, F. Ogliaro, M. Bearpark, J.J. Heyd, E. Brothers, K.N. Kudin, V.N. Staroverov, R. Kobayashi, J. Normand, K. Raghavachari, A. Rendell, J.C. Burant, S.S. Iyengar, J. Tomasi, M. Cossi, N. Rega, N.J. Millam, M. Klene, J.E. Knox, J.B. Cross, V. Bakken, C. Adamo, J. Jaramillo, R. Gomperts, R.E. Stratmann, O. Yazyev, A.J. Austin, R. Cammi, C. Pomelli, J.W. Ochterski, R.L. Martin, K. Morokuma, V.G. Zakrzewski, G.A. Voth, P. Salvador, J.J. Dannenberg, S. Dapprich, A.D. Daniels, Ö. Farkas, J.B. Foresman, J.V. Ortiz, J. Cioslowski, D.J. Fox, Gaussian Inc Wallingford CT, Revision A.1, 2009.

- [25] H. Sakurai, T. Daiko, T. Hirao, *Science*, **2003**, 301, 1878.
- [26] H. Sakurai, T. Daiko, H. Sakane, T. Amaya, T. Hirao, *J. Am. Chem. Soc.* **2005**, 127, 11580.

APPENDIX

In the following, the networks are represented as given by Topos computer program, (on left), where the repetitive cell/unit is enclosed in squares, and by HyperChem program (on right). Before the figures, the crystallographic Topos data are given.

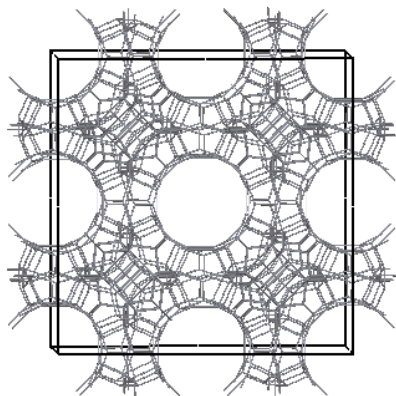
1. NEW: diu1 (D_5 diamond, spongy) $D_{5\text{spo}}$

Point symbol for net: $(5^3)16(5^5.8)36(5^6)17$

3,3,4,4,4,4-c net with stoichiometry (3-c)16(4-c)53; 7-nodal net

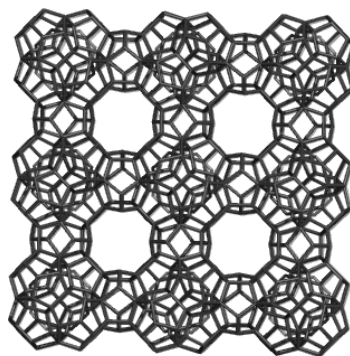
VS [5.5.5] [5.5.5] [5.5.5.5.5.12] [5.5.5.5.5.5] [5.5.5.5.5.12₂] [5.5.5.5.5.5] [5.5.5.5.5.5]

New topology



333cell 333C20_1755_ICIF

Diudea's name **diu1**

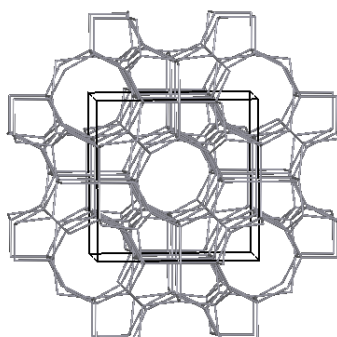


333C20_1755_ICIF

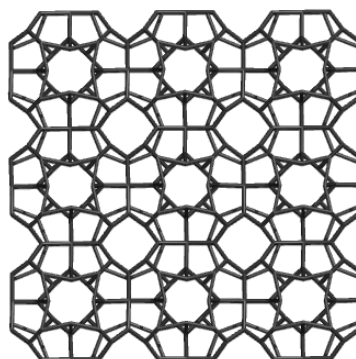
$D_{5\text{spo}}$

**2. NEW: diu2 (Cube, Polygonal P4, Unit, co-net, hexagon 6, X cut edges)
CP4UCo6X**

Point symbol for net: $\{6^3\}4\{6^4.8^2\}3\{6^5.8\}6$
 3,4,4-c net with stoichiometry (3-c)4(4-c)9; 3-nodal net
 VS [6.6.6] [6.6.6.6.6₂.8₂] [6₂.6₂.6₂.6₂.8.8]
 New topology



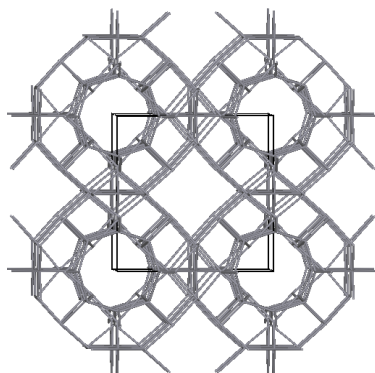
p4u_corecell P4U_Core_6E_333B
 Diudea's name diu2



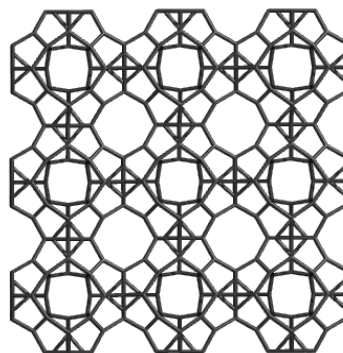
P4U_Core_6E_333B
 CP4UCo6X

**3. NEW: (Cube, Polygonal P4, Unit, co-net, hexagon 6, X cut edges, face 4)
CP4UCo6X4**

Point symbol for net: $\{4.6^4.8\}2\{4.6^5\}2\{6^2.8\}2\{6^3\}2\{6^4.8^2\}\{6^5.8\}4$
 3,3,4,4,4,4,4,4-c net with stoichiometry (3-c)4(4-c)9; 9-nodal net
 VS [6₂.6₂.8₂] [6.6.6] [4.8₂.6₂.6₂.6₂.6₂] [4.8₂.6.6.6.6] [6₂.6₂.6₂.6₂.8.16₂] [4.6₂.6.6.6.6]
 [6.6.6.6.6₂.8₂] [6.6.6.6.6₂.8] [4.6₂.6.6.6.6]
 New topology



p4u_core_6x6cell
 Diudea's name Diu3



P4U_Core_6x6_333_1620
 CP4UCo6X4

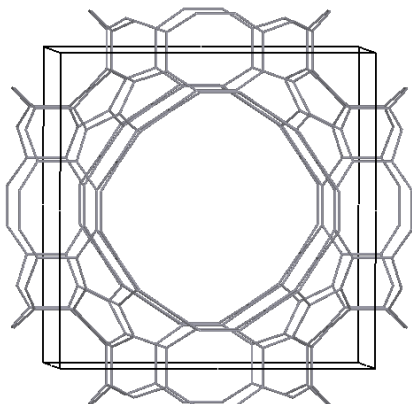
4. NEW (Cube, hexagon triple) diu4=C3Hex

Point symbol for net: $\{6.8^2\}3\{6^2.8\}6\{6^3\}4$

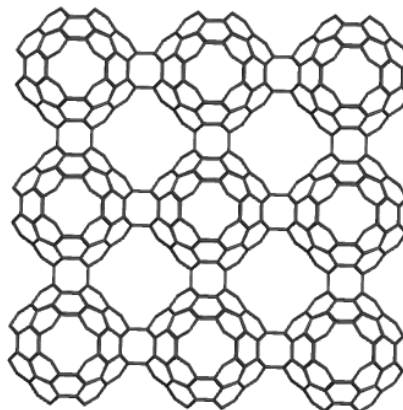
3,3,3,3-c net with stoichiometry (3-c)13; 4-nodal net

VS [6.8.8] [6.6.8] [6.6.6] [6.6.6]

New topology



c3hexcell C3Hex_333
Diudea,s name diu4



C3Hex_333
C3Hex

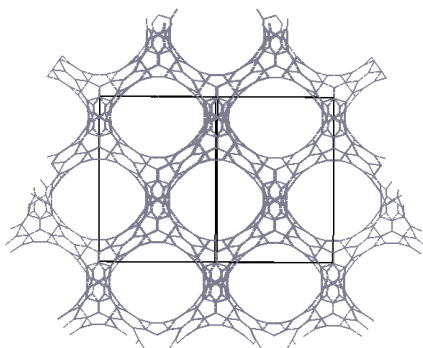
5. NEW diu5= T3HextwDia chiral net derived as decoration of dia net (Tetrahedron, hexagon triple, twisted)

Point symbol for net: $\{6.8^2\}3\{6^2.8\}6\{6^3\}$

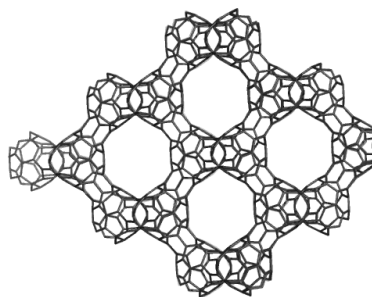
3,3,3,3-c net with stoichiometry (3-c)10; 4-nodal net

VS [6.8.8] [6.6.6] [6.8.8] [6.6.8]

New topology



t3cell
Diudea,s name diu5



T3HextwDia_222_1760
T3HextwDia

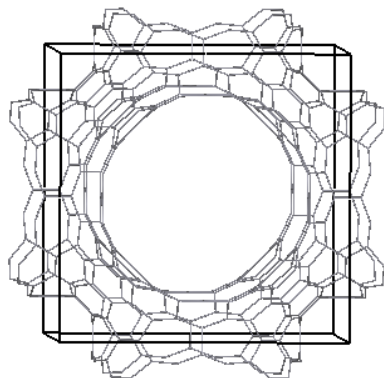
6. NEW (Cube,Coronene) diu6=CCor216

Point symbol for net: $(6.7^2)(6^2.7)5(6^3)2$

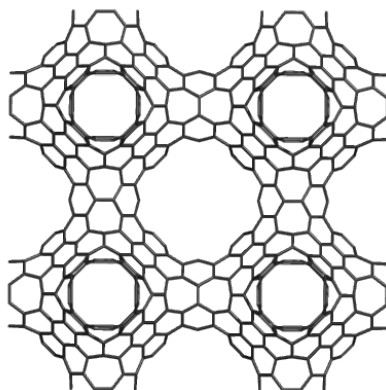
3,3,3,3-c net with stoichiometry (3-c)8; 5-nodal net

VS [6.6.7] [6.6.7] [6.6.6] [6.7.7]

New topology



corcell Cor_268_111_2x2x2
Diudea,s name diu6



Cor_268_111_2x2x2
CCor216

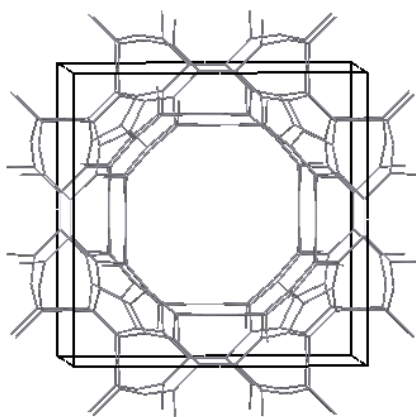
7. NEW diu7=MoZOp

Point symbol for net: $(5.8^2)6(5^2.8)3(5^3)(8^3)3$

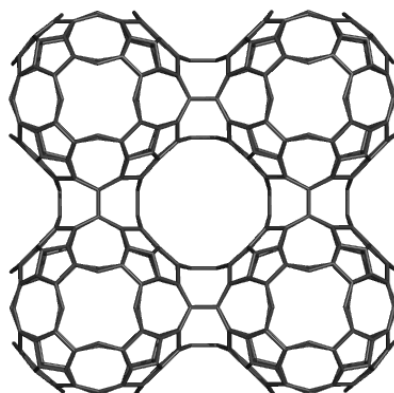
3,3,3,3-c net with stoichiometry (3-c)13; 4-nodal net

VS [5.5.8] [5.8.8] [5.5.5] [8.8.8]

New topology



m_opcell2 M_Op_222_ICIF
Diudea,s name diu7



M_Op_222_ICIF
MoZOp

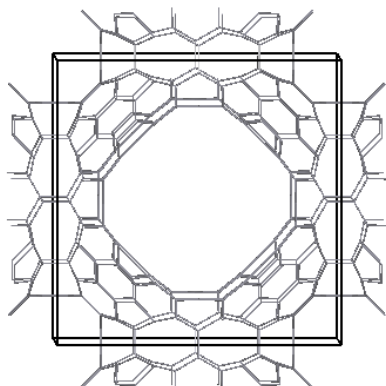
8. NEW (Octahedron, Septupling 2, Leapfrog, normal) diu9=OS2LeN168

Point symbol for net: $(5.6.8)2(5.6^2)2(5.8^2)(6.8^2)(6^2.8)2$

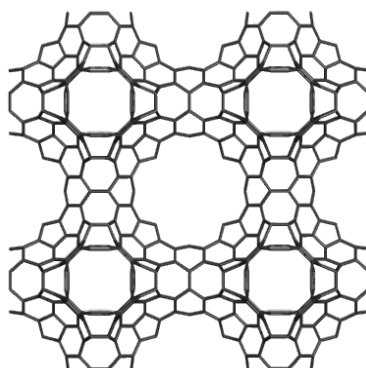
3,3,3,3-c net with stoichiometry (3-c)8; 5-nodal net

VS [6.6.8] [6.8.8] [5.6.8] [5.8.8] [5.6.6]

New topology



168Ocell 168Oct_S2_Le_N_2x2x2CCC
Diudea,s name diu9



168Oct_S2_Le_N_2x2x2CCC
OS2LeN168

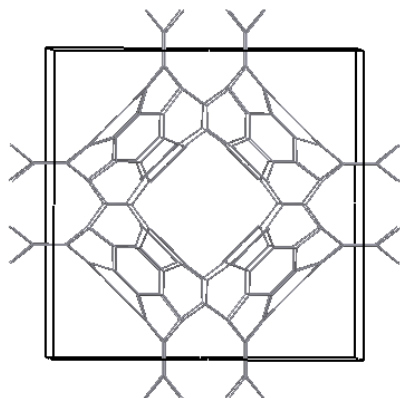
9. NEW (Octahedron, Septupling 2, Leapfrog, Cut edges X) diu10=OS2LeX168

Point symbol for net: $(5.10^2)(5.6.9)2(5.6^2)2(6^2.10)$

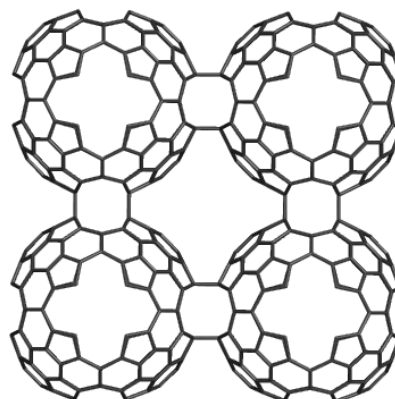
3,3,3,3-c net with stoichiometry (3-c)6; 4-nodal net

VS [5.6.10] [6.6.10] [5.10.10] [5.6.6]

New topology



168cell 168Oct_S2_Le_X_222g
Diudea,s name diu10



168Oct_S2_Le_X_222g
OS2LeX168

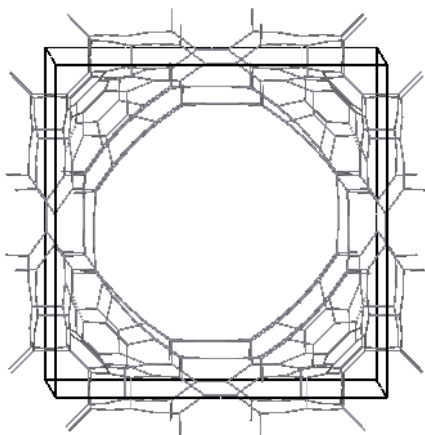
10. NEW (Octahedron, Septupling 2, Leapfrog, Zigzag) diu11=OS2LeZ168

Point symbol for net: $(5.6.7)_2(5.6^2)_2(5.7^2)(6.7.8)_2(7.8^2)$

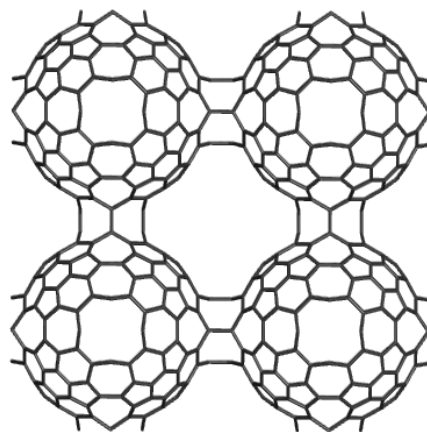
3,3,3,3,3-c net with stoichiometry (3-c)8; 5-nodal net

VS [5.6.7] [7.8.8] [5.7.7] [5.6.6] [6.7.8]

New topology



168octcell 168Oct_S2_Le_Z_222
Diudea,s name diu11



168Oct_S2_Le_Z_222
OS2LeZ168

OMEGA AND SADHANA POLYNOMIALS OF TWO CLASSES OF MOLECULAR GRAPHS

LUBANG WANG^a AND MINGJUN HU^b

ABSTRACT. The *Omega polynomial* of a connected graph G , denoted by $\Omega(G; x)$, is defined as $\Omega(G; x) = \sum_c m(G; c)x^c$ and the *Sadhana polynomial* of G is defined as $Sd(G; x) = \sum_c m(G; c)x^{|E(G)|-c}$, where $m(G; c)$ is the number of strips of length c and $|E(G)|$ is the number of edges in G . In this paper, we obtain explicit computing formulas for Omega and Sadhana polynomials of bridge graphs and chain graphs. As applications, Omega and Sadhana polynomials of some spiro-chains composed of four-member or six-member rings are deduced.

Keywords: *Quasi-orthogonal cut; Omega polynomial, Sadhana polynomial, bridge graph; chain graph*

INTRODUCTION

Let G denote a graph with vertex set $V(G)$ and edge set $E(G)$. The distance between two vertices x and y in $V(G)$, denoted by $d(x, y)$, is equal to the length of the shortest path connecting x and y . Two edges $e=uv$ and $f=xy$ in $E(G)$ are said to be *codistant*, denoted by $e \text{ co } f$, if $d(x, u) = d(y, v)$ and $d(x, v) = d(y, u) = d(x, u) + 1 = d(y, v) + 1$. The relation "co" is reflexive, symmetric, but not necessarily transitive. Let $C(e) = \{f \in E(G) : f \text{ co } e\}$. If the relation "co" is transitive on $C(e)$, then $C(e)$ is called an *orthogonal cut* "co" of the graph G .

Let $e=uv$ and $f=xy$ be two edges of a graph G , which are *opposite* or *topological parallel*, and this relation is denoted by $e \text{ op } f$. A set of opposite edges, within the same face or ring, eventually forming a strip of adjacent

^a School of Modern Logistics, Zhejiang Wanli University, Ningbo, Zhejiang 315100, P.R. China, lub_wang@163.com

^b Department of Mathematics and Physics, Anhui Jianzhu University, Hefei, Anhui 230601, P.R. China, mjhu_123@126.com

faces/rings, is called an *opposite edge strip ops*, which is a quasi-ortogonal cut *qoc* (i.e., the transitivity relation is not necessarily obeyed). Note that the „co” relation is defined in the whole graph while the relation „op” is defined only in a face/ring. We will always assume that the length of *ops* is maximal irrespective of the starting edge.

Let $m(G; c)$ be the number of *ops* strips of length c . The Omega polynomial of a connected graph G , denoted by $\Omega(G; x)$, is then defined as [1, 2]: $\Omega(G; x) = \sum_c m(G; c)x^c$ and the Sadhana polynomial of G is defined as [3]: $Sd(G; x) = \sum_c m(G; c)x^{|E(G)|-c}$, where $|E(G)|$ is the number of edges in

G . For recent results concerning the above two computing polynomials, the reader is referred to [4-11] and the references cited therein.

In this paper, we obtain Omega and Sadhana polynomials for the bridge graphs and chain graphs. As applications, Omega and Sadhana polynomials of some spiro-chains composed of four-member or six-member rings are obtained.

RESULTS AND DISCUSSION

In this section, we shall compute the Omega and Sadhana polynomials for the bridge graphs and chain graphs ([see, 12,13]). Let G_1, G_2, \dots, G_d be a set of finite pairwise disjoint graphs with $v_i \in V(G_i)$. The *bridge graph* $G = B(G_1, G_2, \dots, G_d; v_1, v_2, \dots, v_d)$ is obtained by connecting the vertices v_i and v_{i+1} by an edge for each $i=1, 2, \dots, d-1$, see Figure. 1.

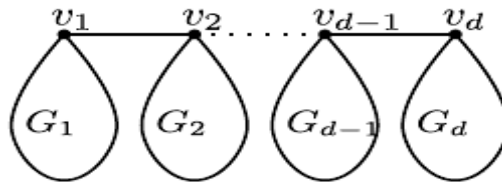


Figure1. The bridge graph $G = B(G_1, G_2, \dots, G_d; v_1, v_2, \dots, v_d)$.

The following theorem give the formulas for Omega and Sadhana polynomials of the bridge graphs.

Theorem 1. Let $G = B(G_1, G_2, \dots, G_d; v_1, v_2, \dots, v_d)$ be the bridge graph with m edges, as shown in Figure1. Suppose that each G_i has m_i edges. Then

$$\begin{aligned} \Omega(G; x) &= \sum_c m(G; c)x^c \\ &= \Omega(G_1; x) + \dots + \Omega(G_d; x) + (d - 1)x \end{aligned}$$

and

$$\begin{aligned} Sd(G; x) &= \sum_c m(G; c)x^{|E(G)|-c} \\ &= x^{m-m_1}Sd(G_1; x) + x^{m-m_2}Sd(G_2; x) + \dots + \\ &\quad x^{m-m_d}Sd(G_d; x) + (d - 1)x^{m-1}. \end{aligned}$$

Proof. Suppose that S_c is a strip of length c in G . If $c \geq 2$, then S_c lies entirely within some $G_i (1 \leq i \leq d)$. Suppose to the contrary that there are two edges e and f in S_c satisfying that e belongs to some given G_i , but f does not belong to G_i . But then two edges e and f can not be topological parallel to each other, a contradiction. That is, S_c lies entirely within some $G_i (1 \leq i \leq d)$. By the same reasoning, we know that there exists no other edges can be added into this strip such that we can get a new strip of length greater than c . By these arguments, we claim that the number of strips in G of length $c \geq 2$ does not change. So we have

$$\begin{aligned} \Omega(G; x) &= \sum_c m(G; c)x^c \\ &= \Omega(G_1; x) + \dots + \Omega(G_d; x) + (d - 1)x. \end{aligned}$$

Note that for each strip S_c of length c in some G_i , we have $m(G; c) = m(G_i; c)$ (not including the case of $c = 1$) and $x^{|E(G)|-c} = x^{m-m_i}x^{m_i-c}$. Thus,

$$\begin{aligned} Sd(G; x) &= \sum_c m(G; c)x^{|E(G)|-c} \\ &= x^{m-m_1}Sd(G_1; x) + x^{m-m_2}Sd(G_2; x) + \dots + \\ &\quad x^{m-m_d}Sd(G_d; x) + (d - 1)x^{m-1}. \end{aligned}$$

This completes the proof.

If we let $G_i = H$ and $v_i = v$ for each $i=1,2,\dots,d$ in above theorem, we immediately have the following result. In this case, for each $i=1,2,\dots,d$, $m_i = \frac{m-d+1}{d}$.

Corollary 1. Let $G = B(H, H, \dots, H; v, v, \dots, v)$ (d times) be the bridge graph with m edges, as shown in Figure 1. Then

$$\begin{aligned} \Omega(G; x) &= \sum_c m(G; c) x^c \\ &= d\Omega(H; x) + (d-1)x \end{aligned}$$

and

$$\begin{aligned} Sd(G; x) &= \sum_c m(G; c) x^{|E(G)|-c} \\ &= x^{m-\frac{m-d+1}{d}} [d \cdot Sd(H; x)] + (d-1)x^{m-1} \\ &= d \cdot x^{\frac{(m+1)(d-1)}{d}} Sd(H; x) + (d-1)x^{m-1}. \end{aligned}$$

Now, we consider some examples of bridge graphs.



Figure 2. The graph $B_{d,3}$.

Example 1. Consider the bridge graph $B_{d,3} = (P_3, P_3, \dots, P_3; v, v, \dots, v)$ (d times), where P_3 is the 3-vertex path with the middle vertex being v , see Figure 2. Note that $\Omega(P_3; x) = 2x$ and $Sd(P_3; x) = 2x$. Then by Corollary 1, we obtain $\Omega(B_{d,3}; x) = d \cdot (2x) + (d-1)x = (3d-1)x$ and

$$Sd(B_{d,3}; x) = x^{3(d-1)} \cdot d \cdot (2x) + (d-1)x^{3d-2} = (3d-1)x^{3d-2}.$$

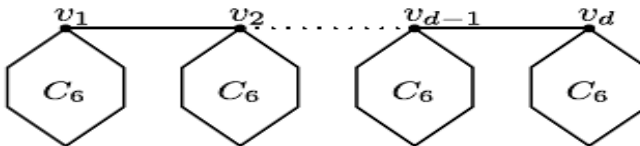


Figure 3. The bridge graph of the hexagon C_6 .

Example 2. Consider the bridge graph $G = B(C_6, C_6, \dots, C_6)$ (d times), see Figure 3. Note that $\Omega(C_6; x) = 3x^2$ and $Sd(C_6; x) = 3x^4$. Then by Corollary 1, we obtain $\Omega(B(C_6, C_6, \dots, C_6; v_1, v_2, \dots, v_d); x) = 3dx^2 + (d-1)x$ and $Sd(B(C_6, C_6, \dots, C_6; v_1, v_2, \dots, v_d); x) = x^{7(d-1)} \cdot 3dx^4 + (d-1)x^{7d-2} = 3dx^{7d-3} + (d-1)x^{7d-2}$.

Let G_1, G_2, \dots, G_d be a set of finite pairwise disjoint graphs with $v_i, w_i \in V(G_i)$. The *chain graph* $C(G_1, G_2, \dots, G_d; v_1, w_1, v_2, w_2, \dots, v_d, w_d)$ is obtained by identifying the vertex w_i and the vertex v_{i+1} for each $i=1, 2, \dots, d-1$, see Figure 4.

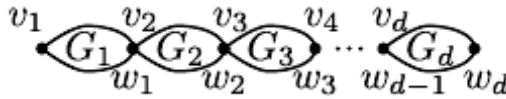


Figure 4. The chain graph $C(G_1, G_2, \dots, G_d; v_1, w_1, v_2, w_2, \dots, v_d, w_d)$.

Theorem 2. Let $G = C(G_1, G_2, \dots, G_d; v_1, w_1, v_2, w_2, \dots, v_d, w_d)$ be the chain graph with m edges, as shown in Figure 2. Suppose that each G_i has m_i edges. Then

$$\begin{aligned} \Omega(G; x) &= \sum_c m(G; c)x^c \\ &= \Omega(G_1; x) + \dots + \Omega(G_d; x) \end{aligned}$$

and

$$\begin{aligned} Sd(G; x) &= \sum_c m(G; c)x^{|E(G)|-c} \\ &= x^{m-m_1}Sd(G_1; x) + x^{m-m_2}Sd(G_2; x) + \dots + \\ &\quad x^{m-m_d}Sd(G_d; x). \end{aligned}$$

Proof. Suppose that S_c is a strip of length c in G . If $c \geq 2$, then S_c lies entirely within some $G_i (1 \leq i \leq d)$. Also, there is no other edges can be added into this strip such that we can get a new strip of length greater than c . By these arguments, we thus have

$$\begin{aligned}\Omega(G; x) &= \sum_c m(G; c)x^c \\ &= \Omega(G_1; x) + \dots + \Omega(G_d; x)\end{aligned}$$

and

$$\begin{aligned}Sd(G; x) &= \sum_c m(G; c)x^{|E(G)|-c} \\ &= x^{m-m_1}Sd(G_1; x) + x^{m-m_2}Sd(G_2; x) + \dots + \\ &\quad x^{m-m_d}Sd(G_d; x).\end{aligned}$$

This completes the proof.

If we set $G_i = H$ and $v_i = v$ for each $i=1,2,\dots,d$ in Theorem 2, we immediately have the following result.

Corollary 2. *Let $G = C(H, H, \dots, H; v, v, \dots, v)$ (d times) be the chain graph. Then*

$$\begin{aligned}\Omega(G; x) &= \sum_c m(G; c)x^c \\ &= d\Omega(H; x)\end{aligned}$$

and

$$\begin{aligned}Sd(G; x) &= \sum_c m(G; c)x^{|E(G)|-c} \\ &= dx^{m-\frac{m}{d}}Sd(H; x) \\ &= dx^{\frac{(d-1)m}{d}}Sd(H; x).\end{aligned}$$

Now, we consider some examples of chain graphs as shown in Figures 5-7.

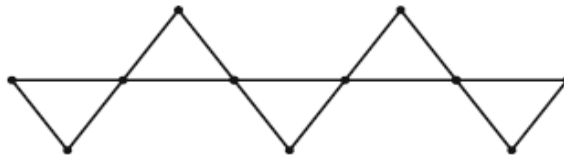


Figure 5. The spiro-chain graph of C_3 with $d=5$.

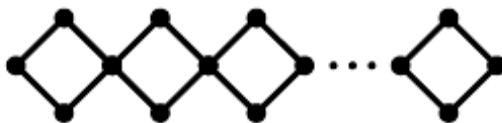


Figure 6. The spiro-chain graph $C_4(1,3)$.



Figure 7. The spiro-chain graph $C_6(1,4)$ with $d=4$.

Example 3. Consider the spiro-chain graph as shown in Figure 5. Note that $\Omega(C_3; x) = 3x$ and $Sd(C_3; x) = 3x^2$. Then by Corollary 2, we obtain $\Omega(G; x) = 15x$ and $Sd(B(C_6, C_6, \dots, C_6); x) = 15x^{14}$.

Example 4. Consider the spiro-chain graph as shown in Figure 6. Note that $\Omega(C_4; x) = 2x^2$ and $Sd(C_4; x) = 2x^2$. Then by Corollary 2, we obtain $\Omega(G; x) = 2dx^2$ and $Sd(G; x) = 2dx^{4d-2}$.

Example 5. Consider the spiro-chain graph as shown in Figure 7. Note that $\Omega(C_6; x) = 3x^2$ and $Sd(C_3; x) = 3x^4$. Then by Corollary 2, we obtain $\Omega(G; x) = 12x^2$ and $Sd(G; x) = 12dx^{22}$.

CONCLUSIONS

In this paper, we obtained explicit computing formulas for Omega and Sadhana polynomials of bridge graphs and chain graphs. As applications, Omega and Sadhana polynomials of some spiro-chains composed of four-member or six-member rings are deduced. It may be interesting to investigate Omega and Sadhana polynomials for other molecular graphs and nanostructures.

ACKNOWLEDGMENTS

This work was partially supported by the keyproject of Zhejiang Province Philosophy Social (grant no. 11JDLG01YB), NSFC (grant no. 71071145) and NSF of Guangxi Province (grant no. 2013GXNSFBA019022).

REFERENCES

- [1] M.V. Diudea, *Carpath. J. Math.*, **2006**, 22, 43.
- [2] P.E. John, A.E. Vizitiu, S. Cigher, M.V. Diudea, *MATCH Commun. Math. Comput. Chem.*, **2007**, 57, 479.
- [3] P.V. Khadikar, S. Joshi, A.V. Bajaj, D. Mandloi, *Bioorg. Med.Chem. Lett.*, **2004**, 14, 1187.
- [4] A.R. Ashrafi, M. Ghorbani, M. Jalali, *Ind. J. Chem.*, **2008**, 47, 535.
- [5] M.V. Diudea, B. Parv, E. C.Kirby, *MATCH Commun. Math. Comput. Chem.*, **2003**, 47, 53.
- [6] M. Ghorbani, M. Jalali, *Digest Journal of Nanomaterials and Biostructures*, **2010**, 5, 843.
- [7] M. Ghorbani, *Optoelectronics and Advanced Materials, Rapid Communications*, **2010**, 4, 540.
- [8] M. Jalali, M. Ghorbani, *Studia UBB Chemia*, **2009**, 1, 25.
- [9] M.V. Diudea, *Iranian. J. Math. Chem.*, **2010**, 1, 69.
- [10] M. Ghorbani, *Iranian. J. Math. Chem.*, **2010**, 1, 105.
- [11] L. Yang, H. Hua, M. Wang, *Digest Journal of Nanomaterials and Biostructures*, **2011**, 6, 717.
- [12] T. Mansour, M. Schork, *Discrete Appl. Math.*, **2009**, 157, 1600.
- [13] T. Mansour, M. Schork, *J. Math. Chem.*, **2010**, 47, 72.
- [14] R. Xing, B. Zhou, *C. R. Acad. Sci. Paris, Ser. I*, **2011**, 349, 489.

EFFICIENT DEGRADATION OF PHENOL WITH *PSEUDOMONAS PUTIDA* CELLS FOR THE PRODUCTION OF PURE WATER

DOINA A. TODEA^a, SZENDE TONK^b, ANCUȚA E. TIUC^c,
ANAMARIA TÖRÖK^d, CARMEN MÂNZATU^d,
GABRIEL KATONA^d, CORNELIA MAJDIK^{*d}

ABSTRACT. An efficient procedure of phenolic wastewater purification with immobilized *Pseudomonas putida* cells is presented. The selection of the proper microorganism is described. The influence of the initial phenol concentration upon the efficacy of the phenol remove using free and immobilized cells is discussed.

Keywords: *Pseudomonas putida*, phenol degradation, immobilized cells, alginate, wastewater treatment, human health

INTRODUCTION

The contamination of the environment with toxic chemical materials is considered one of the major problems of industrialisation in our days. The phenol, which is found in industrial- and wastewaters, is regarded by the National Environmental Protection Agency as a primary compound of contamination. Due to the highly toxic nature of this substance, removing it with the help of microorganisms is of critical importance. Various types of microorganisms, including bacteria, yeast, algae and fungi evolved metabolically for degrading different concentrations of phenol [1-3]. The versatility and adaptability of microorganisms in degrading phenols from wastewaters shows their technological usefulness to dephenolate soil and waters.

^a "Iuliu Hatieganu" University of Medicine and Pharmacy Cluj-Napoca, Str. B.P. Hasdeu Nr. 6., Cluj-Napoca; Ro-400371; Romania

^b Department of Environmental Sciences, Science and Art Faculty, Sapientia University, Str. Matei Corvin, Nr. 4. Ro-400112 Cluj-Napoca, Romania

^c Technical University of Cluj-Napoca, Bulevardul Muncii 103-105, Ro-400641, Cluj-Napoca, Romania

^d Babeş-Bolyai University, Faculty of Chemistry and Chemical Engineering, Str. Kogălniceanu, Nr. 1, RO-400084 Cluj-Napoca, Romania, majdik@chem.ubbcluj.ro

The process of the microbial degradation of phenol is a result of the combination of enzymatic and cellular activities, as well as the activities of cellular communities in microorganisms [4-6]. These activities depend on environmental factors, including the level of nutrients, the availability of alternative substrates, microbial population density, the concentration of contaminated substrates, and bioavailability.

Widespread use of toxic phenols has led to their accumulation in large quantities in the environment. This phenomenon calls for a scientific assessment of the impact of phenols on the environment and their influence on microorganisms, the development of analytical methods for a qualitative and quantitative evaluation, the study of processes of phenol degradation to find the most optimal methods for environmental remediation. Water pollution and implicitly the contamination of aquatic organisms with various types of organic pollutants such as phenols has stimulated research in developing technologies to depollute and especially degrade contaminants from natural and wastewaters.

Using microorganisms for dephenolating polluted waters is a simple and inexpensive method, almost as efficient as the enzymatic technology. By making use of the entire enzymatic equipment of the cells, we can reach complete degradation up to the formation of CO₂, H₂O, halogen ions (for halogenophenols) or non-toxic organic molecules, such as acetic acid in case of acetobacteria, or methane in case of methanogenic bacteria [7, 8].

One of the methods involving low costs in maintaining the bioremediation activity by prolonging the life of microorganisms without nutrient supplementation is based on the use of immobilized cells. In the process of immobilization, the biological stability of microorganisms increases when facing toxic compounds in nutrient-poor environments. By immobilization, cells increase their tolerance for organic environments and a number of chemical materials like phenols or halogenophenols [9-13]. Using immobilized cells has several advantages over against processes using cells not immobilized:

- retention of a larger quantity of microorganisms in the reactor;
- protection of cells from toxic substrates;
- separation of suspended biomass from wastewater effluents.

Cells can be immobilized in various materials, including alginates, agar, agarose, chitosan, activated carbon, polyacrylamide, polyurethane, cellulose, collagen and polymeric membranes. Using immobilized cells allows the realisation of continuous processes and an increasing productivity of industrial installations.

RESULTS AND DISCUSSIONS

Selecting the microorganism

A comparative study of phenol degradation was made with immobilized and free cells of *Pseudomonas putida*, *Acinetobacter sporulens* and *Rhodotula glutinis*, cultured with an initial concentration (0.176 g of dry biomass / flask) in both systems. In order to identify the optimal microorganism, a preliminary study was made only with free cells. The residual concentration of phenol in the water was determined after 24, 48, 72, 96 and 120 hours. The results obtained are presented in Figure 1.

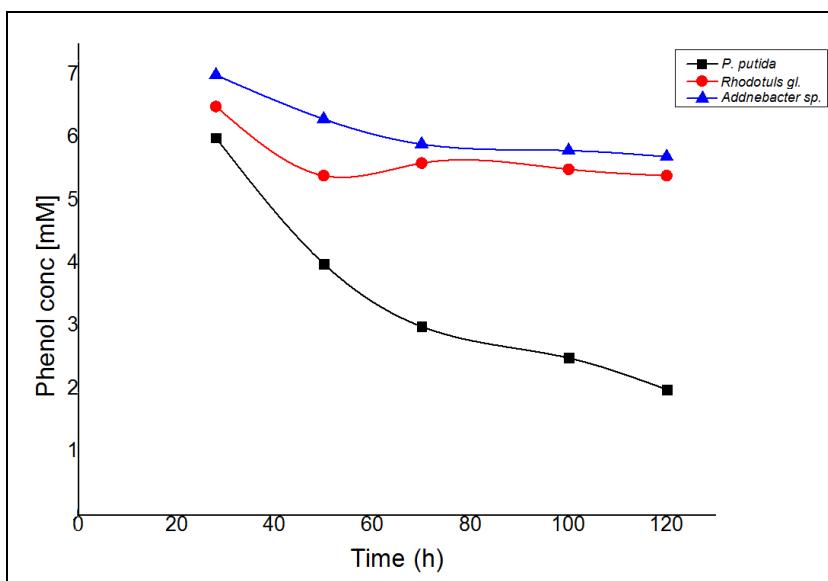


Figure 1. The study of phenol degradation with *Pseudomonas putida*, *Acinetobacter sporulens* and *Rhodotula glutinis* cells.

The influence of the initial concentration of the phenol solution

As it can be observed, maximal efficiency in phenol removal was obtained with the *Pseudomonas putida* culture. Therefore further experiments were made with cultured cells of *Pseudomonas putida* in both suspended and immobilized form in calcium alginate gel.

Simultaneously, in order to distinguish between phenol concentration decrease resulting from biodegradation and alginate adsorption respectively, an identical experiment was made with alginate beads without biomass, using the same recipe.

The experiments were made in Erlenmeyer flasks of 250 ml containing 40 mL of saline solution with different phenol concentrations (2, 6, 10, 16, 20, 26 and 30 mM). 10 g of biomass immobilized in alginate or non-immobilized biomass was put into the flasks and incubated at 30 °C for 120 hours. After complete mixture, samples were taken from the cultures at regular intervals (14, 24, 36, 48, 72 and 96 hours) in order to analyse the phenol and determine cellular density. In parallel, in other Erlenmeyer flasks control samples were incubated under the same conditions, but without inoculum to exclude phenol loss through evaporation.

The degradation capacity of phenol was studied and compared with the help of suspended and immobilized cells of *Pseudomonas putida* (Figures 2 and 3). The degree of phenol degradation and the time of degradation depends on the initial concentration of the phenol in the environment. An increase in the time of biodegradation was observed with the increase of the initial phenol concentration.

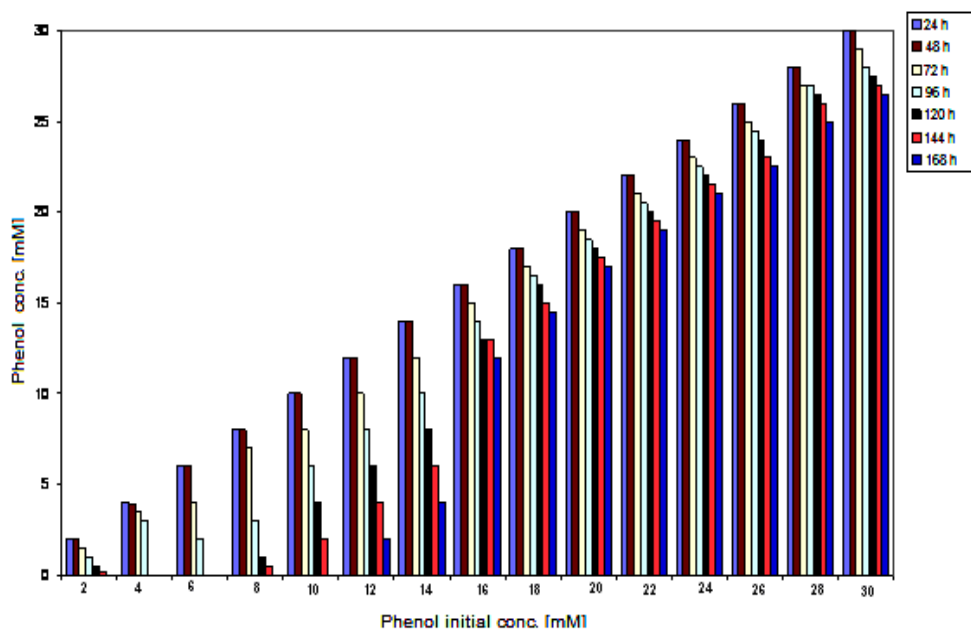


Figure 2. Phenol degradation in *Pseudomonas putida* suspension

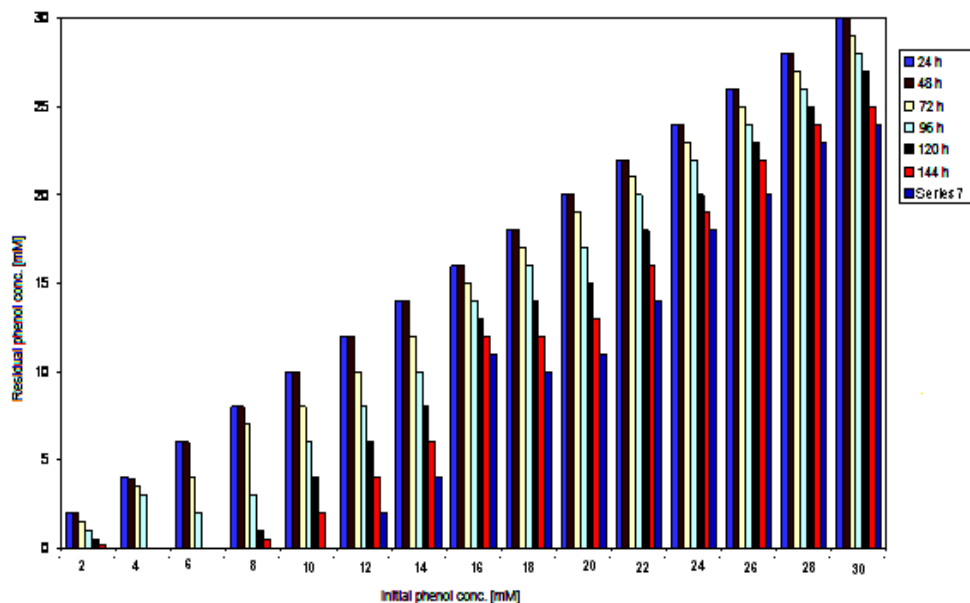


Figure 3. Phenol degradation with *Pseudomonas putida* cells immobilized in alginate

The phenol was completely removed in the experiments where the solution's initial phenol concentration was 16 mM using non-immobilized cells, and 18 mM using immobilized cells. For these initial phenol concentrations, more than 87% of the total phenol quantity was degraded in less than 72 hours.

For larger phenol concentrations, one can observe a decrease in the degree of phenol degradation and incomplete degradation in all experiments. This can probably be explained by the toxic effect of large concentrations of phenol upon the cells. Larger phenol concentrations presumably inhibit cell growth. In case of immobilized cells, the effect of this inhibition is smaller in comparison with its effect upon non-immobilized cells. In the control samples, no phenol degradation or decrease of phenol concentration was observable, which shows that no physical or chemical degradation had taken place. Concerning the alginate-sample without biomass, no significant decrease of phenol concentration was discernible.

The variations of the phenols volumetric degradation speed with initial concentrations between 2-30 mM for free and immobilized cells is presented in Figure 4.

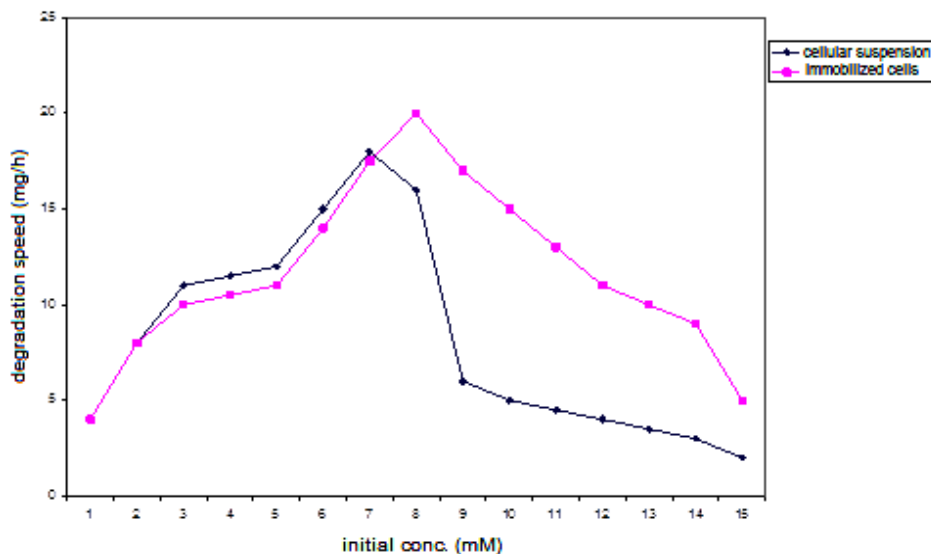


Figure 4. The phenol degradation velocity with *Pseudomonas putida* cells

As it is recognisable, with the increase of the phenols initial concentration, the phenols degradation speed also increases, reaching a maximum value of 20.45 mg/L*h (immobilized cells) and 18.35 mg/L*h (non-immobilized cells), with initial concentrations of 18 mM (immobilized cells) and 16 mM (non-immobilized cells). After this, the degradation speed decreases progressively. For initial concentrations smaller than 16 mM, the values of volumetric degradation speed show no variation between immobilized and non-immobilized cells (Figure 5). However, for initial concentrations of 20-28 mM, the specific degradation speed of immobilized cells was 2.8-3.5 times higher than in case of non-immobilized cells, while for an initial concentration of 30 mM, the specific degradation speed of immobilized cells was 1.7 times higher than in case of non-immobilized cells.

The microencapsulation mechanism using natural polysaccharides as encapsulating material presupposes polyelectrolyte complexation. Polyelectrolyte complexes form ionic interactions between two polyelectrolytes charged differently in aquatic solutions, which characterise a hydrophilic microenvironment with a large water content and electronic density. Hydrophilic polymers such as the alginate retain water. This hydrophilic capacity of the alginate can reduce the phenol-concentration around the alginate beads as a result of the partition effect.

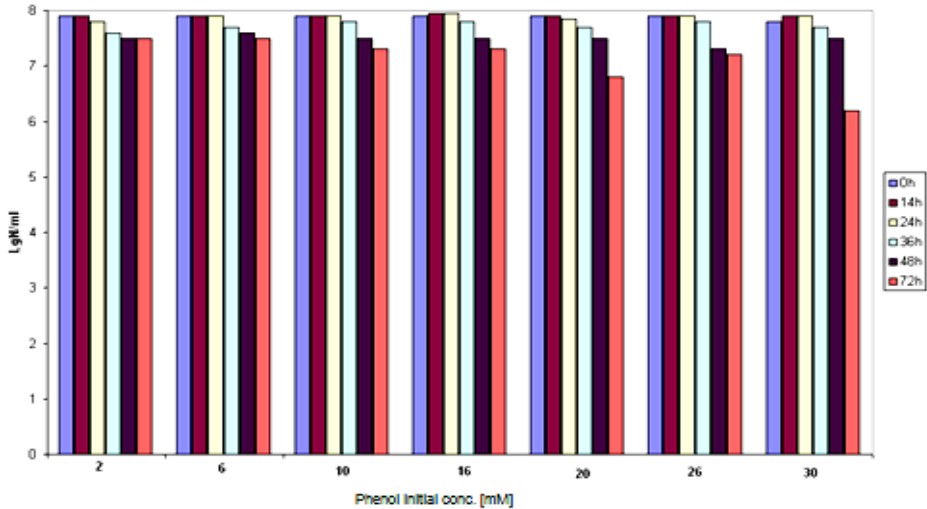


Figure 5. The viability of cellular suspension at different phenol concentrations

The viability in time of free and immobilized cells at different phenol-concentration levels is graphically presented in Figure 6. As it can be observed, enzymatic activity depends on the phenol-concentration and the used inoculum type (free or immobilized cells). The viability of free cells suspended in phenol-concentrations of 16 mM increases in the first 48 hours, followed by a decrease in time. For solutions with higher concentrations, cell activity is reduced even within the first 14 hours. The stability of immobilized cells increases in time even with higher phenol-concentrations suggesting that the process of enzyme release is continuous.

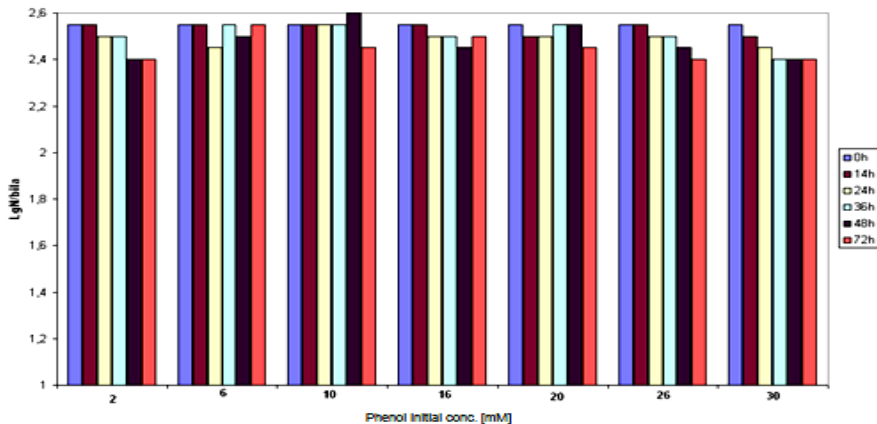


Figure 6. The viability of immobilized cells at different phenol-concentrations

CONCLUSIONS

It can be concluded that *Pseudomonas putida* proved to be the most efficient microorganism for the dephenolation of phenolic wastewaters. The initial phenol concentration is crucial upon the efficacy of the process. By immobilization the efficacy of the dephenolation process was increased.

EXPERIMENTAL SECTION

Materials

The microorganisms *Pseudomonas putida*, *Acinetobacter sporulens* and *Rhodotula glutinis* were obtained from Sigma Life Science Research. The phenol and the sodium alginate were acquired from Sigma-Aldrich.

Culture media

The microorganisms *Pseudomonas putida*, *Acinetobacter sporulens* and *Rhodotula glutinis* were cultivated on a minimal culture media containing (g/l) 3.4 K₂HPO₄, 4.3 KH₂PO₄, 0.3 MgCl₂·2H₂O, 1 (NH₄)₂SO₄, glucose, lactate, succinate and benzoate were added as carbon sources. The cultures were incubated at 30 °C for 120 hours.

Inoculation

Colonies grown for 72 hours on agar plates with minimal culture media were inoculated in Erlenmeyer flasks containing 500 mL of the same media, and were grown for 48 hours in an incubator at 30 °C. Afterwards, cells were separated by centrifugation (at 1500 rpm) at 5 °C for 10 minutes and washed with sterilised water to eliminate small residues and intermediary components. The residue was suspended in a small volume of sterilised distilled water. Samples from this suspension were used as inoculum for the experiments of phenol degradation with both immobilized and non-immobilized cells.

Immobilization in alginate gel

2 g of sodium alginate was dissolved in 80 mL of distilled water in order to obtain a polymeric alginate solution. After sterilising the alginate (for 15 minutes at 120 °C), 20 mL of cellular suspension was added and homogenised by stirring. The mixture of cells and sodium alginate was put into a syringe. The solution of alginate and yeast was added slowly from a distance of 20 cm to a vessel containing 100 mL solution of 1M CaCl₂. Beads of various diameters were formed, depending on the diameter of the needle and the applied pressure. The beads were preserved in CaCl₂ for 0.5-3 hours. Subsequently they were decanted and washed several times with distilled water.

Analytic methods

Phenol concentration was determined with spectrophotometer at 270 nm. For each phenol concentration used, the degradation speed corresponding to the degraded phenol quantity (gl^{-1}) was calculated after 24 hours. The maximal volumetric degradation speed corresponds to the highest value obtained for each phenol concentration. All experiments and determinations were carried out three times, reporting the medium of the obtained measurements.

REFERENCES

- [1] V.V. Vel'kov, *Biotekhnologiya*, **1995**, 3–4:20.
- [2] F.M. Khabibulina, A.A. Shubakov, I.B. Archegova, G.G. Romanov. *Biotekhnologiya*, **2002**, 6:57.
- [3] Anokhina, T.O., Kochetkov, V.V., Zelenkova, N.F., Balakshina, V.V., Boronin, A.M. *Prikladnaia Biokhimiia Mikrobiolgiya*, **2004**, 40:654.
- [4] F. Bux, B. Akkinson, K. Kasan. *Water Science Technology*, **1999**, 39:127.
- [5] A. Zumriye, A. Derya, R. Elif. *Process Biochemistry*, **1999**, 35:301.
- [6] A, Fialova', E. Boschke, T. Bley. *Biodegradation*, **2007**, 18:719.
- [7] A.R. Bielefeldt, H.D. Stensel. *Biodegradation*, **1999**, 10:1.
- [8] V. Kavitha, K. Palanivelu. *Chemosphere* **2004**, 55:1235.
- [9] S.H. Yuan, X.H. Lu. *Journal of Hazardous Materials*, **2005**, 118:85.
- [10] Z. Ai, P. Yang, X.H. Lu. *Journal of Hazardous Materials*, **2005**, 124:147.
- [11] Z. Aleksieva, D. Ivanova, T. Godjevargova. *Process Biochemistry*, **2007**, 37:1215.
- [12] Y.J. Liu, A.N. Zhang, X.C. Wang, *Biochemical Engineering Journal*, **2009**, 44:187.
- [13] A. Banerjee, A.K. Ghoshal, *International Biodeterioration & Biodegradation*, **2011**, 65:1052.

CONTINUOUS FLOW WASTE WATER PURIFICATION WITH IMMOBILIZED CELLS

DOINA A. TODEA^a, SZENDE TONK^b, ANCUȚA E. TIUC^c,
ANAMARIA TÖRÖK^d, CARMEN MÂNZATU^d,
GABRIEL KATONA^d, CORNELIA MAJDIK^{*d}

ABSTRACT. An efficient procedure using a fixed bed column reactor for phenolic wastewater purification with immobilized *Pseudomonas putida* cells is presented. The influence of several parameters like, temperature, pH and the size of the immobilized cell particles upon the efficacy of the phenol remove is discussed.

Keywords: *Pseudomonas putida*, optimal phenol degradation, immobilized cells, optimal temperature and pH, fixed bed column reactor

INTRODUCTION

One of the methods involving low costs in maintaining the bioremediation activity by prolonging the life of microorganisms without nutrient supplementation is based on the use of immobilized cells. In the process of immobilization, the biological stability of microorganisms increases when facing toxic compounds in nutrient-poor environments. By immobilization, cells increase their tolerance for organic environments and a number of chemical materials like phenols or halogenophenols[1-3]. Using immobilized cells has several advantages over against processes using cells not immobilized:

- retention of a larger quantity of microorganisms in the reactor;
- protection of cells from toxic substrates;
- separation of suspended biomass from wastewater effluents.

^a "Iuliu Hatieganu" University of Medicine and Pharmacy Cluj-Napoca, Str. B.P. Hasdeu Nr. 6, Cluj-Napoca; Ro-400371; Romania

^b Department of Environmental Sciences, Science and Art Faculty, Sapientia University, Str. Matei Corvin, Nr. 4, Ro-400112 Cluj-Napoca, Romania

^c Technical University of Cluj-Napoca, Bulevardul Muncii 103-105, Ro-400641, Cluj-Napoca, Romania

^d Babeş-Bolyai University, Faculty of Chemistry and Chemical Engineering, Str. M. Kogălniceanu Nr. 1, RO-400084 Cluj-Napoca, Romania, majdik@chem.ubbcluj.ro

Cells can be immobilized in various materials, including alginates, agar, agarose, chitosan, activated carbon, polyacrylamide, polyurethane, cellulose, collagen and polymeric membranes. Using immobilized cells allows the realisation of continuous processes and an increasing productivity of industrial installations [4-6].

There is a relatively wide range of industrial bioreactors in which reactions are carried out with immobilized biocatalysts like stirred-tank reactors, continuously operated stirred-tank reactors, fixed bed reactors, fluidised bed reactors and membrane reactors.

In the industrial application of the process of phenol degradation, the immobilization of the biocatalyst is the most advantageous method. Immobilising biomass in solid structures makes it possible to retain a material with the necessary characteristics depending on the type of equipment used in the technological procedure [7-9]. These solid structures, with the necessary dimensions and mechanic resistance, are rigid and porous enough to be used in conventional unit operations. Another advantage of using immobilized cells is that they allow the regeneration of the biocatalyst, confirming once again that the adopted method allows the elaboration of an optimal technological procedure.

RESULTS AND DISCUSSIONS

The objective of the current study was to investigate the capacity of *Pseudomonas putida*, cells, immobilized in alginate gel, in the biodegradation of the phenol, in a continuously operating system. The effects of several key parameters that can influence the biodegradation process were also studied: temperature, the pH-value of the solution, as well as the dimension of the alginate beads. Phenol degradation tests were made using both immobilized and non-immobilized cells for a comparative study.

The influence of temperature

Knowing that both the process of the phenols metabolism by the microorganism and the process of cellular growth is highly influenced by the temperature, one has to determine the optimal value of this parameter. The experiment was made in suspension, as well as with immobilized cells in a vessel with magnetic stirring (at low speed of 150 rpm to avoid the mechanic degradation of the cells or the alginate beads), thermostated at temperatures in the range of 25-50 °C. The initial phenol concentration was 8 mM in all cases. The efficiency of the process was assessed by determining the residual phenol concentrations after 24 hours. It can be noticed that dephenolation reaches the maximum degree at 37 °C both in cellular suspension and with cells immobilized in alginate gel. At temperatures higher than 40 °C, the decrease of phenol concentration is almost insignificant, which is a sign that cells are less viable at such temperature levels (Figure 1).

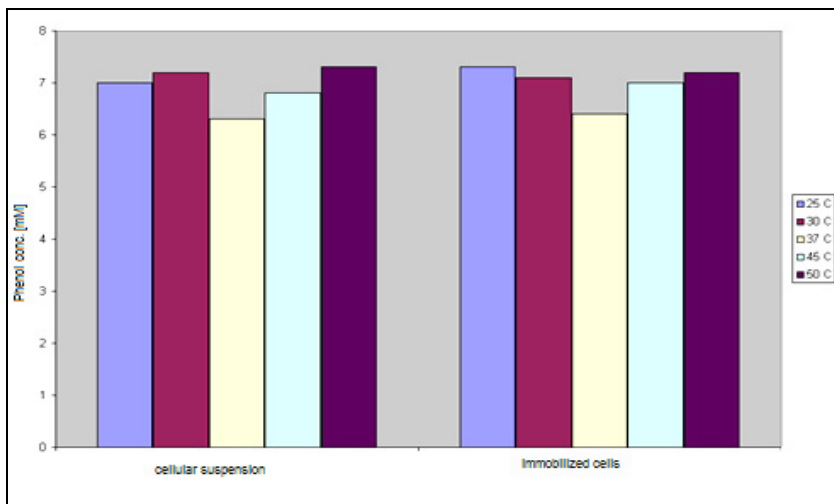


Figure 1. The influence of temperature on phenol degradation

Influence of pH

The influence of pH was studied in five series of experiments, with *Pseudimonas putida* cells in suspension (free form) with pH-values between 4 and 8. In order to reach the required parameters, phosphate buffers were used in preparing the culture environment. After adding all nutritive components to the environment, pH values were corrected as applicable with diluted solutions of either NaOH or HCl. Phenol concentration was determined by spectrophotometric method after 24 and 48 hours. The results are presented in Figure 2.

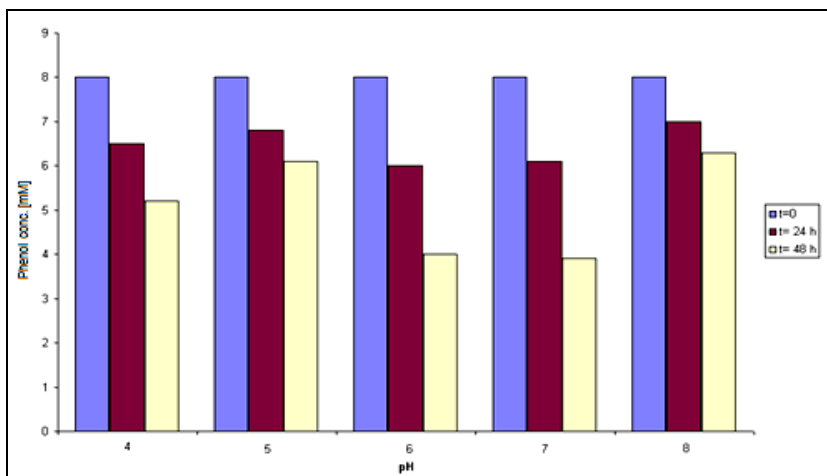


Figure 2. The influence of pH on phenol degradation

As it can be observed, at pH values of 6 and 7 one reaches a maximum decrease of concentration after the first day (ca. 24%), and after two days phenol concentration decreased to about 50%. At more acidic or basic values of the pH, the concentration decrease in the solution was lower.

The influence of the dimension of the alginate beads

As in all processes taking place in a heterogeneous system, this process is strongly influenced by mass transfer. When immobilising the cells in alginate gel, the dimension of the alginate beads determines the size of the surface of contact between the biocatalyst and the phenol, which influences significantly the efficiency of the degradation process. The alginate beads of different dimensions can be prepared with syringe needles of different diameters. The prepared beads were then sorted and used in the dephenolation experiments.

It can be observed that the efficiency was low at diameters of 5 mm and below, as well as for beads of 7 mm and above. Small alginate volumes possibly include insignificant quantities of biocatalyst even while contact surface is at maximum value. In case of beads of large dimensions, mass transfer processes are limited by the reduced contact surface size as shown in Figure 3.

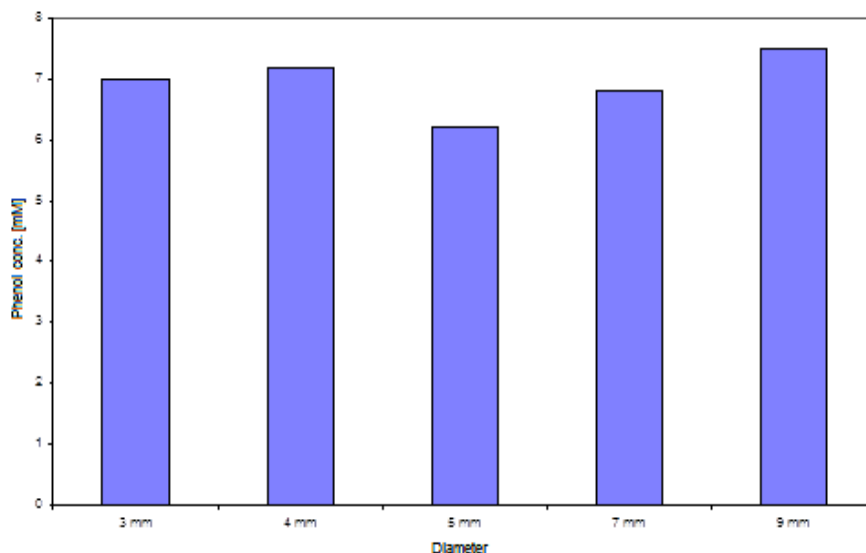


Figure 3. The influence of the diameters of the alginate beads on phenol degradation

Continuously operated fixed bed reactor for phenol degradation

Based on these experiments aiming to determine the optimal conditions under which phenol degradation takes place in wastewaters, a continuously operated fixed bed reactor was constructed for the degradation process of the phenol in presence of immobilized *Pseudomonas putida* cells in alginate gel in a packed column reactor.

The equipment was relatively simply constructed from a column in which the immobilized biocatalyst is introduced and a peristaltic pump was used to recirculate a certain volume of the phenolic solution.

Experiments with the installation for optimisation

The column reactor was continuously supplied with phenol solution with 18 mM concentration. Depending on the flow rate used, a certain degree of microbial dephenolation of the water was reached (Figure 4). At a flow rate of 0.2 mL/s, phenol concentration decreases with ca. 50%. If a further reduction of concentration level needs to be attained, the effluent is recirculated into the column. In practice, by recirculating the phenolic solution three times through the biocatalyst, the concentration of the phenol falls below the maximum level admitted by current regulations. Due to the long duration of the process and implicitly the low productivity of the proposed equipment, a flow rate below 0.2 mL/s is disadvantageous from an economic point of view. On the other hand, at higher flow rates, the higher energy consumption of the pump increases significantly the costs of operation of the installation.

CONCLUSIONS

The optimal pH, temperature and immobilized particle size for the efficient phenol remove was set up. The continuous flow procedure was superior in the phenol degradation process.

EXPERIMENTAL SECTION

Materials

- 100 g of immobilized cells
- 350 mL phenol solution, with an initial phenol concentration of 18 mM (the used peristaltic pump has a flow rate of 0.2 mL/s).

After putting the equipment into operation, solution samples were taken and their concentration established to illustrate the evolution in time of the biosorption process.

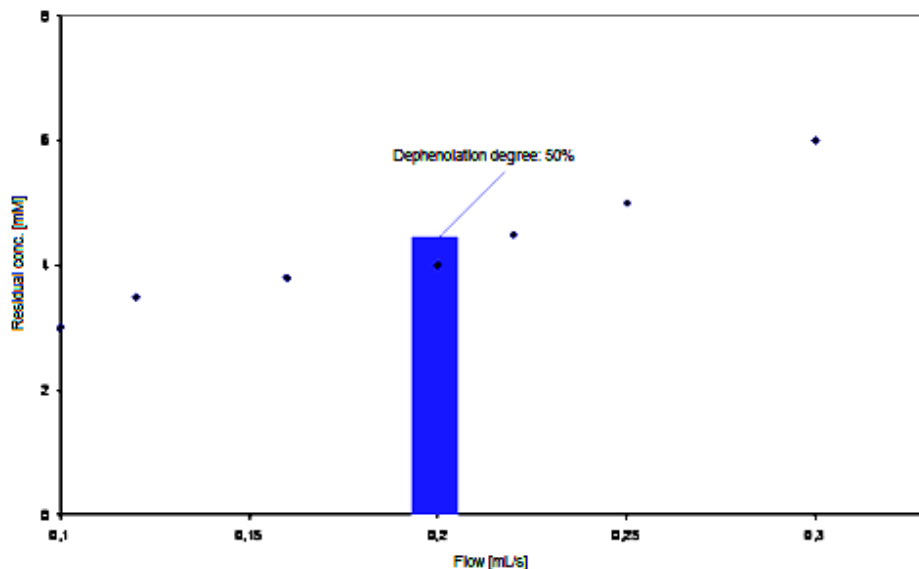


Figure 4. The influence of flow rate on the dephenolation degree

Culture media

The microorganism *Pseudomonas putida*, was cultivated on a minimal culture media containing (g/l) 3.4 K_2HPO_4 , 4.3 KH_2PO_4 , 0.3 $MgCl_2 \cdot 2H_2O$, 1 $(NH_4)_2SO_4$, glucose, lactate, succinate and benzoate were added as carbon sources. The cultures were incubated at 30 °C for 120 hours.

Inoculation

Colonies grown for 72 hours on agar plates with minimal culture media were inoculated in Erlenmeyer flasks containing 500 mL of the same media, and were grown for 48 hours in an incubator at 30 °C. Afterwards, cells were separated by centrifugation (at 1500 rpm) at 5 °C for 10 minutes and washed with sterilised water to eliminate small residues and intermediary components. The residue was suspended in a small volume of sterilised distilled water. Samples from this suspension were used as inoculum for the experiments of phenol degradation with both immobilized and non-immobilized cells.

Immobilization in alginate gel

2 g of sodium alginate was dissolved in 80 mL of distilled water in order to obtain a polymeric alginate solution. After sterilising the alginate (for 15 minutes at 120 °C), 20 mL of cellular suspension was added and homogenised by stirring. The mixture of cells and sodium alginate was put into a syringe. The solution of alginate and yeast was added slowly from a distance of 20 cm

to a vessel containing 100 mL solution of 1M CaCl₂. Beads of various diameters were formed, depending on the diameter of the needle and the applied pressure. The beads were preserved in CaCl₂ for 0.5-3 hours. Subsequently they were decanted and washed several times with distilled water.

Analytic methods

Phenol concentration was determined with spectrophotometer at 270 nm. For each phenol concentration used, the degradation speed corresponding to the degraded phenol quantity (gl⁻¹) was calculated after 24 hours. The maximal volumetric degradation speed corresponds to the highest value obtained for each phenol concentration. All experiments and determinations were carried out three times, reporting the medium of the obtained measurements.

REFERENCES

- [1] J. Karam, J.A. Nicell, *J. Chem. Technol. Biot.*, **1997**, 69, 141.
- [2] E. Abadulla, T. Tzanov, S. Costa, K.H. Robra, A. Covaco-Paulo, G.M. Gubitz, *Appl. Environ. I Microb.*, **2000**, 66, 3357; N. Durán, E. Esposito, *Appl. Catal. B: Environ.*, **2000**, 21(8), 83; A. M. Mayer, R.C. Staples, *Phytochemistry*, **2002**, 60, 551; A.A. Dias, R.M. Bezerra, P.M. Lemos, A.N. Pereira, *World J. Microb. Biot.*, **2003**, 19, 969.
- [3] C. Crecchio, P. Ruggiero, M.D.R. Pizzigallo, *Biotechnol. Bioeng.*, **1995**, 48, 585.
- [4] A.M. Klibanov, B.N. Alberti, Morris E.D., Felshin L.M., *J. Appl. Biochem.*, **1980**, 2, 414.
- [5] J. Karam, J.A. Nicell, *J. Chem. Technol. Biot.*, **1997**, 69, 141.
- [6] W.P. Thygesen, I.B. Dry, S.P. Robinson, *Plant Physiol.*, **1995**, 109, 525; J.E. Lourenco, V.A. Neves, M.A. Da Silva, *J. Agric. Food Chem.*, **1992**, 40 (12), 2369.
- [7] Y.K. Cho, H.K. Ahn, *J. Food Biochem.*, **1999**, 23, 593.
- [8] S. Palanisami, S.K. Saha, U. Lakshmanan, *World J. Microbiol. Biotechnol.*, **2010**, 26, 63.
- [9] I.D. Buchanan, J.A. Nicell, M. Wagner, *J. Environ. Eng.*, **1998**, 124, 794.

INFLUENCE OF SUPRAMOLECULAR STRUCTURE IN THE CRYSTALS ON WATER/AROMATIC PARALLEL ALIGNMENT INTERACTIONS

GORAN V. JANJIĆ^{a*}, MILOŠ K. MILČIĆ^b, VESNA B. MEDAKOVIĆ^b

ABSTRACT. The parallel alignment interactions between water molecules and C₆-aryl groups in crystal structures and influence of supramolecular structures in crystals were studied by analyzing data in the Cambridge Structural Database (CSD). Analyses of crystal structures from the CSD reveal that the water/aromatic parallel alignment interactions, where the water molecule or one of its O-H bonds is parallel to the aromatic ring plane, are very frequent at large horizontal displacements. These orientations, observed in crystal structures, were compared with the results of *ab initio* calculations and explained by influence of supramolecular structures in crystals.

Keywords: water/aromatic parallel alignment interactions, crystal structures, influence of supramolecular structures in crystals.

INTRODUCTION

Understanding the nature of the interaction between aromatic and polar molecules, such as water, is of great importance for many areas [1] from materials to biological molecules. It is known that interactions of aromatic and water molecules have a significant role in systems such as aquaporins (water-transporting proteins) [2], nanotubes [3], and nanoporous materials [4]. Therefore, these interactions have been the subject of extensive experimental and theoretical investigations.

A substantial number of theoretical investigations have focused on characterizing the interaction between aromatic and polar molecules. The water-benzene dimer has very often been used as a prototype for aromatic-polar interactions. The OH/ π [5] and CH/O [6] and parallel alignment interactions [7] between the aromatic ring and water molecules are well known in the literature. The energies of these interactions are $\Delta E_{\text{CCSD(T)}(\text{limit})} = -3.19$ kcal/mol, [5b] $\Delta E_{\text{CCSD(T)}(\text{limit})} = -1.41$ kcal/mol [7a] and $\Delta E_{\text{CCSD(T)}(\text{limit})} = -2.45$ kcal/mol [7b] respectively.

^a Institute of Chemistry, Technology and Metallurgy, University of Belgrade, Njegoševa 12, P.O. Box 473, 11001 Belgrade, Serbia, janjic_goran@chem.bg.ac.rs

^b Department of Chemistry, University of Belgrade, Studentski trg 16, 11000 Belgrade, Serbia

In spite of the fact that the interaction of nonpolar groups with polar solvent is somewhat weaker than a classical hydrogen bond, the experimental results showed that approximately one interaction is formed between liquid water and each dissolved benzene molecule [8].

Interestingly, by analyzing data in crystal structures from the Cambridge Structural Database (CSD) it was found that the largest number of interactions are of the CH/O type, at the expense of the OH/ π interactions, even though the latter are computed to be stronger (Fig. 1). One may then conclude that packing has an important influence on the frequency of such interactions in crystal structures.

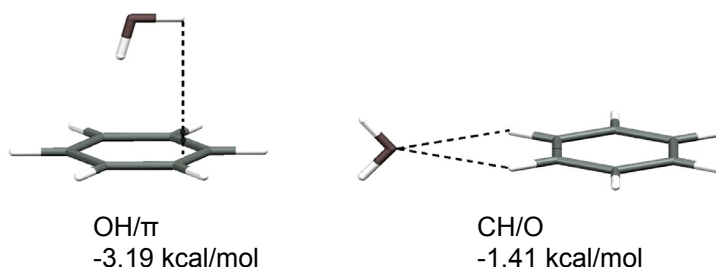


Figure 1. Water/benzene dimers that represent the most stable OH/ π and CH/O interactions.

The earlier analysis of the CH/O interactions in the crystal structures showed that aromatic C–H donors do not have strong preference for linear contacts [6] and this is the result of the tendency of the C–H donors for additional stabilization by simultaneous interactions.

In our previous work [7], the water/benzene parallel alignment interactions with the whole water molecule (both O–H bonds) parallel to the aromatic ring plane (set A), and with one O–H bond parallel to the ring plane (set B) were analyzed. A much larger number of contacts in the set B was observed. The CSD results also showed that parallel O–H bonds are on the normal distance which are common for interactions of aromatic groups with approximately parallel molecular planes (3.3–3.8 Å) [9,10], while the normal distances for contacts at long offsets (in the C–H bond region and beyond) can be below 3.0 Å. The calculations reveal that the most stable conformation of parallel alignment interactions, with one O–H bond parallel to the plane of benzene ring, can be significantly strong ($\Delta E_{\text{CCSD(T)}(\text{limit})} = -2.45$ kcal/mol) at large horizontal displacements, out of the aromatic ring and out of the C–H bond region (Fig. 2) [7b]. For the investigated water-benzene systems, the calculated normal distances were decreasing with increasing the horizontal displacement, and these results are in accord with the data found in crystal structures.

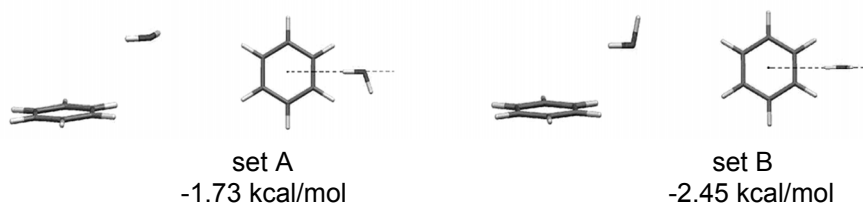


Figure 2. Water/benzene dimers that represent the most stable parallel alignment interactions with the whole water molecule (both O-H bonds) parallel to the aromatic ring plane (set A), and with one O-H bond parallel to the ring plane (set B).

Here, we present our new study of the parallel alignment water/aromatic interactions, based on analyses of crystal structures from the CSD. The reasons for this study are detailed examination of the geometry of these interactions in the crystal structures in order to investigate the influence of supramolecular structure on water/aromatic parallel alignment interactions. To the best of our knowledge, this is the first study that describes how the steric hindrance and conformational freedom of the system affect the frequency of interactions in the crystal structures.

RESULTS AND DISCUSSION

To study the influence of supramolecular structures in crystals on geometry of water/aromatic parallel alignment interactions, detailed statistical analysis was performed. We were interested in a number of structures satisfying the searching criteria and not in a preference for contacts to be at or near to the ring, hence, the area-corrected diagrams are not discussed.

The scattergram for the correlation between normal distance R_o and the offset r_o , for contacts in set A, reveals that most of the normal distances are in the range 3.0- 4.0 Å (Fig. 3).

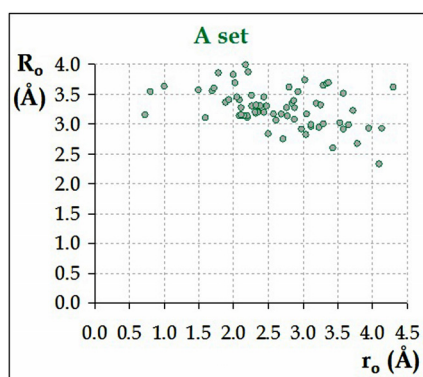


Figure 3. The correlation of the normal distance R_o with the offset r_o for intermolecular contacts of the set A.

These distances (3.3 - 3.8 Å) are common for the interactions of aromatic groups with approximately parallel molecular planes [9a]. The contacts are concentrated in the offset interval of 2.0 to 3.5 Å, suggesting that the oxygen atom may be placed above the ring but it is mostly found outside of the ring. However, while normal distances are in the range 3.0 - 4.0 Å, for the water molecule atoms above the aromatic ring, normal distances for the offsets larger of 2.5 Å can be below 3.0 Å. One should have in mind that in the aromatic ring the H atoms are at the offset ~ 2.4 Å, hence shorter normal distances are out of C-H bond region.

In order to assess mutual projections of water hydrogen and oxygen atoms onto the ring plane, Δr_1 ($\Delta r_1 = r_1 - r_0$) and Δr_2 ($\Delta r_2 = r_2 - r_0$) parameters were defined. The pattern of the results displayed in Fig. 4a shows great overall prevalence for an interaction in which the O-H₁ bond aligns itself with the H₁ atom pointing inside (Δr_1 is negative). The distribution of Δr_2 values, depicted in Fig. 4b, shows small overall prevalence for an interaction in which the O-H₂ bond points toward the ring center with the H₂ atom pointing outside (Δr_2 is positive). The typical geometry with positive Δr_1 values and negative Δr_2 value is reflected in the example shown in Fig. 5. The crystallographic evidence from the CSD search is in line with the results of *ab initio* calculations, that showed higher energy values of the complexes with water molecule outside of the ring comparing to the energies of the complexes with water directly above the ring [7].

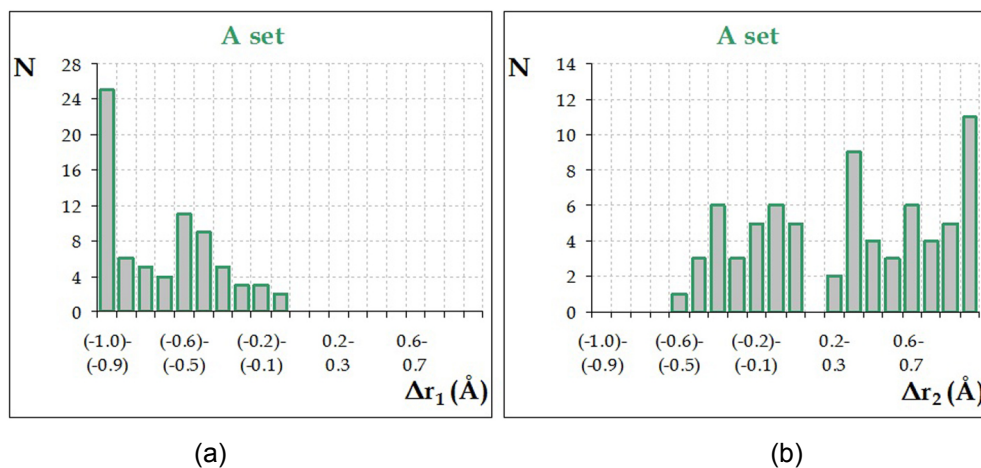


Figure 4. The histograms of the parameters Δr_1 (a) and Δr_2 (b) in retrieved crystal structures of set A.

In the set B are collected the structures where the O-H₁ bond is nearly parallel to the ring plane. Fig. 6 presents the distribution of normal distances R_0 versus offsets r_0 for this set of structures. Since the O-H₁ bond is almost

parallel to the ring plane, most of the observed molecular contacts are in the range 3.0 – 4.0 Å above the ring. Similar to the normal distances of the set A, normal distances for H_1 are below 3.0 Å for the offset values larger of 2.5 Å. The population distribution, presented in Fig. 6, shows that the contacts are concentrated in the offset interval of 3.0 to 4.0 Å, and indicating that most of the oxygen atom projections are outside of the ring.

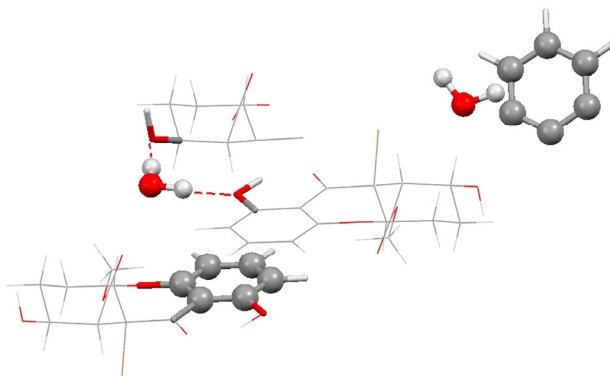


Figure 5. The fragment of crystal structure DELVIC [11] (*8ab-bromo-5aa,5,6,7,8,8a-hexahydro-1,7a-dihydroxy-8a-methoxycarbonylxanthone monohydrate*) selected as an example of the typical geometry for set A ($r_O = 2.09$ Å, $\Delta r_1 = -0.96$ Å and $\Delta r_2 = 0.35$ Å). The water molecule also builds two additional intermolecular OH/O interactions: $H_1 \cdots O_1 = 1.80$ Å and $O-H_1 \cdots O_1 = 179.7^\circ$; $H_2 \cdots O_2 = 1.71$ Å and $O-H_2 \cdots O_2 = 179.0^\circ$.

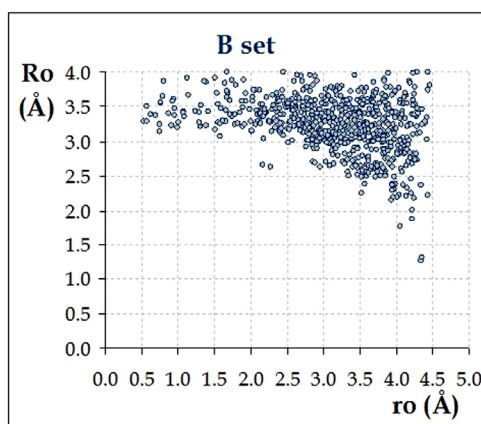


Figure 6. The correlation of the normal distance R_O with the offset r_o in intermolecular contacts of the set B.

To define the positions of hydrogen atoms, with respect to the oxygen atom and the plane of aryl group, Δr_1 ($\Delta r_1 = r_1 - r_O$) and ΔR_2 ($\Delta R_2 = R_2 - R_O$) parameters were defined. The distributions of these parameters, for set B, are shown in Fig. 7. The maximum of the Δr_1 distribution (Fig. 7a) indicates toward-center orientation of the O-H₁ bond with the H₁ atom pointing inside. The histogram of distribution of parameter ΔR_2 (Fig. 7b) shows two maxima, around -0.9 \AA and a smaller one around $+0.9 \text{ \AA}$ (O is closer to the plane of the aryl ring than H₂). In the first (densely) populated group, with $\Delta R_2 < 0 \text{ \AA}$, the O-H₂ group is directed towards to the ring plane, and is mainly involved in the interaction with the substituent of the aromatic group. However, in a second populated region, with $\Delta R_2 > 0 \text{ \AA}$, the O-H₂ group is directed upwards with respect to the ring plane. The typical geometry with negative Δr_1 and ΔR_2 values is reflected in the example shown in Fig. 8.

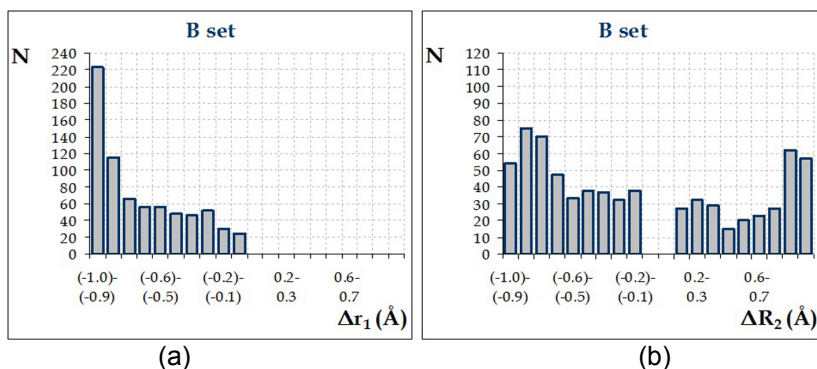


Figure 7. The histograms of the parameters Δr_1 (a) and ΔR_2 (b) in retrieved crystal structures of set B.

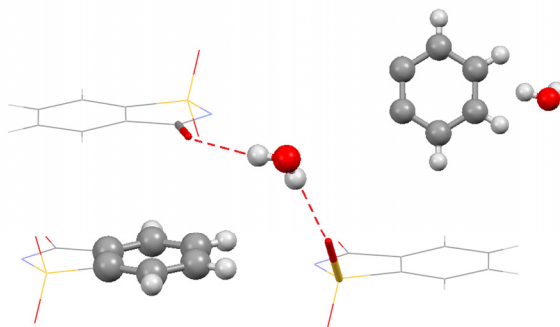


Figure 8. The fragment of crystal structure XUVHUR [12] bis(2,6-dimethanopyridine)-nickel(II) bis(saccharinate) dihydrate selected as an example of the typical geometry for set B ($r_O = 3.84 \text{ \AA}$, $\Delta r_1 = -0.97 \text{ \AA}$ and $\Delta R_2 = -0.83 \text{ \AA}$). The water molecule also builds two additional intermolecular OH/O interactions: $H_1 \cdots O_1 = 2.00 \text{ \AA}$ and $O-H_1 \cdots O_1 = 171.1^\circ$; $H_2 \cdots O_2 = 2.09 \text{ \AA}$ and $O-H_2 \cdots O_2 = 158.3^\circ$.

The results of crystallographic analysis showed that the interactions of set B (716 contacts) are ten times more numerous than the interactions of set A (71 contacts), suggesting that crystal packing has a very important influence on the geometry of water/aromatic parallel alignment interactions in the crystal structures. In order to illustrate and detail this influence, a few examples are given in the following paragraphs.

The examples given here should provide an explanation for the differences in the frequency, geometry and strength of investigated types of interactions.

Among the A complexes considered, the structures corresponding to the energy minimum have a positive Δr_2 value. However, the distribution of Δr_2 values, depicted in Fig. 4b, shows that a large number of structures (~36%) have a negative Δr_2 value, in which the O-H₂ bond is directed towards the ring (Fig. 6). The visual analysis of the crystal structures reveals that such orientation of water molecule and aromatic group is a consequence of the interaction between both water hydrogen atoms with the group from environment, which simultaneously interacts with the aromatic group. The typical geometry with a negative Δr_2 value is reflected in the example shown in Fig. 9. In crystal structure IVENIG [13], besides parallel interaction with phenyl group, both water hydrogen atoms build additional OH/Cl interactions with Cl atoms from the environment, that simultaneously form interactions with the phenyl group, included in parallel interaction with the water molecule.

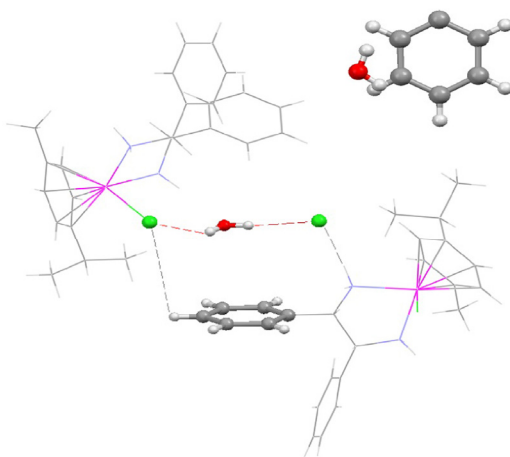


Figure 9. The fragment of crystal structure IVENIG ((η^6 -1-isopropyl-4-methylbenzene)-chloro-(1,2-diphenylethylenediamine-N,N')-ruthenium(II) chloride dichloromethane solvate monohydrate) selected as an example of set A ($r_0 = 2.61 \text{ \AA}$, $\Delta r_1 = -0.49 \text{ \AA}$ and $\Delta r_2 = -0.34 \text{ \AA}$). The water molecule also builds two additional intermolecular OH/Cl contacts: $H_1 \cdots Cl_1 = 2.35 \text{ \AA}$ and $O-H_1 \cdots Cl_1 = 170.3^\circ$; $H_2 \cdots Cl_2 = 2.50 \text{ \AA}$ and $O-H_2 \cdots Cl_2 = 148.6^\circ$.

In the structures of set B, the water O-H₂ group has greater conformational freedom than the water O-H₂ group in the structures of set A. Namely, in the structures of set A, the water O-H₂ group is parallel to aryl group, in other words the O-H₂ group forms an angle of less than with the plane of the aryl group. The range of this angle values for structures of set B (from 10° to 90°) is much larger than the range for structures of set A, explaining the previous assertion that the water O-H₂ group has greater conformational freedom in the structures of set B. The higher interaction energies and greater conformational freedom of the O-H₂ group in the structures of set B are the reasons why the contacts of set B are about ten times more frequent than the contacts of set A in the crystal structures.

In spite of being somewhat weaker than OH/π interaction between water molecule and aryl group (-3.19 kcal/mol) [5b], we found that parallel alignment interactions occur more frequent in crystal structures. These results indicate that the influence of supramolecular structure on mutual orientation of water molecule and aromatic group is very important in the crystal structures. In the parallel alignment interaction, the additional stabilization is achieved, as all atoms of the water molecule can form additional interactions simultaneously, while one of these is eliminated by the OH/π interaction.

The number of additional supramolecular interactions, satisfying the criteria specified in Methodology section, including the parallel O-H₁ bonds, for contacts of set B is 913. The total number of contacts in set B is 716, what implies that in 200 contacts the parallel O-H₁ groups simultaneously form two additional interactions. The classical hydrogen bonds (or OH₁/X, where X=O, N, F, Cl, and S) have a majority in forming of additional supramolecular interactions (38.5%), while OH₁/π interactions have a slightly smaller contribution (37.6%).

However, using the criteria for OH/π interactions, specified in Methodology section, 545 interactions of non-coordinated water and C₆-aromatic groups were found, that is less than the number of contacts with parallel alignment interactions. In these 545 contacts, water O-H₁ bonds build 410 additional supramolecular interactions. Hence, 135 water O-H₁ bonds, included in OH/π interactions, do not build additional interactions. It is obvious that the geometry of the parallel alignment orientations allows the molecules of benzene and water to form larger number of additional interactions. Therefore these interactions are more numerous than the OH/π interactions in crystal structures.

To provide further illustration for these unexpected results, the fragment of crystal structure EBAQII [14] is shown at Fig. 10.

In this structure, beside the water/aromatic parallel alignment interaction, the water O-H₁ group builds two classical hydrogen bonds with two O-H groups of the pyrogallol fragment from the environment. One of pyrogallol O-H groups forms an OH/π interaction with the aryl ring, that is included in water/aromatic parallel alignment interactions. However, as can be seen from Fig. 10, from

steric reasons, the pyrogallol OH group is involved in building up only one (OH/ π) interaction. It means that the position of water molecule, in structures with water/aromatic parallel alignment interactions, is more stabilized by additional interactions, than in structures with OH/ π interactions.

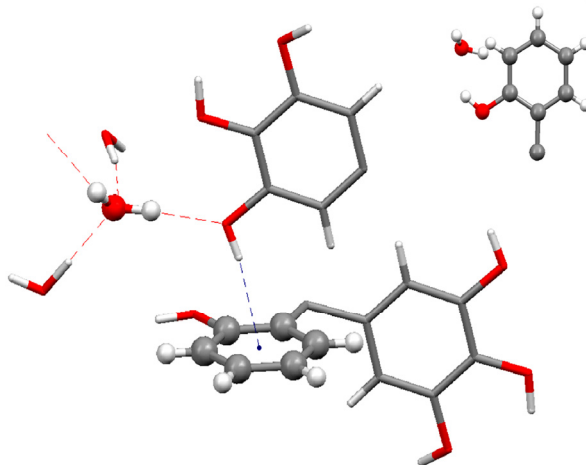


Figure 10. The fragment of crystal structure EBAQII (5-(bis(2-hydroxyphenyl)methyl)phenyl-1,3,5-triol tetrahydrate) selected as an example of B set ($r_O= 3.56 \text{ \AA}$, $\Delta r_1= -0.92 \text{ \AA}$ and $\Delta R_2= 0.66 \text{ \AA}$). The water O-H₁ group also builds two additional classical hydrogen bonds with two O-H groups of pyrogallol fragment ($H_1 \cdots O_a= 1.87 \text{ \AA}$ and $O-H_1 \cdots O_a= 165.9^\circ$, $H_1 \cdots O_b= 2.61 \text{ \AA}$ and $O-H_1 \cdots O_b= 118.1^\circ$). One of the pyrogallol O-H group forms OH/ π interaction with aryl ring ($H \cdots \Omega= 2.66 \text{ \AA}$ and $O_a-H \cdots \Omega= 152.1^\circ$) included in water/aromatic parallel alignment interactions.

CONCLUSIONS

The data presented here show that in parallel interactions water molecules are mostly found outside of the aromatic ring. The number of interactions with one water O-H bond parallel to the plane of aromatic ring is much larger than the number of interactions with the whole water molecule parallel. The results of calculations cannot explain completely the results of CSD analysis. The reason for this disagreement can be the influence of supramolecular structure on interactions in the crystals.

METHODOLOGY SECTION

The statistical study is based on the crystal structures archived in the Cambridge Structural Database (November 2011 release, version 5.33) [15]. The crystal structures involving non coordinated water molecule and C₆-aromatic group were screened for intermolecular contacts. The CSD search program

ConQuest 1.14 [16] was used to retrieve structures satisfying the following criteria: a) the crystallographic R factor < 10% b) the error-free coordinates according to the criteria used in the CSD c) the H-atom positions were normalized using the CSD default X-H bond lengths (O-H = 0.983 Å; C-H = 1.083 Å) d) no polymer structures. The geometric parameters used throughout in the text and the atom labeling scheme are displayed in Fig. 11.

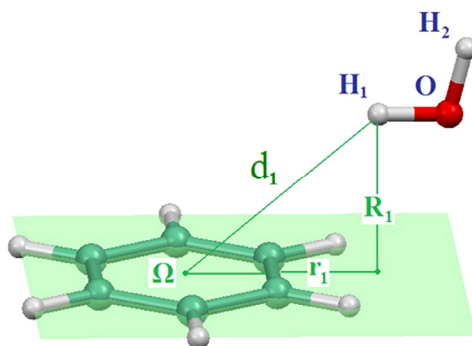


Figure 11. The geometric parameters and atoms labeling, used for the description of parallel interaction. Ω marks the centroid of the benzene ring. The hydrogen atom of the water molecule that is closer to the center of the ring, comparing to the second hydrogen atom of the water molecule, is denoted by H_1 . The distances between H_1 , H_2 , and O, and the centroid of the ring are referred to as d_1 , d_2 , and d_O , respectively. The distances R_1 , R_2 , and R_O mark the normal distances from the ring plane to the H_1 , H_2 , and O atoms, respectively. The offsets r_1 , r_2 , and r_O are the distances from the ring centroid to the projection of the H_1 , H_2 , and O atom position, respectively, on the plane of the ring. In the benzene ring the distance from the ring centroid to the center of the carbon-carbon bond is about 1.2 Å and the distance between the center of the ring and the carbon atom is ~ 1.4 Å.

It is considered that parallel alignment interaction occurs if the offset value r_1 is less than 3.5 Å, the normal distance R_1 is less than 4.0 Å (**Fig. 11**), Δr_1 value is less than 0.0 Å ($\Delta r_1 = r_1 - r_O$) and the absolute value of ΔR_1 is less than 0.1 Å ($\Delta R_1 = R_1 - R_O$) [7b] The absolute value of ΔR_1 less than 0.1 Å corresponds to the parallel orientation of water O- H_1 bond and aromatic ring. A negative value of Δr parameter indicates the orientations where the projection of O-H bond points to ring with the H atom inside.

The contact was considered as a OH/ π interaction if the distance between a hydrogen atom of water molecule and the center of any C_6 -aromatic ring (Ω) was less than 3.5 Å, α angle (O- $H_1 \cdots \Omega$ angle) larger than 110° and β angle (the angle between the $H_1 \cdots \Omega$ line and the normal to the aromatic ring) less than 30° (**Fig. 11**).

The contacts between O-H₁ group and X species from environment, where O...X distance was shorter than 4.0 Å and O-H₁...X angle is larger than 110°, [17] were considered as "additional supramolecular interactions".

ACKNOWLEDGMENTS

This work was supported by the Serbian Ministry of Education and Science (grant no. 172065).

Authors would also like to acknowledge Dr Horst Borrmann, Max-Planck-Institut für Chemische Physik fester Stoffe, Dresden, Germany.

REFERENCES

- [1] (a) J.F. Malone, C.M. Murray, M.H. Charlton, R. Docherty, A.J. Lavery, *Journal of the Chemical Society, Faraday Transactions*, **1997**, 93, 3429. (b) T. Steiner, G. Koellner, *Journal of Molecular Biology*, **2001**, 305, 535. (c) S.D. Zarić, D. Popović, E.W. Knapp, *Chemistry - A European Journal*, **2000**, 3935. (d) S.D. Zarić, *European Journal of Inorganic Chemistry*, **2003**, 2197. (e) M.K. Milčić, Z.D. Tomić, S.D. Zarić, *Inorganica Chimica Acta*, **2004**, 357, 4327. (f) S.J. Kim, H.I. Seo, B.H. Boo, *Molecular Physics*, **2009**, 107, 1261. (g) M. Prakash, K. Gopal Samy, V. Subramanian, *The Journal of Physical Chemistry A*, **2009**, 113, 13845. (h) S. Li, V.R. Cooper, T. Thonhauser, A. Puzder, D.C. Langreth, *The Journal of Physical Chemistry A*, **2008**, 112, 9031. (i) L.V. Slipchenko, M.S. Gordon, *The Journal of Physical Chemistry*, **2009**, 113, 2092.
- [2] (a) P. Agre, *Angewandte Chemie International Edition*, **2004**, 43, 4278. (b) D. D. Kozono, M. Yasui, L.S. King, P. Agre, *Journal of Clinical Investigation*, **2002**, 109, 1395.
- [3] (a) G. Hummer, J.C. Rasaiah, J.P. Noworyta, *Nature*, **2001**, 414, 188. (b) D. Takaiwa, I. Hatano, K. Koga, H. Tanaka, *Proceedings of the National Academy of Sciences of the USA*, **2008**, 105, 39.
- [4] R. Natarajan, J.P.H. Charmant, A.G. Orpen, A.P. Davis, *Angewandte Chemie International Edition*, **2010**, 49, 5125.
- [5] (a) S. Tsuzuki, *Structure and Bonding*, **2005**, 115, 149. (b) D. Z. Vojislavljević, G.V. Janjić, D.B. Ninković, A. Kapor, S.D. Zarić, *CrystEngComm*, **2013**, 15, 2099.
- [6] D.Ž. Veljković, G.V. Janjić, S.D. Zarić, *CrystEngComm*, **2011**, 13, 5005.
- [7] (a) B.D. Ostojić, G.V. Janjić, S.D. Zarić, *Chemical Communications*, **2008**, 28, 6546. (b) G.V. Janjić, D.Ž. Veljković, S.D. Zarić, *Crystal Growth & Design*, **2011**, 11, 2680.
- [8] (a) M. Besnard, Y. Danten, T. Tassaing, *Journal of Chemical Physics*; **2000**, 113, 3741. (9) (b) K.P. Gierszal, J.G. Davis, M.D. Hands, D.S. Wilcox, L.V. Slipchenko, D. Ben-Amotz, *The Journal of Physical Chemistry Letters*, **2011**, 2, 2930.

- [9] (a) C.J. Janiak, Chem. Soc., *Dalton Transactions*, **2000**, 3885. (b) G. V. Janjić, J. Andrić, A. Kapor, Ž.D. Bugarčić, S.D., Zarić, *CrystEngComm*, **2010**, *12*, 3773. (c) G.V. Janjić, P.V. Petrović, D.B. Ninković, D.Ž. Veljković, A.J. Kapor, S.D.; Zarić, *Studia UBB Chemia*, **2010**, *55*, 165.
- [10] (a) M.O. Sinnokrot, C.D. Sherrill, *The Journal of Physical Chemistry A*, **2006**, *110*, 10656. (b) R. Podeszwa, R. Bukowski, K. Szalewicz, *The Journal of Physical Chemistry A*, **2006**, *110*, 10345. (c) M. Pitonak, P. Neogrady, J. Rezac, P. Jurecka, M. Urban, P. Hobza, *Journal of Chemical Theory and Computation*, **2008**, *4*, 1829. (d) T. Janowski, P. Pulay, *Chemical Physics Letters*, **2007**, *447*, 27.
- [11] G. Ferguson, B. Kaitner, J. Gilmore, V.O.T. Omuaru, W.B. Whalley, *Journal of the Chemical Society, Perkin Transactions*, **1985**, *1*, 1343.
- [12] V.T. Yilmaz, S. Guney, O. Andac, W.T.A. Harrison, *Journal of Coordination Chemistry*, **2003**, *56*, 21.
- [13] M.D. Jones, F.A.A. Paz, J.E. Davies, R. Raja, J. Klinowski, B.F.G. Johnson, *Inorganica Chimica Acta*, **2004**, *357*, 1247.
- [14] B. Venkataramanan, W.L.G. James, J.J. Vittal, V. Suresh, *Crystal Growth & Design*, **2004**, *4*, 553.
- [15] F.H.Allen, *Acta Crystallographica Section B*, **2002**, *58*, 380.
- [16] F.H. Allen, J.E. Davies, J.J. Galloy, O. Johnson, O. Kennard, C.F. Macrae, E.M. Mitchell, G.F. Mitchell, J.M. Smith, D.G. Watson, *Journal of Chemical Information and Modeling*, **1991**, *31*, 187.
- [17] J.M. Andrić, G.V. Janjić, D.B. Ninković, S.D. Zarić, *Physical Chemistry Chemical Physics*, **2012**, *14*, 10896.

CONTINUOUS PRECIPITATION: A MODEL BASED STABILITY ANALYSIS

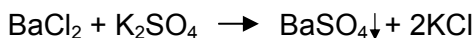
SZILÁGYI BOTOND^a, BARABÁS RÉKA^a

ABSTRACT. In the current study a model based stability analysis of a continuous mixed suspension mixed product removal crystallizer, widely used in pilot and industrial scale, is investigated. The population balance approach is used to model the size distribution of solid particulate phase, taking into consideration the nucleation and size independent growth of particles. The model was solved with the standard method of moments, computing the leading moments of particle size distribution. The Lyapunov's stability theory is used for mapping the unstable operation regions of the crystallizer, by computing the eigenvalues of Jacobian matrix of the governing equation system. In unstable region numerical simulations are performed to visualize the effects of the generated temporal oscillations into particulate properties. Based on the simulations, useful conclusions can be made from the point of view of operating, optimizing and control of the continuous crystallizer.

Keywords: *population balance, CMSMPR crystallizer, stability, method of moments*

INTRODUCTION

The crystallization is a widely used separation, purification and particle formation technique used in chemistry and chemical industry. The motoric force of crystallization is the thermodynamic instability of liquid phase caused by the supersaturation of a given compound, what will lead to nucleation and growth of solid crystals [1]. The trivial techniques of supersaturation generation are the cooling and the chemical reaction. The supersaturation can also be achieved by salting out and by other techniques. Both of nucleation and growth rate of crystals depends on supersaturation ratio. In this study the crystallization kinetics of the barium sulphate is used, based on following chemical reaction



^a *Universitatea Babeş-Bolyai, Facultatea de Chimie și Inginerie Chimică, Str. Kogălniceanu, Nr. 1, RO-400084 Cluj-Napoca, Romania, botiszilagyi@yahoo.com*

The feed concentrations of reagents are denoted with C_A and C_B , respectively C_i for the barium sulphate. The barium sulphate was chosen because its crystallization kinetics is very well studied and described by earlier experimental works.

In laboratory scale, the crystallization is usually performed in batch conditions. Moving to pilot and industrial scale, continuous techniques are applied in tubular reactor or in continuous batch crystallizer. A classical device is the continuous mixed suspension mixed product removal crystallizer (from here CMSMPR, illustrated by Fig. 1): the reactor is continuously fed with the crystallizing material (in the case of precipitation – crystallization with the reagent solutions) and the suspension is continuously evacuated without particle classification. If particle classification is needed, it can be carried out, for instance in a decanter (or any other solid-liquid classification method) and the fines can be recirculated continuously into CMSMPR.

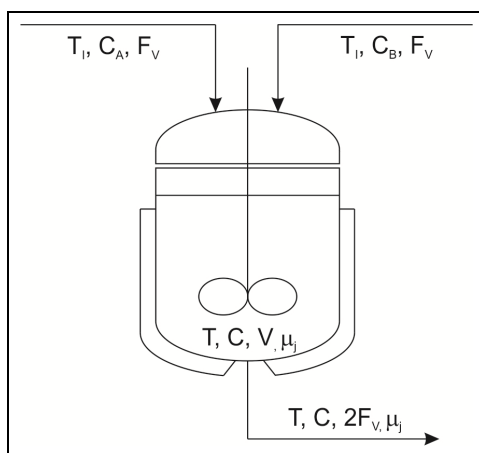


Figure 1. Scheme of a CMSMPR crystallizer

As the system achieves the steady state, a solid crystalline material with well-defined particle properties is produced. However, there are some cases, when the steady state is never achieved and the parameters oscillate in CMSMPR (concentration, number of particles etc.). This is the unstable operation, what is an interesting aspect of the particle production but, as the process is designed to produce particles of desired quality, in practice should strictly be avoided.

The current study presents a model based stability analysis of a CMSMPR crystallizer. For modeling the crystallization a monovariate population balance model is considered, taking in consideration the nucleation and

growth of particles [2]. The moment transformation is used to calculate the leading moments of distribution [3]. The mass balance for the crystallizing material should be added. For analyzing the dynamics of the crystallizer, the Lyapunov stability theory is used: if and only if all Re of eigenvalues < 0 the equilibrium is asymptotically stable [4]. A bifurcation analysis was also performed by [5].

After mapping the unstable operation zone of the crystallizer, numerical simulations are performed to investigate the dynamics of system when switching from an operation mode to another. These simulations are useful when trying to operate, optimize and control a CMSMPR [6-8].

BUILDING THE MODEL

The model was written up with the next simplifying hypotheses:

- the crystallizer is fed with stoichiometric reagent ratio,
- the mixing of the inlet stream is instant,
- the chemical reaction producing the barium sulphate is instant,
- the solution in crystallizer is perfectly mixed,
- isothermal operation is considered,
- the accumulation is 0 and
- the composition of the outlet stream is identical with the solution of crystallizer.

The mass balance for the crystallizing material in these conditions:

$$\frac{dc(t)}{dt} = \frac{F_V c_I}{V} - k_V \rho L_n^3 B(S) - 3\rho k_V G(S) \mu_2(t) - \frac{F_V c(t)}{V} \quad (1)$$

where the first term on the right side represents the quantity of crystallizing material introduced into crystallizer with feed streams, the second term denotes the liquid phase concentration decrease due to the nucleation of solid state particles, the third term is the concentration decrease caused by the growth of solid particles and the last term of right side takes in consideration the material evacuated with the outlet stream, subject to $c(0) = 0$ initial condition. In Eq. (1) c represents the concentration of crystallizing material, c_I is the feed concentration, resulted from the instant reaction of the feed streams, ρ is the molar density (measured in kmol/m^3), $B(S(t))$ denotes the nucleation rate, and $G(S)$ the growth rate, what can be expressed as a power-law relation [9,10]:

$$B(S) = k_b (S - 1)^b \quad (2)$$

$$G(S) = k_g (S - 1)^g \quad (3)$$

where S denotes the relative supersaturation expressed as $S = c - c_{sol}$, $k_V \mu_3$ denotes the total volume of crystals in a unit volume of suspension, expressed using the third order moment of the linear crystal size:

$$\mu_2(t) = \int_0^{\infty} L^2 n(L, t) dL \quad (4)$$

In Eq. (4), $n(L, t)$ denotes the population density function of crystals population by means of which $n(L, t) dL$ provides the number of crystals from the interval of size $(L, L+dL)$ at time t .

The population balance equation governing the temporal evolution of the population density function is written in the form

$$\frac{\partial n(L, t)}{\partial t} + \frac{\partial}{\partial L} [G(S)n(L, t)] = 0 \quad (5)$$

The first term of the equation denotes the temporal evolution of the size distribution of particles and the second term computes the net change in the particle size distribution due to particle nucleation and growth, subject to the initial condition $n(L, 0) = 0$. Here, the boundary conditions are written as

$$\lim_{L \rightarrow L_n} G(S)n(L, t) = B(S) \quad (6)$$

$$\lim_{L \rightarrow \infty} n(L, t) = 0 \quad (7)$$

The meaning of the presented boundary conditions are the next: the growth rate of number of nucleons existing in the system is exactly the nucleation rate and the particles has finite sizes.

The equilibrium solubility of barium sulphate is 1.144×10^{-5} kmol/m³ and the kinetic constants of precipitation are presented in Table 1 based on the experimental data given by [11]:

Table 1. Kinetic constants of the precipitation

B		k_b [#/((m ³ s(kmol/m ³) ^b))]]	b [without U.M.]
	$c_{sat} < C < 0.0097$	6×10^{15}	1.775
	$C > 0.0097$	2.523×10^{42}	15
G		k_g [m/(s(kmol/m ³) ^g)]	g [without U.M.]
	$c_{sat} < C < 0.0006125$	2.645×10^{-3}	2
	$C > 0.0006125$	1.62×10^{-5}	1

With the given constants the B and G are continuous functions of the concentration.

SOLUTION AND STABILITY ANALYSIS

The complex system of equations (1) and (5) is solved by using the method of moments. Introducing the moment transformation [3]:

$$\mu_j(t) = \int_0^{\infty} L^j n(L, t) dL, \quad j = 0, 1, 2, \dots \quad (8)$$

In this approximation, from the mathematical point of view the method of moments is a trade-off between an (n+1) dimensional (n dimensions of space, and the L as internal coordinate) differential equation and an infinite set of n dimensional (n dimensions of space) ordinary differential equations.

The moments of distribution can be approximated with different numerical methods instead of solving directly the integral expressed by Eq. (8), resulting the quadrature method of moments [12], direct quadrature method of moments [13] etc. The advantage of the moment transformation is that it reduces the dimensionality of the population balance model equation to the dimensionality of transport equations, consequently permits the simultaneous solution of the population balance with the mass and energy balances.

The first four leading moments are proportional with the next physical quantities: total number, length, surface and volume of particles in an m³ of suspension and in majority of cases are enough for the engineering calculations.

After applying the moment transformation on Eq. (5) and integrating together with Eq. (1) results the system (Eqs. (9) - (13)):

$$\frac{d\mu_0(t)}{dt} = V \cdot B(S) - \frac{\mu_0}{\tau} \quad (9)$$

$$\frac{d\mu_1(t)}{dt} = G(S) \cdot \mu_0(t) - \frac{\mu_1}{\tau} + L_n \cdot V \cdot B(S) \quad (10)$$

$$\frac{d\mu_2(t)}{dt} = 2 \cdot G(S) \cdot \mu_1(t) - \frac{\mu_2}{\tau} + L_n^2 \cdot V \cdot B(S) \quad (11)$$

$$\frac{d\mu_3(t)}{dt} = 3 \cdot G(S) \cdot \mu_2(t) - \frac{\mu_3}{\tau} + L_n^3 \cdot V \cdot B(S) \quad (12)$$

$$\frac{dc(t)}{dt} = \frac{c_I - c(t)}{\tau} - k_V \rho L_n^3 B(S) - 3 \rho k_V G(S) \mu_2(t) \quad (13)$$

Note: in this case the first four moments are computed from the infinite set of moments, what permits the solving of the current stability problem.

In the actual representation the chemical reaction was considered to be instant. In Eqs. (9) – (13) τ denotes the mean residence time in reactor as follows:

$$\tau = \frac{V}{F_V} \quad (14)$$

Writing the system in matrix form, $x = (m_0, m_1, m_2, m_3, c)$, $dx/dt = F(x)$ the Jacobian is defined as dF/dx expressed by Eq. (15). As B and G are positive, strictly increasing continuous functions of $C > c_{\text{sat}}$, exists an unique equilibrium denoted as $(m_{0,\text{eq}}, m_{1,\text{eq}}, m_{2,\text{eq}}, m_{3,\text{eq}}, c_{\text{eq}})$.

$$J = \begin{pmatrix} \frac{\partial F_{\mu_0}}{\partial \mu_0} & \frac{\partial F_{\mu_0}}{\partial \mu_1} & \frac{\partial F_{\mu_0}}{\partial \mu_2} & \frac{\partial F_{\mu_0}}{\partial \mu_3} & \frac{\partial F_{\mu_0}}{\partial c} \\ \frac{\partial F_{\mu_1}}{\partial \mu_0} & \frac{\partial F_{\mu_1}}{\partial \mu_1} & \frac{\partial F_{\mu_1}}{\partial \mu_2} & \frac{\partial F_{\mu_1}}{\partial \mu_3} & \frac{\partial F_{\mu_1}}{\partial c} \\ \frac{\partial F_{\mu_2}}{\partial \mu_0} & \frac{\partial F_{\mu_2}}{\partial \mu_1} & \frac{\partial F_{\mu_2}}{\partial \mu_2} & \frac{\partial F_{\mu_2}}{\partial \mu_3} & \frac{\partial F_{\mu_2}}{\partial c} \\ \frac{\partial F_{\mu_3}}{\partial \mu_0} & \frac{\partial F_{\mu_3}}{\partial \mu_1} & \frac{\partial F_{\mu_3}}{\partial \mu_2} & \frac{\partial F_{\mu_3}}{\partial \mu_3} & \frac{\partial F_{\mu_3}}{\partial c} \\ \frac{\partial F_c}{\partial \mu_0} & \frac{\partial F_c}{\partial \mu_1} & \frac{\partial F_c}{\partial \mu_2} & \frac{\partial F_c}{\partial \mu_3} & \frac{\partial F_c}{\partial c} \end{pmatrix} \quad (15)$$

For testing the stability of the given operating point, the eigenvalues of the Jacobian are computed, denoted with $\lambda_{i,i} = 1, 2, 3, 4, 5$. The equilibrium point is asymptotically stable if and only if the real part of eigenvalue is negative for all λ_i . In unstable operation mode strong sustained oscillations are expected.

In the next section these eigenvalues will be investigated in function of feed flowrate (sum of inlet flowrates), feed concentration (resulted from reagents of feed streams in instant chemical reaction) and volume of CMSMPR. Dynamic numerical simulations will also be performed.

RESULTS AND DISCUSSIONS

The stability is studied for the operation zone noted by Table 2.

Table 2. Boundary values of process parameters in stability analysis

	Min	Max
Feed flowrate [m ³ /s]	0.00001	0.0001
Feed concentration [kmol/m ³]	0.01	0.3
CMSMPR volume [m ³]	0.0005	0.01

The equilibrium point is computed by solving the algebraic equation system resulting from the Eqs. (9) – (13) making the left side terms equally with 0. For solving the equation system, the *fsolve* code of the Matlab was used, what used the trust region dogleg nonlinear optimization algorithm.

For the numerical solution of the complex equation system the introduction of two additional steps was necessary:

1. Solving the differential equation for a 10000 s integration time to estimate the initial guess point for the *fsolve*,
2. Creating a while loop, which restarts the *fsolve* computation when it fails (in case of complex systems *fsolve* sometimes converges to a non-root point as the initial guess is not a well chose) with a plus-minus 3 % random fluctuation in values of initial parameters.

Fig. 2, indicate the results of analysis: the stable and unstable operation zones of the CMSMPR.

As it seems, under the current simulation conditions unstable operation zones were found. The stability zone is growing with the increasing volume of CMSMPR and at $V = 10$ L it disappears. Based on tendency appearing of Fig. 2., probably the unstable zone moved in direction of higher input flowrates. The oscillations occur at lower concentrations ($C_1 < 0.25$ kmol/m³), independently of reactor size.

Numerical simulations can be run investigating the effect of switching between the operation modes into the temporal evolution of one of most important parameters of particle formation process: the mean particle diameter. In this study, the Sauter mean diameter is considered, denoted with d_{32} and defined as follows:

$$d_{32} = \frac{\mu_3}{\mu_2} [m] \quad (15)$$

The differential equation was solved with the *ode15s* function of Matlab, what is based on the numerical differentiation formulae of Klopfenstein and Reiher.

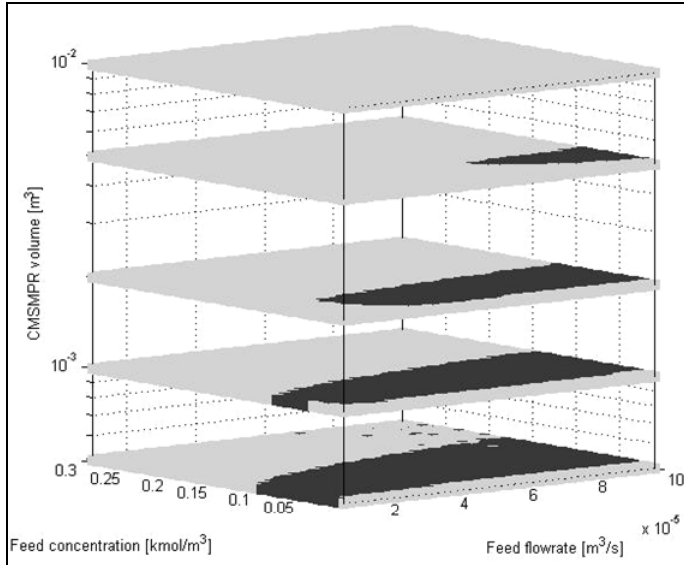


Figure 2. Stability zones of CMSMPR: light grey: stable operation, grey: unstable operation

The Fig. 3. shows the routes of numerical simulation on stability map ($V = 1$ L). The route of three numerical simulations is indicated: the first from a stable to unstable operation mode, the second from unstable to unstable operation, the third from unstable to stable operation. In next part the result of these simulations will be presented.

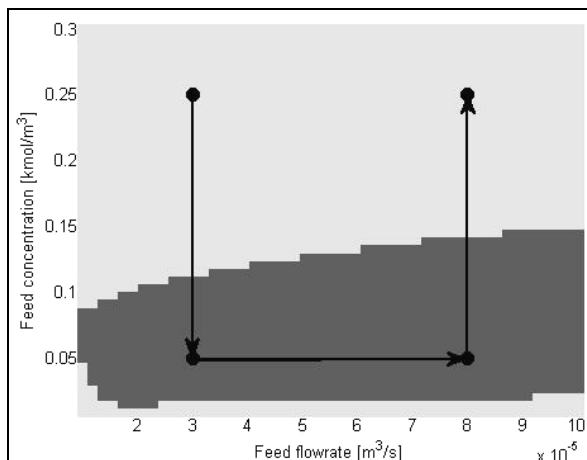


Figure 3. Stability zone of CMSMPR of 1 L, light grey: stable operation, grey: unstable operation, indicating the routes of 3 simulations

The Fig. 4. shows the dynamics of switching from stable to unstable operation (constant $3 \times 10^{-3} \text{ m}^3/\text{s}$ feed flowrate).

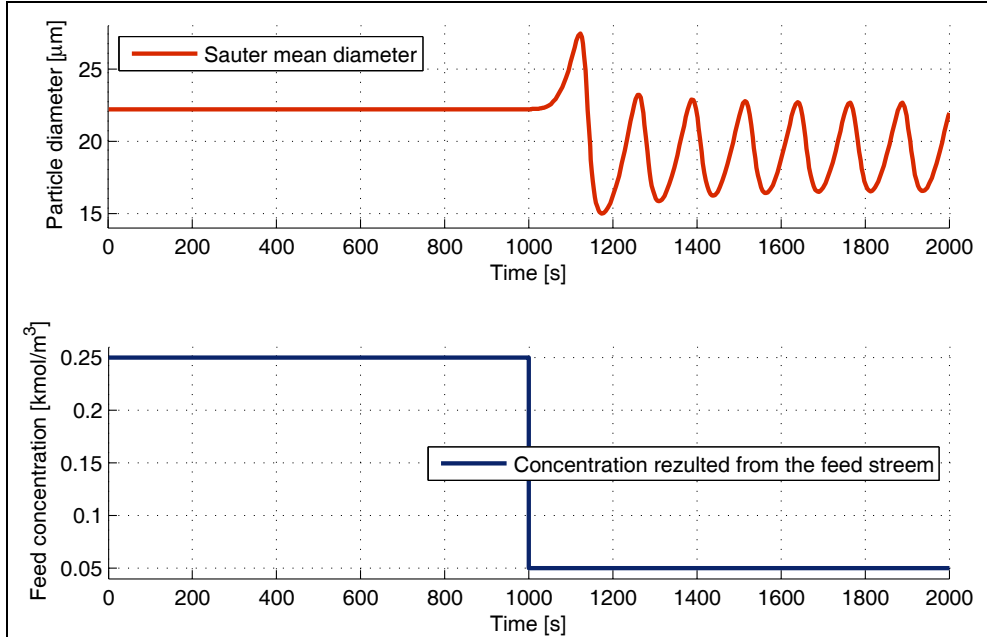


Figure 4. Stable to unstable operation switch

As the Fig. 4 illustrates, as the system enters to the unstable operation, the particle diameter shows a strong, sustained temporal evolution. These types of situation can occur, for instance, when the concentration of at least one of reagents decreases for some reason.

The second simulation (Fig. 5) presents the switch from unstable – to unstable operation mode (constant 0.05 kmol/m^3 feed concentration).

The result of raising the feed flowrate will bring the system to another unstable operation; the oscillations still exist around of another equilibrium point with different amplitude and frequency. These types of situation can occur, for instance, if the reactor operator (or the poorly configured control system) modifies the flowrate to stabilize the system.

The Fig. 6. shows the dynamics of switching from unstable to stable operation (constant 8×10^{-5} feed flowrate). As it seems, in stable operation mode damped oscillations exists but probably the system, after a few more oscillations are stabilizing. Based on simulations, the particle diameters are decreasing (right after the concentration switch) followed by the increasing to steady-state values (after the damped oscillations).

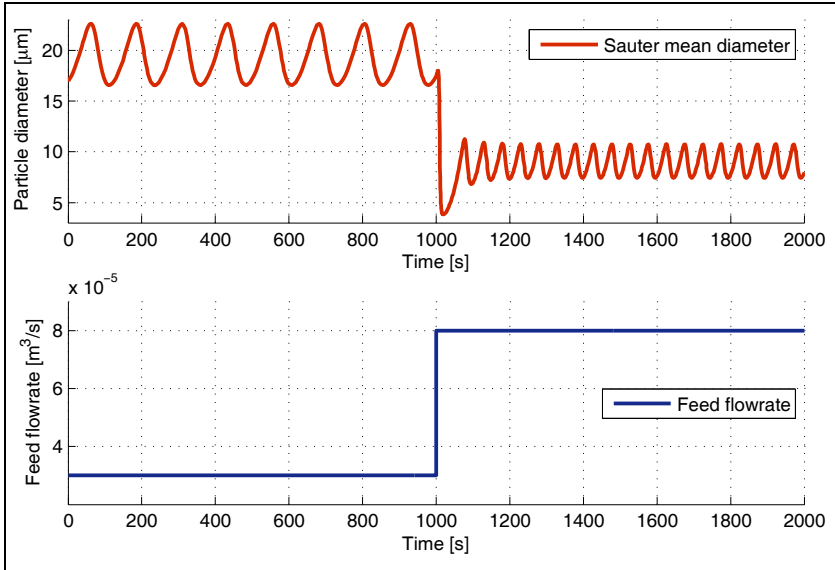


Figure 5. Unstable to unstable operation switch

The controllability of these types of systems is poor, in these cases a detailed stability analysis is needed and build in into the – usually model predictive - control system.

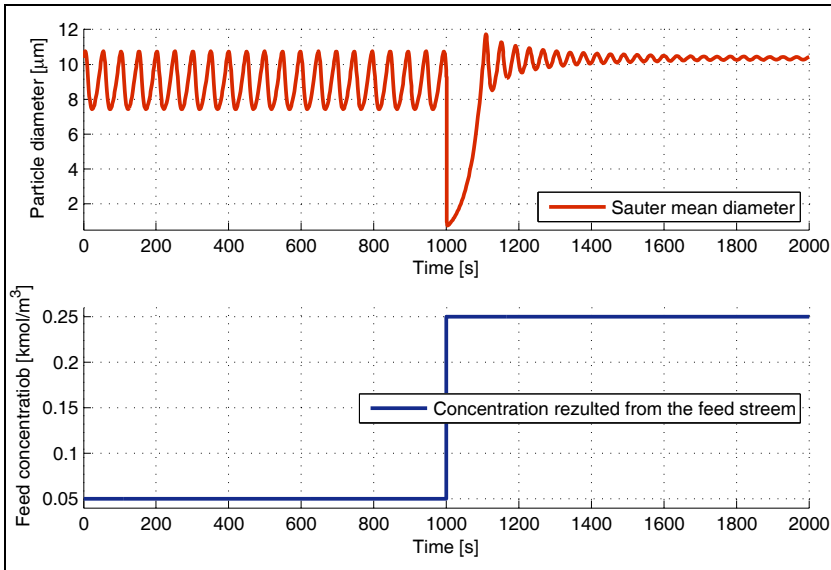


Figure 6. Unstable to stable operation switch

CONCLUSIONS

In the current work the continuous crystallization process was studied. A detailed model based stability analysis was carried out for the case of barium phosphate precipitation and it was proved that for the investigated case the crystallizer has unstable operation zones. A stability map was structured what corresponds from a laboratory to a pilot scale crystallizer (based on volume of reactor, flowrates and concentrations). The numerical simulations showed that in unstable operation regime strong, sustained oscillations exists in temporal evolution of particle diameter. It was showed that, as the system entered to oscillation mode, a random change in input parameter (e.g. feed flowrate) not necessarily eliminates the oscillations; the system can remain inside of the unstable operation zone what will only change the attractor, the frequency and amplitude of oscillations. As a final consequence, as the oscillations appears in a crystallizing system, a detailed stability analysis is needed to map the unstable operation regimes, what should strictly be avoided when operating a crystallizer. For safety reasons, mapping the unstable zones is necessary before starting the operation of the crystallizer. However, in this study the well-studied crystallization kinetics of barium sulphate was used, it could be carried out for any other material as the crystallization kinetics is known.

REFERENCES

- [1] D. Ramkrishna, "Population balances. Theory and Applications to Particulate Systems in Engineering", Academic press, San Diego, **2000**.
- [2] H.M. Hulburt, S. Katz. *Chemical Engineering Science*, **1964**, *19*, 555.
- [3] A.D. Randolph, M.A. Larson, "Theory of Particulate Processes. 2nd Edition" *Academic Press*, New York, **1988**.
- [4] A.M. Lyapunov, "The General Problem of the Stability of Motion (In Russian)", *Doctoral dissertation*, Univ. Kharkov **1892** English translation: "Stability of Motion", *Academic Press*, New-York & London, **1966**.
- [5] P.K. Pathath, A. Kienle, *Chemical Engineering Science*, **2002**, *57*, 4391.
- [6] V. Gamez-Garci, H.F. Flores-Mejia, J. Ramirez-Muñiz, H. Puebla, *Procedia Engineering*, **2012**, *42*, 471.
- [7] C. Bastos, B. Costa, M. Regina, W. Maciel, R.M. Filho, *Computers & Chemical Engineering*, **2007**, *31*, 206.

- [8] Z.K. Nagy, G. Fevotte, H. Kramer, L.L. Simon, *Chemical Engineering Research and Design*, **2013**, in press, available online, DOI: 10.1016/j.cherd.2013.07.018
- [9] J.V.P. Schmelzer, *Nucleation Theory and Applications*, Wiley, New York, **2005**.
- [10] N.A. Mancuso, J.P. Isaac, *Crystal Growth: Theory, Mechanisms and Morphology*, Nova Science, **2004**.
- [11] M. Angerhofer, "Untersuchungen zur Kinetik der Fallungskristallisation von Bariumsulfat", Doctoral Thesis, Technical University on Munich, **1994**.
- [12] R. McGraw, *Aerosol Science and Technology*, **1997**, 27: 2, 255.
- [13] D.I. Marchisio, R.O. Fox, *Chemical Engineering Science*, **2005**, 36, 43.

AN ULTRAHIGH PERFORMANCE LIQUID CHROMATOGRAPHY - MASS SPECTROMETRY METHOD FOR THE ANALYSES OF PHENOL DERIVATIVES FROM WATERS

ELENA PREDA^{a,b}, MANUELA MARIA MINCEA^{a,b}, COSMIN IONAȘCU^{a,b},
ALEXANDRU VALENTIN BOTEZ^a, VASILE OSTAFE^{a,b*}

ABSTRACT. In this study, a new procedure, based on solid-phase extraction (SPE) and analysis by Ultrahigh Performance Liquid Chromatography coupled with Mass Spectrometry method (UPLC-MS/MS), has been developed for the simultaneous, multianalyte determination of 15 selected phenols in water. SPE was carried out on LiChrolut RP-18 and Oasis HLB cartridges by percolating 500 mL water samples. The analytical methods allowed the separation of the 15 phenols in less than 8 minutes, with a recovery higher than 70%, and a quantification limit between 3 – 5 ng/L. The developed UPLC-MS/MS method showed high precision, as it was confirmed by the low values of relative standard deviation (RSD) for water samples spiked with 10 and 100 ng/L analytes. In the optimized method, LOQ higher than 5 ng/L, satisfactory precision (relative standard deviations < 20%) and accuracies (recovery percentages between 70 and 95%) were obtained for most investigated compounds.

Keywords: Phenol derivatives, UPLC-MS/MS, SPE

INTRODUCTION

The development of sensitive methods for the determination of organic contaminants in wastewater has become a major issue, because of both the presence of many different toxic compounds in this type of samples and of the strict European Union legal requirements for surface water quality [1, 2]. General reviews relating to surface water analysis and emerging environmental pollutants [3-6] have drawn the attention of the scientific community. For the

^a Department of Biology – Chemistry, Faculty of Chemistry – Biology – Geography, West University of Timisoara, 16 Street Pestalozzi, Timisoara 300115, Romania

^b Advanced Research Environmental Laboratories, Multidisciplinary Research Platform “Nicholas Georgescu - Roegen”, 4 Street Oituz, Timisoara 300086, Romania.

* Corresponding author: e-mail: vostafe@cbg.uvt.ro

analysis of organic compounds from rivers and lakes, the most used techniques are gas chromatography (GC) and liquid chromatography (LC), both coupled to mass spectrometry (MS). Enrichment by solid-phase extraction (SPE) using relatively low sample volumes, followed by the above mentioned analytical techniques may resolve complex samples, containing more than a dozen compounds in less than 10 minutes [7-10]. LC-MS, at high pressure, is the most appropriate analytical technique [11-14] for polar contaminants analysis and for monitoring plasma samples [15].

Identification and determination of phenol derivatives is a challenging task because of the extremely low levels at which they are present in the environment. Compared to other European countries, only limited research on distribution, occurrence and fate of phenol derivatives has been done in Romania.

In order to detect the pollution of rivers caused by industrial activities, there were successfully developed methods that use UPLC with UV detection and SPE procedure, as an alternative solution for the activity of a laboratory that does not possess expensive LC-MS/MS equipment [16].

Phenol derivatives, and especially chlorophenols, are toxic and they can affect both the odour and the taste of drinking water even at concentrations as low as a few $\mu\text{g/L}$ [17]. Chlorophenols and nitrophenols are included in the list of priority pollutants of both the US Environmental Protection Agency (EPA) and the European Union (EU) [18, 19]. In fact, the maximum concentration of these compounds for drinking water is set up at $0.5\mu\text{g/L}$ by EU Directive 2455/2001/EC.

In this context, the main objective of this work was to develop a LC-MS/MS method for the simultaneous multianalyte determination of phenol derivatives from water samples. As target analytes (see Table 3), different compounds representative of diverse classes of phenols (chlorinated and alkyl-derivatives), were selected based on the extent of their use, ubiquity and consideration as priority pollutants.

RESULTS AND DISCUSSION

Sample Extraction

In order to concentrate the sample and eliminate as much as possible the interferences of other compounds with the target analytes, an off-line SPE pre-concentration step was applied. In this step there were used two types of SPE cartridges: LiChrolut RP-18 and Oasis HLB (divinylbenzene-N-vinylpyrrolidone copolymer). Slightly better results were obtained with Oasis HLB, because some of the target compounds are relatively polar (with $\log P$ smaller than 2).

The influence of the volume of the sample was studied by passing through the SPE cartridge 100, 200 and 500 mL water sample. The best results were obtained with 500 mL sample volume. The weak step of the sample preparation procedure was the evaporation to dryness of the extract. The loss of analytes was somehow reduced by adding protecting solvents, like diethyl ether, acetone and acetonitrile. The best results were obtained when the SPE cartridge was eluted with a mixture of diethyl ether–methanol (9:1; v/v). For the studied analytes, having the logP between 1.4 and 5.8, the optimized procedure for sample preparation by solid phase extraction consisted in adding 500 μ L of 20% aqueous methanol solution (v/v) containing 1% acetic acid (v/v) to the residuum obtained after the evaporation of the organic solvents from the SPE eluate. In this way, a 1000-fold pre-concentration was obtained in the off-line SPE procedure.

Sample Analysis

Previous to the coupling with the mass spectrometer, an optimization of the liquid chromatographic separation was carried out using a PDA [20]. In order to optimize the separation and the peak shapes of all the target analytes, different mobile phases were studied. The two organic solvents, acetonitrile and methanol, commonly used in reversed phase liquid chromatography were tested. Taking into consideration the resolution of the separated peaks, the methanol gave slightly better results than acetonitrile. It was noticed that, to suppress the ionic mobility of the analytes, acidification of the LC mobile phases was necessary. For this, there were tested formic acid, acetic acid and trifluoroacetic acid. The best ionization and separation of target analytes was obtained using 1% acetic acid as additive in the mobile phases. To obtain a good resolution for the 15 compounds, taken under study, an elution gradient program was used, that allowed their separation in 7 minutes (8 min with column re-equilibration).

The main parameters for ESI interface in negative ionization modes were: desolvation temperature 350°C, source temperature 150°C, cone gas flow rate 50 L/h, desolvation gas flow rate 650 L/h, vaporizer gas (nitrogen) pressure 7.0 bar, and capillary voltage 4 kV. Full-scan data were acquired in negative mode by scanning from m/z 50 to 250, using a MS inter-scan 0.003 s, and inter-channel delays 0.003 s. For optimization of MS-ESI parameters, the analytes were injected directly in MS interface (direct infusion) at 15 μ L flow (concentration around 1 mg/mL). In this case, the scan time was set to 0.1 s. For each analyte, the most abundant and characteristic ion was chosen for quantification as shown in the Table 1.

Table 1. Retention times and optimized MRM parameters of the target compounds

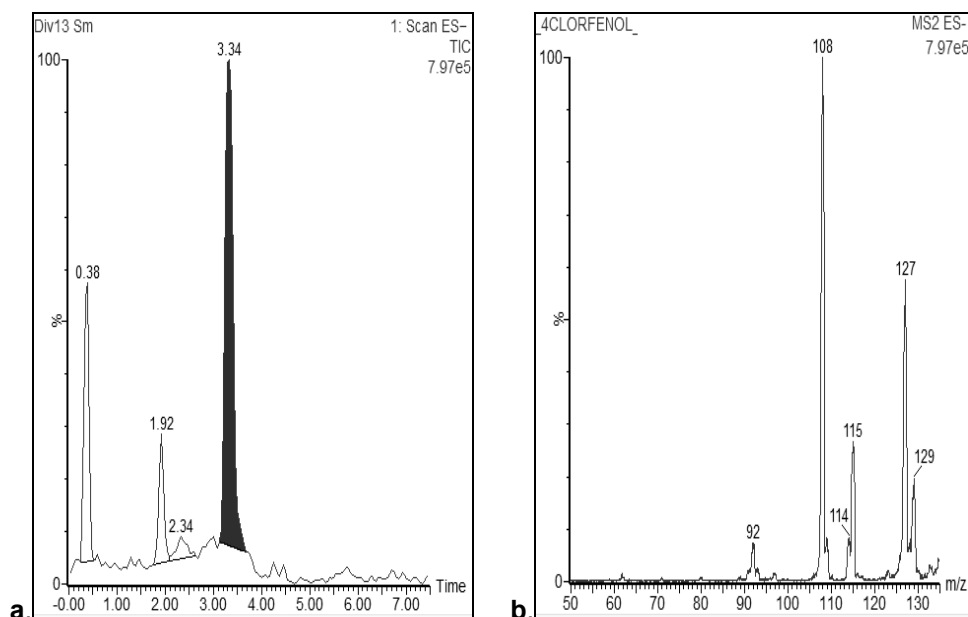
Analyte	Rt range (min)	Con voltage (V)	Collision energy (kV)	Quantification transition	Collision energy (kV)	Confirmation transition
Phenol	0.34-0.45	15	17	93>65	22	93>35
2,4-Dinitrophenol	0.51-0.84	20	15	183>137	20	183>91
4-Nitrophenol	0.91-1.32	15	15	138>93	25	138>65
4-Methylphenol	1.78-1.93	20	20	107>79	25	107>51
2-Methyl-4,6-dinitrophenol	2.25-2.43	25	25	197>105	30	197>51
3,5-Dimethylphenol	2.5-2.88	25	25	121>107	30	121>79
4-Chlorophenol	3.05-3.34	20	20	127>100	25	127>91
3-Methyl-4-nitrophenol	3.38-3.6	20	18	152>106	25	152>78
2,4,6-Trimethylphenol	3.96-4.05	22	23	134>119	35	134>79
4-Chloro-3,5-dimethylphenol	4.3-4.6	28	22	217>182	30	217>90
Bisphenol A	5.2-5.59	20	15	227>212	20	227>133
3,5-Dichlorophenol	5.71-5.98	20	20	162>127	25	162>91
2,4,6-Trichlorophenol	6.25-6.5	15	25	196>160	33	196>90
4-Tert-octylphenol	6.5-6.8	25	27	205>147	35	205>106
4-Nonylphenol	6.7-7.1	25	27	220>133	35	220>106

Method validation

Linearity of the method was good up to 250 µg/L (equivalent to 250 ng/L in samples, taking into account the pre-concentration factor) for all target compounds. The correlation coefficients were higher than 0.99. Recovery of the overall analytical procedure was evaluated by spiking tap water samples (n = 3) at two levels (10 and 100 ng/L). Recovery, expressed in percentage, represents the amount of analyte obtained in the last quantification step (after sample extraction procedure) in relation to the amount of compound added to the initial sample. These results can be seen in Table 2. The method was found to have good precision (with RSD < 20%), with recovery values ranged between 70 and 95% for all analytes. The limit of quantification (LOQ) was established at 5 ng/L for the majority of the analytes, and at 3 ng/L for those compounds having a recovery better than 80%. The procedure was found to be highly specific as no relevant signals were observed in the blanks at the retention times of the analytes.

Table 2. Average recoveries and relative standard deviations for three replicates of tap water spiked at two levels of analytes

Compound	10 ng/L		100 ng/L	
	Rec.(%)	RSD (%)	Rec.(%)	RSD (%)
Phenol	77.33	12.99	84.47	10.45
2,4-Dinitrophenol	78.33	11.27	83.57	9.80
4-Nitrophenol	77.67	12.97	85.43	10.33
4-Mehtylphenol	80.67	9.81	84.87	9.00
2-Methyl-4,6-dinitrophenol	81.33	9.52	88.33	8.46
3,5-Dimethylphenol	86.33	7.63	87.33	7.33
4-Clorophenol	84.67	8.50	95.03	5.21
3-Methyl-4-nitrophenol	83.00	9.22	96.00	6.22
2,4,6-Trimethylphenol	78.33	13.10	82.67	9.83
4-Chloro-3,5-dimethylphenol	76.33	13.28	81.33	9.49
Bisphenol A	83.67	8.96	87.67	6.80
3,5-Dichlorophenol	81.67	9.60	86.00	7.94
2,4,6-Trichlorophenol	81.67	12.84	82.67	8.98
4-Tert-octylphenol	74.33	13.65	78.00	14.48
4-Nonylphenol	71.00	16.32	76.00	13.04

**Figure 1. a.** The chromatogram of a sample of water collected from Bega watershed in the vicinity of Margina village (Timiș county); **b.** the MS spectrum which prove that the eluted peak at 3.34 minute is 4-chlorophenol (daughters of $m/z = 127$)

The UPLC-MS/MS method was used to determine the target analytes in water samples collected from Bega watershed. An example of such analysis is presented in Figure 1. An assessment of the pollution with some phenol derivatives from Bega superior watershed is presented elsewhere [21].

CONCLUSIONS

In this work, a method based on UPLC-MS/MS analysis, has been developed for the simultaneous, multianalyte determination of some selected phenol derivatives. With this method, most of the selected compounds can be determined with acceptable precision and accuracy, according to the method performance evaluation carried out with spiked tap water, at concentrations lower than 100 ng/L.

EXPERIMENTAL SECTION

Chemicals and Reagents

The working standards were all purchased from Sigma – Aldrich and some of their characteristics are listed in Table 3. For the stock solution there was used 1 µg/mL of each phenol derivative prepared in HPLC-grade methanol (14262 Fluka).

Table 3. List of target compounds included in the analyses

Compound	Abbreviation	CAS registry number	Elemental composition	Molecular mass
Phenol	Ph	108-95-2	C ₆ H ₆ O	94.11
2,4-Dinitrophenol	DNP	51-28-5	C ₆ H ₄ N ₂ O ₅	184.11
4-Nitrophenol	NP	100-02-7	C ₆ H ₅ NO ₃	139.11
4-Meethylphenol	MP	95-48-7	C ₇ H ₈ O	108.14
2-Methyl-4,6-dinitrophenol	MDNP	534-52-1	C ₇ H ₆ N ₂ O ₅	198.14
3,5-Dimethylphenol	DMP	108-68-9	C ₈ H ₁₀ O	122.17
4-Chlorophenol	CP	106-48-9	C ₆ H ₅ ClO	128.56
3-Methyl-4-nitrophenol	MNP	59-50-7	C ₇ H ₇ NO ₃	153.14
2,4,6-Trimethylphenol	TMP	527-60-6	C ₉ H ₁₂ O	136.2
4-Chloro-3,5-dimethylphenol	CDMP	88-04-0	C ₈ H ₉ ClO	156.61
Bisphenol A	BS	80-05-7	C ₁₅ H ₁₆ O ₂	228.29
3,5-Dichlorophenol	DCP	591-35-5	C ₆ H ₄ Cl ₂ O	163
2,4,6-Trichlorophenol	TCP	88-06-2	C ₆ H ₃ Cl ₃ O	197.45
4-Tert-octylphenol	TOP	140-66-9	C ₁₄ H ₂₂ O	206.33
4-Nonylphenol	NOP	25154-52-3	C ₁₅ H ₂₄ O	220.36

The other solvents and reagents were of chromatography quality, purchased from Sigma – Aldrich: mobile phase additive acetic acid 99% p.a. (A6283-ReagentPlus), diethyl ether (CHROMASOLV, 309966 Sigma), methanol LC-MS Ultra CHROMASOLV, tested for UHPLC-MS (14262 Fluka). SG Ultra Clear 2001-B Water Deionization System (Cole-Parmer) was used for the preparation of HPLC grade water and then filtered through syringe filters PTFE 0,22 µm (Teknokroma, Barcelona, Spain) right before use.

Sample Extraction

The sample preparation procedure was optimized using tap water samples that do not contain any trace of target analytes, fortified with a mixture of analytes of interest as a surrogate, at a concentration of 30 ng/L each. The solid-phase extraction cartridges (LiChrolut RP-18 and Oasis HLB) were conditioned with 5 mL of diethyl ether, 5 mL methanol and 5 mL of deionized water on a SPE manifold (Merck, Darmstadt, Germany) at a rate of 1–2 mL/min. A volume of 500 mL of water sample (neat tap water, tap water fortified with the analytes or real sample from Bega watershed), acidified with acetic acid to pH 5, was passed through the SPE cartridges at a flow rate of 2–3 mL/min. During the subsequent washing step, basic interferences were reduced by washing the cartridge with 5 mL of 5% methanol aqueous solution (v/v) containing 2% acetic acid (v/v) and 5 mL of deionized water; thereafter, the acidic interferences were removed by washing the cartridge with 5 mL of 5% methanol aqueous solution (v/v) containing 2% ammonium hydroxide (v/v) and 5 mL of deionized water. The compounds of interest were eluted with 6 mL of a mixture of diethyl ether–methanol (9:1; v/v). After elution, the solutions were evaporated to dryness at 40°C under a gentle stream of nitrogen. A volume of 500 µL of initial mobile phase was added in order to re-dissolve the residues and the resulting extracts were injected into the LC system after filtration through PTFE syringe disk filter.

Sample Analysis

Chromatographic analyses were performed using an AcquityUPLC™ system (Waters, Milford, MA, USA) and separations were carried out using an AcquityUPLC™ BEH C18 column (100×2.1 mm, 1.7 µm particle size) from Waters. The C18 column was equilibrated at 30°C. The analytes were separated with a gradient elution profile realized with a mobile phase consisting of methanol with acetic acid 1% (v/v) (eluent A) and an aqueous solution of acetic acid 1% (v/v) (eluent B). The analysis started with 20% of eluent A at a flow rate of 0.35 mL/min, for 0.3 minute. Then, the percentage of mobile phase A was increased linearly up to 75% in 3.0 minutes and further to 100% in 2.2 minutes; this composition was held for 2.0 minutes before being returned to 20% of eluent A, in 0.1 min, followed by a re-equilibration time of 0.4 minutes (total run time, 8 minutes). The injection volume was always 5 µL (full sample loop).

The UPLC system was coupled to a XevoTQD (T-wave quadrupole) mass spectrometer with an orthogonal Z-spray–electrospray interface (Micromass, Manchester, UK). For the purpose of optimizing the MS parameters, the selected analytes were dissolved in methanol: water mixture (50:50, v/v) with acetic acid 0.1%, at a concentration of 0.1 $\mu\text{g/mL}$ and infused at 15 $\mu\text{L/min}$. The MS was operated in the negative electrospray (ESI⁻) mode with a capillary voltage 4 kV [22]. The source and desolvation temperatures used were 150 and 350°C, respectively. Nitrogen was used as the desolvation and cone gas at the corresponding flow rates of 650 and 50 L/h, respectively. Collision-induced dissociation was performed using argon (99.995%, Linde, Timisoara, Romania) at a pressure of 2×10^{-3} mbar in the T-wave cell. The selected precursor ions of the analytes were fragmented to their product ions in the collision cell and the two most intensive product ions per analyte were chosen for quantitative and confirmation purposes. The ions were monitored for a dwell time of 0.022 or 0.036 s. Data acquisition was performed using MassLynx 4.0 software with QuanLynx program (Waters, Milford, MA, USA).

ACKNOWLEDGMENTS

This work was supported by the project 464 RoS-NET financed by the EU Instrument for Pre-Accession (IPA) funds, under the framework of the Romania-Republic of Serbia IPA Cross-border Cooperation Programme.

REFERENCES

- [1] Directive 98/83/EC of 3 November 1998 on the quality of water intended for human consumption, European Council, *Official Journal of the European Communities*, **1998**.
- [2] Directive 2000/60/EC of the European Parliament and of the Council of 23 October 2000 establishing a framework for Community action in the field of water policy, European Council, *Official Journal of the European Communities*, **2000**.
- [3] M.S. Diaz-Cruz, D. Barcelo, *Chemosphere*, **2008**, 72, 333.
- [4] S.P. van Leeuwen, J. de Boer, *J. Chromatogr., A*, **2008**, 1186, 161.
- [5] W. Giger, *Anal. Bioanal. Chem.*, **2009**, 393, 37.
- [6] N.S. Thomaidis, A.G. Asimakopoulos, A.A. Bletsou, *Global NEST Journal*, **2012**, 14, 72.
- [7] U. Bolz, W. Körner, H. Hagenmaier, *Chemosphere*, **2000**, 40, 929.
- [8] M. Kojima, S. Tsunoi, M. Tanaka, *J. Chromatogr., A*, **2004**, 1042, 1.
- [9] R. Liu, J.L. Zhou, A. Wilding, *J. Chromatogr., A*, **2004**, 1022, 179.

- [10] E. Pitarch, C. Medina, T. Portoles, F.J. Lopez, F. Hernandez, *Anal. Chim. Acta*, **2007**, *583*, 246.
- [11] J. Sun, F. Liang, Y. Bin, P. Li, C. Duan, *Molecules*, **2007**, *12*, 679.
- [12] R. Loos, G. Hanke, G. Umlauf, S.J. Eisenreich, *Chemosphere*, **2007**, *66*, 690.
- [13] A. Plazonic, F. Bucar, Z. Males, A. Mornar, B. Nigovic, N. Kujundzic, *Molecules*, **2009**, *14*, 2466.
- [14] H.-J. Chen, B.S. Inbaraj, B.-H. Chen, *Int. J. Mol. Sci.*, **2011**, *13*, 260.
- [15] L. Vlase, D. Mihiu, D.S. Popa, A. Popa, C. Briciu, F. Loghin, R. Ciortea, C. Mihiu, *Studia UBB Chemia*, **2013**, *58(1)*, 31.
- [16] I. Baranowska, B. Kowalski, *Bull. Environ. Contam. Toxicol.*, **2012**, *89*, 8.
- [17] C. Mahugo Santana, Z. Sosa Ferrera, M. Esther Torres Padron, J. Juan Santana Rodriguez, *Molecules*, **2009**, *14*, 298.
- [18] USEPA, "Sampling and Analysis Procedure for Screening of Industrial Effluents for Priority Pollutants", Method Report No. EPA 600-R-77-006, United States Environmental Protection Agency, **1977**.
- [19] Decision No 2455/2001/EC of the European Parliament and of the Council of 20 November 2001 establishing the list of priority substances in the field of water policy and amending Directive 2000/60/EC, European Council, *Official Journal of the European Communities*, **2001**.
- [20] A. Crăciun, E. Preda, M. Mincea, V. Ostafe, *Ann.W.U.T-Ser. Chem.*, **2010**, *19*, 105.
- [21] E. Preda, M. Mincea, C. Ionascu, A.V. Botez, V. Ostafe, *Environ. Eng. Manag. J.*, **2013** (*submitted paper*).
- [22] E. Preda, C. Ionașcu, M. Mincea, V. Ostafe, *Ann. W.U.T-Ser. Chem.*, **2012**, *21*, 101.

==ERRATUM==

1. STUDIA UBB CHEMIA, Volume 55 (LV), no. 4, 2010, pp. 161-168,

Title: OBTAINING PYRAZINE-2,3-DICARBOXYLIC ACID THROUGH
ELECTROCHEMICAL OXIDATION OF QUINOXALINE ON NICKEL
ELECTRODE

Author(s): POPA IULIANA, DRAGOȘ ANA, VLĂTĂNESCU NANDINA,
MARIUS DOBRESCU, ȚĂRANU BOGDAN

It also appeared in STUDIA UBB CHEMIA, Volume 56 (LVI), no. 2, 2011,
pp. 125-132. The remaining article is the one published in Volume 56 (LVI),
no. 2, 2011, pp. 125-132.

Article published in Volume 55 (LV), no. 4, 2010, pp. 161-168 is withdrawn.